Generalized Finite Elements for Transient Heat Diffusion Problems

Muhammad Iqbal

Institute for Infrastructure and Environment

Heriot-Watt University

This dissertation is submitted for the degree of
Doctor of Philosophy

School of Energy Geoscience
Infrastructure and Society

March 2019

Abstract

For many decades, the classical Finite Element Method (FEM) was successfully used to solve a wide range of problems that are governed by the scalar transient diffusion equation. It produced robust solutions with remarkable accuracy for a variety of problems with complex geometries and boundary conditions. However, the numerical solution still poses a serious challenge when it diffuses with steep gradients. This situation arises in many engineering problems, such as in glass cooling, where the temperature difference between the cooling object and the ambient environment is so large that it leads to severe thermal stresses. To properly model this behaviour, the conventional FEM uses highly refined mesh grids to accommodate the sharp change in the temperature field. Given that the problem is time dependent, computing the solution over refined meshes for thousands of time steps leads to prohibitively expensive solutions. To address this limitation, this thesis aims to assess a novel approach based on time-independent field enrichment for efficiently solving time-dependent heat diffusion problems over coarse mesh grids.

The approach consists to incorporate *a-priori* knowledge in the finite element approximation space through carefully selected functions that exhibit similar behaviour as of the true solution. In this work, Gaussian functions with various rates of decay are employed in combination with linear Lagrange polynomial-based finite elements, such that inter-element continuity is automatically satisfied. This technique provides a remarkable reduction of the computational cost, in comparison to the widely used classical low order polynomial-based FEM.

To test the accuracy and reliability of this approach, computable *a-posteriori* residual

error estimates that are mathematically rigorous; are developed and implemented for both two and three-dimensional problems. The proposed estimates are straightforward to implement and are shown to provide reliable and practical upper bounds for the numerical errors, independent of the heuristically chosen enrichment functions. The estimates accurately capture the decrease of the error as the number of enrichment functions is increased or the time step is reduced. However, ill-conditioning is shown to be an inherent feature of the field enrichment. Therefore, the proposed error estimates are used to adaptively enrich the element field in subdomains with relatively higher errors. Both the global error, in the whole space–time domain, and local error indicators in the individual elements of the mesh are investigated, for the adaptive selection of the enrichment functions. An adaptive algorithm is proposed to identify the elements with higher errors so that further enrichments are added locally; leading to significant savings in comparison to the case with uniform enrichments.

I would like to dedicate this work to my loving parents. I lost both of them during the course of my studies.

Acknowledgements

First of all, I would like to offer my profound gratitude to Prof. Omar Laghrouche for his inspiring supervision, insightful advice, and encouragements throughout my Ph.D. He provided not only the primary motivation for this work but also lots of invaluable suggestions and comments throughout the progress of the research. Despite his busy schedule, he has always been available for discussion of the findings and rationalization of new ideas, which was critical to the successful completion of this thesis. His in-depth knowledge of numerical analysis in general and enriched FEM, in particular, has been invaluable. I am also thankful to him for his patience, kindness and continuous support. It has been a privilege to work with him.

I would also like to acknowledge the support and supervision of Dr. Shadi Mohamed; he provided a lot of invaluable suggestions to improve my work. He is the one who was easily approachable and always available for help and advice. He always provided me guidance whenever I got distracted during the course of my work. He motivated me and helped me to keep positive throughout my Ph.D, whenever the going got tough. His broad knowledge of computer programming and finite elements has offered countless critical and very valuable suggestions for the improvement of my research.

Dr. Heiko Gimpelein, my supervisor, and a truly dedicated mentor; this work would not have possible without his continuous support and supervision. His helping, compassionate and supportive role played a very important role in the completion of this thesis. Day or night, weekdays or weekends, even holidays; he was always there to provide me help and support. Due to his commitments, whenever he was not

able to meet in the university; he offered me coffee in the city centre to discuss the problem and provided me the way forward. I learnt a lot from him. His far-reaching knowledge of enriched finite elements and the underlying theories was the great source of learning for me. I would not be wrong in mentioning that I learnt the physics of enriched FEM from him. It has been an amazing experience to work with him and I thank him wholeheartedly.

To my friends and colleagues, thank you for supporting, offering me advice, and guiding me through this entire process. The much needed emotional support and motivation provided by Ali Hassnain, Afaq Ahmad and Mubbashar Mehmood was really encouraging. Special thanks to Mayank Drolia and Konstantinos Christodoulou who were always there for help and support whenever I got stuck in my work.

I am greatly indebted to Heriot-Watt University for the financial support provided to me through the prestigious James Watt scholarship. Without this financial support, this work would not have been possible.

Finally, I gratefully acknowledge my beloved family for their much needed constant support, encouragement and love throughout this work.

Declaration

The work in this thesis is based on the research carried out in the Institute of Infrastructure and Environment, School of Energy, Geoscience, Infrastructure and Society, Heriot-Watt University. I hereby declare that except where specific reference is made to the work of others, the contents of this dissertation are original and have not been submitted in whole or in part for consideration for any other degree or qualification in this, or any other University. This dissertation is the result of my own work and includes nothing which is the outcome of work done in collaboration, except where specifically indicated in the text.
Part of this work have been published, submitted or presented in the following journal papers and conferences; where the co-authors mentioned in the publications are my PhD supervisors.

Journals

Iqbal, M., Gimperlein, H., Mohamed, M. S., and Laghrouche, O. (2017). An a posteriori error estimate for the generalized finite element method for transient heat diffusion problems. *International Journal for Numerical Methods in Engineering*, 110(12):1103–1118.

Conferences

Iqbal, M., Mohamed, M. S., Laghrouche, O., Gimperlein, H., Seaid, M., Trevelyan, J. Solution of three dimensional transient heat diffusion problems using an enriched

finite element method. *Proceedings of the* 24^{th} *UK Conference of the Association for Computational Mechanics in Engineering*, Cardiff University, UK, 31 March–01 April 2016.

Iqbal, M., Gimperlein, H., Mohamed, M. S., Laghrouche, O. An investigation of the accuracy of the partition of unity method for time dependent heat transfer problems. *Proceedings of the* 3^{rd} *Infrastructure and Environment Scotland Conference*, Heriot-Watt University, UK, December 2015.

Iqbal, M., Gimperlein, H., Mohamed, M. S., Laghrouche, O. a-posteriori error estimate for the partition of unity method for transient heat diffusion problems. *Proceedings of the* 23^{rd} *UK Conference of the Association for Computational Mechanics in Engineering*, Swansea University, UK, 8–10 April 2015.

Iqbal, M., Gimperlein, H., Mohamed, M. S., Laghrouche, O. Partition of unity finite element method for time-dependent diffusion problems: an error estimate for the method *Proceedings of the* 2^{nd} *Infrastructure and Environment Scotland Conference*, University of Edinburgh, UK, September 2014.

Muhammad Iqbal

March 2019

Table of Contents

List of Figures

List of Tables

Nomenclature & Abbreviations

(ξ, η, ζ)	element coordinates
(r, θ)	polar coordinates
(x, y, z)	Cartesian coordinates
A_j^q	amplitude of enrichment function at a nodal point
C_1, C_2	constants in hyperbolic tangent function
E	element edges
G_q	enrichment function
G_q^{tanh}	hyperbolic tangent function
K	total number of elements
K_b	elements on the boundary
M	total number of nodes
M_b	nodes on the boundary
N_i	polynomial shape functions
P_r	weight function in GFEM
$P_{(j-1)Q+q}$	new shape function in GFEM

Q	total number of enrichment functions
R_c, C	constants in the enrichment function G_q
T	total solution time
W	weight function in FEM
$[S]$	global stiffness matrix
$[S^e]$	element stiffness matrix
Δt	time step value
Δ	Laplace operator
Γ	domain boundary
Γ_e	element boundary
Ω	problem domain
Ω_e	element domain
κ	condition number
λ	heat diffusion co-efficient
∇	gradient operator
∂	partial derivative
$\mathbf{n}$	outward unit normal
$\{F\}$	force vector
$\{F^e\}$	element force vector
$\{G\}$	boundary integral vector

$\{G^e\}$	element boundary integral vector
d_i	inner diameter
d_o	outer diameter
f	heat source/sink
g	boundary source
h	element size
n_x, n_y, n_z	outward unit normals in x, y and z directions
p	order of polynomial
q	enrichment function number
r_i	inner radius
r_o	outer radius
t	time variable
u	temperature at any point
h	convection heat transfer co-efficient

Acronyms / Abbreviations

1D	one-dimensional
2D	two-dimensional
3D	three-dimensional
DOFs	degrees of freedom
FDM	finite difference method

FEM	finite element method
GFEM	generalized finite element method
PDEs	partial differential equations
PU	partition of unity
PUFEM	partition of unity finite element method
PUM	partition of unity method
QoI	quantity of interest
TOTDOF	total degrees of freedom
XFEM	eXtended finite element method

Chapter 1

Introduction

1.1 Background

The scalar time-dependent diffusion equation describes the evolution of heat transfer in many physical, chemical and biological phenomena. From daily life to industrial applications, there are numerous examples involving heat transfer processes. Such examples include heating food and cooling down drinks. They also include metal forming and glass manufacturing, among many other applications. For the latter case, for example, the hot molten material is cooled down to the ambient temperature to obtain the sought glass. For good quality product, this cooling process must be carefully controlled to avoid excessive thermal gradients, which may lead to cracking of the material and hence affecting its quality [188, 192]. The time-dependent heat diffusion equation can be used to model such problems to predict the temperature variation during this cooling process. It is also used to solve problems in thermal radiation [66] and in biomedical engineering to model the process of optical tomography [99]. Further applications can be found in the references [126, 129, 130].

1.2 Motivation

For decades, the standard finite element method has been successfully used for the accurate and robust solution of 2D steady-state and transient heat diffusion equations. Although the computer architecture and design have become much more advanced in recent times, the solution of most practical 3D problems using classical finite element methods is still a complex and computationally extensive task. For an acceptable accuracy, an unreasonably large number of DOFs are required for 3D problems [139], which makes the efficient simulation very difficult and challenging. This difficulty is further augmented with the transient nature of the problems. The solution of excessively large number of equations at every time step makes the solution very time consuming. The very fine mesh grids required for FEM solution also require very refined time step values, which further complicates the simulation [140]. Another difficulty arises when diffusion equations need to be solved in combination with problems governed by hyperbolic PDEs [165]. The presence of steep fronts and boundary layers in these coupled parabolic-hyperbolic problems pose severe numerical complications [98, 164, 165]. The standard finite element with piecewise continuous polynomial interpolation functions cannot resolve these steep fronts unless a substantially refined mesh grid, or higher order polynomial basis functions are used [187].

In the past two decades, domain based methods with field enrichment have been developed to overcome such difficulties. The main idea of the field enrichment consists to incorporate *a-priori* knowledge about the problem to be solved by introducing specifically designed functions into the approximation space. Such techniques include the Partition of Unity Finite Element Method (PUFEM), the Ultra-Weak Variational Formulation (UWVF), the Discontinuous Enrichment Method (DEM), the Generalised Finite Element Method (GFEM), the Variational theory of Complex Rays (VTCR) and many other techniques which will be discussed in the literature review. This current work is motivated by the use of GFEM for transient heat diffusion problems in 2D and 3D domains.

1.3 Aim and objectives

Field enrichment methods were mainly explored and tested for short wave modelling problems and crack propagation problems, while their use for the simulation of transient heat transfer problems is relatively recent and still developing. The main aim of this work is to further develop the two-dimensional finite element model with time-independent Gaussian functions enrichment and extend the concept to three dimensions, for the solution of transient heat diffusion problems. The main objectives to achieve this aim are as follows:

- Carry out a literature review on the development of domain based methods with field enrichment for the solution of challenging engineering problems and demonstrate the need for an efficient technique for the solution of transient heat diffusion problems with sharp gradients.
- Revisit the two-dimensional time-independent Gaussian function enriched finite elements and develop computable *a-posteriori* residual error estimates to provide reliable and practical upper bounds of the associated numerical errors.
- Extend the time-independent Gaussian function enriched finite elements to three dimensions and present the related *a-posteriori* residual error estimates.
- Develop an adaptive approach with variable enrichment whereby subdomains with relatively higher errors are further enriched.
- Carry out numerical investigations to assess the effectiveness of the developed enriched elements, the associated *a-posteriori* residual error estimates as well as the proposed adaptive approach to effectively solve transient heat diffusion problems.

1.4 Thesis outline

This work is presented in eight chapters with the first chapter giving the background for the research and stating the aim and objectives to achieve. In Chapter 2, a review of the most widely used numerical technique, FEM, for various engineering problems is discussed along with its merits and limitations. To address the shortcomings of the conventional FEM, various enriched finite element approaches are discussed including their applications.

The formulation of the Gaussian function enriched FEM, names here the Generalised FEM (GFEM), for transient heat diffusion problems is discussed in Chapter 3. The boundary value problem and its weak formulation are presented stating the approximate solutions for both classical FEM and GFEM. The integration of the element matrices and the solution of the resulting global system for both models are discussed. Some numerical results showing the advantages of GEFM over low-order FEM to deal with heat diffusion problems exhibiting sharp gradients are presented.

Chapter 4 deals with the developed three-dimensional version of GFEM and its assessment against FEM. Three problems are considered to assess the approach, with one problem exhibiting a known analytical solution to allow the computation of the modelling errors. In the two other problems, the GFEM solution progress in time is compared to a reference FEM solution on a well refined mesh.

In Chapter 5, the need for error estimation for approximate numerical methods is emphasized and the contributions to address the issues of reliability and accuracy of these approximate methods are also highlighted. An *a-posteriori* error estimate is then developed to test the robustness of GFEM. A Detailed mathematical derivation of the proposed error estimate is presented for two-dimensional problems, followed by numerical experiments to show its validity.

The previously developed error estimate is used to formulate, in Chapter 6, an adaptive algorithm to allow variable local enrichment. A detailed iterative procedure to spot elements in the computational domain with high errors is presented. Extra enrichment

functions are then added locally to improve the quality of the results and reduce the overall error. This further reduces the required Degrees of Freedoms (DOFs), in comparison to uniform enrichment, for the same accuracy.

In Chapter 7, the use of the error estimate presented in Chapter 5 is extended to the three-dimensional case with test examples confirming the conclusions drawn for the two-dimensional case.

Chapter 8 summarises the main concluding remarks and gives some recommendations for potential future work.

Chapter 2

Enriched finite element methods – An introduction and review of past work

2.1 Introduction

Many of the real world phenomena arising in physical, chemical, biological and mathematical sciences are governed by partial differential equations (PDEs). These equations arise in the mathematical modelling of diverse subject areas like material sciences, fluid dynamics, heat transfer, electromagnetism, financial modelling as well as economy. In the majority of the situations today, it is found necessary to obtain approximate numerical solutions to these problems rather than the exact solutions. The reason being that the equations are so complex that to find their solution by exact analytical methods is either impractical or impossible and one has to seek approximate numerical solutions to the problems under consideration. The advancement in digital computations made it possible to solve these complex problems approximately, and it became a common tool for engineers and scientists to analyze practical problems arising in different fields of engineering and sciences. To solve these complex problems approximately, the two commonly used techniques are the finite difference method (FDM)

and FEM. In both of these methods, the complex differential equations are replaced by a set of linear or non-linear algebraic equations. In FDM the governing differential equations are converted to finite difference equations by using Taylor's expansion. It is one of the oldest technique and can provide quick approximate numerical solutions to certain types of PDEs [9]. The usage of FDM is limited, however, to simple geometries only as it cannot handle large problems with complicated geometries. As a consequence, its usage is restricted to simple academic problems [44]. FEM, on the other hand, is a well established numerical technique for a wide variety of problems and can handle complex geometries easily. Due to this capability, FEM is the most widely used numerical technique for engineering and scientific computations.

This Chapter will focus mainly on FEM approaches starting with the polynomial based approach and then extend the review to enriched approaches. It is worth mentioning that the Boundary Element Method (BEM) has also seen similar developments to FEM in the sense that enriched approaches were also developed for various problems but will not be included in this literature review. As one of the main objectives of this current thesis is to investigate the accuracy of enriched FEM using *a-posteriori* error estimate, a concise discussion on different error estimation procedures for finite element methods in general and enriched FEM in particular is also presented in this chapter.

2.2 Finite Element Method

The finite element method is a numerical technique that can be used to accurately solve complex problems in engineering and sciences. This method originated in the 1950s for the solution of structural mechanics problems. The main motivation was to solve complex problem arising in the aerospace industry [109]. Later its potential was recognized for different complex problems in engineering and other areas of applied sciences. In FEM, a continuous problem is discretized into finite number of small regions called elements. The overall governing equation for the problem is ob-

tained by combining the stiffness matrices and force vectors of the individual elements. This discrete representation is then solved to calculate an approximate solution of the continuous problem.

In recent years, the finite element method has become one of the well established and most widely used numerical technique. Due to its capability to handle various complexities, this method became an active research area in applied mathematics. One of the main reasons for the popularity of this method in different fields of science is its general purpose programming. A general computer program once written can be used for a wide variety of applications by simply changing the input information [159]. Many of the commercially available platforms to calculate the approximate numerical solutions of many real-world problems are based on the FEM formulation. In engineering, this method became popular due to its capability to handle complex geometries easily, and thanks to the development of high computing power, the solution of complex engineering problems is nowadays more convenient than before.

The finite element method is used effectively for solving complex problems in engineering and sciences that are governed by steady-state partial differential equations. FEM provided very robust and accurate solutions to many potential steady state problems, but there are many engineering applications which are governed by time dependent PDEs. These problems may involve complex geometries and need discretization both in spatial and time variables [126]. The solution of these problems with classical FEM is still a considerable task and computationally very intensive. Problems in thermal radiation [66, 129, 166], optical tomography [99], the cooling down of molten glass [188, 192] and transient wave propagation problems [79] are some other applications requiring high computational effort and resources. There are also problems in fracture mechanics requiring very fine meshes to solve the problems of crack propagation and capture the involved singularities.

Various meshless and generalized finite element methods have been formulated to overcome these difficulties. A survey of meshless methods can be found in [12, 32], and their mathematical theory in [114, 115]. PUFEM, GFEM and XFEM are examples of

the methods that have emerged in the literature to ease the need of very fine meshes and high computation costs. The main idea of these techniques is to use *a-priori* knowledge about the problem in hand and enrich the finite element approximation space with special functions. The basis of the partition of unity concept was developed by Melenk and Babuška [123]. A brief introduction to the history and the basic concept of these methods is given in the coming sections followed by a detailed list of contributions by different researchers who used these methods to solve complex problems in a variety of applications.

2.3 Partition of Unity Finite Element Method

The roots of PUFEM lie in the idea to use *a-priori* knowledge about the differential equation to be solved with FEM. In classical FEM the approximation is made with polynomial trial functions, but in PUFEM the formulation of the trial functions incorporates known information about the solution of the problem under consideration. The core idea of PUFEM was originally proposed by Babuška et al. [14, 15]. Later Melenk [122] worked on the details of the method in his Ph.D thesis titled "On Generalized Finite Element Methods". In their work, Melenk and Babuška [123] presented the complete mathematical basis of PUFEM. They detailed how to construct efficient and robust methods by including *a-priori* knowledge about the solution of the differential equation under consideration. They showed that the partition of unity property of the classical interpolation functions allows to include suitable enrichment functions in FEM approximation space for a more effective and efficient solution. The motivation behind this method was to develop a technique which can solve those problems efficiently, where the classical FEM technique is prohibitively expensive. A similar approach to model the electromagnetic scattering phenomena was also used by de La Bourdonnaye [45]. Mayer and Mandel [121] reported similar approach with the name Finite Ray Element Method. They solved the Helmholtz equation with this method using plane waves as basis functions.

PUFEM emerged as a powerful technique capable of solving complex engineering problems governed by steady-state and time-dependent partial differential equations. The method has shown a significant reduction in computation time and memory requirements for complex engineering problems.

The main features of PUFEM are:

1. It allows to include *a-priori* information about the differential equation of the problem in the ansatz spaces.

2. It permits the construction of ansatz spaces of any required regularity; this allows the construction of trial spaces for the variational formulation of higher order differential equations.

The above two features characterise the core theme of PUFEM. The first point is associated with the local approximation properties of the trial spaces, and the second point is closely associated with the conformity of the constructed spaces.

2.4 Generalized Finite Element Method

The main idea of the Generalized Finite Element Method was originally introduced under different names; Babuška et al. [15] called it 'special finite element methods on one occasion and the 'partition of unity method' [17] on another, and later on it was called as 'generalized finite element' [122]. At the same time, Duarte and Oden independently introduced this method under the name '*hp* clouds' [54, 58, 59], while Liszka et al. [113] termed it as '*hp* meshless cloud method'. In a later work, it was called as 'cloud-based *hp* finite element method' by Oden et al. [136]. The fundamental idea of $h-p$ cloud spaces is based on the partition of unity. The Partition of Unity method (PUM) developed by Melenk and Babuška [123] allows using any Partition of Unity with the local enrichment functions. GFEM, in fact, is a particular instance of the PUM where the conventional "hat-functions" of FEM serves as the PU [27, 92].

The partition of unity in a domain Ω is a set of functions $\varphi_I(\mathbf{x})$ such that

$$\sum_{\forall I} \varphi_I(\mathbf{x}) = 1, \quad \forall \mathbf{x} \in \Omega$$

For GFEM, the function $\varphi_I(\mathbf{x})$ is the piecewise linear polynomial shape function used in the standard Galerkin method. The partition of unity property allows the field enrichments to be reproduced exactly. If $G(\mathbf{x})$ is a function used to enrich a finite element solution space; then in case of GFEM, the multiplication of standard "hat-functions" with $G(\mathbf{x})$ will reproduce $G(\mathbf{x})$ exactly [32]. With the introduction of parameters A_j, the ansatz functions to approximate the numerical solution is written as

$$u^n(\mathbf{x}) = \sum_{\forall I} \varphi_I(\mathbf{x}) \; A_j \; G(\mathbf{x})$$

where $u^n(\mathbf{x})$ is the approximate numerical solution at any time instant n and A_j are the new nodal unknowns. The parameters A_j adjust the amplitudes of the enrichment functions $G(\mathbf{x})$ such that they best approximate the solution of the problem at hand. In GFEM, the finite element shape functions $N_j(\mathbf{x})$ constitutes the partition of unity, i.e.,

$$\sum_{j=1}^{M} N_j(\mathbf{x}) = 1, \; \forall \mathbf{x} \in \Omega$$

Strouboulis et al. [174, 176] introduced GFEM as a combination of standard finite elements and the enriched partition of unity finite element method. They multiplied the special functions of the partition of unity method with the standard vertex shape-functions which were then used in combination with the existing finite element basis to make an augmented conforming finite element space. They described following three major advantages of GFEM

1. As in standard FEM, the necessary boundary conditions are imposed exactly, which is a major issue in other partition of unity based finite element methods.

2. The accuracy of the constructed approximation space is not affected by errors

in the integration of the applied special functions.

3. The problem of linear dependencies in the system of equations are eliminated with an easy adjustment in the direct solver

Also in their later work [177], GFEM is described as an extension of the finite element method. The authors argue that complex engineering problems which are practically impossible to be solved by standard FEM can be accurately solved by GFEM. They used GFEM for the 2D Laplacian in domains containing hundreds of cracks and voids. They argue that to solve such kind of problems would be practically impossible with standard FEM. Duarte et al. [55] also described the GFEM formulation and the main idea behind it. They solved 3D elasticity problems and demonstrated the advantages of GFEM over the standard FEM through numerical examples. Babuška et al. [13] represented an overview of the core theme of GFEM. They presented some basic results and future prospects of this method. Duarte and Simone [53] also presented an introduction of PUFEM and GFEM.

GFEM has not only shown its effectiveness for steady–state elliptic equations [123], but it has also been proposed to overcome similar difficulties for transient problems [52, 79, 126, 129, 130, 132, 144]. As it is based on a variational formulation of the underlying PDE, GFEM inherits the stability and accuracy of finite elements, but allows to adapt the trial and test functions to reflect *a-priori* information about the physical properties of the considered problem. Similar to the time–independent case, the method shows a reduction in computation time and memory requirements for complex engineering problems, given reasonable enriched approximation spaces.

2.5 eXtended Finite Element Method

The eXtended finite element method [31, 49] was introduced by Belytschko and Black in 1999. They used the information from the analytical solution of a problem and introduced this information in the FE approximation space using the concept of the partition of unity. Their work launched a large body of information in the field of

computational mechanics. In a recent review, Belytschko et al. [32] presented the development and application of XFEM for solving different engineering problems. The modelling of crack propagation is the most established application of XFEM with multiscale modelling as the recent interests. Rannou et al. [158] presented a multi-grid XFEM for the modelling of 3D crack growth. They also included the multi-level adaptive refinement procedure around the surface of the crack. XFEM has also been incorporated in some of the commercial codes, e.g., ABAQUS and LS-DYNA [1, 118]

2.6 Selection of the enrichment functions for enriched finite element methods

Enriched finite elements incorporate special functions into the finite element method approximation to solve the problem. These special functions called enrichment functions are chosen based on an approximate analytical solution of the problem. Suitably chosen enrichment functions provide better approximation than the standard polynomial shape functions used in the classical finite element method. In fact, the effectiveness of the enriched FEM depends on the proper selection of the enrichment functions [11]. Babuška and Banerjee [10] also mentioned that the accuracy of GFEM solution depends on the choice of the enrichment function. Some examples of suitable enrichment functions for specific application can be found in [13]. Munts et al. [132] used polynomial and exponential enrichment functions to solve 1-D convection-diffusion problems. For the considered problem, it was concluded that exponential enrichment functions are more efficient than the polynomial enrichments.

In an ideal scenario, the enrichment functions should comprise the asymptotic solution space or represent the solution of the PDE at hand. Instances of taking enrichment functions that are known to be complete for the PDE are found in solving wave propagation problems. In order to solve Helmholtz and elastic wave problems, the wave potentials are expressed as linear combinations of plane waves which are known to be the solution of the underlying problem. This idea has been adapted to

solve these potential problems using the PUFEM [61, 106, 107], ultraweak formulations [40, 83, 84], boundary element methods [108, 152], and discontinuous Galerkin methods [186, 187, 196]. It has also been presented in the context of the GFEM [56, 175, 179].

A prominent example in a different direction, fracture mechanics, is given by XFEM [31, 181]. Here the enrichment functions are taken from the asymptotic solution space and reproduce the singular displacements or stresses locally around a crack tip [49]. Similar enrichment functions have been used for modelling crack propagation using meshless [133] and boundary element methods [168, 169]. An overview of XFEM and its applications can be found in the work of Fries and Belytschko [68]. Hansbo and Hansbo [80] presented a technique similar to XFEM to deal with strong discontinuities within FEM framework. Aquino et al. [8] generated enrichment functions for the GFEM using experimental and simulated data. They used the proper orthogonal decomposition (POD) technique. POD produces low-order subspaces containing general information regarding the solution of the problem in hand.

Other enrichments may include functions that do not represent the actual solution but somehow approximate the solution of the problem in hand. An intuitive knowledge can be used to form enrichment functions that are not necessarily solutions of the PDE of the problem. This is particularly helpful for problems where no exact solution space is available. Mohamed et al. [126] showed that such approximate enrichment functions allow for improved accuracy for a prescribed number of degrees of freedom. In their work, they used Gaussian functions to construct the enrichment functions to capture the time varying temperature fields. They argue that these functions are easy to formulate and implement, with their implementation in existing codes not requiring major changes. Similar enrichments for solving transient heat transfer problems are also proposed in [129, 130]. A comprehensive discussion on the selection of enrichment functions is also detailed there.

2.7 Applications of the enriched finite element methods

The enriched finite element methods are effectively used to solve engineering problems both in solid and fluid mechanics. In solid mechanics, they were effective in the solution of problems involving discontinuities, voids, cracks and complex geometries. In fluid-dynamic applications it would be effective to capture strong continuous variations in the domain using coarse meshes, for instance, it would be beneficial in viscous flow regions associated with wall-bounded flows. Munts et al. [132] considered the performance of enriched FEM on a model problem for such phenomena. In their work, they presented the solution of linear diffusion equation for 'Stokes' second problem. The solution of steady state and transient heat problems are among the other phenomena where enriched FEM can be used effectively. Various application of the extended finite elements can be found in [2, 32, 68] and the citations therein. The remaining of this chapter details the most relevant areas where these methods are used and have shown their effectiveness. The literature reveals that enriched finite element methods are mainly explored for the analysis of crack propagation and short wave modelling problems. For the completeness of review, besides the heat transfer problems, the usefulness of enriched finite element methods for short wave modelling and fracture mechanics problems is also discussed here.

2.7.1 Applications to wave propagation problems

Enriched FEM has been thoroughly investigated for time–harmonic wave problems in acoustics and elasticity. For wave problems it appears in different forms; there is the nodal plane wave basis [61, 104, 128, 146], the least square method [131], the ultraweak variational formulation (UWVF) [85] and the variational theory of complex rays (VTCR) [101, 102]. There are also other more powerful methods for efficiently solving wave problems with coarse mesh grids, namely the generalized finite element

method [174, 176], the discontinuous enrichment method (DEM) [65, 187, 196], Plane wave discontinuous Galerkin (PWDG) [69] and a more recent stable discontinuous Galerkin method [6].

Laghrouche and Bettess and co-authors [103–105] used the PUFEM approach for solving short wave diffraction problems. They used plane waves at different angles as the basis functions to capture the solution. For an acceptable accuracy, the usually used many nodes per wavelength was avoided by using the PUFEM approach. The overall size of the whole system was greatly reduced as each element spanned many wavelengths. In [106], the authors used the PUFEM approach to solve the Helmholtz problems where the wave speed is not constant and presents jumps in the various regions of the solution domain. To ensure the continuity between different regions, they used Lagrange multipliers. For engineering accuracy, around 10 nodes are required per wavelength for the classical linear polynomial based FEM which limits the accuracy of this method. To address this limitation, the authors used *a-priori* knowledge about the waves and formulation. Desmet and Vandepitte [47] reported that, in high frequency acoustic and vibro-acoustic problems, the conventional element based methods are computationally expensive. The main limitation of these methods is that the necessary number of degrees of freedom becomes very large for high frequency problems in large domains. A similar behaviour was previously reported by Chadwick et al. [41] for the diffraction of short waves. Another example is the work of Bettess [34] where the author considered the waves emitted by a radar and intercepted by an aircraft.

Perrey-Debain et al. [151] solved the 3D Helmholtz equation using plane wave based finite elements and boundary elements. The approach largely reduced the required degrees of freedom and complexity of the problem to get an accurate solution. They considered plane waves in different directions which were evenly distributed around a sphere. They reported that accurate solution can be obtained for much higher frequencies than the conventional polynomial based FEM and BEM. Gamallo and Astley [72] used the PUFEM technique to solve non-uniform 2D flows. They enriched the finite element space with plane waves by keeping the wave number as

a function of Mach number. A range of the Mach numbers was considered, and the solution was investigated for accuracy and condition number for a series of frequencies.

Strouboulis et al. also used enriched GFEM to solve Helmholtz problems. In the first part of their work [175], they investigated the convergence of the method. They used different numerical examples to show the effectiveness of the method. In the second part [179], they discussed how the solution is affected by using different approximating functions. They discussed the effect of boundary conditions on the overall error of the solution. Strouboulis and Hidajat [178] also discussed the effect of different approximation functions in the context of PUFEM. They used plane waves and Bessel functions to enrich the solution. They argue that the plane waves, which involve only trigonometric functions, are a better choice as compared to Bessel functions.

El Kacimi and Laghrouche [61, 63] modelled the 2D time harmonic elastic wave problems accurately with PUFEM. They used a low number of elements that contain many wavelengths per nodal spacing without the need of mesh refinement at each frequency. Enrichment based on the plane waves and the standard piecewise linear shape functions provided much better results with less DOFs as compared to standard FEM. The results show very good accuracy in approximating the displacement field. They used 4-noded and 9-noded elements, and discussed the results based on the conditioning and accuracy of the solution. They reported better accuracy for 9-noded elements as compared to 4-noded elements but with poorer conditioning. They extended their work [62] by proposing an improved numerical scheme by using an exact integration scheme to evaluate the oscillatory integrals for time harmonic elastic wave equations. The scheme was also based on the PUFEM approach and pressure (p) and shear (s) plane waves were superimposed locally to improve the results. They used very coarse meshes to solve 2D elastic wave problems. More recently, Banerjee and Sukumar [25] also used the exact integration scheme to evaluate the integrals. They solved two dimensional Helmholtz problems using plane-wave based enriched partition of unity method. The computation of highly oscillatory integrals using the exact integration scheme produced much better results for any wave number. They considered

structured and unstructured triangular meshes to show the accuracy of the method.

Laghrouche and Mohamed [107] used the PUFEM approach for solving the Helmholtz problems at high wave numbers. They used oscillatory shape functions to capture the solution. The oscillatory functions were obtained as a result of the multiplication of piecewise linear shape functions and plane waves or Bessel functions. To test the method they considered the problem of an incident plane wave diffracted by a rigid circular cylinder. At the same time Mohamed et al. [128], discussed numerical aspects of the PUFEM by solving Helmholtz problems in two dimensions. They considered the numerical aspects that affect the efficiency of PUFEM namely plane-wave enrichment, the geometry discretization, h-refinement and the conjugated or unconjugated formulation. More recently Mahmood et al. [119] extended this work to 3D problems.

Ham and Bathe [79] proposed to use a general pattern of multiple waves to capture the solution of high wave numbers. The authors argue that many researchers incorporated specific enrichments for wave propagation problems in the solution space, but the *a-priori* knowledge about many practical problems in wave propagation is not known in general. In reality, the solution is often a combination of unknown waves and different propagations and in cases may involve wave conversions. Therefore they considered enrichment with general multiple wave patterns, a better way to capture the solution.

The work of Ihlenburg and Babuška [86] is a good example where they reported the deterioration of results for high wave number k. They used the h-version of the standard FEM to capture the solution of the Helmholtz equation. They mentioned that the quality of FEM solution significantly depends on the wave number k. The mesh size h should be adjusted to the wave number k for good quality result with the usually followed "rule of the thumb" of $kh = constant$. With a low k, this rule produces significantly better results, but at a high value of k, it leads to deterioration of the results. In their later work [87], they used the hp version of FEM to solve the same problem. Bayliss et al. [30] also show that for $kh = constant$, the error grows with higher values of k. They solve the Helmholtz equation in two dimensions

using the piecewise linear FEM. Ortiz and Sanchez [146] also mentioned that the standard FEM produces reliable results for low and medium frequencies with a moderate number of degrees of freedom. They mentioned that with the increase of the wave number, the results of the numerical solution deteriorate even if the usual rule of thumb of 10 nodes per wavelength is followed. They used the PUFEM approach to get better results to solve wave diffraction problems. The boundary conditions proposed by Higdon [81] were investigated. To avoid the problem of conditioning they used conjugate-gradient type solvers [110]. In later work, Ortiz [145] solved the scattering of surface water-waves using plane waves as basis. They investigated the combined phenomena of diffraction, radiation, refraction and absorption. The integration scheme which was originally formulated for wave diffraction in [146] was extended for the combined phenomena. This greatly reduced the number of required operations to get a given accuracy as compared to the standard numerical integration scheme.

Torii et al. [189] used the GFEM for the modal analysis of 2D wave equation. They used *sine* and *cosine* functions to enrich the approximation space. They used GFEM approach and the high order polynomial FEM to solve the problem. The relative benefits of GFEM were discussed in comparison with the high order polynomial FEM. Drolia et al. [52] used the enriched FEM for the solution of electromagnetic wave equation in the time domain. They formed enrichments by a combination of plane waves with a fixed frequency propagating in different directions. The proposed method is shown to produce accurate results with less degrees of freedom as compared to standard low order polynomial FEM.

2.7.2 Applications to fracture mechanics problems

The enriched FEM has also been applied to enrich approximations locally around some feature; a notable example of this is the eXtended Finite Element Method [31, 49]. Here the enrichment functions are taken from the leading order term in the asymptotic expansions for displacement components immediately surrounding a crack tip. This idea has permeated into enriched meshless methods [133], and boundary element

methods [168, 169] with some considerable benefits found. Fries and Belytschko [68] presented an overview of the XFEM/GFEM with applications to different problems involving non smooth solutions in the domain.

Shao et al. [167] used XFEM to study the effect of fluid flow and heat transfer on the growth of a crack in multilayered porous materials. They discretized the fluid flow using nonconforming Crouzeix–Raviart (CR) finite elements and the advection–diffusion heat transfer was solved by a combination of Discontinuous Galerkin Method and Multi-Point Flux Approximation. To handle the singularities better, XFEM was then used to solve the conduction in the solid phase.

O'Hara et al. [142] solved the static fracture and fatigue crack propagation using a two scale GFEM/XFEM. They defined boundary value problems locally in the area of the cracks and generated the enrichment functions on-thy-fly which were then used for the solution of the global problem. This approach produced accurate results even in the area of multiple cracks interactions. The approach called global-local enrichment function GFEM$^{\text{gl}}$, eliminated the need for having *a-priori* knowledge about the problem in hand. A similar approach is used by Kim and Duarte [97] to solve propagating cohesive fractures in three dimensions. Malekan et al. [120] also used GFEM$^{\text{gl}}$ approach and constructed enrichment functions numerically from the solution of a locally defined problem. The local problem was defined within the domain where high stress gradients were present. They used a very fine mesh in this area. The results of this locally defined problem were used to enrich the global problem. This approach largely reduced the numerical burden and produced improved results of the overall solution. Evangelista et al. [64] utilized GFEM framework to evaluate the propagation of cracks in concrete slabs. They used the two scale GFEM$^{\text{gl}}$ approach to cracks of different geometries placed at different locations. Duarte and Kim [56] used PUFEM for accurately modelling a crack using enrichment functions from the asymptotic expansion of the elasticity in the neighbourhood of the crack. In their work, they presented a procedure to build enrichment functions for PUFEM. They analysed a two-level approach to build enrichment functions for PUFEM and, in particular,

for the generalized FEM. The procedure combines classical global-local finite element method concepts with the partition of unity method. It involved the solution of local boundary value problems using boundary conditions from a global problem defined on a coarse discretization. The local solutions are in turn used to enrich the global space using the partition of unity framework. They investigated the effectiveness of the approach in terms of convergence rates and computational cost. They used three-dimensional fracture mechanics problems to illustrate the main ideas of the procedure. However, the authors argue that the approach is not limited to this particular application. This significantly improves the computational efficiency which was the main focus of their work. In another work Duarte et al. [57], used this approach for the solution of three dimensional crack propagation problems. The global-local approach was used to develop enrichments to improve the efficiency and accuracy of the overall problem. A similar two-scale approach for the solution of propagating 3D fracture mechanics problems is presented by Pereira et al. [150]. Kim et al. [96] also used the two-scale approach for the solution of 3D problems in fracture mechanics using coarse mesh GFEM. They solved the local problems using *hp*-GFEM which were then used to enrich the global problem using PUFEM. They studied the accuracy of the method with Dirichlet, Neumann and Cauchy type boundary conditions. Also in [94], the authors used this approach for the solution of problems involving interacting cracks.

Gupta et al. [77] represented an extension of the two scale GFEM^{gl} approach for the solution of problems involving plastic deformations locally. They defined a local boundary value problem using very fine mesh around the region experiencing plastic deformation. Through the partition of unity framework, the result of this fine scale solution was then used to enrich the remaining coarse-mesh domain. This greatly reduces the computation cost as compared to the standard FEM solution. The authors argue that this approach is much better for many practical problems where only a small confined area undergoes plastic deformations and the rest of the domain remains largely elastic. Kim et al. [95] also applied a similar approach to solve confined plasticity problems. A detailed procedure for the generation of suitable enrichments

from the fine-scale local solution is outlined. Different problems in 3D domains with gradual plastic deformation are solved to show the effectiveness of the proposed technique. Results of the numerical examples show that the two-scale GFEM^{gl} approach produces comparable or even better results as compared to *hp*-GFEM approach. In a recent work, Plews and Duarte [154] used the two-scale approach to a class of problems involving localized transient thermo-elasto-plastic behaviour. Kim et al. [95] and Gupta et al. [77] considered the plastic behaviour which was localized around a fixed small region of the domain, produced by uniform and continuous loading. The work of Plews and Duarte is a step forward to include the effect of thermal loading that varies both in time and space. The same authors also used GFEM^{gl} approach as a tool for bridging micro-macro scale interactions [153]. Gupta et al. [78] in another work discussed the effect of incorrect boundary conditions applied to the domain of local problems. They represented a strategy to improve the *a-priori* error estimate resulting from these incorrect boundary conditions. Numerical examples from 3D fracture mechanics were used to show the effectiveness of their strategy to control the overall error of GFEM^{gl} solution.

Komijani and Gracie [100] used enriched FEM to solve the wave propagation problem in fractured media. They used GFEM to globally enrich the solution space with harmonic functions and Phantom Node Method (PNM) [80, 173], a variant of XFEM, to model cracks locally independent of the mesh. They mentioned that GFEM smooths out the spurious variations that are normally observed in the transient analysis of wave propagation using the classical FEM. Combined PNM-GFEM was reported to model the wave propagation problem in fractured media more accurately as compared to standard FEM and PNM. Crack discontinuities are also modelled by discontinuous enrichment method [50, 51].

2.7.3 Applications to heat transfer problems

Munts et al. [132] are among the early researchers who used the enriched FEM for heat transfer problems. They used PUFEM to solve convection–diffusion problems in

one space dimension using two different enrichment functions; exponential enrichment functions based on approximate analytical solution and polynomial enrichment functions as in [185]. It is shown that the choice of the enrichment has an effect on the solution. They showed that for a given number of DOFs, PUFEM with an exponential enrichment function leads to better results than the standard finite element method. They also used polynomial enrichment functions but concluded that although a higher level of accuracy can be achieved with polynomial enrichments as compared to the standard FEM, but they were generally less efficient than the exponential enrichment functions.

O'Hara et al. [143] investigated the application of the generalized finite element method with global-local enrichments GFEM^{gl} for steady state heat transfer problems with solutions that exhibit highly localized sharp thermal gradients. They considered three-dimensional problems and used the classical FEM and GFEM approaches to solve the problem. They defined a local problem on a fine-mesh to formulate enrichments which were then used to enrich the coarse mesh of the global problem. This methodology prevented the need of *a-priori* information about the problem in hand. Previously O'Hara [139] used the standard FEM version for such problems. The authors extended their work to time dependent problems exhibiting sharp localized thermal gradients [141]. Again the global-local enrichments were used to formulate the problem. The authors used coarse FEM meshes with specially tailored shape functions to yield a high level of accuracy. Based on the solution of local boundary value problems, they numerically built appropriate functions to enrich the solution. The proposed method enabled the use of uniform, coarse, global meshes for transient heat transfer problems with localized features. This eliminated the need to refine global meshes, which is usually complex and computationally expensive. Also with the proper discretization order, GFEM^{gl} produced results that were in very good agreement with the reference curves generated using *hp*-GFEM and significantly more degrees of freedom. The authors concluded that the size of the enriched global problem does not depend on the size or discretization used in the local problems. They

also comment that GFEM^{gl} uses a large amount of information (solution, their derivatives etc) which can be calculated once and reused at each subsequent time step. In another work [140], the authors investigated the effect of localized thermal loading on the response of structures. The main motivation of their work was to study the effect of localized thermal loads on the outer skin of hypersonic aircrafts. They solved the transient heat equation using the linear FEM and GFEM and studied the effect of time step size on the solution of both methods. A sufficiently small time-step was first used to generate a stable linear FEM solution. The coarse meshed GFEM was then used and for a stable solution, the time step size was investigated. High order elements were also used to compare the solution with linear FEM. It was concluded that with a given mesh size the high order elements generate better results but do not allow the use of large time steps. With GFEM using special functions, better accuracy can be achieved with coarse meshes, and the large size of elements allow the use of large time steps. Also in [144], GFEM is presented as an efficient way for obtaining solutions to time dependent heat transfer problems with localized thermal gradients. Again, the enrichments were calculated on-the-fly from the local problems and then used to enrich the coarse meshed global problem avoiding the need of *a-priori* information of the exact solution.

Van der Meer et al. [190] analysed transient geothermal problems using the enriched FEM. Their algorithm considered the use of enrichment functions that were updated at each time step and the solution at each time step was calculated using these updated enrichment functions. Time-dependent variables were used to make the shape functions adapted to the transient process. This eliminated the need to make the mesh adaptive to the transient thermal gradients, and no extra degrees of freedom were added to the system. They presented two different approaches to optimise the approximation functions. In their first approach ,they used exponential functions to approximate the solution, and to make them optimized at each time step; these functions were updated iteratively during the solution process. In their second approach, they proposed to incorporate the analytical solution of a simplified problem in the

shape functions which were again updated at each time step. The basic formulation of finite elements was made time-dependent for the implementation of these approximation functions. The proposed method was tested for different numerical examples where it is shown to capture high thermal gradients using very coarse mesh grids as compared to the standard FEM. Cosimo et al. [43] also used time-dependent enrichment functions for the solution of solidification process. The varying interface between solid and liquid regions was captured with time-dependent enrichment functions. Similar enrichment functions were previously proposed by Coppola-Owen and Codina [42] for two-phase flow problems.

A notable development using PUFEM for transient heat transfer problem is the work done by Mohamed et al. [126]. They solved time-dependent heat diffusion equation using multiple enrichments. To enrich the FEM solution space they used Gaussian functions of different standard deviations in combination with linear polynomial shape functions. An interesting aspect of their work is that time variation of the solution was taken into account in the enrichment functions, and the same enrichments are used at every time step. This eliminated the need for updating enrichment functions at every time step. The computation time is reduced remarkably by this approach as the system matrix was assembled at the first time step only and retained for the subsequent time steps. The presented numerical results showed that for a comparable accuracy the reduction in the required DOFs was up to 90% as compared to the standard FEM. In their further work, they used the same approach for other conduction and radiation heat transfer problems [129, 130]. In [130], the authors modelled the radiative cooling process in the glass industry. Hyperbolic enrichment functions are used to efficiently capture the solution. The glass cooling process in two different enclosures, one in a plate enclosure and the other in a disk enclosure was studied using the standard FEM and the proposed PUFEM. It was concluded that PUFEM provides better and more stable results as compared to standard FEM with a huge reduction in computational cost. To solve problems of transient heat transfer that involve both conduction and radiation, the authors used a combination of Gaussian and hyperbolic enrichment

functions [129]. They used the Gaussian functions to solve the diffusion heat transfer inside the domain while the hyperbolic enrichments were used to capture the temperature variations across the boundary layer. Diwan et al. [48] used mixed enrichments for the FEM solution of problems involving heterogeneous materials. They studied the application of PUFEM to heat transfer and wave scattering problems. A mix of plane waves and exponential functions were used to enrich the solution space. A significant reduction in the required DOFs was noted as compared to the standard FEM. Heterogeneous materials for steady and unsteady temperature fields are also simulated by Yu and Gong [195] using XFEM approach. Kalashnikova et al. [90] used the discontinuous Galerkin FEM to solve the high Pe'clet advection–diffusion problems. The problems with strong boundary layers associated with high Pe'clet number were solved by employing enrichment functions on element level. Advection–diffusion problems are also solved by Borker et al. [38] using the discontinuous Galerkin FEM. The authors used polynomial Lagrange multipliers to force the continuity across the element boundaries. Interface-enriched generalized FEM is also used to solve heat transfer problems with discontinuous gradient fields [170–172].

2.8 Error estimation procedures for approximate numerical methods

Different numerical methods evolved over the years to reduce the computation cost and memory requirements for large complex problems. One of the features of all these numerical methods is that they are subject to various sources of numerical errors [29, 183] which can question the reliability of the results. In their book, Babuška and Strouboulis [22] emphasized on the reliability of the FEM computations and mentioned that unreliable finite element results can lead to very serious consequences. Over the years, different researchers devised methods for the error estimation of h, p and $hp-$versions of FEM [24, 70, 91, 125, 135, 160]. The basic mathematical theory of FEM and its error estimation can be found in the book of Babuška et al. [23]. A

comprehensive explanation of the error estimation procedures and their theory is also presented by Ainsworth and Oden [5]. They also presented their work in [4], addressing the use of *a-posteriori* estimates for FEM solutions of structural mechanics problems.

The computation of numerical errors in approximate numerical methods remains the main source of concern for research communities. The practitioners and researchers in computational methods have always been concerned with questions like;

1. What are the approximation errors in numerical computations?

2. How can these errors be quantified?

3. How these errors can be controlled and minimized?

To address these questions, several types of estimates have been developed since late 1970s, aimed to evaluate the discretization errors of the numerical methods [75]. In a broad sense, these estimates are categorized into two types; *a-priori* error estimates and *a-posteriori* error estimates. The *a-priori* error estimates are designed to provide information about the asymptotic behaviour of the discretization errors. They show convergence and convergence rate, but do not give information about the actual errors for a given discretization. They can be used to provide information about the stability and convergence of different methods. The *a-posteriori* estimates on the other hand are based on the actual finite element solution of the problem. These estimates provide a basis for adaptive refinement schemes of these methods. The *a-posteriori* error estimators are subdivided into two broad categories; the *residual based* error estimates [3, 20] and the *recovery based* error estimates [60, 197].

The *residual based* error estimates are aimed to calculate the errors in every element of the discretization by satisfying the governing equations of the problem. The errors in the whole domain are then evaluated as a summation of the errors in each element. If u is the exact solution of a problem and u_h represents the approximate numerical solution, then the residual in any norm is given by $\|e\| = \|u - u_h\|$. Babuška and Rheinboldt [19] were among the pioneers to develop *a-posteriori* error estimation for FEM solution of elliptic boundary value problems. They extended their work by

suggesting a strategy to calculate *a-posteriori* error estimation in terms of quantities which are localized to a discretization [20]. This provided an adaptive algorithm for the mesh refinement of FEM computations. They also developed a theory for *a-posteriori* error estimation under different norms ranging from L_2 norm to L_∞ norm for 1D problems [21]. Babuška and Miller [18] also presented theory and some practical aspects of error estimation for the solution of linear elasticity problems using the finite element method. FEM has also been investigated for the accuracy and reliability of results for the Helmholtz equation by Babuška et al. [16]. Bouillard and Ihlenburg [39] investigated the accuracy and adaptivity of the FEM for the solution of sound propagation problems.

The *recovery-based* error estimators [138, 197] are motivated by the fact that in general, the gradient of a piecewise linear FEM solution is discontinuous at the inter-element boundaries. In recovery based error estimators, the gradient of the solution is post-processed and is then compared to the non post-processed solution gradient to estimate the true error of the solution. To visualize these errors across the element boundaries a simple way could be to display these results using iso-bands where no averaging of the results is done across the element boundaries. Sussman and Bathe [182] presented a visual method called "stress band plots" to display the stress solution of a finite element mesh. In contrast to the conventional stress plots which present average stress values in an element, the "stress band plots" display results which are un-averaged and are calculated directly from the solution variables. These kind of contours are helpful in finding out the accuracy of the FEM solution across the element boundaries. Recent modifications in the *recovery based* error estimation lead to the development of *superconvergent patch recovery* method [198, 199].

Most of the early developed *a-posteriori* error estimates focus on calculating global errors in the energy norm. A recent extension of these procedures is to find errors in a particular quantity of interest (QoI). These new procedures are commonly named as goal-oriented error estimation procedures [33, 76, 93, 137, 156, 157]. In heat transfer problems, a representative example of QoI could be the maximum temperature at a

particular point in the domain, and in fracture mechanics problems it could be the stress intensity factor (SIF) of a crack tip.

2.8.1 Error estimation for the enriched finite element methods

Similar to the standard FEM, error estimates are also studied for the enriched FEM. In fact, the error estimation procedures started at the very beginning of the development of these methods [124], with later works carried out by Strouboulis, Babuška and co-authors [175, 179, 180].

Melenk and Babuška [124], while introducing PUFEM, provided a basic procedure to calculate *a-posteriori* error estimates for their newly developed method. They outlined patches and defined local problems on these patches. The *a-posteriori* error estimates were based on the solution of these patches. Upper and lower bounds for the method were defined by considering a model problem. Strouboulis et al. [180] addressed the reliability of *a posteriori* error estimates for GFEM based on the partition of unity method. They defined both lower and upper bounds for the error. They represented the error bounded by two-sided estimates as

$$\mathscr{E}^L \leq \|e\| \leq \mathscr{E}^U$$

where $\|e\| = \|u - u_h\|$ denotes the error in the solution and $\mathscr{E}^L$ and $\mathscr{E}^U$ represent the lower and upper bounds, respectively. They underlined the difference between the theoretical upper estimator, the computed version of the estimator and the computable estimator.

More recently a variety of *a-posteriori* error estimates for the extended finite element method has been explored, i.e. for enrichments localized in a small part of the mesh, with a particular emphasis on crack problems. Bordas et al. [37] proposed error estimators for XFEM by calculating the enhanced strain fields and the XFEM strains. Their proposed error estimator is then the L_2 norm error calculated by considering

the difference of the enhanced strains and XFEM strains. The enhanced strains were computed as intrinsically enriched eXtended Moving Least Squares (XMLS) approximations of the raw XFEM strains. They used the derivative recovery technique based on the ideas of Tabbara et al. [184]. The concept was proven in a 1D problem with a singular solution and a 2D fracture mechanics problem. A generalization of the MLS derivative recovery concept of Tabbara et al. [184] is also presented by the same authors [36]. They tailored the construction of XMLS to the nature of the problem. The method was tested on 2D and 3D problems in linear elastic fracture mechanics and it is shown that the enhanced strain fields are very smooth. For the problem considered, they mention that the proposed estimator is better than the *superconvergent patch recovery* technique proposed by Zienkiewicz and Zhu [198].

Duflot and Bordas [60] used the extended global recovery techniques for the *a-posteriori* error estimation of XFEM. They calculated the L_2 norm error based on the difference of the raw strains and the recovered strains. The authors mentioned their methodology as the extension of the idea of Hinton and Campbell [82] and Oden and Brauchli [134]. They tested their methodology on 2D and 3D linear elastic fracture mechanics problems. The authors added that due to the simplicity of the proposed methodology it is ideal for industrial applications. With their proposed estimators, they also evaluated the optimum enrichment radius for the enrichment functions at crack tip. More recently Jin et al. [89] used the technique of Duflot and Bordas to calculate the interpolation error for linear elastic fracture mechanics problems using XFEM. They solved the crack propagation problem in a 3D domain and presented an approach for error estimation along with mesh adaptivity for these problems. They aimed to provide an approach that is robust and simple as well as provide a mesh adaptation *on-the-fly* during the crack propagation. Prange et al. [155] addressed the problem of discretization error of XFEM for crack propagation problems. They used the recovery based error estimation technique to assess the errors of XFEM. Their method is based on the error estimator of Zienkiewicz and Zhu [197]. To avoid the spurious discontinuities in the results, the corrected XFEM [67, 116] was used which

produced improved results near the crack tip without artificial discontinuities in the temperature fields. The idea of corrected XFEM is also used by Loehnert et al. [117] to predict the interaction between micro and macro cracks.

Pannachet et al. [149] proposed error estimation and adaptivity technique for modelling discontinuous failure. The partition of unity approach is used to simulate the crack using the *cohesive zone concept* [193]. In cohesive zone the failure due to crack is modelled as the separation of crack surfaces across an extended crack tip, a cohesive zone, where the resistance is provided by the cohesive tractions. Later Pannachet et al. [148] proposed error estimation and mesh adaptivity for structure failure problems. They choose to use the gradient enhanced damage model. A residual based error estimator introduced in [149] was used in their work. Barros et al. [27] used the Equilibrated Element Residual Method to address the issue of reliability of GFEM. They presented the *p-adaptivity* for the GFEM solution. They used an iterative procedure to solve the problem and the nodes in the domain having highest values of local error were selected for *p-refinement* to improve the accuracy of the solution in the next iteration. The Element Residual Method introduced in [26, 46] was used to approximate the energy norm of the local error at each element. A global error measure was also introduced. In another work, Barros et al. [28], proposed error estimates for GFEM considering the solution of elasticity problems in 2D domains exhibiting stress singularities.

Ródenas, Estrada and co-authors [161–163] use the *recovery-based* error estimators for XFEM. In [163], Ródenas et al. proposed to estimate the discretization error by splitting the enhanced strain fields into smooth and non-smooth parts. They analysed the linear elastic fracture mechanic problems with XFEM. They referred to their method as a variation of the *superconvergent patch recovery* (SPR) technique and was called SPR_{XFEM}. They tested their method on a problems with an exact solution and a problem without a known solution. The numerical experiments show good accuracy of the proposed method for both local and global errors in the energy norm. In their further work [162], they presented an alternative technique to the superconver-

gent patch recovery (SPR) method. They proposed estimates in the energy norm for the FEM and XFEM methods based on the nearly equilibrated moving least squares (MLS) recovery technique. Numerical results of the method are shown to have very good accuracy. In another work [161], they addressed the role of statically admissible recovery method for error estimation of XFEM. Similar approaches are also used in [73] and [194]. More recently Lins et al. [112] studied the *recovery-based a-posteriori* error estimation for the 2D fracture mechnics porblems using the framework of the stable generalized finite element method (SGFEM).

There are applications in which the error in particular observables may sometimes be of more interest than the error of the whole solution. The goal oriented error estimates (GOEE) which find the error in a particular quantity of interest has been studied by many authors. González-Estrada et al. [74], developed a goal oriented error estimate for XFEM using the equilibrated recovery technique. They considered the stress intensity factor as quantity of interest as the SIF was envisaged to be one of the characteristic parameters to give a more realistic description of the behaviour around the crack tip. They used the locally equilibrated superconvergent patch recovery to obtain enhanced stress fields. They mention that to properly describe the behaviour at the crack tip in Linear Elastic Fracture Mechanics (LEFM), it is essential to precisely calculate SIF. Goal oriented error estimates have also been investigated for linear elastic fracture mechanics problems in [71, 111, 147]. Goal-oriented adaptivity for Generalized Multiscale Finite Element Method (GMsFEM) are also studied by Ancey et al. [7].

2.9 Overview

This chapter started with a brief introduction of the approximate numerical solutions of different problems arising in engineering and various fields of science. This is relevant in the context because the rest of the followed discussion is based on the approximate numerical solution of different engineering problems in general and heat

transfer problems in particular. The most relevant and widely used approximate numerical method, FEM, is then discussed along with some of its merits and limitations. To address the limitations of FEM, various meshless and enriched finite element methods are developed by the research community. A brief overview of the most relevant enriched methods is outlined. Examples of applications of the enriched finite element methods in different fields of engineering and scientific computation are also presented.

Chapter 3

GFEM for two-dimensional transient heat diffusion problems

3.1 Introduction

In this Chapter, the transient heat diffusion problem is first defined with initial and boundary conditions, for which the variational form is then developed. The latter form is obtained by considering the weighted residual scheme in space and then adopting an implicit Euler method in time. The polynomial based FEM and the enriched field approximations are then presented with the former based on linear shape functions. The enriched approach is based on the use of Gaussian functions with the linear shape functions and will be called GFEM throughout the whole thesis. Computational aspects, such as enrichment functions selection, numerical integration and solution method are also indicated.

3.2 Boundary value problem and weak form

Given an open bounded domain $\Omega \subset \mathbb{R}^n$ where $n = 2, 3$; with polygonal boundary Γ and a given time interval $]0, T]$, we are interested to solve the following transient heat

diffusion equation

$$\frac{\partial u}{\partial t} - \lambda \Delta u = f, \qquad \text{in }]0,T] \times \Omega \ , \tag{3.1}$$

where $\lambda > 0$ is the diffusion coefficient and the right hand side f represents the effects of internal sources/sinks. An initial condition

$$u(t=0,\mathbf{x}) = U_0(\mathbf{x}), \qquad \mathbf{x} \in \Omega \ , \tag{3.2}$$

and a Robin–type boundary condition

$$\frac{\partial u}{\partial n} + hu = g, \qquad \text{in }]0,T] \times \Gamma \ , \tag{3.3}$$

are imposed. Here $\mathbf{n}$ denotes the outward unit normal to the boundary Γ, and $h \geq 0$ is the heat convection coefficient on Γ, and g represents boundary sources.

We will numerically solve a weak formulation of the initial–boundary problem (3.1) - (3.3). Multiplying by a smooth test function W, then integrating over Ω we obtain

$$\int_\Omega W \frac{\partial u}{\partial t} \ d\Omega - \int_\Omega W \lambda \Delta u \ d\Omega = \int_\Omega W f \ d\Omega \ . \tag{3.4}$$

or

$$\int_\Omega \left(W \frac{\partial u}{\partial t} - \lambda W \Delta u \right) d\Omega = \int_\Omega W f \ d\Omega \ . \tag{3.5}$$

In order to get rid of the second derivative term in above equation, we use the divergence theorem. Suppose we have a function S, such that

$$S = W \nabla u = \left\{ \begin{array}{c} W \frac{\partial u}{\partial x} \\ W \frac{\partial u}{\partial y} \\ W \frac{\partial u}{\partial z} \end{array} \right\} \tag{3.6}$$

We find the divergence of the function S,

$$\nabla \cdot S = \nabla W \cdot \nabla u + W \Delta u \tag{3.7}$$

The divergence theorem states that

$$\int_\Omega \nabla \cdot S d\Omega = \int_\Gamma S \cdot n d\Gamma \tag{3.8}$$

substituting (3.6) and (3.7) into (3.8)

$$\int_\Omega \nabla W \cdot \nabla u + W \Delta u \; d\Omega = \int_\Gamma W \nabla u \cdot n d\Gamma \tag{3.9}$$

then rearranging gives

$$\int_\Omega W \Delta u \; d\Omega = \int_\Gamma W \nabla u \cdot n d\Gamma - \int_\Omega \nabla W \cdot \nabla u \; d\Omega \tag{3.10}$$

Finally, substituting (3.10) into (3.5) results

$$\int_\Omega \left(W \frac{\partial u}{\partial t} + \lambda \nabla W \nabla u \right) d\Omega - \int_\Gamma \lambda W \nabla u \cdot n \; d\Gamma = \int_\Omega W f \; d\Omega \; , \tag{3.11}$$

and with the boundary condition (3.3) we conclude the weak formulation of the heat diffusion problem: Find a solution u on $[0, T] \times \Omega$ such that $u(0, \mathbf{x}) = U_0(\mathbf{x})$ and for all test functions W on Ω and all $t \in]0, T]$ such that

$$\int_\Omega \left(W \frac{\partial u}{\partial t} + \lambda \nabla W \nabla u \right) d\Omega + \int_\Gamma \lambda W h u \; d\Gamma = \int_\Omega W f \; d\Omega + \int_\Gamma \lambda W g \; d\Gamma \; . \tag{3.12}$$

Our concern is to find approximate numerical solution of (3.12). As time–discretization, we choose an implicit Euler method: The time interval is divided into $N_t + 1$ subintervals $[t_n, t_{n+1}]$ of size $\delta t = t_{n+1} - t_n$ for $n = 0, 1, ...N_t$ and approximate the time derivative in (3.12) by a difference quotient. Expression (3.12) is then written as

$$\int_\Omega \left(W \frac{u^{n+1} - u^n}{\delta t} + \lambda \nabla W \nabla u^{n+1} \right) d\Omega + \int_\Gamma \lambda W h u^{n+1} d\Gamma = \int_\Omega W f^{n+1} d\Omega + \int_\Gamma \lambda W g^{n+1} d\Gamma \; . \tag{3.13}$$

Rearranging the terms we conclude the time–discretized variant of the weak formulation (3.12): Find a solution u^{n+1} on Ω such that $u^0 = u_0$ and for all test functions W

on Ω and all $n \in \mathbb{N}$ such that

$$\int_\Omega (\nabla W \cdot \nabla u^{n+1} + W k u^{n+1}) d\Omega + \int_\Gamma W h u^{n+1} d\Gamma = \int_\Omega W F^{n+1} d\Omega + \int_\Gamma W g^{n+1}\, d\Gamma\,, \quad (3.14)$$

where u_0 is a discretization of U_0, and F^{n+1} and k are defined as

$$F^{n+1} = k\Big(\delta t f(t_{n+1}, \mathbf{x}) + u^n\Big), \qquad k = \frac{1}{\lambda \delta t}.$$

Our aim is to find an approximate solution u^{n+1} of the weak form (3.14) using the finite element method and GFEM.

3.3 Approximation of the weak form with FEM and GFEM

To solve the weak form (3.14) with finite elements, the domain Ω is discretized into finite number of elements. We assume that Ω is a polygon and generate a quasi-uniform mesh $\Omega = \cup K$. The edges of the elements K are denoted by E. The solution in each element is then approximated by sum of the combination of nodal values and piecewise linear shape functions, i.e., we look for u^{n+1} of the form

$$u^{n+1}(\mathbf{x}) = \sum_{j=1}^{M} N_j(\mathbf{x}) u_j^{n+1}(\mathbf{x}) \quad (3.15)$$

where u_j^{n+1} are the unknown nodal solution values, N_j are the piecewise linear shape functions, and M is the number of nodes in the element. The FEM is used to find out the unknown nodal values. In GFEM the solution space is enriched with basis functions that incorporates *a priori* knowledge about the problem in hand thus provide better approximation as compared to conventional piecewise linear basis functions. For GFEM solution we modify (3.15) and take nodal values u_j^{n+1} as combination of

enrichment functions, i.e.

$$u^{n+1}(\mathbf{x}) = \sum_{j=1}^{M} \sum_{q=1}^{Q} A_j^q N_j(\mathbf{x}) G_q(\mathbf{x}) \tag{3.16}$$

with

$$u_j^{n+1} = \sum_{q=1}^{Q} A_j^q G_q(\mathbf{x}) \tag{3.17}$$

where $G_q(\mathbf{x})$ are the enrichment functions and A_j^q are their amplitude at nodal points of the domain. Q denotes the number of enrichment functions. In (3.16) the finite element shape functions $N_j(\mathbf{x})$, $j = 1, ...M$, constitutes the partition of unity, i.e., $\sum_{j=1}^{M} N_j(\mathbf{x}) = 1$ for all $\mathbf{x}$ in Ω covered by the FE mesh. To solve (3.15), the FEM is used to calculate the nodal solution values u_j^{n+1}, but now in (3.16) the system is solved for new unknowns A_j^q instead of u_j^{n+1}. The literature reveals instances where enrichments are applied locally [139–141, 143, 144], but for our proposed GFEM formulation, we use multiple global functions of varying standard deviations. Unless otherwise stated, for the majority of the computations in this thesis, the following global enrichment functions as proposed in [126] are used.

$$G_q(\mathbf{x}) = \frac{e^{-\left(\frac{R_0}{C}\right)^q} - e^{-\left(\frac{R_c}{C}\right)^q}}{1 - e^{-\left(\frac{R_c}{C}\right)^q}}, \qquad q = 1, 2, \ldots, Q \ . \tag{3.18}$$

Here $R_0 = |\mathbf{x} - \mathbf{x}_c|$ is the distance from a fixed point $\mathbf{x}_c$ to the point $\mathbf{x}$. R_c and C are constants which control the shape of the enrichment function $G_q(\mathbf{x})$. Figure 3.1 depicts the shape of $G_q(\mathbf{x})$ with different values of q for 2D spatial domain. The global nature of the enrichment functions ensures efficient solution in the whole computational domain with very course mesh grids. A unique feature of these enrichment functions is that the same functions are used to enrich the approximation space throughout the solution time. The time variation of temperature fields is embedded in the definition of the enrichment functions. This eliminates the need for updating enrichment functions and the same enrichments are used at every time step. The more rapidly varying

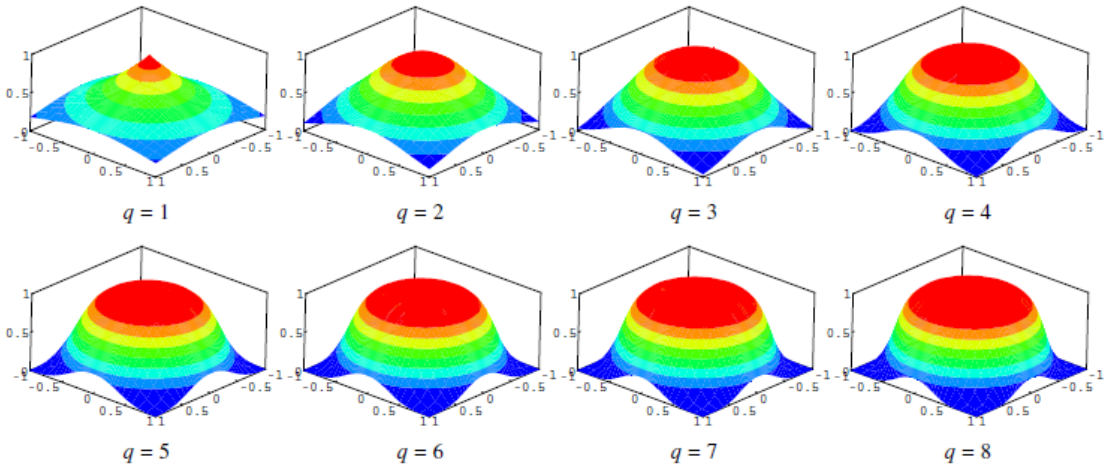

Fig. 3.1 Illustration of enrichment function $G_q(\mathbf{x})$ for different values of q. This figure is adapted from [126].

enrichment functions capture the solution at early time steps when the temperature gradients are high, while flatter enrichment functions behave well in the far field as well as when the solution approaches towards the steady state condition.

For simplicity, the multiplication of $G_q(\mathbf{x})$ with the polynomial shape function N_j is considered to be the new shape function $P_{(j-1)Q+q}$

$$P_{(j-1)Q+q} = N_j(\mathbf{x})\ G_q(\mathbf{x}) \tag{3.19}$$

or

$$P_{(j-1)Q+q} = N_j \frac{e^{-\left(\frac{R_0}{C}\right)^q} - e^{-\left(\frac{R_c}{C}\right)^q}}{1 - e^{-\left(\frac{R_c}{C}\right)^q}} \tag{3.20}$$

The derivatives of the new shape function are given as

$$\begin{aligned}\begin{Bmatrix} \frac{\partial P_{(j-1)Q+q}}{\partial x} \\ \frac{\partial P_{(j-1)Q+q}}{\partial y} \\ \frac{\partial P_{(j-1)Q+q}}{\partial z} \end{Bmatrix} &= \left(e^{-\left(\frac{R_0}{C}\right)^q} - e^{-\left(\frac{R_c}{C}\right)^q}\right) \begin{Bmatrix} \frac{\partial N_j}{\partial x} \\ \frac{\partial N_j}{\partial y} \\ \frac{\partial N_j}{\partial z} \end{Bmatrix} \\ &\quad - \frac{q}{C^q} e^{-\left(\frac{R_0}{C}\right)^q} R_0^{(q-2)} N_j \begin{Bmatrix} (x-x_c) \\ (y-y_c) \\ (z-z_c) \end{Bmatrix} \frac{1}{1-e^{-\left(\frac{R_c}{C}\right)^q}}\end{aligned} \tag{3.21}$$

Second derivatives of the new shape function are

$$\begin{aligned}\begin{Bmatrix} \frac{\partial^2 P_{(j-1)Q+q}}{\partial x^2} \\ \frac{\partial^2 P_{(j-1)Q+q}}{\partial y^2} \\ \frac{\partial^2 P_{(j-1)Q+q}}{\partial z^2} \end{Bmatrix} &= G_q \begin{Bmatrix} \frac{\partial^2 N_j}{\partial x^2} \\ \frac{\partial^2 N_j}{\partial y^2} \\ \frac{\partial^2 N_j}{\partial z^2} \end{Bmatrix} - 2 \begin{Bmatrix} \frac{\partial N_j}{\partial x} \\ \frac{\partial N_j}{\partial y} \\ \frac{\partial N_j}{\partial z} \end{Bmatrix} \frac{q}{C^q} \frac{e^{-\left(\frac{R_0}{C}\right)^q}}{1-e^{-\left(\frac{R_c}{C}\right)^q}} R_o^{(q-2)} \begin{Bmatrix} (x-x_c) \\ (y-y_c) \\ (z-z_c) \end{Bmatrix} \\ &+ N_j \frac{q}{C^q} \frac{e^{-\left(\frac{R_0}{C}\right)^q}}{1-e^{-\left(\frac{R_c}{C}\right)^q}} \left(1 - \frac{q}{C_q} R_0^{(q-2)} \begin{Bmatrix} (x-x_c)^2 \\ (y-y_c)^2 \\ (z-z_c)^2 \end{Bmatrix} + \frac{q-2}{R_o^2} \begin{Bmatrix} (x-x_c)^2 \\ (y-y_c)^2 \\ (z-z_c)^2 \end{Bmatrix}\right)\end{aligned} \tag{3.22}$$

Second derivatives of the polynomial shape function N_j are zero so we have

$$\begin{aligned}\begin{Bmatrix} \frac{\partial^2 P_{(j-1)Q+q}}{\partial x^2} \\ \frac{\partial^2 P_{(j-1)Q+q}}{\partial y^2} \\ \frac{\partial^2 P_{(j-1)Q+q}}{\partial z^2} \end{Bmatrix} &= -2 \begin{Bmatrix} \frac{\partial N_j}{\partial x} \\ \frac{\partial N_j}{\partial y} \\ \frac{\partial N_j}{\partial z} \end{Bmatrix} \frac{q}{C^q} \frac{e^{-\left(\frac{R_0}{C}\right)^q}}{1-e^{-\left(\frac{R_c}{C}\right)^q}} R_o^{(q-2)} \begin{Bmatrix} (x-x_c) \\ (y-y_c) \\ (z-z_c) \end{Bmatrix} \\ &+ N_j \frac{q}{C^q} \frac{e^{-\left(\frac{R_0}{C}\right)^q}}{1-e^{-\left(\frac{R_c}{C}\right)^q}} \left(1 - \frac{q}{C_q} R_0^{(q-2)} \begin{Bmatrix} (x-x_c)^2 \\ (y-y_c)^2 \\ (z-z_c)^2 \end{Bmatrix} + \frac{q-2}{R_o^2} \begin{Bmatrix} (x-x_c)^2 \\ (y-y_c)^2 \\ (z-z_c)^2 \end{Bmatrix}\right)\end{aligned} \tag{3.23}$$

The above derivatives are written for three dimensional case; for two dimensional problems, the derivative with respect to the third variable z is simply eliminated. With

$W = P_r$, the resulting GFEM discretization of the weak formulation (3.14) then reads: Find u^{n+1} of the form (3.16) such that $u^0 = u_0$ and for all $r = 1, \ldots, MQ$

$$\int_\Omega (\nabla P_r \cdot \nabla u^{n+1} + P_r k u^{n+1}) d\Omega + \int_\Gamma P_r h u^{n+1} d\Gamma = \int_\Omega P_r F^{n+1} d\Omega + \int_\Gamma P_r g^{n+1}\, d\Gamma\ . \quad (3.24)$$

The functions P_r are written in terms of global coordinates but modulated locally as they also include the local shape functions N_j. On the other hand, the global nature of the enrichment functions makes the functions P_r highly efficient in modelling the behaviour of the solution in time as well as in space. The choice of enrichment functions is mainly motivated by the physical behaviour of the solution. However, their choice can be optimized by accurately assessing the error of the numerical solution. The next section gives a brief discussion on the selection of enrichment functions for specific application.

3.4 Galerkin finite element and the global system of equations

To solve the boundary value problem numerically, the standard Galerkin finite element is used. Therefore the weight functions W in the weak form (3.14) are taken to be the same as the shape functions; i.e.

$$W = N_i \quad (3.25)$$

With the definition of approximate solution in each element (3.15), the weak form (3.14) for FEM solution can be written as

$$\int_\Omega \left(\nabla N_i \cdot \nabla (\sum_{j=1}^{M} N_j u_j^{n+1}) + N_i k (\sum_{j=1}^{M} N_j u_j^{n+1}) \right) d\Omega + \int_\Gamma N_i h (\sum_{j=1}^{M} N_j u_j^{n+1}) d\Gamma = \int_\Omega N_i F^{n+1} d\Omega + \int_\Gamma N_i g^{n+1}\, d\Gamma\ , \quad (3.26)$$

Taking the summation sign out

$$\sum_{j=1}^{M}\left(\int_{\Omega}(\nabla N_i\cdot\nabla N_j+kN_iN_j)d\Omega+h\int_{\Gamma}N_iN_j\,d\Gamma\right)u_j^{n+1}=\int_{\Omega}N_iF^{n+1}d\Omega+\int_{\Gamma}N_ig^{n+1}\,d\Gamma\,, \tag{3.27}$$

This equation can be written in the following compact matrix notation

$$([A]+k[B]+h[C])\{u\}=\{F\}+\{G\} \tag{3.28}$$

or in a more compact form

$$[S]\{u\}=\{F\}+\{G\} \tag{3.29}$$

Equation (3.29) is known as global equation system where $\{u\}$ is the vector of unknown nodal values with M entries, $[S]=([A]+k[B]+h[C])$ is the global stiffness matrix having $M\times M$ entries, given below

$$S_{ij}=\left(\int_{\Omega}(\nabla N_i\cdot\nabla N_j+kN_iN_j)d\Omega+h\int_{\Gamma}N_iN_j\,d\Gamma\right) \tag{3.30}$$

$\{F\}$ is the force vector and $\{G\}$ the boundary integral vector of size $M\times 1$. The integrals $[S]$ and $\{F\}$ are evaluated on the whole problem domain whereas the boundary integral $\{G\}$ is evaluated only on the boundaries of the domain. The entries of $\{F\}$ and $\{G\}$ are given as

$$F_i=\int_{\Omega}N_i\,F\,d\Omega \tag{3.31}$$

$$G_i=\int_{\Gamma}N_i\,g\,d\Gamma \tag{3.32}$$

In case of GFEM, the global stiffness matrix $[S]$ has $MQ\times MQ$ entries, and the vectors $\{u\}$, $\{F\}$ and $\{G\}$ have $MQ\times 1$ entries.

3.5 Element matrices and numerical integration

As in most FEM computer codes, the global integrals are evaluated as a sum of the integrals of individual elements, as

$$[S] = \sum_{e=1}^{K} [S^e] \tag{3.33}$$

$$\{F\} = \sum_{e=1}^{K} \{F^e\} \tag{3.34}$$

$$\{G\} = \sum_{e=1}^{K_b} \{G^e\} \tag{3.35}$$

where $[S^e]$ is the element stiffness matrix and $\{F^e\}$ the element force vector with K as the total number of elements in the domain. $\{G^e\}$ is the element boundary integral vector with K_b as the total number of elements on the boundaries. The vector $\{G\}$ is evaluated only on the boundaries of the domain. For two dimensional problems, the boundaries of the domain will be line segments and the boundary integrals will be line integrals. For three dimensional problems, they are area integrals. The entries of $[S^e]$, $\{F^e\}$ and $\{G^e\}$ are given as

$$S_{ij}^e = \left(\int_{\Omega_e} (\nabla N_i \cdot \nabla N_j + k N_i N_j) d\Omega + h \int_{\Gamma_e} N_i N_j \, d\Gamma \right) \tag{3.36}$$

$$F_i^e = \int_{\Omega_e} N_i \, F \, d\Omega \tag{3.37}$$

$$G_i^e = \int_{\Gamma_e} N_i \, g \, d\Gamma \tag{3.38}$$

with Ω_e and Γ_e as the domain and boundary of the element. The assembly of elemental matrices leads to the global system of equations (3.29). The system is solved by using the $\mathbf{LDL^T}$ decomposition, where $\mathbf{L}$ is the lower triangular matrix with $\mathbf{L^T}$

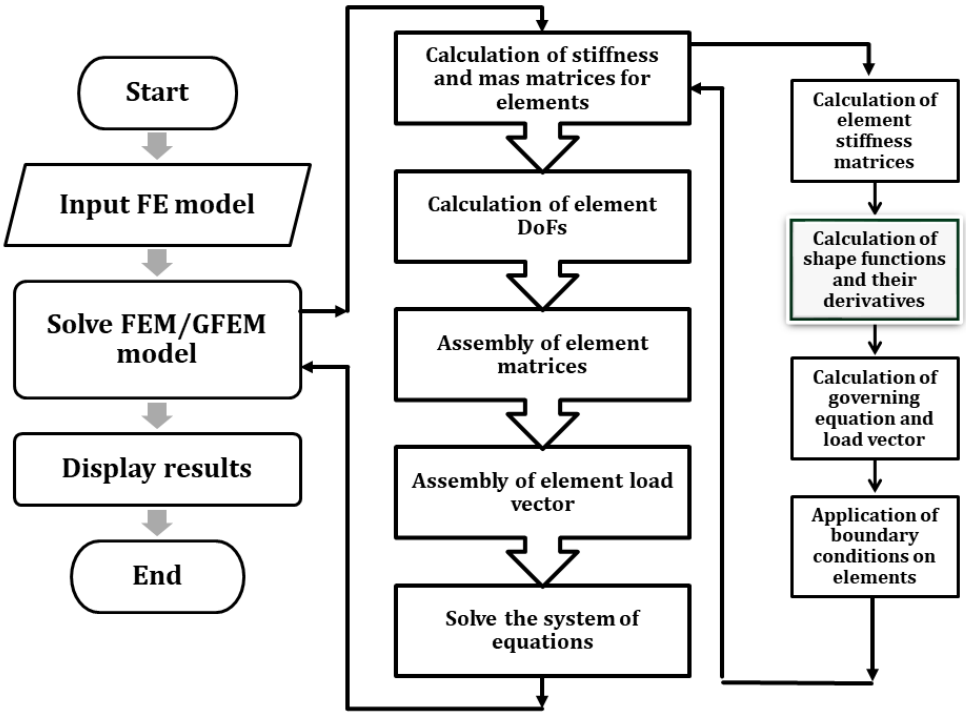

Fig. 3.2 Flowchart for basic FEM/GFEM calculations.

as its transpose and $\mathbf{D}$ is a real diagonal matrix [35]. All the integrals are evaluated numerically using Gauss-Legendre quadrature using 2 integration points in each direction for FEM solution whereas for GFEM solution 20 integration points are used in each spatial direction. The higher integration points in the case of GFEM are used to minimize the error from spatial discretization and to accurately capture the variation of the exponential enrichment functions. A direct solver is used to solve the resulting system of equations.

3.6 Calculation of FEM and GFEM results

The GFEM is considered as a sub-class of meshless methods where it not only keeps all the advantages of a standard FEM but also allows to use any approximation functions that best describe the physics of the problem at hand. The approximation spaces in GFEM are built using the concept of partition of unity and known information

```
      SUBROUTINE SF3H8GAUSS (SF,ISF, K_W, NANGL, BETA, IBETA, X, Y, Z,
     1                                  NUMSRCS, X0, Y0, Z0, SFN)

      !SHAPE FUNCTION SUBROUTINE GAUSS

      !-----------------------------------------------------------------
      ! PURPOSE
      !         Calculates the Gauss functions to enrich the
      !         solution space. Multiple enrichment functions
      !         are used in combination at each node.
      !
      ! HISTORY
      !      Written May 2014
      !
      ! ARGUMENTS IN
      !      SF     Shape function array
      !      SFDL   Array of shape function derivatives
      !             with respect to local co-ordinates
      !      ISF    First dimension of shape function array
      !      ISFDL  First dimension of shape function derivative array
      !      JSFDL  Second derivative of shape function derivative array
      !      NANGL  Number of directions per node
      !      BETA   Array of directions
      !      IBETA  First dimension of BETA
      !      X & Y  Global coordinates
      !
      ! ARGUMENTS OUT
      !      SFN    New shape functions
      !*****************************************************************

      DOUBLE PRECISION SFN
      DOUBLE PRECISION X, Y, Z, X0(4), Y0(4),Z0(4), K_W, BETA
      DOUBLE PRECISION  SF, EXP1, EXP2, EXP3, EXP,R0, Rc, C
      INTEGER  ISF, I, NANGL, IBETA, K, J, NUMSRCS, DOFN, q
      DIMENSION  SF(ISF), SFN(ISF), BETA(IBETA)

     C=sqrt (1.0D0/1.195D0)          ! Constant used in the Gq(x)
     Rc= sqrt (14.0D0/1.195D0)       ! Constant used in the Gq(x)

     !Find the nodal degrees of freedom

     DOFN = NANGL

     ! Centre of the enrichment functions Gq(x)
     X0(1)=1.0D0
     Y0(1)=1.0D0
     Z0(1)=1.0D0

     !Form the element "NEW" shape functions
      DO  I = 1,8
             DO q = 1,DOFN                  ! DOFN is the no of enrichment functions
                    DO  J = 1,NUMSRCS       ! NUMSRCS is the no of heat sources

               R0 = sqrt ((X-X0(J))**2+(Y-Y0(J))**2+(Z-Z0(J))**2)
               EXP1=  DEXP(-1.0D0*R0**q*(1/C)**q)
               EXP2 = DEXP(-1.0D0*Rc**q*(1/C)**q)
               EXP3 = 1.0D0 - DEXP(-1.0D0*Rc**q*(1/C)**q)
               EXP = (EXP1 - EXP2)/EXP3

               SFN(DOFN*(I-1)+NUMSRCS*(q-1)+J) = SF(I)*EXP

                    ENDDO
             ENDDO
          ENDDO
     RETURN
     END

   !*********************************************************************
```

Fig. 3.3 Subroutine for calculation of new shape functions for GFEM.

```
      SUBROUTINE DSF3H8GAUSS (SF, ISF, SFDG, ISFDG, JSFDG, K_W,
     1    NANGL, BETA, IBETA, X, Y,Z, NUMSRCS, X0, Y0,Z0, SFDGN,SFDGN2)

    !DERIVATIVES OF new SHAPE FUNCTIONS
    !---------------------------------------------------------------------
    ! PURPOSE
    !        Calculates the derivatives of the Gauss functions
    ! ARGUMENTS IN
    !      SF     Shape function array
    !      SFDG   Array of shape function derivatives
    !             with respect to global co-ordinates
    !      ISFDG  First dimension of SFDG
    !      JSFDG  Second dimension of SFDG
    !      NANGL  Number of directions per node
    !      BETA   Array of directions
    !      IBETA  First dimension of BETA
    !      X & Y  Global coordinates
    ! ARGUMENTS OUT
    !      SFDGN  Global derivatives of new shape functions
    !*********************************************************************

       DOUBLE PRECISION SFDGN, SFDGN2, C, Rc, R0, SF, SFDG, EXP1, EXP2, EXP3, EXP4, EXP5
       DOUBLE PRECISION X, Y, X0(4), Y0(4),Z0(4), Z, K_W, BETA
       DOUBLE PRECISION EXP4x1, EXP4x2, EXP4y1, EXP4y2, EXP4z1, EXP4z2
       INTEGER          ISF, ISFDG, JSFDG, I, NANGL, IBETA, J, K, NUMSRCS, DOFN, q
       DIMENSION  SF(ISF), SFDG(ISFDG,JSFDG), SFDGN(ISFDG,JSFDG), BETA(IBETA), SFDGN2(ISFDG,JSFDG)

        C=sqrt (1.0D0/1.195D0)
        Rc= sqrt (14.0D0/1.195D0)
        X0(1)=1.0D0
        Y0(1)=1.0D0
        Z0(1)=1.0D0
        !Find the nodal degrees of freedom
        DOFN = NANGL
         DO 20 I = 1,8
               DO 30 q = 1,DOFN
                     DO 40 J = 1,NUMSRCS
                  R0 =   sqrt ((X-X0(J))**2+(Y-Y0(J))**2+(Z-Z0(J))**2)
                  EXP1=  DEXP(-1.0D0*R0**q*(1/C)**q)
                  EXP2 = DEXP(-1.0D0*Rc**q*(1/C)**q)
                  EXP3 = 1.0D0 - EXP2
                  EXP4 = (EXP1 - EXP2)/EXP3
                  EXP5=  (-1.0D0)*(EXP1/EXP3)*q*(1/C)**q
                  !
                  EXP4x1= EXP5 *(R0)**(q-2)*(X-X0(J))
                  EXP4y1= EXP5 *(R0)**(q-2)*(Y-Y0(J))
                  EXP4z1= EXP5 *(R0)**(q-2)*(Z-Z0(J))
                  !
                  EXP4x2=EXP5* R0**(q-2)+ (q-2)*R0**(q-4)* (X-X0(J))**2
                  EXP4y2=EXP5* R0**(q-2)+ (q-2)*R0**(q-4)* (Y-Y0(J))**2
                  EXP4z2=EXP5* R0**(q-2)+ (q-2)*R0**(q-4)* (Z-Z0(J))**2

        !************* 1st derivatives of new shape functions ********
        SFDGN(1,DOFN*(I-1)+NUMSRCS*(q-1)+J)=SFDG(1,I)*EXP4 + SF(I)*EXP4x1
        SFDGN(2,DOFN*(I-1)+NUMSRCS*(q-1)+J)=SFDG(2,I)*EXP4 + SF(I)*EXP4y1
        SFDGN(3,DOFN*(I-1)+NUMSRCS*(q-1)+J)=SFDG(3,I)*EXP4 + SF(I)*EXP4z1

        !************* Second derivatives of new shape functions ********
        SFDGN2(1,DOFN*(I-1)+NUMSRCS*(q-1)+J) = 2.0D0*SFDG(1,I)*EXP4x1+SF(I)*EXP4x2
        SFDGN2(2,DOFN*(I-1)+NUMSRCS*(q-1)+J) = 2.0D0*SFDG(2,I)*EXP4y1+SF(I)*EXP4y2
        SFDGN2(3,DOFN*(I-1)+NUMSRCS*(q-1)+J) = 2.0D0*SFDG(3,I)*EXP4z1+SF(I)*EXP4z2

    40    CONTINUE
    30    CONTINUE
    20    CONTINUE
          RETURN
          END
```

Fig. 3.4 Subroutine for calculation of derivatives of new shape functions for GFEM.

about the solution of the problem to be solved. One can say that GFEM generalizes or extends the possibilities of standard FEM. Strouboulis et al. [177] also described GFEM as an extension of the finite element method. The new shape function $P_{(j-1)Q+q}$ defined by (3.19), is the critical ingredient of this method. In FEM,the solution space is approximated with standard polynomial shape functions $N_j(\mathbf{x})$, while in GFEM new approximation functions defined by (3.19) are used. A basic methodology used for of any FEM calculations is illustrated in Figure 3.2. In this current work a self-written FORTRAN code is used that can execute both FEM and GFEM calculations where the main difference is the calculation of the approximate ansatz functions. The shaded box in Figure 3.2 is the main area where new enrichment functions for GFEM are calculated. The subroutines for calculating new shape functions and their derivatives are given respectively, in the Figure 3.3 and Figure 3.4.

3.7 Recap of 2D results

To show the performance of the proposed GFEM and to compare its efficiency with the standard FEM, we recapitulate some numerical results for problems in 2D domains. Two different numerical examples are considered to highlight the benefits of the proposed GFEM in comparison with FEM. As a first example we take a transient heat diffusion problem defined by equations (3.1) – (3.3) with a known analytical solution. The second example considers a heat transfer problem in an L-shape domain with multiple heat sources. We use the standard FEM and GFEM approaches to solve the weak formulation (3.14). To compute the solution numerically, we used a 3 noded triangular mesh with piecewise bilinear shape functions. In case of GFEM, the approximate solution space is enriched with various Gaussian functions defined by (3.18). All the computations are performed on Intel® Core™ i5-6200 CPU @ 2.30 GHz processor speed with 12 GB installed RAM. The codes are not parallel, that is, the computations are performed sequentially.

3.7.1 Solution of a problem with a known analytical solution

To assess the accuracy of GFEM, we take a heat diffusion problem considered in [126] as our first test example. The problem is considered in a square domain $\Omega = [0, 2]^2$ with a known analytical solution. We solve the transient heat diffusion problem with source term $f(t, \mathbf{x})$, the boundary function $g(t, \mathbf{x})$ and the initial condition $u_0(\mathbf{x})$ such that the exact solution of (3.1)–(3.3) is given by

$$U(\mathbf{x}, t) = x^{20}(2 - x)^{20}y^{20}(2 - y)^{20}(1 - e^{-\lambda t}) \tag{3.39}$$

where $\mathbf{x} = (x, y)^T$ are the spatial coordinates, t is the time variable and λ is the heat diffusion coefficient. The errors in both FEM and GFEM solutions are quantified by calculating the relative L_2 error (ε) defined as

$$\varepsilon = \frac{||U - u||_{L^2(\Omega)}}{||U||_{L^2(\Omega)}} \times 100 \tag{3.40}$$

where u and U are the numerical and exact solutions, respectively. For all the computations, the time step value is taken to be $\Delta t = 0.1$ with a total computation time of $t = 10$. The convection heat transfer coefficient is set at h=1 and the heat diffusion coefficient λ is selected to be 0.1.

Th purpose of this example problem is to compare the accuracy of the GFEM with the standard FEM. To calculate the GFEM solution, the approximation space is enriched by different number of enrichment functions $Q = 5, 6, ..8$. The terminology GFEM5Enr will be used in the following discussion to refer to the GFEM solution with $Q = 5$. Similarly GFEM6Enr, GFEM7Enr and GFEM8Enr are the GFEM solutions with $Q = 6, 7$ and 8, respectively. To demonstrate the convergence of the FEM and GFEM solutions, the $h-$refinement strategy is used. Figure 3.5 shows the convergence of GFEM solutions with different number of enrichment functions Q, at three different simulation times, $t = 2, 5, 10$. At $t = 10$, all the solutions converge to a relative error of $\varepsilon = 0.09\%$.

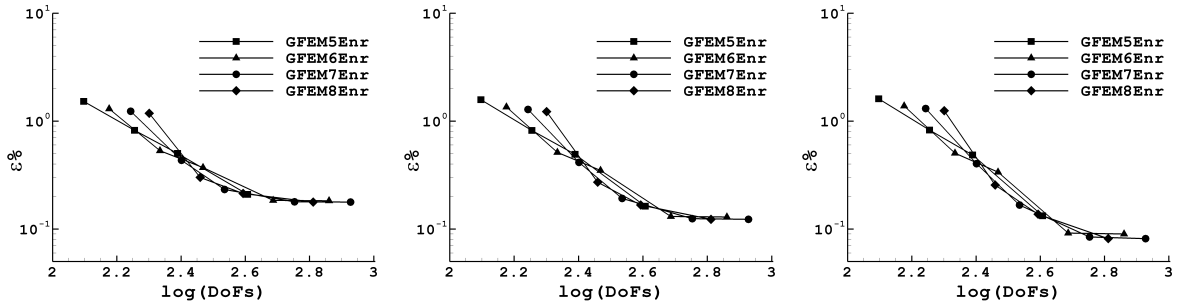

$t = 2$ $t = 5$ $t = 10$

Fig. 3.5 Convergence history of relative error ε for GFEM solutions

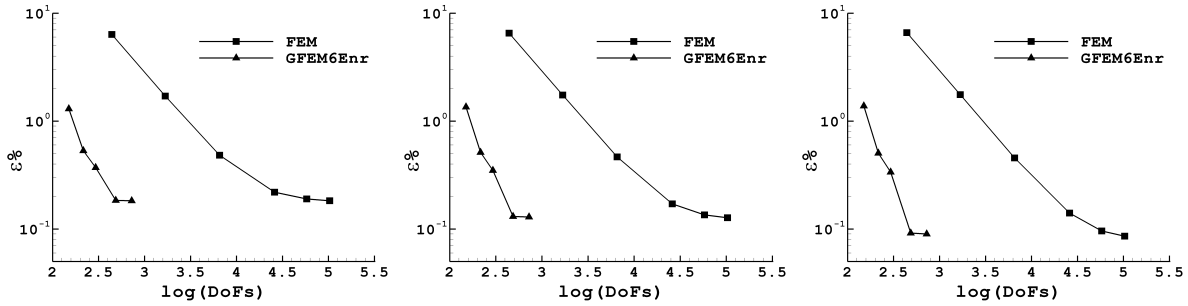

$t = 2$ $t = 5$ $t = 10$

Fig. 3.6 Comparison of relative error ε for FEM and GFEM solutions with $h-$refinement.

Figure 3.6 compares the convergence of the FEM solution with GFEM6Enr. It is clear from this figure that GFEM converges more rapidly than the FEM solution. To reach a converged solution, GFEM uses fewer DOFs as compared to FEM. Figure 3.7 shows the finite element meshes for converged solutions. To achieve a relative error of $\varepsilon = 0.09\%$, the FEM solution needed 58081 DOFs, while the same was achieved with only 486 DOFs in case of GFEM. The FEM solution took 87.16s to build the linear system at the first time step, and another 9.04s to solve the resulting system of equations. For GFEM, the corresponding times are only 0.78s and 0.016s, respectively.

Figure 3.8 shows the temperature distributions at the three specified simulation times for exact, FEM and GFEM solutions. Both FEM and GFEM solutions show temperature profiles very similar to the exact solution, but the DOFs used in case

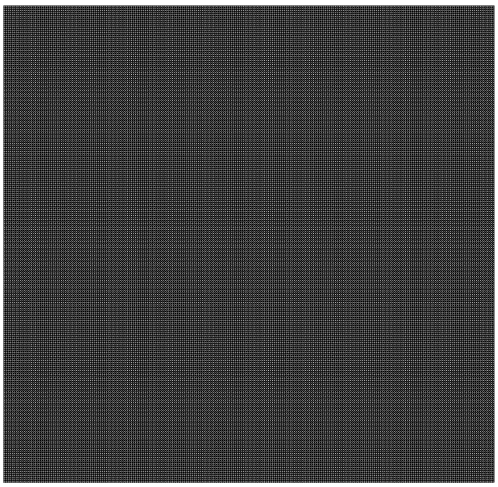

FEM (115200 elements, 58081 DOFs)

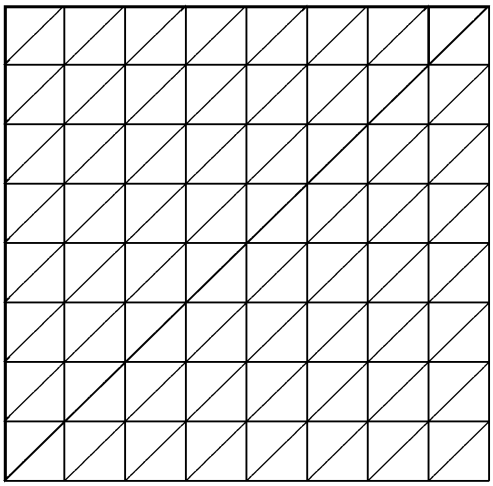

GFEM (128 elements, 486 DOFs)

Fig. 3.7 Finite element meshes with converged solutions.

of GFEM are only a small fraction of those used for the FEM solution. A similar problem in 3D domain is considered in the next chapter with detailed discussion on different numerical aspects of GFEM solution. The next example shows the working of the GFEM for a problem with multiple heat sources.

3.7.2 Solution of a problem with an L-shape domain having multiple heat sources

The second problem considers the heat diffusion problem governed by (3.1) – (3.3) in an L-shape domain having multiple heat sources at different locations of the domain. Figure 3.9 illustrates the domain configuration with three embedded heat sources defined as;

$$f = \left\{ \begin{array}{ll} 2000 & \text{if} \quad (x,y) \in [0.4, 0.4] \times [0.6, 0.6] \\ 1800 & \text{if} \quad (x,y) \in [1.4, 0.4] \times [1.6, 0.6] \\ 1600 & \text{if} \quad (x,y) \in [0.4, 1.4] \times [0.6, 1.6] \\ 0 & \text{elsewhere} \end{array} \right\} \tag{3.41}$$

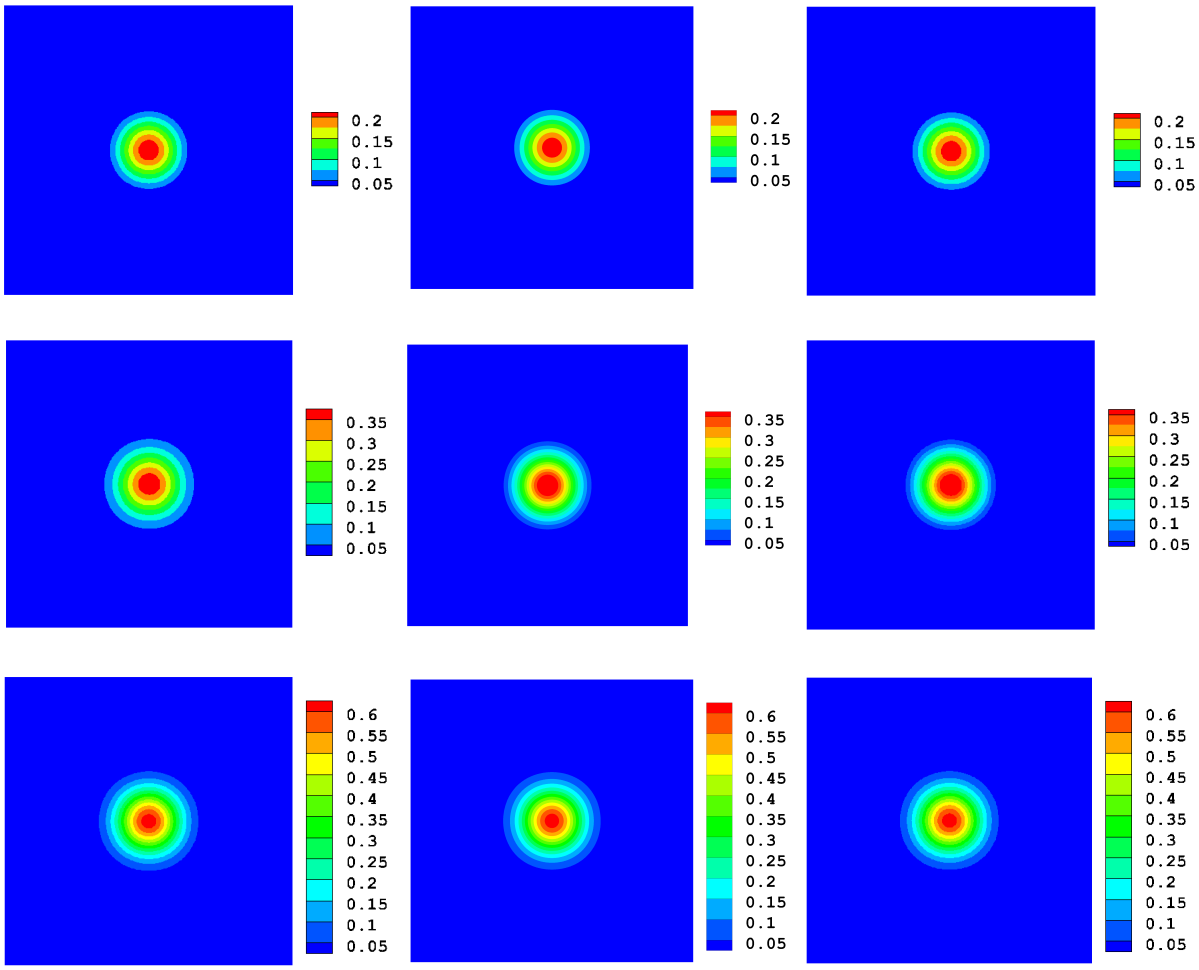

Fig. 3.8 Temperature distribution in the domain for exact (left), FEM (middle) and GFEM solutions (right). From top to bottom, the simulation times are $t = 2$, 5, and 10.

All the quantities are measured in SI units. Initial temperature of the domain and the boundary source are set at $u_0 = 300$ and $g = 300$. The heat diffusion coefficient and convection heat transfer coefficient for the problem are selected to be $\lambda = 0.1$ and h $= 1$, respectively. The time step value is fixed at $\Delta t = 0.1$ with total solution time, $t = 10$. The numerical results are presented at different simulation times, $t = 1, 5, 10, 20$.

The purpose of this example problem is to compare the accuracy of the proposed GFEM with the standard FEM for non-symmetric heat sources. Due to the non-

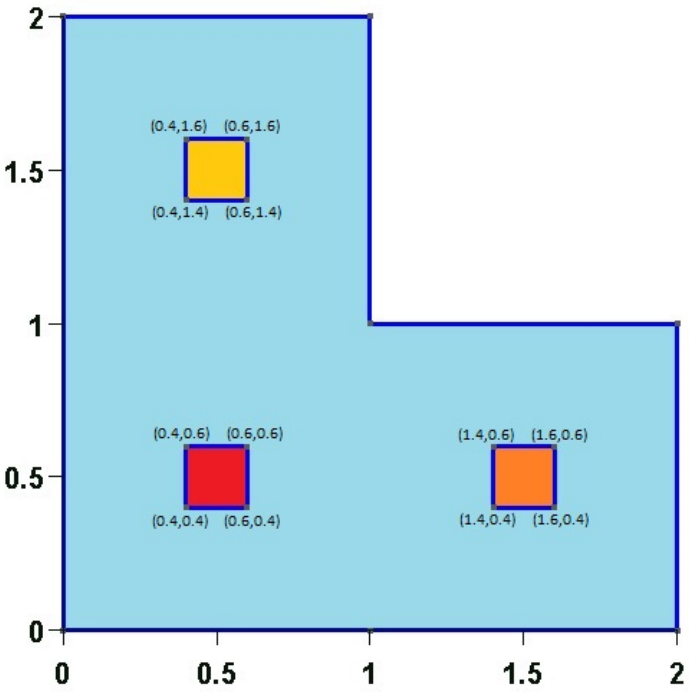

Fig. 3.9 Configuration of the L-shape domain with multiple heat sources, heat source 1 (■), heat source 2 (■), heat source 3 (■).

symmetric nature of heat sources, the symmetry of the temperature field is not preserved, and pose a relatively difficult numerical problem to be handled. Besides, the transient nature of the problem make it more challenging and a good numerical accuracy is required to capture the steep temperature gradients.

To compare the numerical results of the GFEM and standard FEM, we first compute a reference FEM solution (FEMR) with a fine mesh. The FEMR solution is used as a benchmark against which the solutions obtained with GFEM and the standard FEM are compared. Figure 3.10 shows the mesh grids used for the FEMR, FEM and GFEM solutions. FEMR solution is obtained with a fine mesh having 18855 elements and 9564 nodes. The mesh grids for FEM and GFEM are selected such that both have comparable DOFs. With the selected meshes, FEM solution is calculated using 856 DOFs, whereas GFEM solution is computed with 828 DOFs using six enrichment functions. To capture the temperature gradients at three different heat sources, each

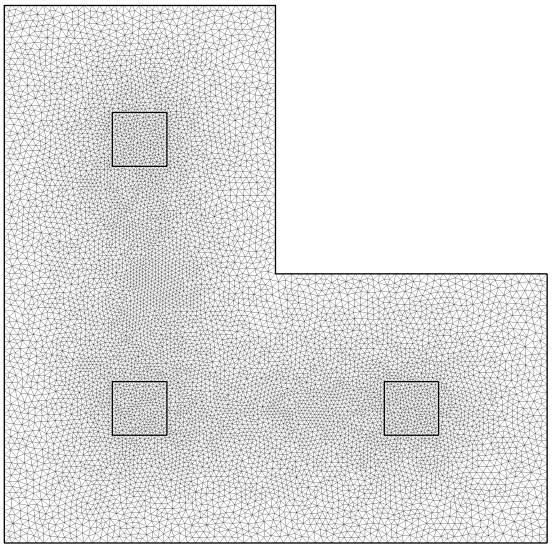

FEMR (9564 nodes, 18855 elements)

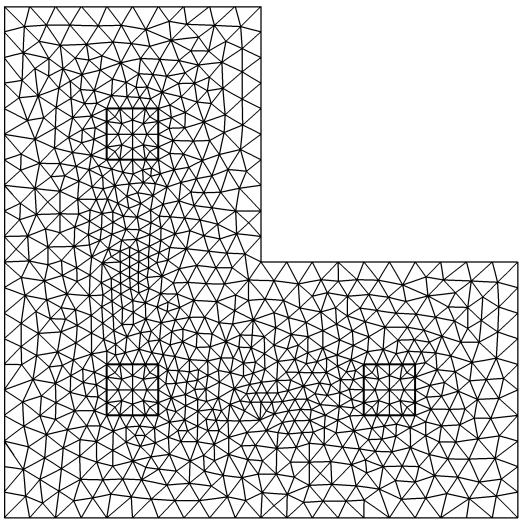

FEM (856 nodes, 1630 elements)

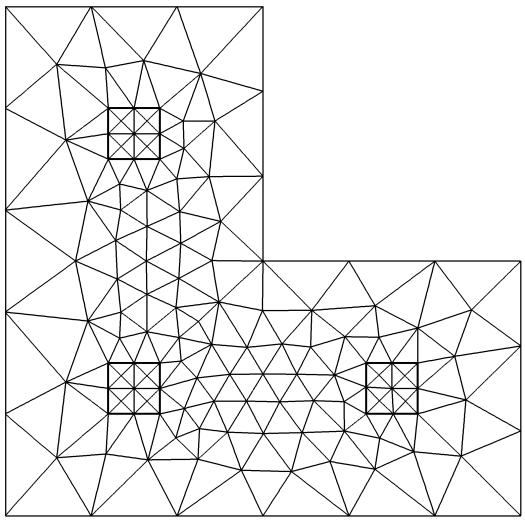

GFEM (138 nodes, 251 elements)

Fig. 3.10 Finite element meshes for the L-shape domain with multiple heat sources.

enrichment is taken as the combination of three functions, each centred at a different heat source.

Figure 3.11 shows the temperature distributions obtained using FEMR, FEM and GFEM solutions at four different computation times. The displayed plots show that for the considered thermal conditions, very smooth temperature profiles are obtained with GFEM similar to those obtained with FEMR. The FEM on the other hand shows comparatively coarse profiles. This ascertains that GFEM with a very coarse mesh was able to capture the same solution dynamics as those obtained on a very fine mesh FEMR solution. To capture the sharp thermal gradients, GFEM uses only 828 DOFs whereas the FEMR solution is obtained with 9564 TOTDOF. The FEM solution, although using comparable number of DOFs, was not able to capture the solution as accurately as GFEM. The figures show that the temperature of the medium is increasing continuously as all the three heat sources are dissipating heat for whole of the simulation time. The temperature of the domain is maximum at the centre of heat source 1, followed by heat source 2 and heat source 3 respectively. The heat moves towards the boundaries where the temperature is minimum. Being the highest of all the three sources, maximum heat is dissipated by heat source 1 and maximum boundary temperature is observed at the boundaries near this heat source, followed by boundaries which are near heat source 2, and minimum at boundaries near heat source 3. Figure 3.12 shows the temperature profiles at different simulation times as 3D surfaces. All the plots are drawn on the same contour level for easy visualization of the time evolution of the temperatures.

To quantify the accuracy of GFEM, we compare in Figure 3.13 the absolute differences in temperatures along a horizontal centre line between the FEMR and FEM solutions (top four figures) and between FEMR and GFEM solutions (bottom four figures) at the selected simulation times. The horizontal line starts from [0,0.5], passes through the centres of heat sources 1 and 2 and ends at [2,0.5]. It is clear from the plots that the differences in temperatures are much higher in case FEM as compared to GFEM. The peaks are observed around the centres of the heat sources with the

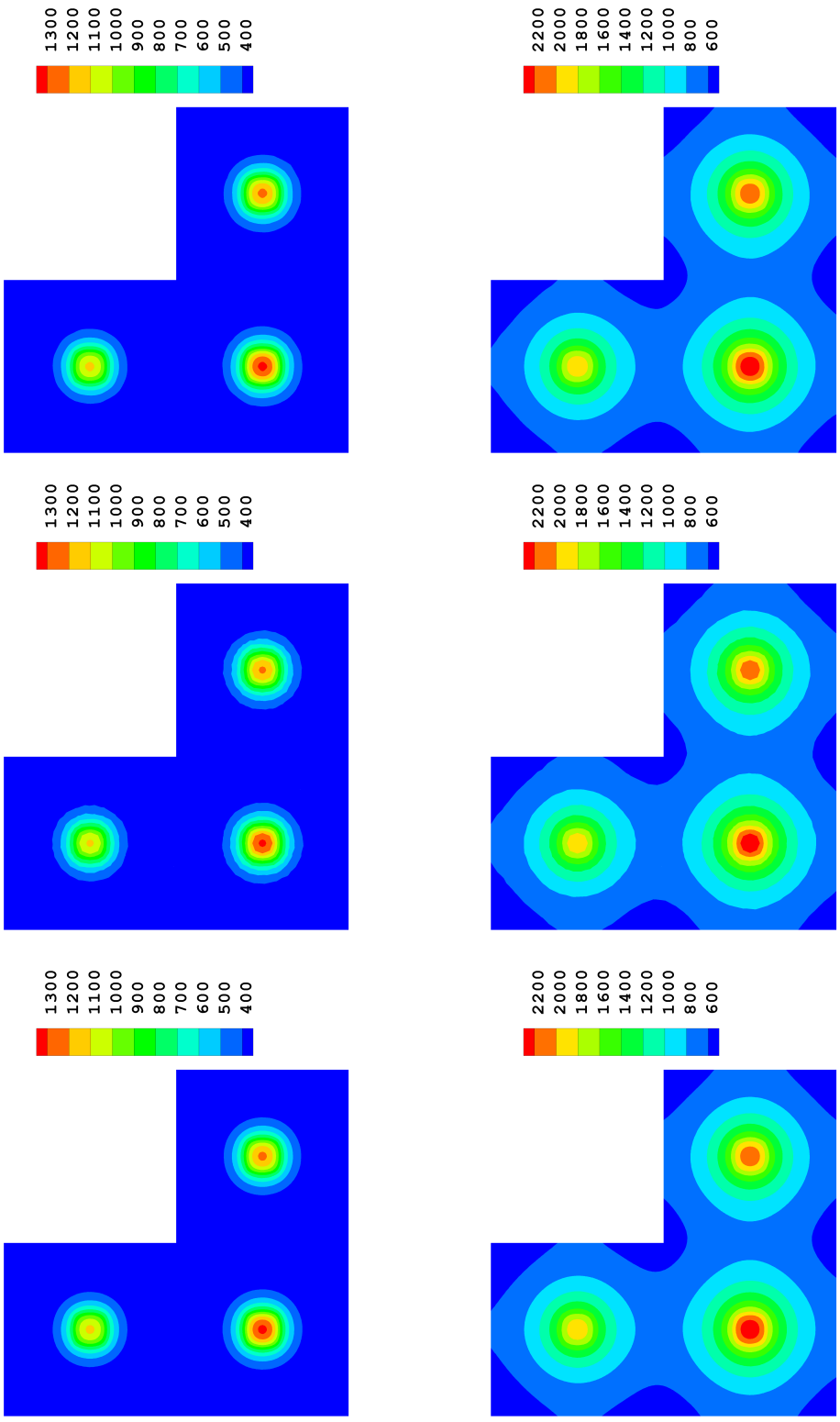

Fig. 3.11 Temperature distribution in the L-shape domain obtained with FEMR (left), FEM (middle) and GFEM (right). The simulation times are $t = 1$ (top row) and $t = 10$ (bottom row).

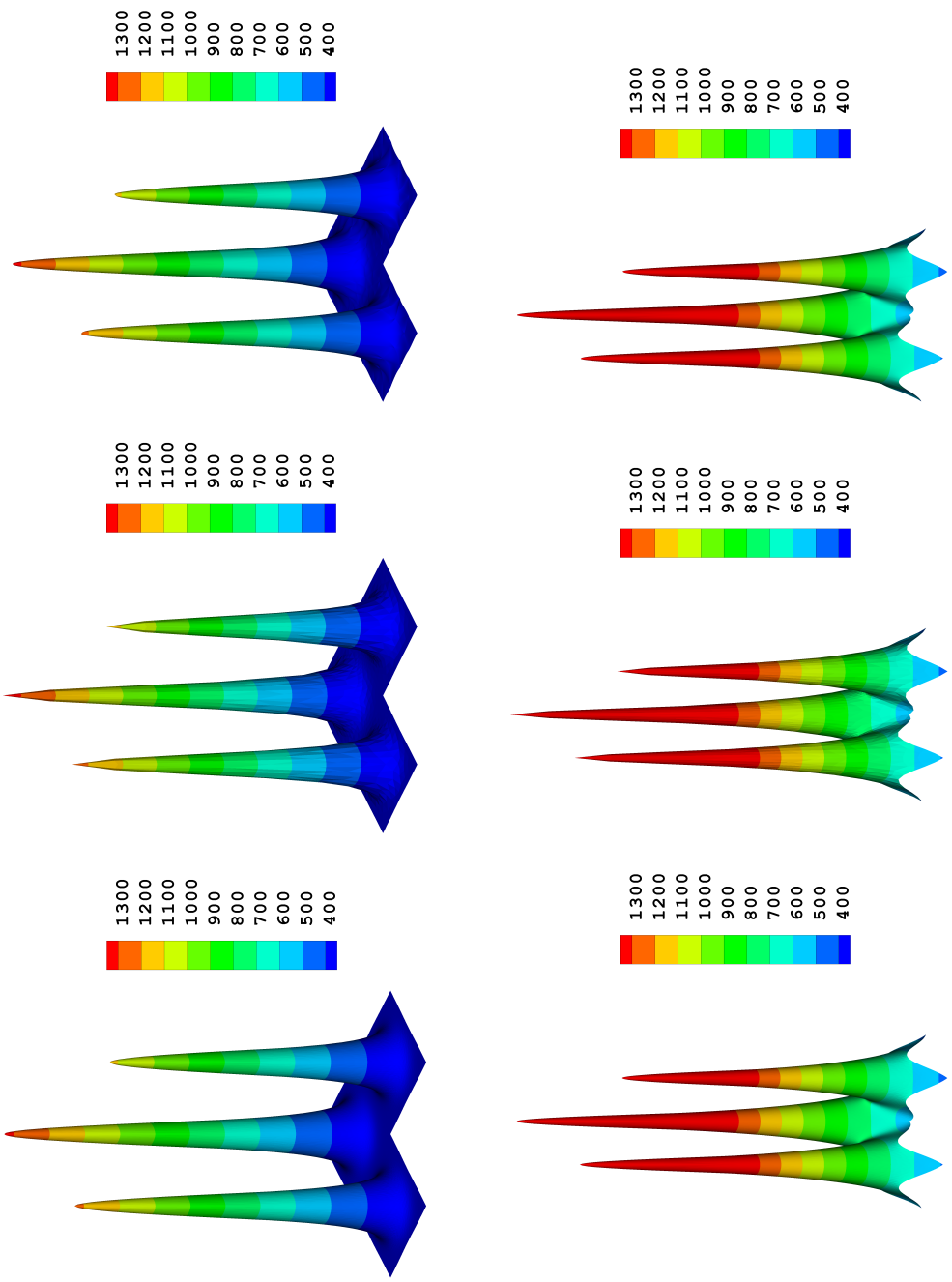

Fig. 3.12 Temperature profiles displayed as 3D surfaces. The distributions are obtained with FEMR (left), FEM (middle) and GFEM (right).. The simulation times are $t = 1$ (top row) and $t = 10$ (bottom row).

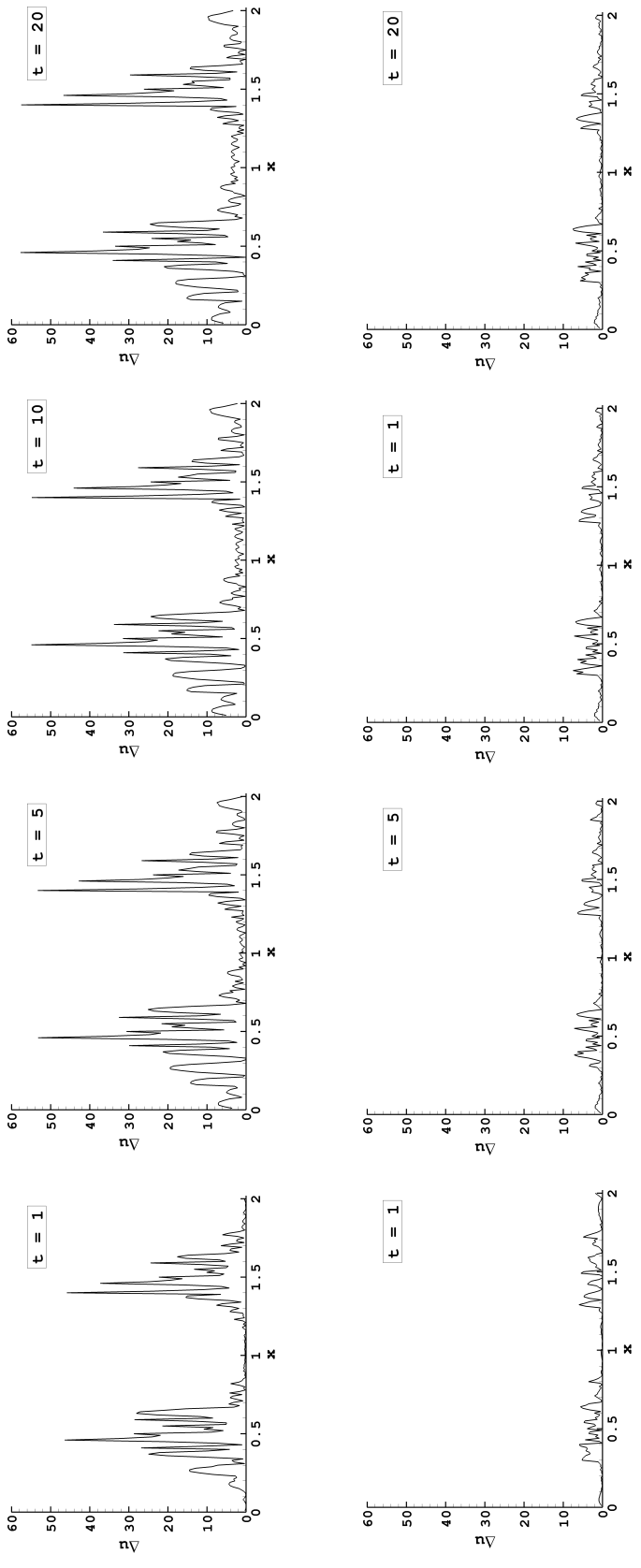

Fig. 3.13 Variation of the temperature differences between the FEM solution and reference FEMR solution (top row), and the GFEM and FEMR solution (bottom row) along the horizontal direction.

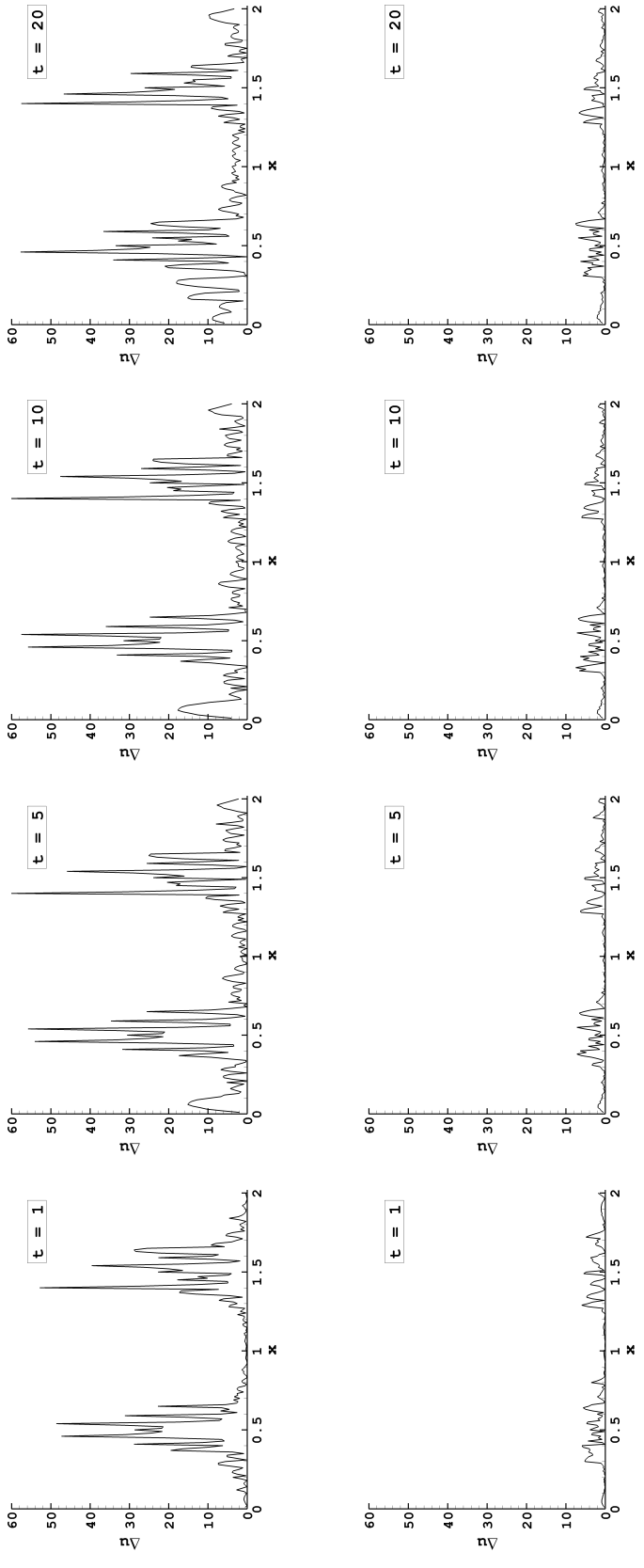

Fig. 3.14 Variation of the temperature differences between the FEM solution and reference FEMR solution (top row), and the GFEM and FEMR solution (bottom row) along the vertical direction.

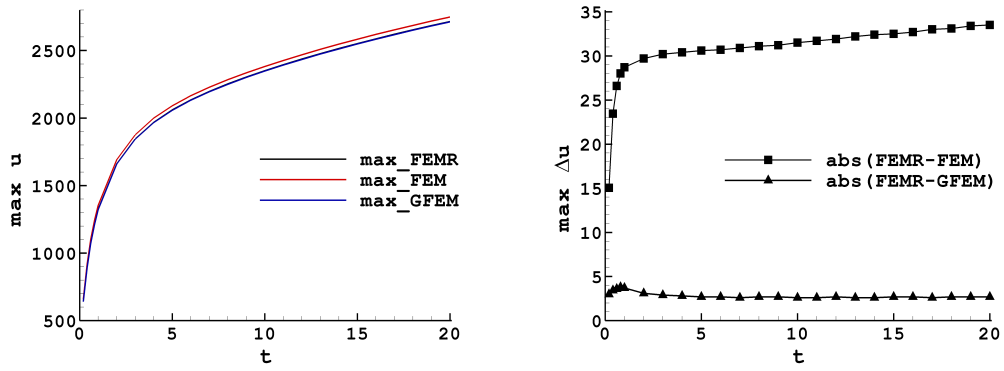

(a) (b)

Fig. 3.15 Time evolution of (a) maximum temperatures and (b) difference in maximum temperatures between FEMR and FEM, and FEMR and GFEM.

maximum value observed around centre of heat source 1. In case of FEM solution, the maximum difference reaches to a value as high as 60 which in the case of GFEM stays around 6. An important observation made from this figure is that as the time passes, the difference in temperatures in case of FEM solution increases, which in the case of GFEM almost stays at the same level. This suggests that in case of FEM solution, the difference in temperatures will increase further with extended simulation times. For lengthy simulation times, this offers another advantage of GFEM over FEM. A similar set of results with same observations is plotted in Figure 3.14 along the vertical centre line. The vertical line starts from [0.5,0], passes through heat sources 1 and 3 and ends at [0.5,2].

To further quantify the results of this example problem, in Figure 3.15(a) we plot the time evolution of maximum temperatures obtained with FEMR, FEM and GFEM solutions. Figure 3.15(b) plots the absolute differences in the maximum temperatures between FEMR and FEM, and FEMR and GFEM. The results shown in these figures further strengthens the claim made previously and the behaviour described earlier becomes more evident. Figure 3.15(a) depicts that the maximum domain temperatures obtained with GFEM are almost identical with FEMR. Both the curves are almost overlapping. Temperatures obtained with FEM shows comparably higher differences and the gap between FEM and FEMR curves increases as time marches. These dif-

ferences can be clearly seen in Figure 3.15(b). The absolute difference in maximum temperatures between FEMR and FEM starts from a value of around 15 at $t = 0.2$ and reaches to around 34 at $t = 20$ which in case of GFEM stays between 3.5 and 4.0 for whole of the simulation time. As the curves suggest, the differences in the case of FEM solution are expected to grow higher with extended simulation times whereas negligible variations are expected in the case of GFEM.

3.8 Overview

In this Chapter, the initial boundary value problem is presented with its variational formulation form to be solved. Both FEM and GFEM approximate solutions are discussed with related computational aspects including numerical integration and solution procedure. The choice of the enrichment functions was also discussed emphasizing on the fact that they are time-independent and hence will lead to huge savings in the computational effort. To show the working of the GFEM, some numerical results for problems in 2D domains are presented and the benefits of GFEM are highlighted. It is shown that for a comparable accuracy, GFEM requires fewer DOFs than the standard FEM.

In the next Chapter, GFEM will be extended to solve transient heat transfer problems in three dimensions.

Chapter 4

GFEM for three-dimensional transient heat diffusion problems

4.1 Introduction

Real world problems are three dimensional. Although in some cases the problem may be simplified with suitable assumptions to treat it as a 2D or even 1D, but in general this simplification is not possible, and hence the 3D approach is necessary to treat the problem. This may be due to the complexity of geometry that cannot be simplified enough to take advantage of the symmetry or may be due to the non-symmetric loading effect or boundary conditions.

In recent years, the simulation of complex 3D problems is becoming more and more common in practice. Although the computer architecture and design have become much more sophisticated, and more advanced computing facilities are available in recent times, the solution of most 3D practical problems using classical finite element methods is still complex and computationally intensive.

This chapter is dedicated to extend GFEM to three-dimensional transient heat diffusion problems. The GFEM has been proved to provide efficient solution for 2D transient heat diffusion problems [126]. In this work, we exploit its efficiency for the solution of 3D transient heat diffusion problems with steep gradient. As in the 2D

case, multiple enrichment functions are used to capture the sharp variation of the temperature. As explicated in the previous chapter, the enrichment functions are time independent, therefore the system matrix is assembled only at the first time step and retained for subsequent time steps. Only the right hand side of the linear system of equations is updated for every time step, which is expected to significantly reduce the computational cost in 3D.

Since the theory is practically similar to the 2D case, it is not repeated in this Chapter. However, key computational aspects related to the 3D geometry will be discussed. To assess the performance of the GFEM approach, three different test problems are considered.

4.2 Weak formulation of the 3D boundary value problem

Given an open bounded domain $\Omega \subset \mathbb{R}^3$, we are interested to numerically solve the transient heat diffusion problem defined by expressions (3.1)−(3.3). The weak formulation (3.14) is rewritten as

$$\int_\Omega (\nabla W \cdot \nabla u^{n+1} + W k u^{n+1}) d\Omega + \int_\Gamma W h u^{n+1} d\Gamma = \int_\Omega W F^{n+1} d\Omega + \int_\Gamma W g^{n+1}\, d\Gamma\ , \quad (4.1)$$

where Ω is a 3D domain and Γ represents a surface on the boundary. F^{n+1} and k in the above equation are defined as

$$F^{n+1} = k\Big(\delta t f(t_{n+1}, \mathbf{x}) + u^n\Big), \qquad k = \frac{1}{\lambda \delta t}.$$

here $\mathbf{x} = (x, y, z)^T$ are the spatial coordinates, t is the time variable, λ is the heat diffusion coefficient, and $f(t, \mathbf{x})$ represents the effects of internal sources/sinks. The weak formulation (4.1) is solved for the unknown nodal temperatures u^{n+1} using the standard FEM and GFEM.

4.3 Numerical experiments

This section investigates the performance of the proposed GFEM for three dimensional transient heat diffusion problem defined by (3.1) - (3.3). We use the classical FEM and GFEM approaches to solve the weak formulation (4.1). Three different test problems are considered to assess the performance of the proposed GFEM algorithm and to compare its efficiency with the standard FEM approach. To compute the solution numerically, we used an 8 noded hexahedral mesh with piecewise linear shape functions. All integrals over Ω are evaluated numerically using a Gauss quadrature with 2 integration points in each direction for FEM solution whereas for GFEM 20 integration points are used in each spatial direction. A direct solver is used to solve the resulting system of equations. All the computations are performed on Intel® Xeon® ES-1620 CPU @ 3.50 GHz processor speed with 32 GB installed RAM. The codes are not parallel and only consider the default optimization of the computer.

4.3.1 Approximation of a problem with a known exact solution

To asses the accuracy of the method, we take a problem with a known exact solution as our first example problem. We consider a diffusion problem in 3D domain defined by $\Omega = [0, 2]^3$. For the proposed problem, the reaction term $f(t, \mathbf{x})$, the boundary function $g(t, \mathbf{x})$ and the initial condition $u_0(\mathbf{x})$ are chosen such that the exact solution is given by

$$U(\mathbf{x}, t) = x^{20}(2 - x)^{20}y^{20}(2 - y)^{20}z^{20}(2 - z)^{20}(1 - e^{-\lambda t}) \tag{4.2}$$

where t is the time variable, $\mathbf{x} = (x, y, z)^T$ are the spatial coordinates, and λ is the heat diffusion coefficient. As the exact solution is known, we can quantify the error in

both FEM and GFEM by calculating the relative L_2 error (ε) defined as

$$\varepsilon = \frac{||U-u||_{L^2(\Omega)}}{||U||_{L^2(\Omega)}} \times 100 \tag{4.3}$$

where u and U are the numerical and exact solutions, respectively.

To calculate the GFEM solution, the approximation space is enriched by Gaussian functions of varying standard deviations as defined by (3.18). Both for FEM and GFEM computations, we use the parameter h = 1 and the time step value $\Delta t = 0.001$ with a total solution time of $t = 0.1$. The heat diffusion coefficient λ is selected to be 0.01 for a first set of results. Another set of results is presented with $\lambda = 0.1$.

In order to get a converged solution, we used an $h-$refinement procedure for the FEM, while for GFEM both h and $q-$refinements are considered. To solve the problem with FEM, we start with a mesh grid of 1000 elements with a total of 1331 degrees of freedom (DOFs), which yields an L_2 error of 8.04% at $t = 0.1$. To improve the results, the mesh is refined gradually. Figure 4.1 shows the meshes used for the FEM solutions.

Table 4.1 Variation of L_2 error with $h-$refinement for FEM solutions at $t = 0.1$.

Elements	DOFs	$\varepsilon\%$	
		$\lambda = 0.01$	$\lambda = 0.1$
1000	1331	8.04	9.76
8000	9261	1.10	2.13
15625	17576	0.56	1.31
27000	29791	0.33	0.89
64000	68921	0.15	0.49
125000	132651	0.08	0.31
216000	226981	0.05	0.21

Table 4.1 shows the L_2 error for each mesh along with the total number of DOFs. The first refinement to 8000 elements decreases the L_2 error to 1.10%. The total DOFs (TOTDOF) are increased to 9261. Subsequent mesh refinements improve the

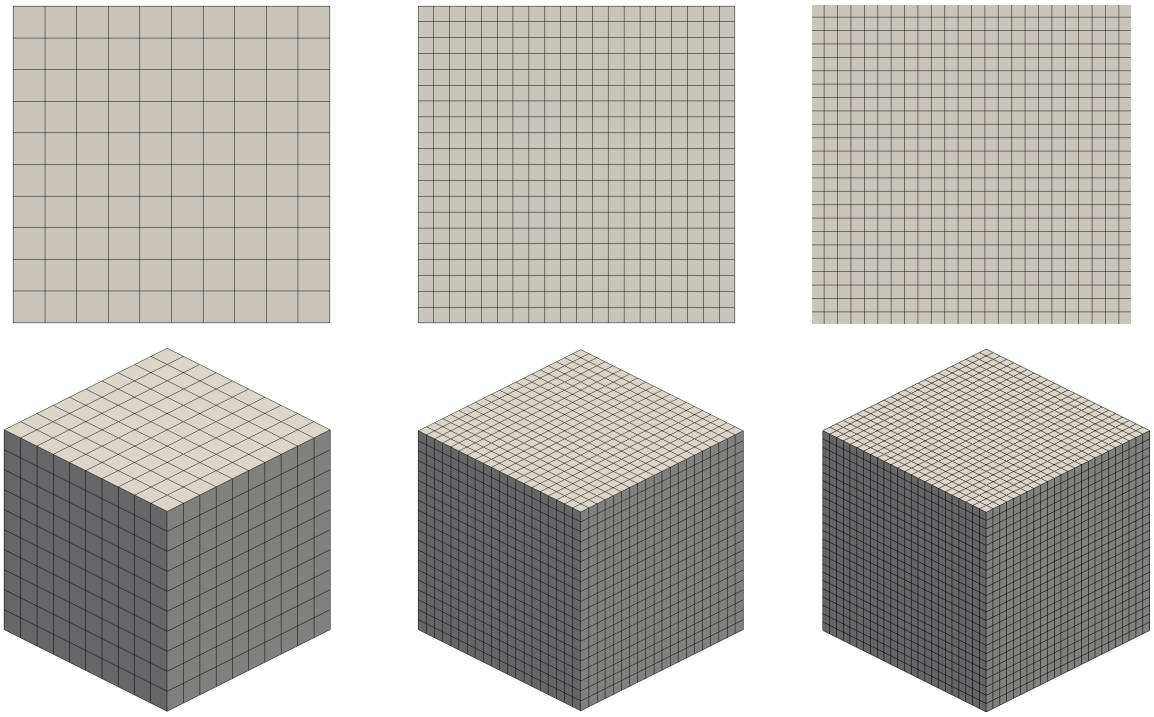

1000 elements,
1331 nodes

8000 elements,
9261 nodes

15625 elements,
17576 nodes

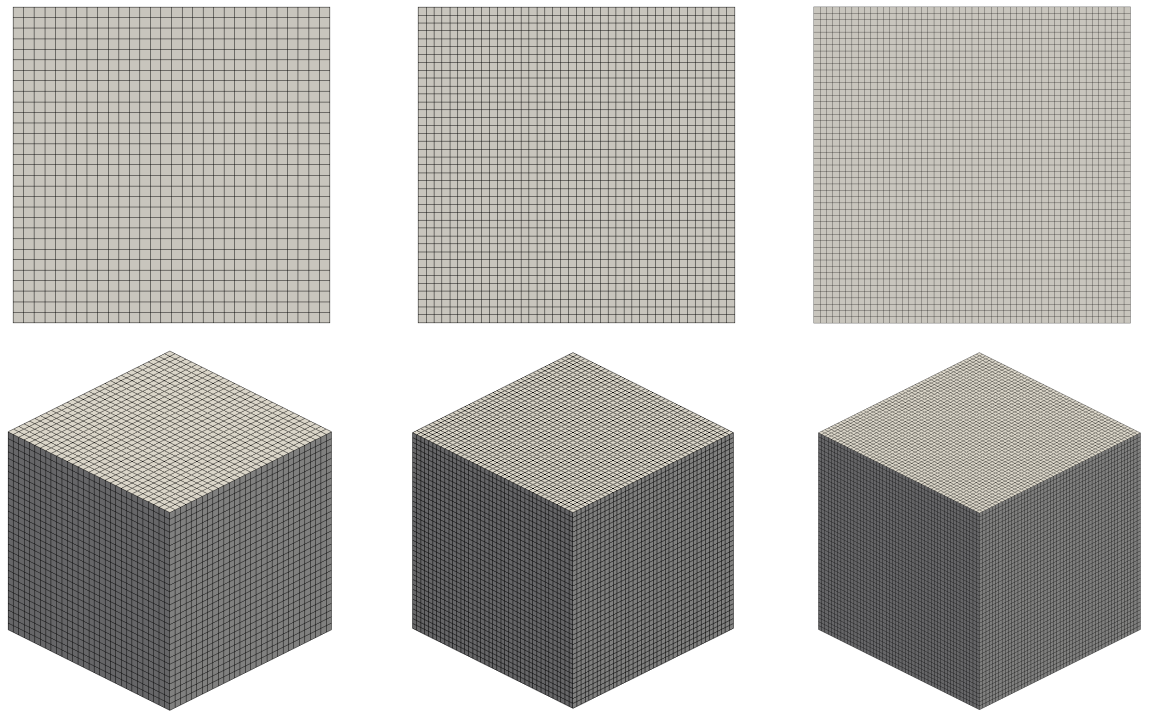

27000 elements,
29791 nodes

64000 elements,
68921 nodes

125000 elements,
132651 nodes

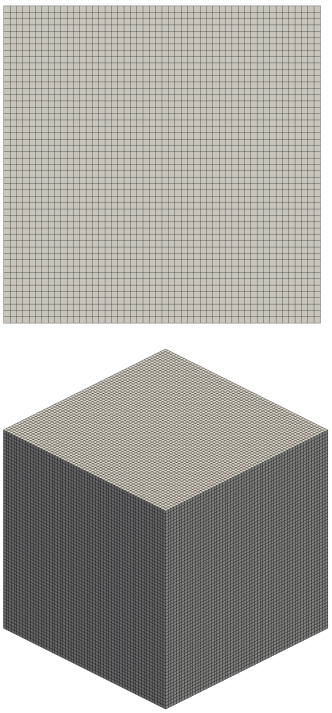

216000 elements,
226981 nodes

Fig. 4.1 3D meshes used for FEM solutions.

results further until we get an L_2 error of 0.08% with 125000 elements and 132651 TOTDOF. A final refinement of 216000 elements reduces the error to 0.05% with 226981 TOTDOF. A similar set of results is presented for $\lambda = 0.1$ in the last column of Table 4.1. For $\lambda = 0.1$, the L_2 error starts from 9.76% for 1000 elements and reduces to 0.22% with the very fine mesh of 216000 elements. The reason for the higher L_2 error for $\lambda = 0.1$ is that the rate of diffusion increases by increasing the value of λ, and the heat travels to more distant areas of the domain for the same computation time.

For GFEM solution, we start with a very coarse mesh of 64 elements in the 3D cube and enrich the solution space with different numbers of enrichment functions Q = 2,3...6. We then refine the mesh to a total of 216 elements in the whole domain, with 6 elements in each direction. Again we consider the same enrichment functions Q = 2,3...6. A third refinement of 512 elements with Q = 2,3...5 is also considered

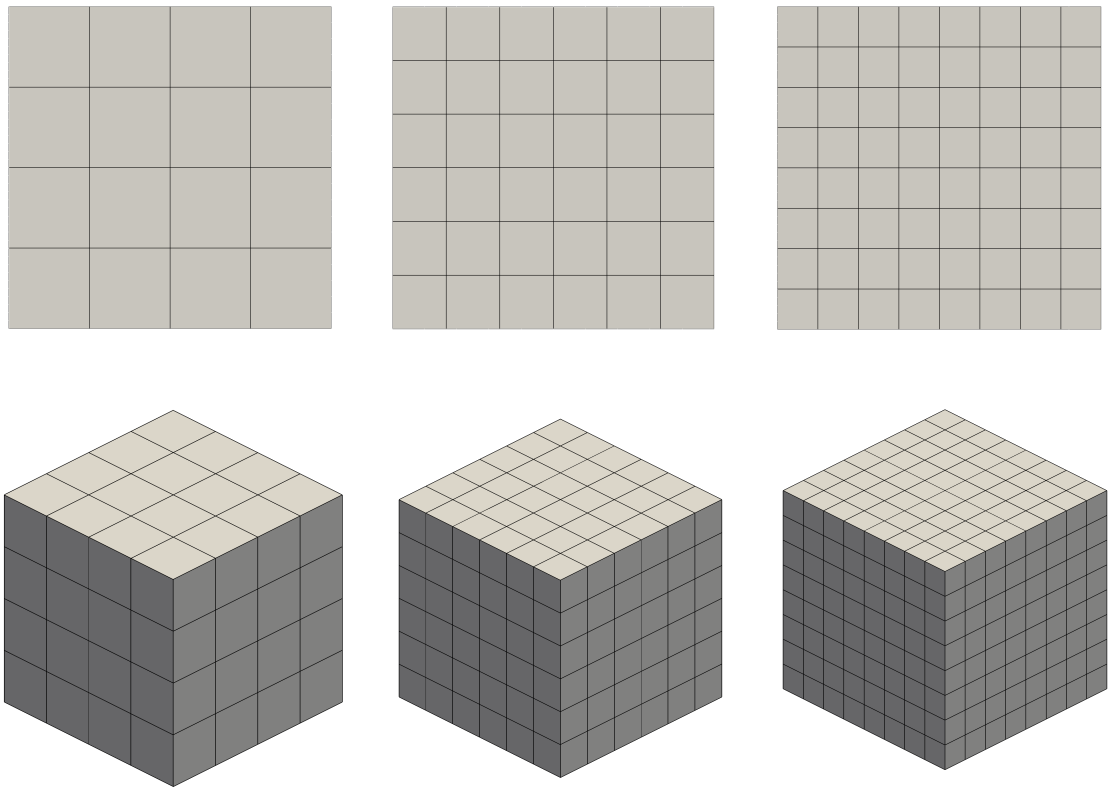

Fig. 4.2 3D meshes used for the GFEM solutions.

to improve the results further. In the coming discussion an analysis with 64 elements will be referred as GFEM1, and with 216 and 512 elements as GFEM2 and GFEM3, respectively. As for the FEM solution, the results are presented for $\lambda = 0.01$ and 0.1. Figure 4.2 shows the meshes used for GFEM solutions.

Table 4.2 shows the variation of L_2 error for each of these computations when the number of enrichment functions are increased using $\lambda = 0.01$. For GFEM1, we get an L_2 error of 9.38% with 2 enrichment functions which reduces to 1.06% with $Q = 6$. To improve the results, the mesh is refined to 216 elements. With $Q = 2$, the L_2 error is 5.33% which reduces to 0.43% with 6 enrichment functions. With 512 elements, the L_2 error decreases further to 0.17% with $Q = 5$. Comparison of the results of GFEM1, GFEM2 and GFEM3 show that using a higher number of enrichment functions we

Table 4.2 Variation of L_2 error with different mesh grids and $q-$refinement for the GFEM solutions at $t = 0.1$ using λ=0.01.

	GFEM1		GFEM2		GFEM3	
Q	DOFs	$\varepsilon\%$	DOFs	$\varepsilon\%$	DOFs	$\varepsilon\%$
2	250	9.38	686	5.33	1458	2.09
3	375	5.52	1029	2.40	2187	0.97
4	500	2.28	1372	1.39	2916	0.43
5	625	1.47	1715	0.65	3645	0.17
6	750	1.06	2058	0.43	-	-

can achieve relatively lower error with less DOFs. For example, GFEM2 with $Q = 4$ gives an L_2 error of 1.39% with 1372 TOTDOF. With GFEM1 we get a better error of 1.06% using 6 enrichment functions and 750 TOTDOF, giving a saving of 622 DOFs. Similarly, with $Q = 4$ and 2916 TOTDOF in GFEM3, the L_2 error is 0.43%, and in case of GFEM2, the same error is achieved with 2058 TOTDOF using $Q = 6$, resulting in a saving of 858 DOFs. This suggests to use a higher number of enrichment functions in GFEM rather than refined meshes. One problem that limits the number of enrichment functions is the conditioning of the system matrix. The conditioning of the system matrix deteriorates very quickly when higher numbers of enrichment functions are used. In their work, Mohamed et al. [126] also reported this problem. The same was observed in [88] as well.

In Table 4.3 are given the errors for GFEM computations using $\lambda = 0.1$. In contrast to the observation made in case of FEM, the diffusion of heat to the larger area of the domain does not affect the L_2 error considerably for the GFEM solution. The global nature of enrichments ensure to efficiently capture the solution in the whole domain. A very small change in the solution accuracy is observed by changing the value of λ from 0.01 to 0.1. The minimum L_2 error for GFEM3 using $Q = 5$ increases from 0.17% to 0.19% only. Similarly for GFEM2 using $Q = 6$, the error slightly increases from 0.43% to 0.47%. For GFEM1 with 6 enrichment functions, the error increases from 1.06% to 1.45%.

Table 4.3 Variation of L_2 error with different mesh grids and $q-$refinement for the GFEM solutions at $t = 0.1$ using λ=0.1.

	GFEM1		GFEM2		GFEM3	
Q	DOFs	ε%	DOFs	ε%	DOFs	ε%
2	250	9.74	686	5.59	1458	2.26
3	375	5.88	1029	2.56	2187	1.04
4	500	2.60	1372	1.53	2916	0.47
5	625	1.80	1715	0.71	3645	0.19
6	750	1.45	2058	0.47	-	-

Comparison of the GFEM results with FEM shows that with FEM we get a maximum accuracy of 0.05% with 226981 DOFs for $\lambda = 0.01$. With GFEM we get a minimum L_2 error of 0.17% with only 3645 DOFs. With FEM a comparable accuracy of 0.15% is achieved with 68921 DOFs. For FEM, this accuracy is achieved with a very fine mesh of 64000 elements, while in case of GFEM we use a very coarse mesh of only 512 elements with $Q = 5$. For $\lambda = 0.1$, the comparison of GFEM and FEM results confirms the above observation. With FEM, the maximum achievable accuracy is 0.21% with a very fine mesh of 216000 elements and 226981 TOTDOF. In comparison, GFEM gives an accuracy of 0.19% with only 3645 TOTDOF resulting in a huge reduction in the total DOFs. The TOTDOF in the case of GFEM is less than 2% of FEM, resulting in a saving of more than 98% in the total DOFs. To process 216000 elements and build the linear system at the first time step, FEM simulation took 228589s (63 hours, 29 min and 49 seconds), and another 5818s (1 hour, 36 min and 58 seconds) to solve the resulting system of equations. The corresponding times for GFEM to process 512 elements with 5 enrichment functions are 883.5s (14 min and 43.5 seconds) and 1.21s to solve the system of equations. Also, to update the right hand side of the system of equations and to recalculate the solution at subsequent time steps, FEM took on average 340s at every step. For GFEM the corresponding time is only 42s. As iterated previously, the enrichment functions are time independent, therefore the system matrix is assembled only at the first time step and retained at

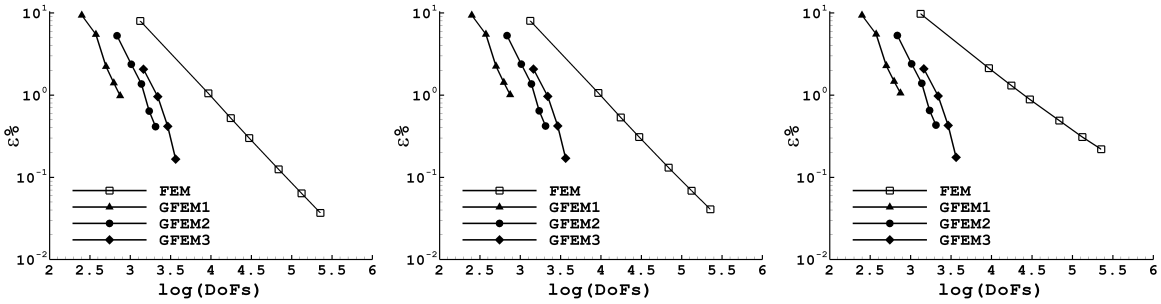

t =0.01 t =0.05 t =0.1

Fig. 4.3 L_2 error for FEM and GFEM solutions with $h-$refinement for FEM and $q-$refinement for GFEM using $\lambda = 0.01$.

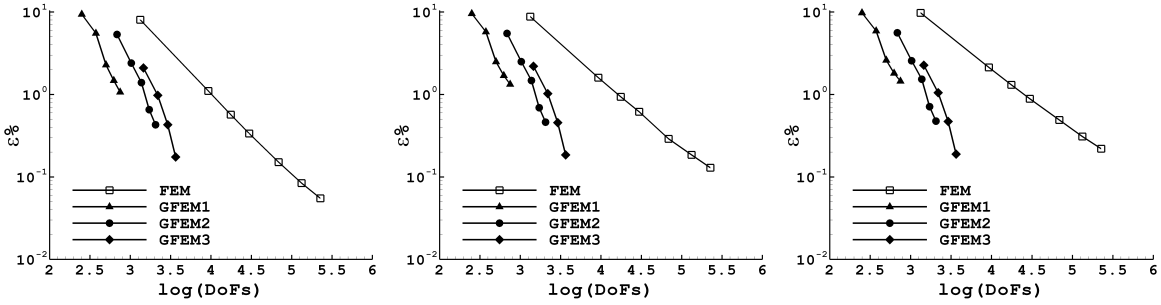

t =0.01 t =0.05 t =0.1

Fig. 4.4 L_2 error for FEM and GFEM solutions with $h-$refinement for FEM and $q-$refinement for GFEM using $\lambda = 0.1$.

the subsequent time steps. As a result the time saving at the subsequent time steps is also obvious in case of GFEM. The is to be emphasized that despite the fact that GFEM uses high number of integration points, yet the small number of elements with GFEM makes the time needed to assemble the system matrix much smaller than that with the FEM. Because the system matrix in case of GFEM is much smaller than the FEM, the CPU time for the solution of GFEM system is only a small fraction of the FEM.

Figure 4.3 compares the L_2 error both for FEM and GFEM at different time intervals using $\lambda = 0.01$, with $h-$refinement for FEM and $q-$refinement for GFEM.

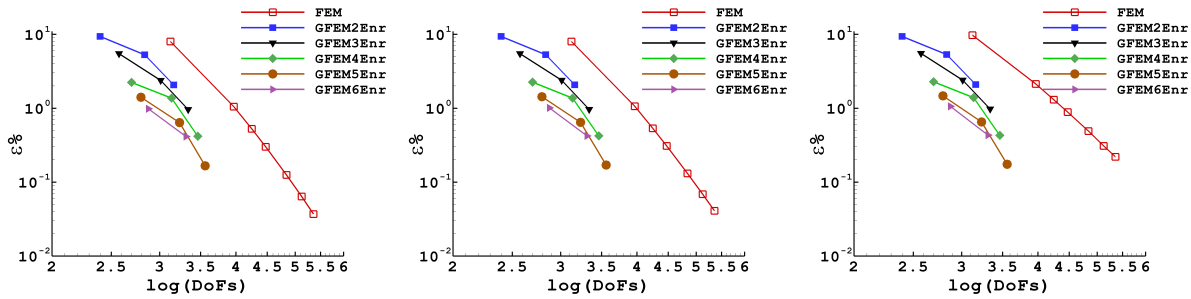

t =0.01 t =0.05 t =0.1

Fig. 4.5 L_2 error for FEM and GFEM solutions with $h-$refinement using $\lambda = 0.01$.

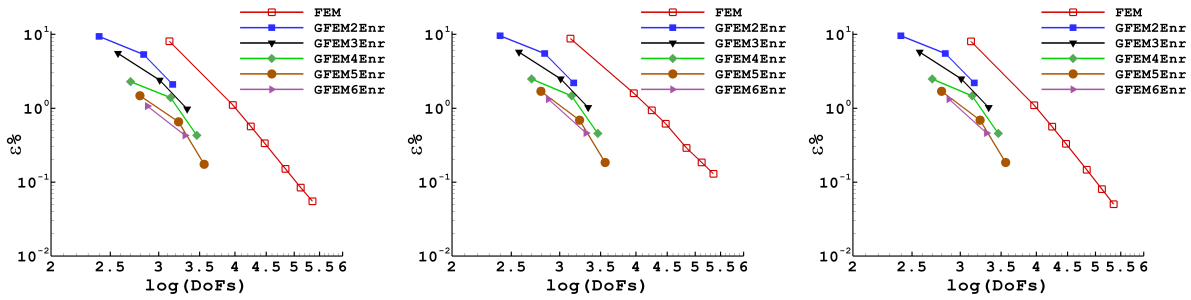

t =0.01 t =0.05 t =0.1

Fig. 4.6 L_2 error for FEM and GFEM solutions with $h-$refinement using $\lambda = 0.1$.

In the figure, the DOFs are plotted on the abscissa while on the ordinate the L_2 error is plotted on a logarithmic scale. It is clear from the graphs that the GFEM solution converges much faster than that of FEM and gives a better L_2 error with less DOFs. A similar comparison is presented in Figure 4.4 for $\lambda = 0.1$.

Another comparison using $h-$refinement for both FEM and GFEM results is given in Figure 4.5 and Figure 4.6 using $\lambda = 0.01$ and 0.1, respectively. GFEM2Enr represents the GFEM results using 2 enrichment functions and with three different mesh densities of 64, 216 and 512 elements. Similarly, GFEM3Enr, GFEM4Enr, GFEM5Enr and GFEM6Enr are the GFEM computations with 3, 4, 5 and 6 enrichment functions, respectively. The FEM results in Figure 4.5, and Figure 4.6 are the same as in Figure 4.3, and Figure 4.4, but GFEM results are now presented with $h-$refinement which

previously were presented with $q-$refinement.

Figure 4.7 and Figure 4.8 show the temperature distribution at different simulation times for the exact, FEM and GFEM solutions using $\lambda = 0.01$ and 0.1, respectively. For GFEM simulations, the presented plots are obtained with 216 elements using 4 enrichment functions. For FEM the results are presented using 216000 elements. Both FEM and GFEM results show the same temperature trends as that of the exact solution but in the case of GFEM, the total DOFs used to get the solution is only a small fraction of that used to obtain the FEM solution.

4.3.2 Approximation of a problem with a cubic domain

The second example considers a transient heat diffusion problem in a 3D domain $\Omega = [0, 1]^3$ with a heat source in the central part. A cross section through the middle of the domain is shown in Figure 4.9. For the central part, $\mathbf{x} \in [0.4, 0.6]^3$, the source dissipates heat at a constant rate of $f = 2000$K/s and is zero in the rest of the domain. The total simulation time is taken to be $t = 0.4$s with a time step value of $\Delta t = 0.001$s. The source dissipates heat for half of the simulation time, i.e., from $t = 0$ to $t = 0.2$s, and then is switched off and the medium is allowed to cool down for the remaining half of the simulation. The initial temperature u_o of the domain and the boundary source g, of expressions (3.2) and (3.3), are set to be 300K and 300K/s, respectively. The convection heat transfer coefficient on the boundaries is taken to be h= 1kg/Ks^2, and the diffusion heat transfer coefficient for the medium is assumed to be $\lambda = 0.01$kgm/Ks^2. Another more challenging case with $\lambda = 0.001$kgm/Ks^2 is also considered to show the usefulness of the proposed GFEM approach.

Example problem 2 considers a problem with sharp local gradients as the heat source is located only in a concentrated area that becomes zero immediately in the adjoining elements and the rest of the domain. Also the source dissipates heat for half of the computation time and turns off suddenly after $t = 0.2$s. For the considered problem, results are compared for GFEM and the standard FEM. For GFEM we use a coarse mesh of 125 elements with 5 enrichment functions, whereas the standard FEM

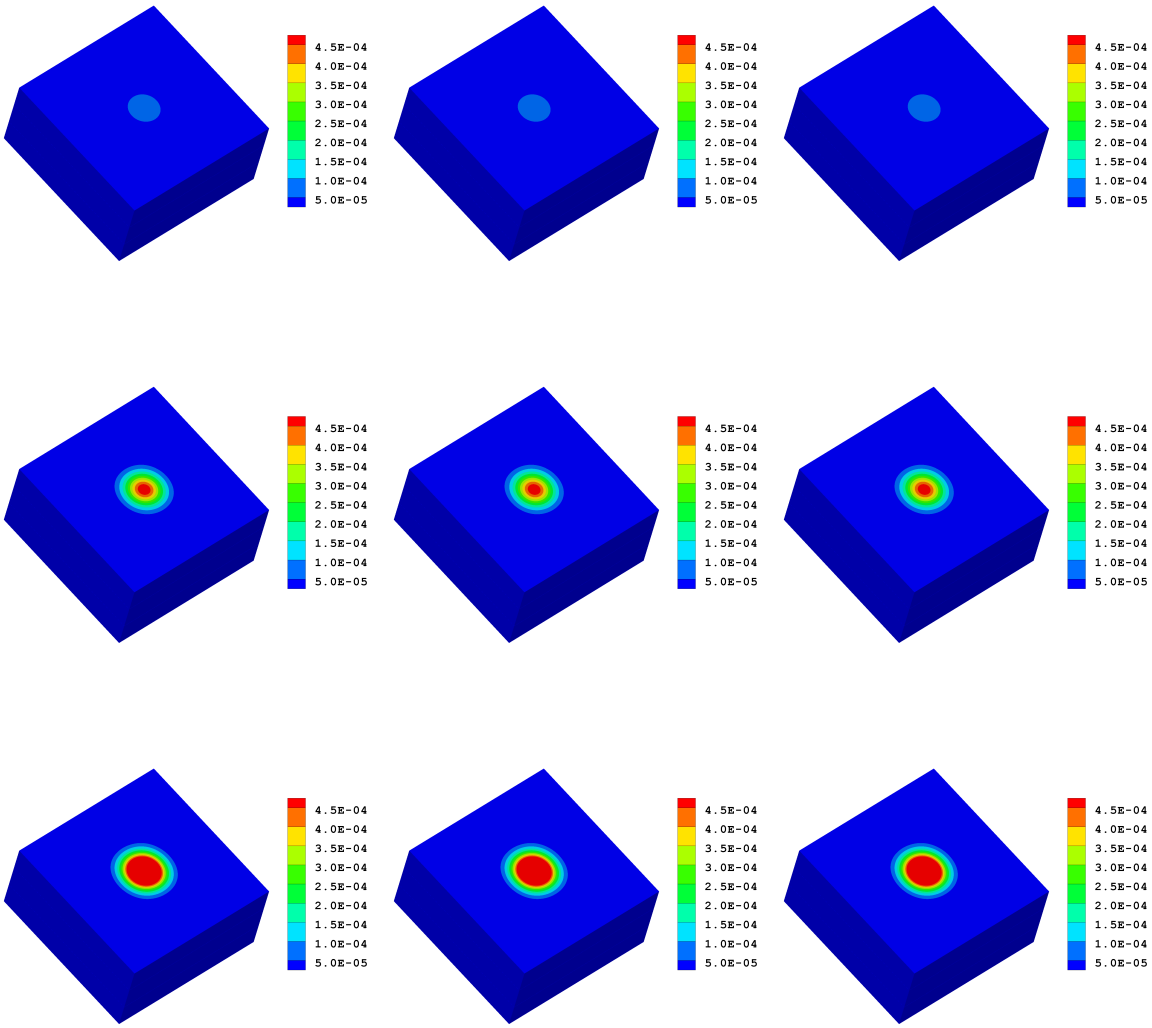

Fig. 4.7 Temperature distribution in the middle of the domain for exact (left column), FEM (centre column) and GFEM solutions (right column) at $t = 0.01$ (top row), $t = 0.05$ (middle row) and $t = 0.1$ (bottom row). The simulations are obtained using $\lambda = 0.01$.

solution is obtained with 1000 elements. Figure 4.10 shows the mesh grids used for FEM and GFEM solutions. The mesh grids are chosen such that both GFEM and FEM have comparable DOFs. For GFEM the TOTDOF is 1080, whereas in case of FEM the solution is obtained with 1331 TOTDOF. In order to calculate the errors of the GFEM and FEM solutions, a reference FEM solution (FEMR) on a very fine mesh

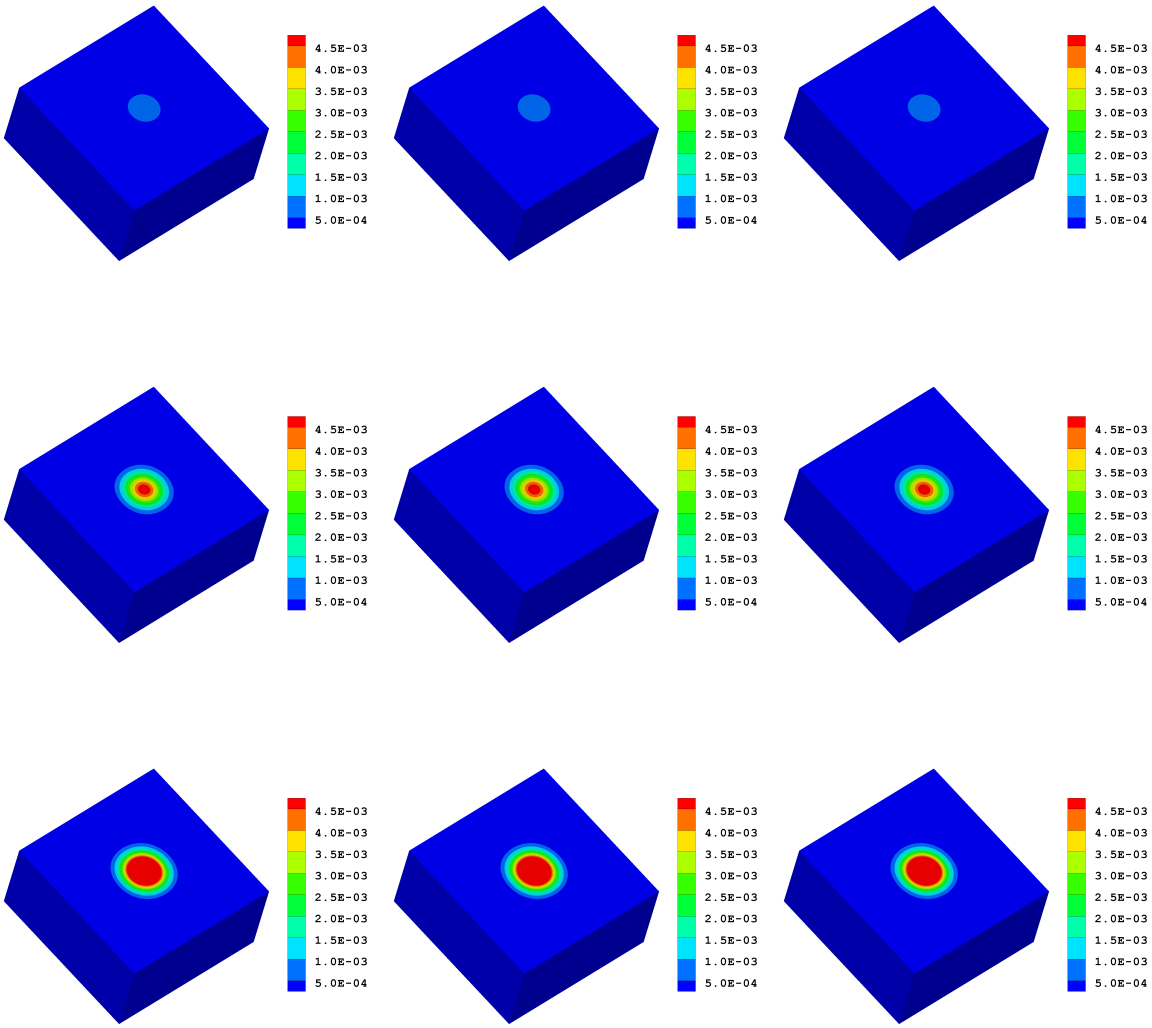

Fig. 4.8 Temperature distribution in the middle of the domain for exact (left column), FEM (centre column) and GFEM solutions (right column) at $t = 0.01$ (top row), $t = 0.05$ (middle row) and $t = 0.1$ (bottom row). The simulations are obtained using $\lambda = 0.1$.

is used. Having FEMR as a reference solution, the accuracy of GFEM is compared against the FEM solution.

To obtain a converged reference solution, we consider h−refinements. To start with, the domain is meshed with 1000 elements, having 10 elements in each spatial direction. The meshed is then refined to 20 elements in each direction, with 8000 total elements

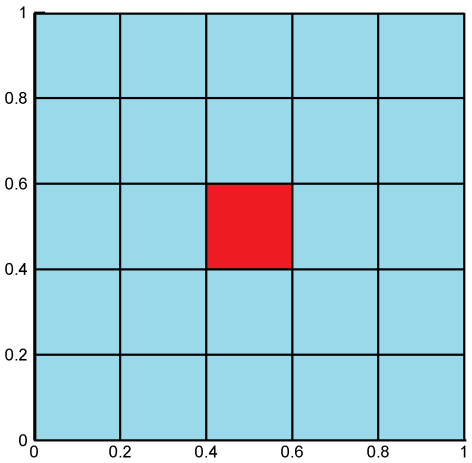

Fig. 4.9 x-section of the 3D domain for Example problem 2 with a heat source in the centre.

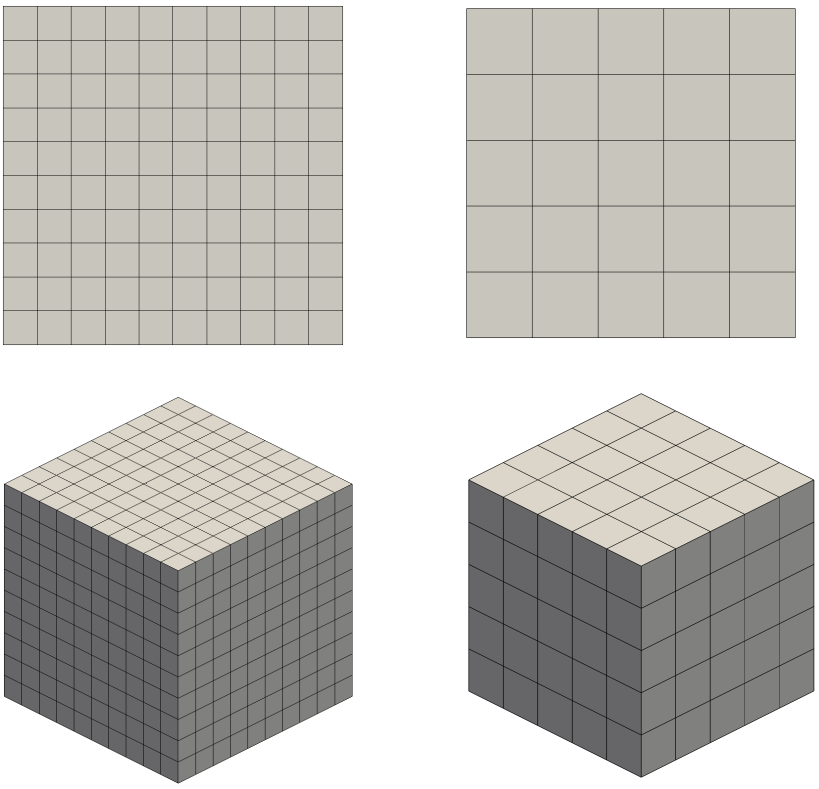

(a) FEM mesh

(b) GFEM mesh

Fig. 4.10 3D meshes used for the computation of Example problem 2

in the domain. Further refinements of 30, 40, 50 and 60 elements in each direction are considered with a total of 27000, 64000, 125000 and 216000 elements, respectively. To determine that the solution has converged, the maximum temperature in the centre of the domain is calculated with each mesh refinement. Figure 4.11 shows these results at three different simulation times, i.e., at $t = 0.05$s, 0.1s and 0.2s. Results are presented for both values of the diffusion coefficient, i.e., $\lambda = 0.01$ and 0.001kgm/Ks^2. The results show that with each refinement, the temperature in the centre of the domain varies and we get almost converged solution with 216000 elements. At $t = 0.2$s the maximum temperature using $\lambda = 0.01$kgm/Ks^2 is approximately 791K with 1000 elements which converges to an approximate value of 661K with 216000 elements. At the same simulation time, for $\lambda = 0.001$kgm/Ks^2, we get a maximum temperature of 1065K with the coarse mesh of 1000 elements, which converges to 700K with mesh refinement. At all simulation times, the results vary more smoothly with the mesh refinement for $\lambda = 0.01$ as compared to $\lambda = 0.001$kgm/Ks^2.

As another indicator that the solution has converged, a cross section in the middle of the domain is considered, and the solution along the centre line of the cross section is calculated. Figure 4.12 shows the temperature distribution along the centre line for different mesh refinements using $\lambda = 0.01$kgm/Ks^2. In the figure, FEM1000 represents the FEM solution with a total of 1000 elements while FEM8000 represents a solution with a total of 8000 elements in the whole domain. Similarly are the results with 27000, 64000, 125000 and 216000 elements. From the figure, it is evident that the temperature profile changes with every refinement until we get almost similar profiles for 125000 and 216000 elements suggesting that the solution has converged. Figure 4.12 shows the results of all these refinements for two different simulation times, i.e., $t = 0.05$s and 0.1s. At both of the simulation times, the results of all the refinements are presented on one graph. Figure 4.13 presents these profiles on separate graphs to show the smoothness of each profile individually with every mesh refinement. The results are shown for only one simulation time $t = 0.05$s in this figure. Another set of similar results for $\lambda = 0.001$kgm/Ks^2 is presented in Figure 4.14 and Figure 4.15. Again the

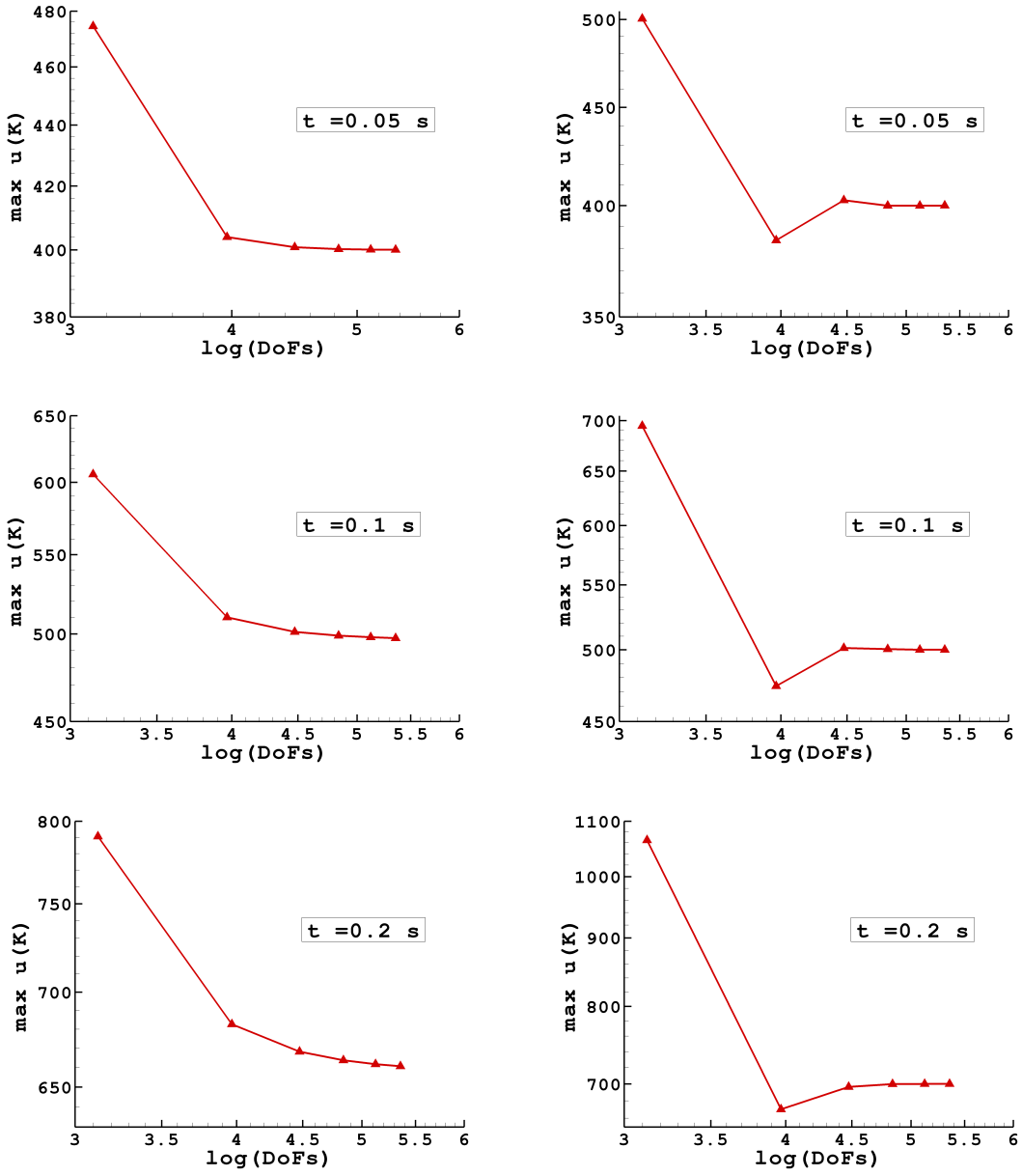

(a) λ=0.01 (b) λ=0.001

Fig. 4.11 Maximum temperature in the middle of the domain with $h-$refinement.

heat dissipates more smoothly for $\lambda = 0.01\text{kgm/Ks}^2$ as compared to results obtained using $\lambda = 0.001\text{kgm/Ks}^2$. In the latter case, the rate of heat diffusion is decreased by a factor of 10. This lower value of λ makes the propagation of heat slower to other areas of the domain resulting in the built-up of temperature in and around the heat source and results in relatively higher thermal gradients. For the very fine mesh

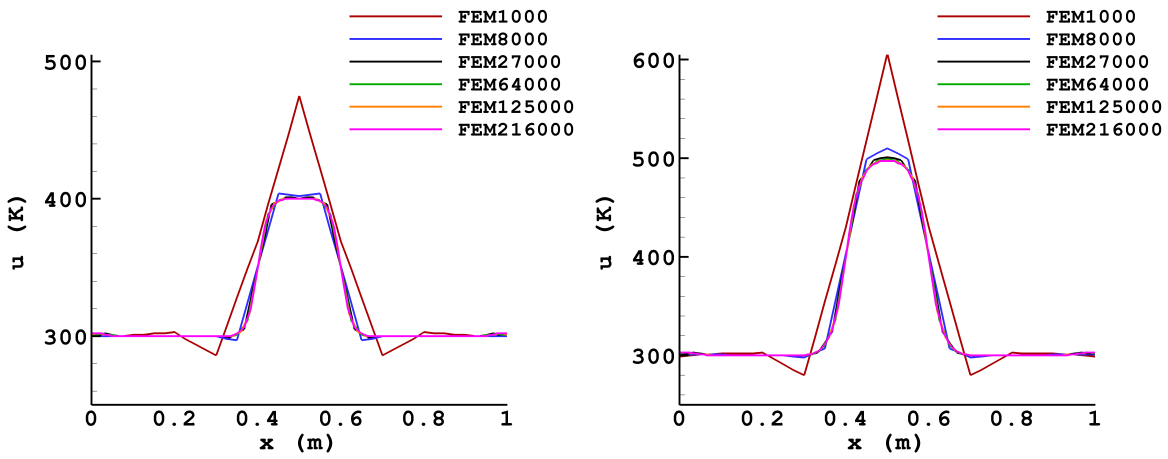

$t = 0.05$s $\qquad\qquad$ $t = 0.1$s

Fig. 4.12 Temperature distribution along a centre line for different FEM meshes using $\lambda = 0.01$.

of 216000 elements, comparison of the results from Figure 4.13(f) and Figure 4.15(f) shows that the temperature profile for $\lambda = 0.01$kgm/Ks^2 is comparatively smoother than for $\lambda = 0.001$kgm/Ks^2. In the latter case, there is a sharp gradient of temperature across the boundaries of the source.

Figure 4.16 shows the temperature distribution for the reference solution FEMR as well as for FEM and GFEM solutions. Results are presented at three different simulation times; $t = 0.1$, 0.2 and 0.4s, that is half of the time the source is on, when the source is switched off, and another 0.2s after the source is switched off. The results captured with GFEM show the same temperature profiles as obtained by the fine mesh reference solution FEMR, whereas the FEM solution shows very coarse profiles. This shows that GFEM with a very coarse mesh was able to capture the same solution dynamics as those obtained on a very fine mesh solution FEMR. GFEM uses only 1081 DOFs to capture the sharp thermal gradients whereas the FEMR solution is obtained with 226981 TOTDOF. This significant reduction in the TOTDOF clearly shows the advantage of GFEM on the standard FEM. The FEM solution was not able to capture the solution accurately despite using higher number of DOFs. The figures show that the temperature of the medium increases for half of the simulation

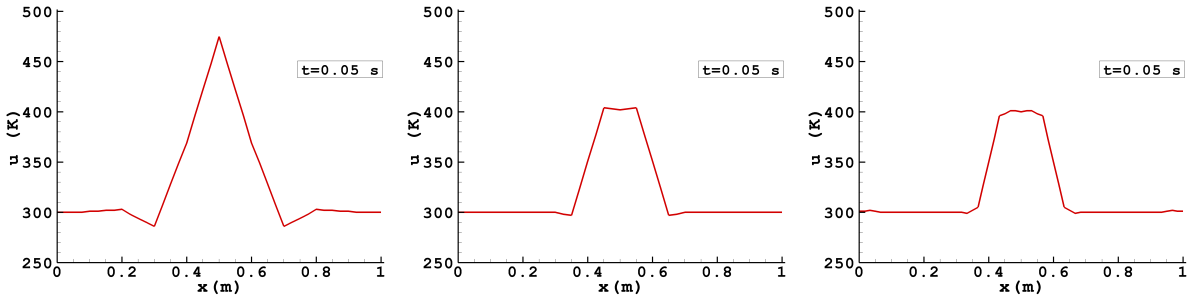

(a) FEM1000 (b) FEM8000 (c) FEM27000

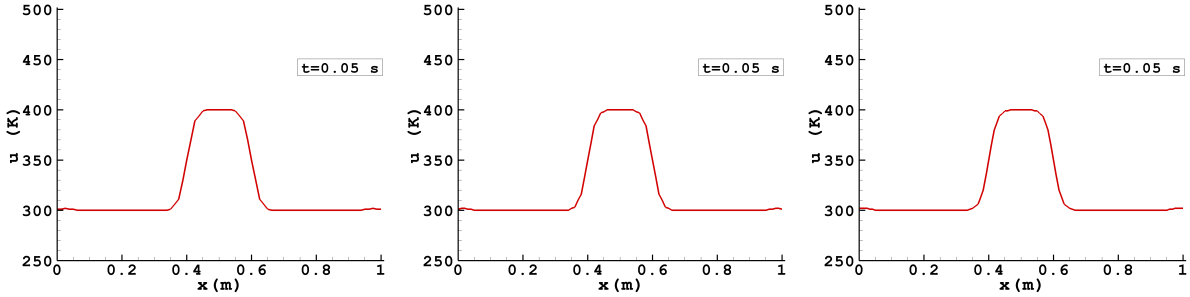

(d) FEM64000 (e) FEM125000 (f) FEM216000

Fig. 4.13 $h-$convergence analysis for reference FEM solution using $\lambda = 0.01$. Temperature distribution is shown along a centre line for different meshes.

time when the source is dissipating heat. The medium starts to cool down when the heat source is switched off. The temperature is maximum in the centre of the domain because of the heat source, and it moves towards the boundaries where the temperature is minimum.

To quantify the accuracy of the GFEM method, we calculate the relative L_2 error of GFEM and FEM solutions against the reference solution FEMR. Figure 4.17 shows the solution along a cross section located in the middle of the domain. Results are obtained using $\lambda = 0.01\text{kgm/Ks}^2$ and are presented at different simulation times. For the FEM solution, the maximum error is observed at the centre of the domain. For half of the simulation time when the source is dissipating heat, the maximum L_2 norm error in the centre of the domain is more than 20%. For GFEM, the error in the

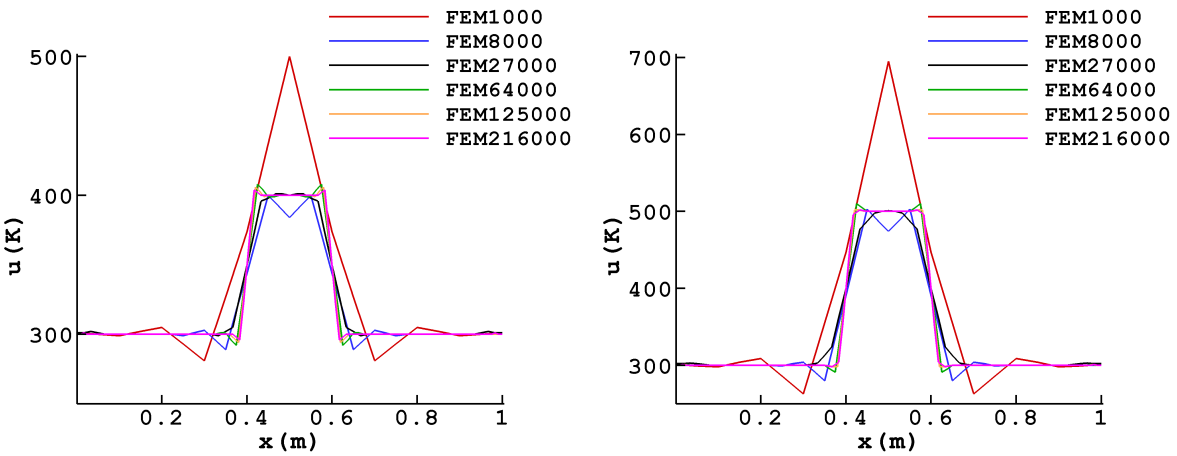

$t = 0.05$s $\qquad\qquad$ $t = 0.1$s

Fig. 4.14 Temperature distribution along a centre line for different FEM meshes using $\lambda = 0.001$.

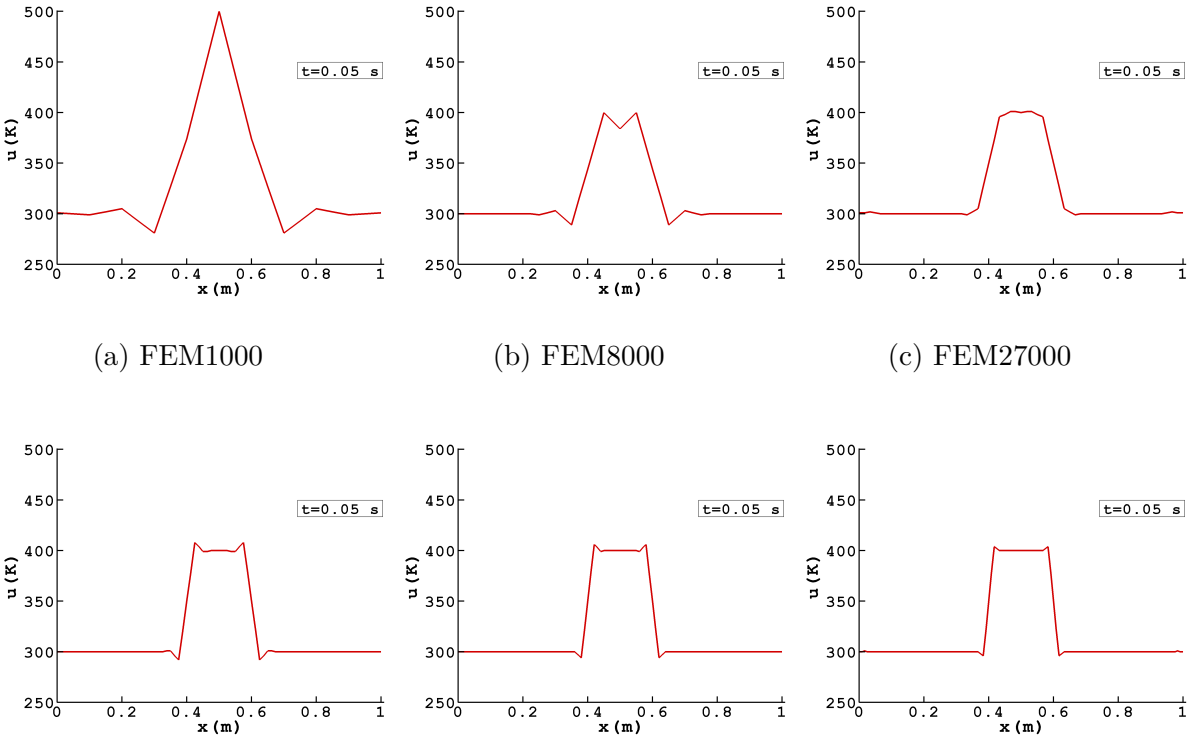

(a) FEM1000 (b) FEM8000 (c) FEM27000

(d) FEM64000 (e) FEM125000 (f) FEM216000

Fig. 4.15 $h-$convergence analysis for reference FEM solution using $\lambda = 0.001$. Temperature distribution is shown along a centre line for different meshes.

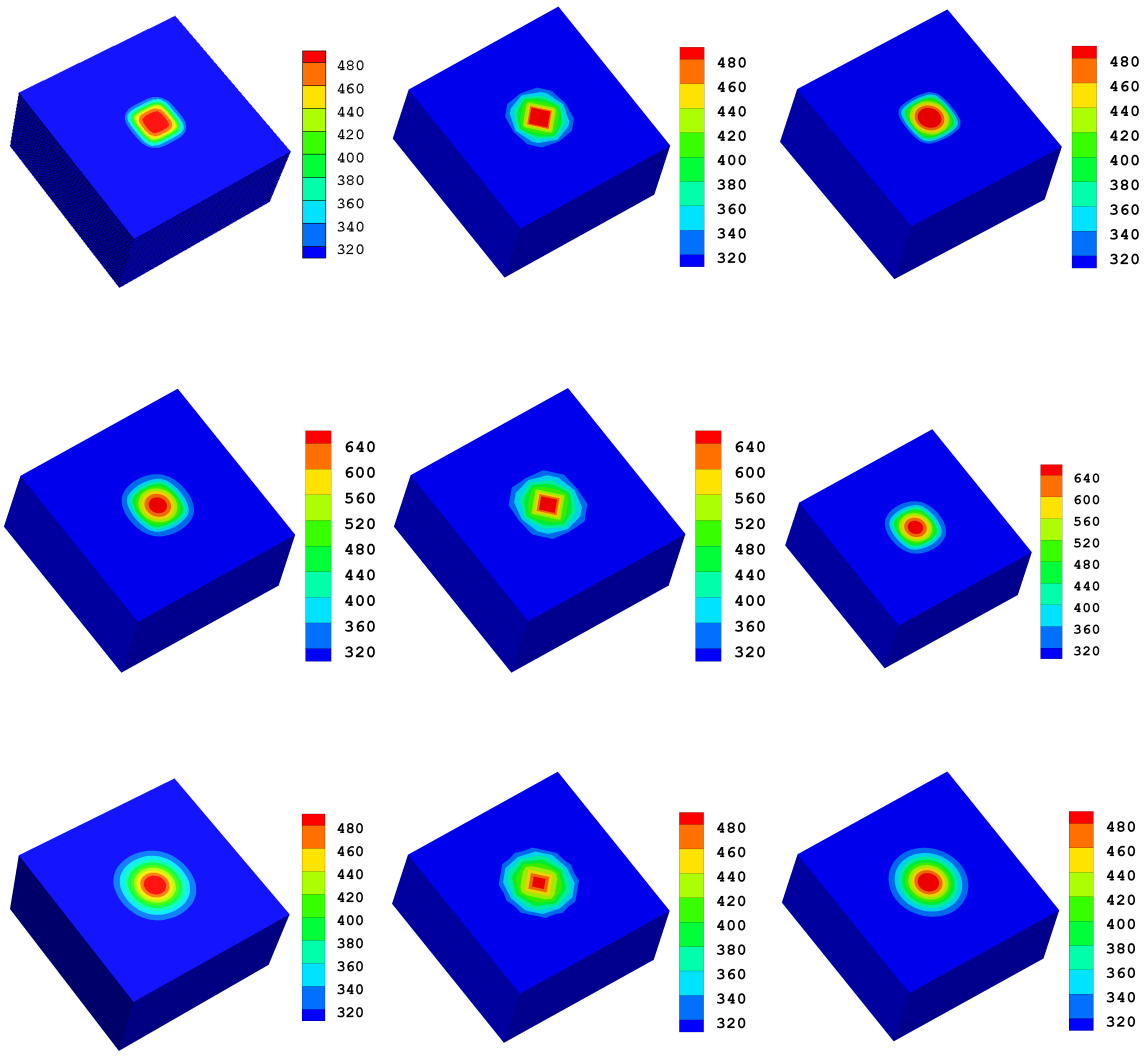

Fig. 4.16 Temperature distribution in the middle of domain for FEMR (left column), FEM (centre column) and GFEM solution (right column) at $t = 0.1$s (top row), 0.2s (middle row) and 0.4s (bottom row). The simulations are obtained using $\lambda = 0.01$.

centre of the domain is less than 1%. In the case of GFEM, the maximum error of around 7% is observed only along the boundaries of the heat source. This error can be minimized by tailoring the enrichment functions according to the shape of the heat source. In the case of FEM, the error around the boundaries of the heat source is more than 15%. For later simulation times, when the heat source is turned off and the medium is cooling down, the error decreases significantly both for FEM and GFEM

solutions. At $t = 0.3$s, the maximum L_2 error for FEM reduces to around 8% and for GFEM it reduces to less than 2%. At the end of the simulation, the error reduces to around 4% for FEM and less than 1% for GFEM. A similar set of results is presented in Figure 4.18 using $\lambda = 0.001\text{kgm/Ks}^2$. The local errors for this case are higher both for FEM and GFEM solutions. In the previous case, the maximum error in the middle of the domain for FEM solution at $t = 0.2$s was around 20% which rises to as high as 50%. For GFEM, we observe an increase from 1% to 10%. Higher errors are observed in the central part even at later simulation times, but far from the heat source the error still remains very low, even lower than the previous case. For the previous case, at $t = 0.4$s the error in the central part dropped to 5% for the FEM solution which in the present case is still around 40%. For GFEM this value was around 1% in the previous case, but in the present case, the maximum error is around 10%. The reason for higher local errors is the build up of heat due to the lower value of λ. The value of heat diffusion co-efficient λ is reduced by a factor 10 as compared to the previous case. The slower rate of heat diffusion makes the rate of heat propagation slower to the other areas of the domain and results in the built up of heat around the source. Also, the heat does not reach to the far areas of the domain, as a result lower errors are observed near the boundaries, as compared to the previous case.

Another representation of the results is depicted in Figure 4.19. Again the results are presented along a centre line of a cross section located in the middle of the domain, but in this case the differences of temperatures between the FEMR solution and both FEM and GFEM solutions are presented rather than the L_2 norm error for the whole domain. This representation is especially important for problems where the local differences at a specific point of the domain are more important than the L_2 norm error. In certain cases, it is often important to know the maximum temperature accurately, as too high temperatures may lead to damage of the material or product. Figure 4.19 compares the reference FEMR and FEM solutions (top row), respectively, the FEMR and GFEM solutions (bottom row) at three different simulation times for $\lambda = 0.01\text{kgm/Ks}^2$. For the FEM solution, the maximum temperature

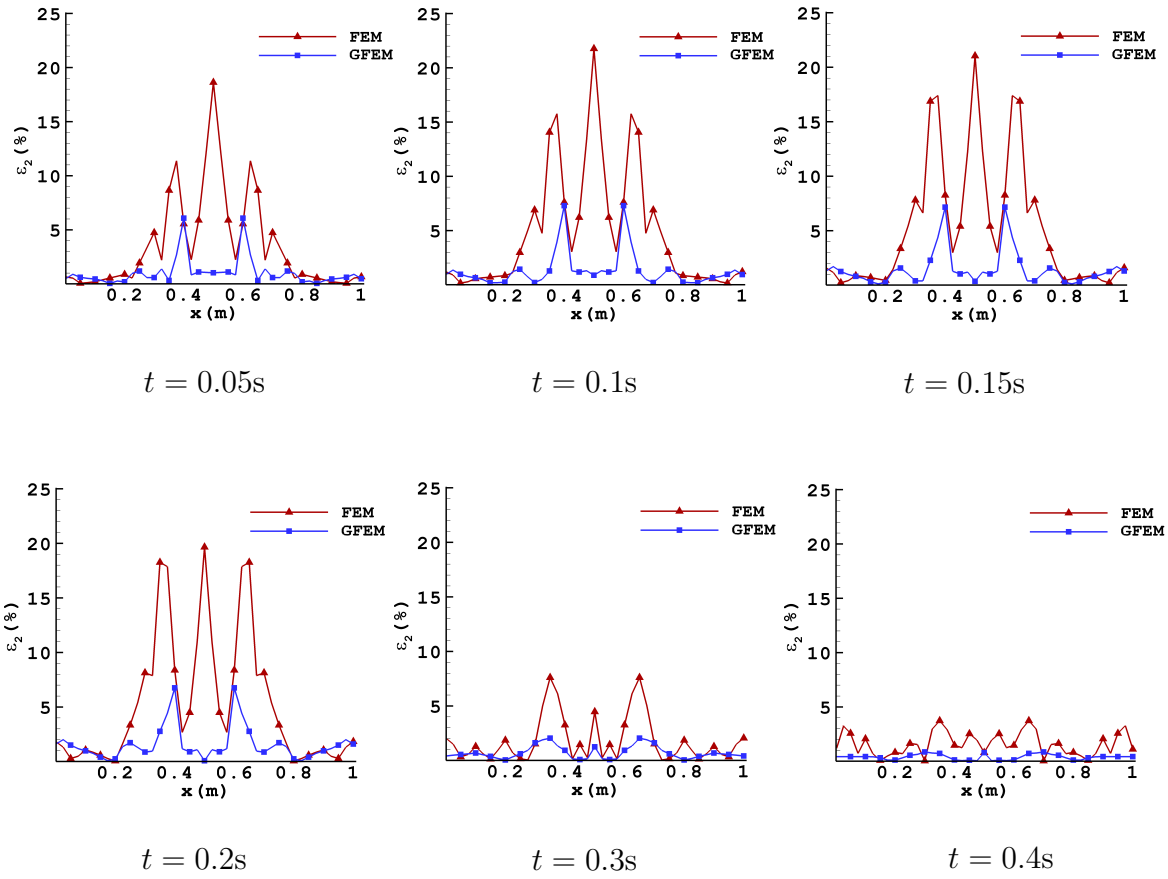

Fig. 4.17 L_2 error for FEM and GFEM solutions calculated along a centre line at different simulation times using $\lambda = 0.01$.

difference occurs in the middle of the heat source. The temperature difference of 125K is observed at half of the simulation time, $t = 0.2$s. In case of GFEM solution, the difference is around 15K only. For GFEM, the maximum difference of around 25K is observed near the boundaries of the heat source while for the FEM solution it is around 65K. At $t = 0.4$s, the difference reduces to around 15K for FEM while for GFEM it is around 2K. This clearly shows the advantage of the proposed GFEM over the standard FEM where both have comparable DOFs. Figure 4.20 shows a similar comparison between the FEM and GFEM solutions using $\lambda = 0.001$kgm/Ks^2. As observed previously, the local errors are higher compared to the $\lambda = 0.01$kgm/Ks^2 case.

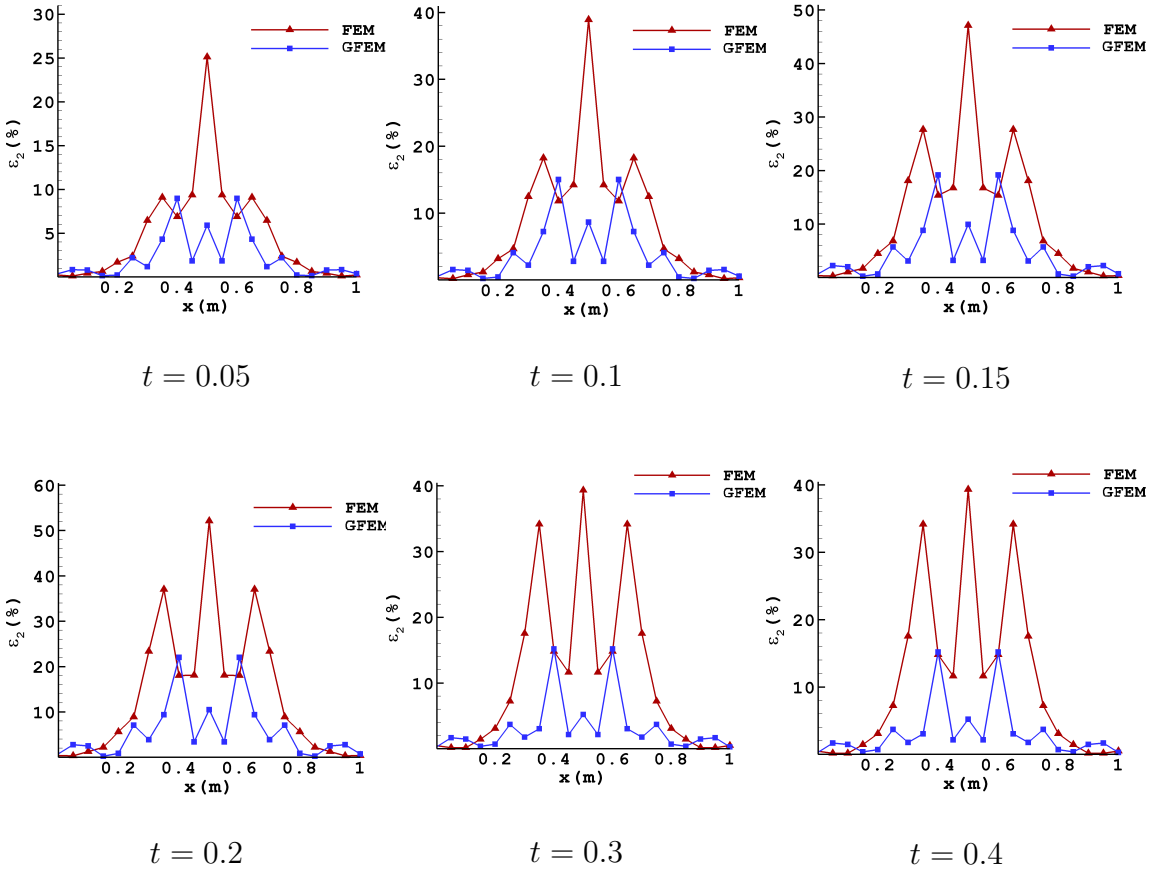

Fig. 4.18 L_2 error for FEM and GFEM solutions calculated along a centre line at different simulation times using $\lambda = 0.001$.

To further analyse the results of Example problem 2, in Figure 4.21 we plot the time evolution of the maximum temperatures and the differences in the maximum temperatures. From the start to the end of the simulation, the variation of maximum temperature is plotted in Figure 4.21(a) for FEMR, FEM and GFEM solutions. Figure 4.21(b) shows the differences of maximum temperatures between the reference FEMR and FEM solutions, and FEMR and GFEM solutions. Figure 4.21(a) shows clearly that the time evolution of maximum temperature for the coarse meshed GFEM solution is almost identical to the fine mesh FEMR solution. Both FEMR and GFEM solutions have very close resemblance for the whole duration of the simulation. On the other hand, the FEM results are far away from the reference FEMR solution for

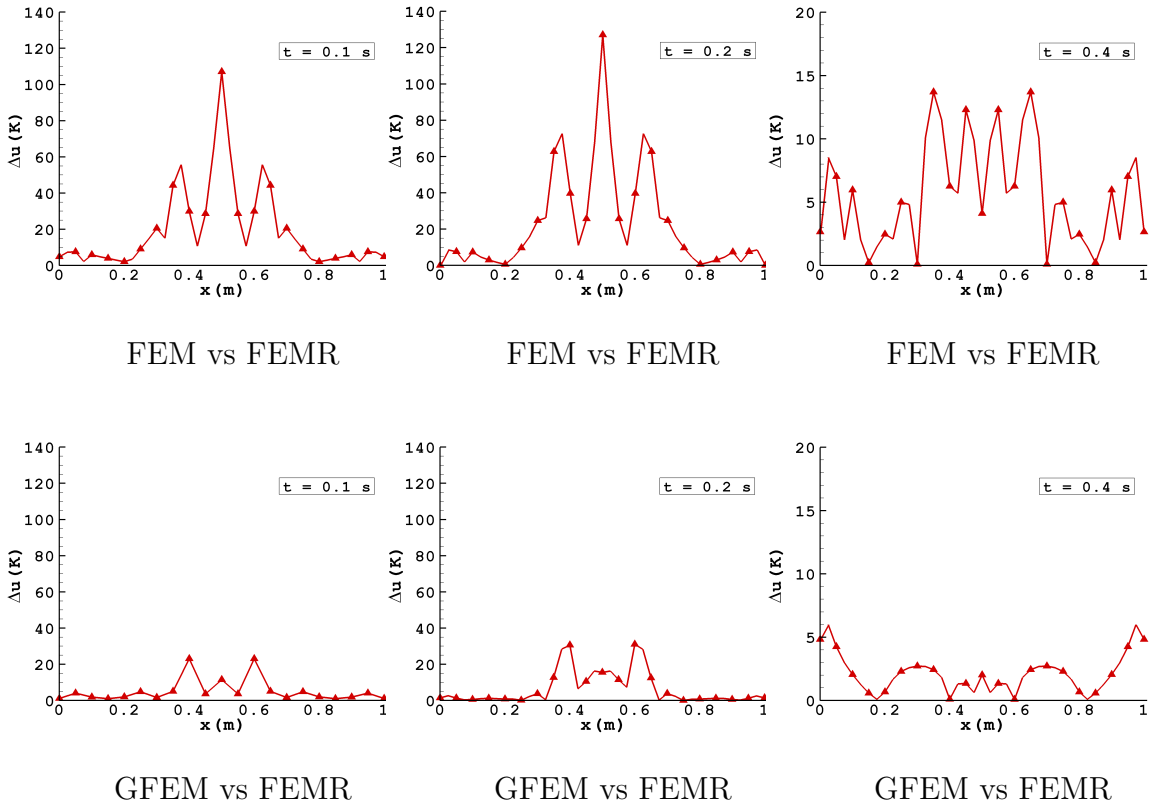

Fig. 4.19 Temperature differences between the reference FEMR solution and (i) FEM solution (top row), (ii) GFEM solution (bottom row), along a centre line using $\lambda = 0.01$.

most of the simulation time. Only at later times, when the medium is cooling down and the solution tends towards the steady state condition, the FEM results become closer to the FEMR solution. Figure 4.21(b) also shows that there is a significant difference in the temperatures between the FEM and FEMR solutions while for GFEM the difference in maximum temperatures is very small for the whole simulation time. In the case of FEM, the maximum difference is about 130K, while in the case of GFEM it stays well below 10K. For FEM, the accuracy deteriorates further when using $\lambda = 0.001\text{kgm/Ks}^2$ as shown in Figure 4.22. As observed in Figure 4.21(a), the FEM results tend to become closer to the FEMR solution in the cooling stage and almost identical at the end of the simulation but in Figure 4.22(a), FEM results are relatively far from the FEMR results even during the cooling stage. The same trend is

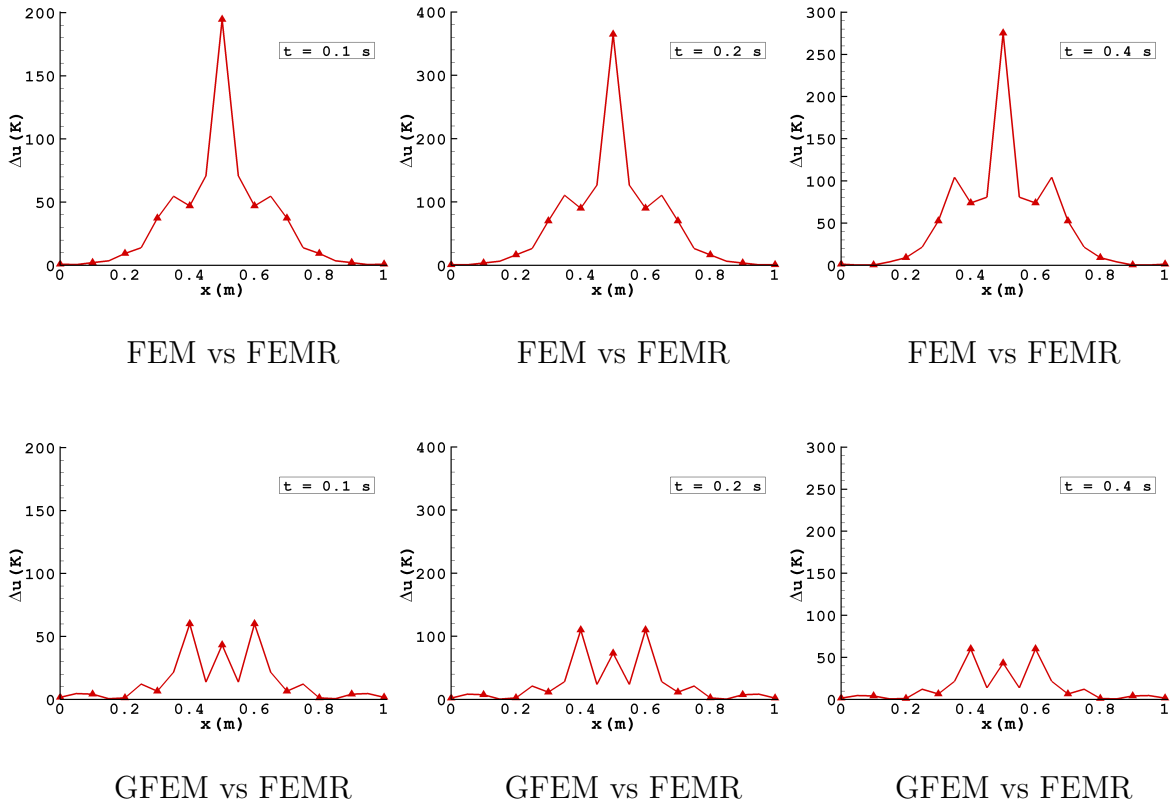

Fig. 4.20 Temperature difference between the reference FEMR solution and (i) FEM solution (top row), (ii) GFEM solution (bottom row) along a centre line using $\lambda = 0.001$.

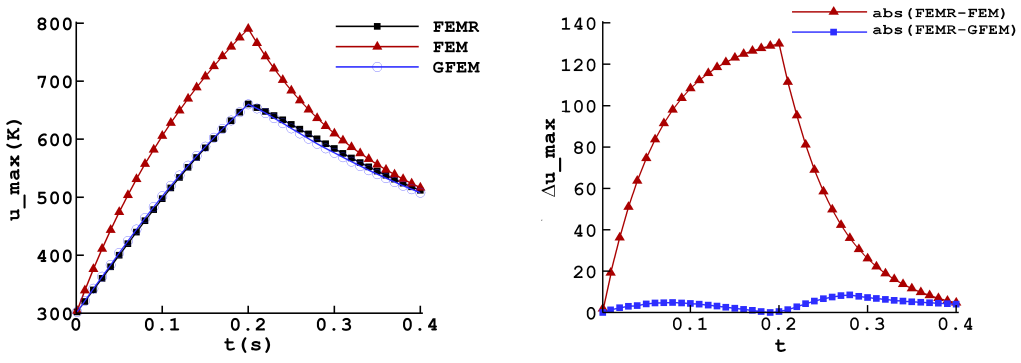

Fig. 4.21 Time evolution of (a) maximum temperature (b) difference in max temperature. Results are obtained using $\lambda = 0.01$.

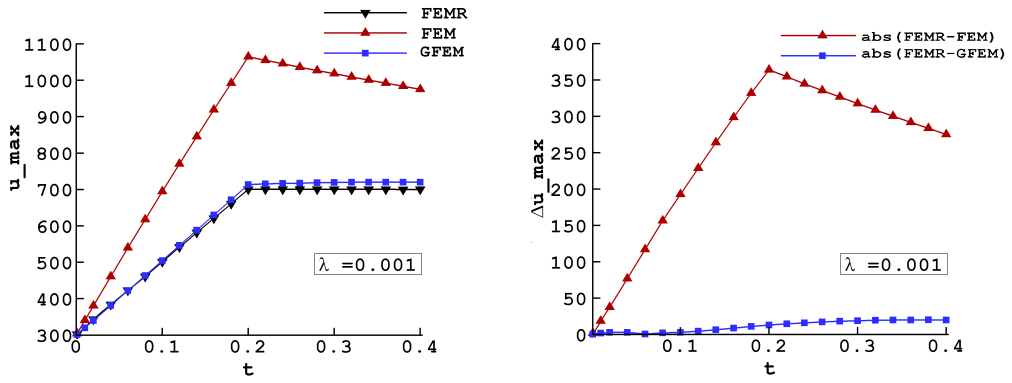

(a) (b)

Fig. 4.22 Time evolution of (a) maximum temperature (b) difference in max temperature. Results are obtained using $\lambda = 0.001$.

observed in Figure 4.22(b) where the maximum difference in temperature at $t = 0.2$s reaches a high value of 400K and stays around 300K even at the end of the simulation. In the case of GFEM, the temperatures are nearly identical to the fine mesh FEMR results which shows the advantage of GFEM.

4.3.3 Approximation of a problem with an annular domain

The third example simulates the transient heat transfer in a 3D annular domain with inner diameter $d_i = 1.0$m and outer diameter $d_o = 1.5$m, as shown in Figure 4.23. The depth of the domain in the $z-$direction is taken to be 0.3m. This example presents one of the representative problems where the domain has curved edges, and the errors from the discretization of the geometry will have a contribution to the overall error of the solution. Mohamed [127] suggested to use elements that describe the exact shape of the curved domain. It is shown that this approach reduces the overall error of the solution. In this current study, the same approach is used and elements are defined such that the geometry is exactly described. The element having curved boundaries are defined by the polar coordinates. For the selected geometry, the problem can be considered as axi-symmetric and may be solved as a 2D problem, but as our purpose here is to show the working of the GFEM for 3D problems, therefore the full 360° geometry is considered for analysis.

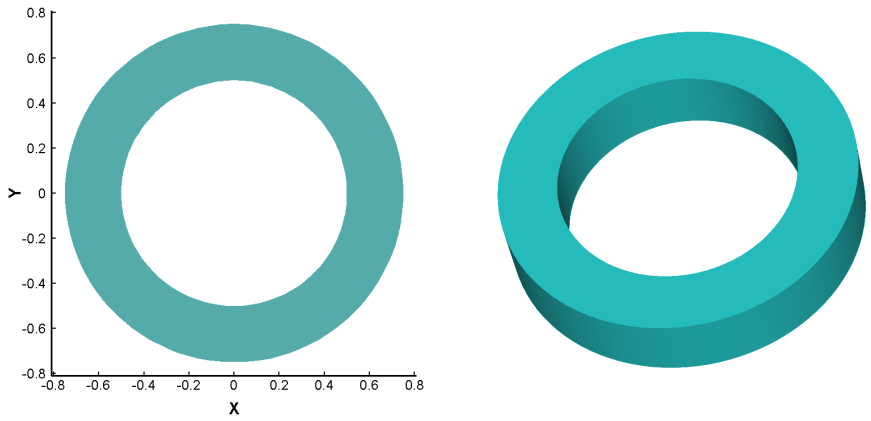

Fig. 4.23 Annular domain for Example problem 3.

Although for the selected geometry, the problem can be selected as an axi-symmetric body where only the problem may be considered as a 2D problem, or

For this example problem, a boundary source at the inner surface of the body is selected which dissipates heat with $g = 2000$K/s. The initial temperature of the domain is set at $u_o = 300$K and the heat source within the domain is set to zero. The time step value is fixed at $\Delta t = 0.0001$s, and the diffusion heat coefficient for the medium is taken as $\lambda = 0.01$kgm/Ks^2. The convection heat transfer coefficient at the outer surface is set to be h= 1kg/Ks^2. The same value of h is used for top and bottom surfaces of the domain.

To capture the high thermal gradients at the boundaries of the domain, hyperbolic tangent basis functions are used to enrich the solution space. These enrichment functions are selected due to the type of temperature behaviour of the selected problem. Mohamed et al. [129, 130] used hyperbolic enrichment functions to capture high thermal gradients in 2D domains which were localized in an otherwise uniform domain. They illustrated two different variations of the hyperbolic tangent functions. For a polygonal domain with an edge e at a position $\mathbf{x} = \mathbf{x}_e$, the enrichment function

is defined as

$$G_q^{\,tanh} = C_1 + C_2 \tanh\Big(\frac{\mathbf{x} - \mathbf{x}_e}{h_q}\Big), \qquad q = 1, 2, \ldots, Q \ . \tag{4.4}$$

where C_1 and C_2 are the control parameters defining the amplitude of the function $G_q^{\,tanh}$ while h_q controls its slope. The other variation of this enrichment functions is defined for a circular edge with $r = r_e$ using the polar coordinates (r, θ)

$$G_q^{\,tanh} = C_1 + C_2 \tanh\Big(\frac{r - r_e}{h_q}\Big), \qquad q = 1, 2, \ldots, Q \ . \tag{4.5}$$

This expression of the enrichment function is used in our present study. The global derivatives of the considered enrichment function are given as

$$\frac{\partial G_q^{\,tanh}}{\partial x} = C_2 \ \frac{x}{r h_q} \ \Big(1 - \tanh^2 \ \Big(\frac{r - r_e}{h_q}\Big)\Big) \tag{4.6}$$

$$\frac{\partial G_q^{\,tanh}}{\partial y} = C_2 \ \frac{y}{r h_q} \ \Big(1 - \tanh^2 \ \Big(\frac{r - r_e}{h_q}\Big)\Big) \tag{4.7}$$

$$\frac{\partial G_q^{\,tanh}}{\partial z} = C_2 \ \frac{z}{r h_q} \ \Big(1 - \tanh^2 \ \Big(\frac{r - r_e}{h_q}\Big)\Big) \tag{4.8}$$

For the considered problem, $r_e = r_i$ is the inner radius of the domain, while $r = \sqrt{x^2 + y^2}$ is the radius at a particular point in the domain. The enrichments are taken to vary only in the x and y directions and are constant in the $z-$direction. This is because in the selected problem the temperature varies only in the radial direction and is constant along the thickness of the domain. The steepness of the enrichment function G_q^{tanh} depends on the value of the parameter h_q. Figure 4.24 illustrates the variation of the enrichment function along the radial direction of the domain for different values of h_q. It is evident that the use of smaller values of h_q leads to functions with high gradients while higher values of h_q produce smoothly varying enrichment functions. The functions with high gradients can recover solutions

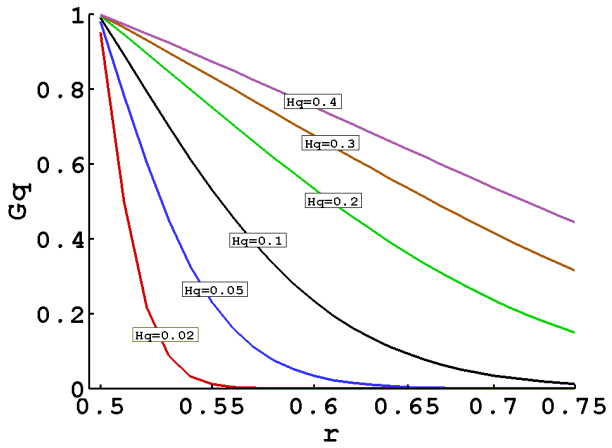

Fig. 4.24 Variation of enrichment function G_q^{tanh} along the radial direction with different values of h_q.

at early time ste ps in the vicinity of a thermal shock while enrichment functions that vary slowly can be useful at later time steps when the temperatures become more uniform. Figure 4.25 shows the distribution of these enrichment functions over the computational domain for different values of h_q.

To compare the accuracy of GFEM with the conventional FEM, two different FEM meshes and one GFEM mesh are considered for the solutions. A coarse FEM mesh termed as FEMc is selected such that it has comparable DOFs to the enriched GFEM model and a fine mesh FEMf which has about ten times more DOFs. Since the exact analytical solution is not known for the considered problem, a reference FEM solution (FEMr) is obtained using a very fine mesh of 30000 elements with 33150 DOFs. Figure 4.26 shows the meshes used for the computations. To compare the results obtained with FEM and GFEM solutions, in Figure 4.27 is plotted the temperature variation along the radial direction of the domain. The temperatures obtained with FEM and GFEM are compared with the reference FEMr solution. For all shown simulation times, GFEM produced very similar results to FEMr; in fact both results are almost identical. FEMc, which has similar DOFs to GFEM, produces very large errors as compared to GFEM. The FEMf although having ten times more DOFs, still leads to considerable differences in the results at the earlier time steps due to the higher temperature gradients. The diffusion nature of the problem makes the

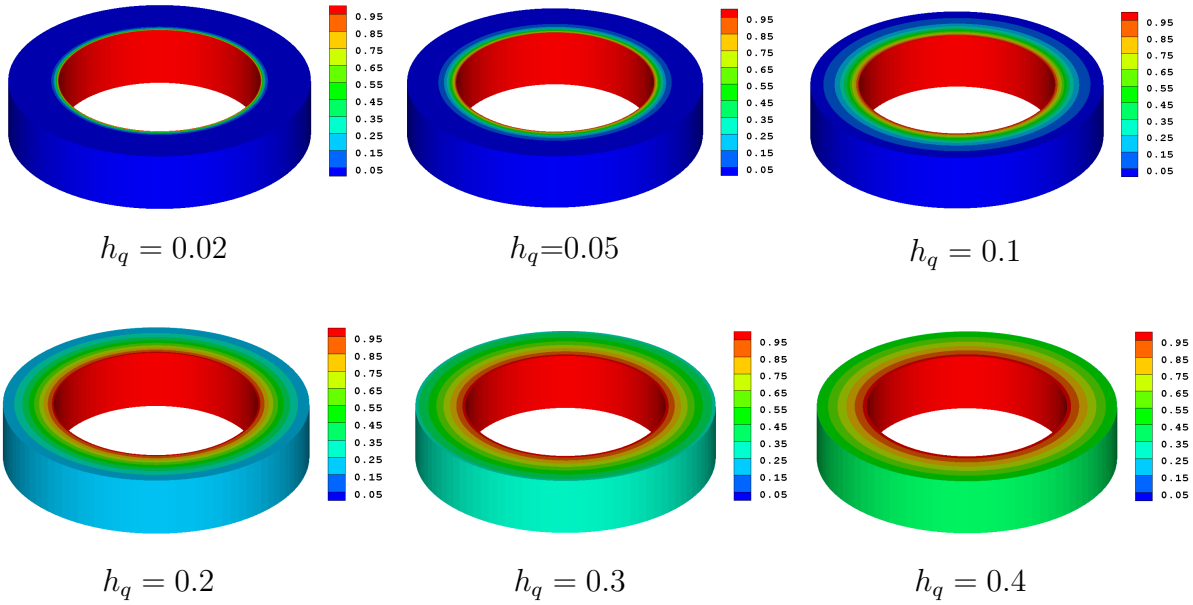

Fig. 4.25 Illustration of the hyperbolic tangent functions for different values of h_q as applied to the considered domain.

solution smoother at later time steps, and the difference between FEMr and FEMf solutions start to decrease. Also it is evident from the graph that the differences in the temperature are more prominent in the inner side of the domain because of the localized large temperature gradient. The temperate field is more uniform in the outer region of the domain, and smaller errors were expected by all methods. Figure 4.28 quantifies the absolute differences between the reference FEMr and FEMc solutions, FEMr and FEMf solutions and FEMr and GFEM solutions at difference simulation times. It is clear from the figure that the difference in temperatures between the reference FEMr and GFEM solutions are very minimal at all the simulation times. FEMc having comparable DOFs shows visible variation in temperature values with the FEMr solution. Even FEMf shows considerable differences in temperatures specially at the inner side of the domain.

The results are further assessed in Figure 4.29 by plotting the maximum domain temperature and the difference in the maximum temperatures between the reference FEMr solution and FEMc, FEMf and GFEM solutions. Figure 4.29(a) shows the vari-

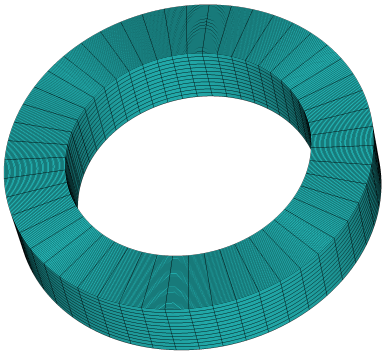

FEMr (30000 elements, 33150 nodes)

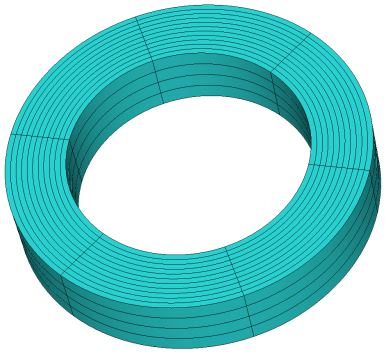

FEMf (264 elements, 360 nodes)

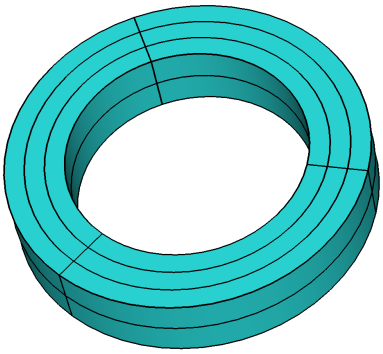

FEMc (18 elements, 36 nodes)

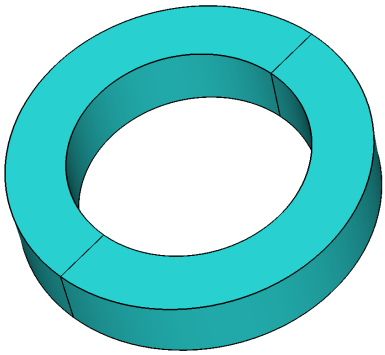

GFEM (2 elements, 8 nodes)

Fig. 4.26 Meshes used for the computations of Example problem 3.

ation of the maximum domain temperature for the whole simulation time while in Figure 4.29(b) is shown the absolute difference in maximum temperature between the FEMr and FEMc, FEMr and FEMf, and FEMr and GFEM solutions. From Figure 4.29(a) it is clear that the temperatures produced by the coarse mesh GFEM solution are almost identical to the fine mesh FEMr solution. The FEMc solution with similar DOFs to the GFEM, produces results that differ significantly from the FEMr results. Even the FEMf results have lower accuracy although they are produced using a mesh grid with ten times more DOFs than the GFEM. This clearly indicates the superiority of the GFEM approach over the standard FEM approach. Also, Figure 4.29(b) shows a close similarity in the results of the GFEM and FEMr solutions.

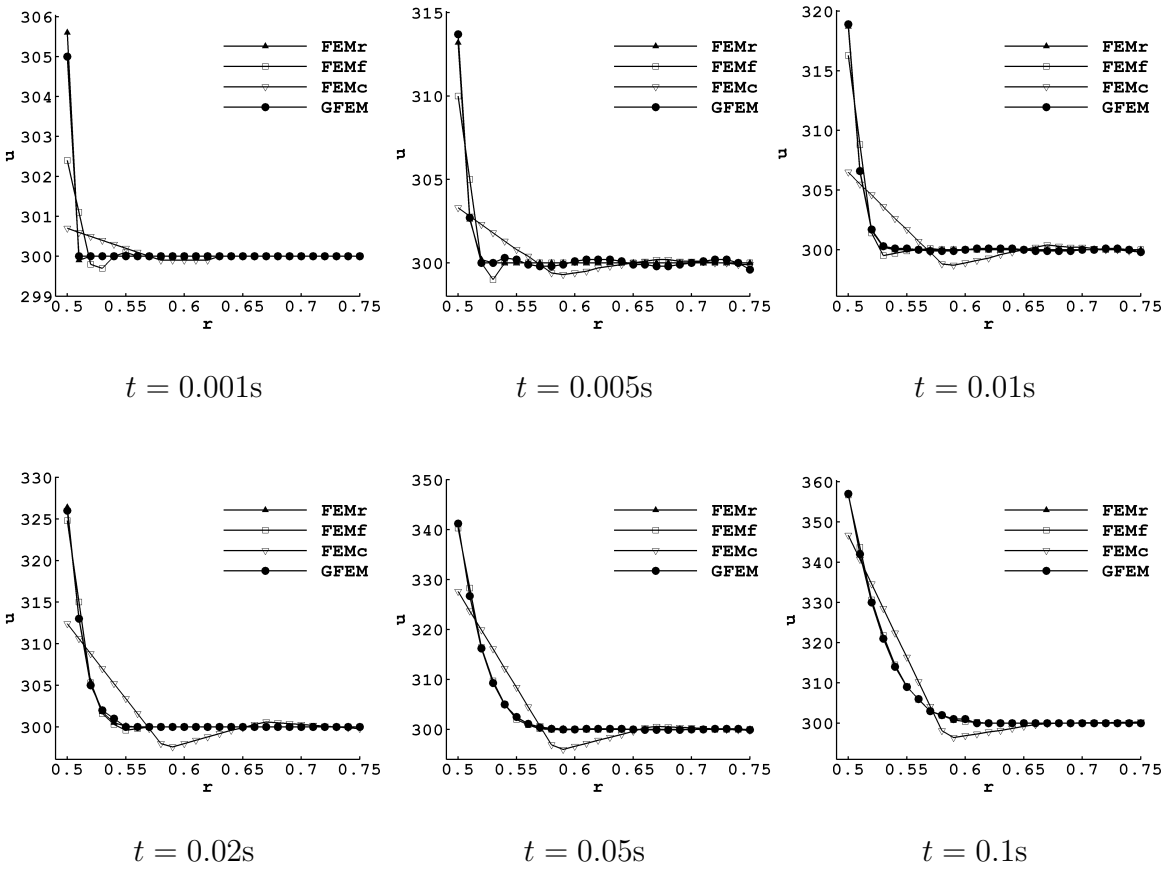

Fig. 4.27 Temperature variation along the radial direction of the domain at different time intervals For FEMr, FEMf, FEMc and GFEM solutions.

The absolute differences in the maximum temperatures are very minimal between the GFEM and FEMr results. The FEMf results, on the other hand, show noticeable variation as compared to FEMr, with the FEMc results further deviated from the FEMr solution.

4.4 Overview

The GFEM approach is used to solve time-dependent heat diffusion problems in 3D domains and is assessed against the FEM solution on refined mesh grids. For GFEM, the solution space is enriched with 3D Gaussian or hyperbolic tangent functions describing the heat diffusion decay with various rates. To show the advantage of the GFEM

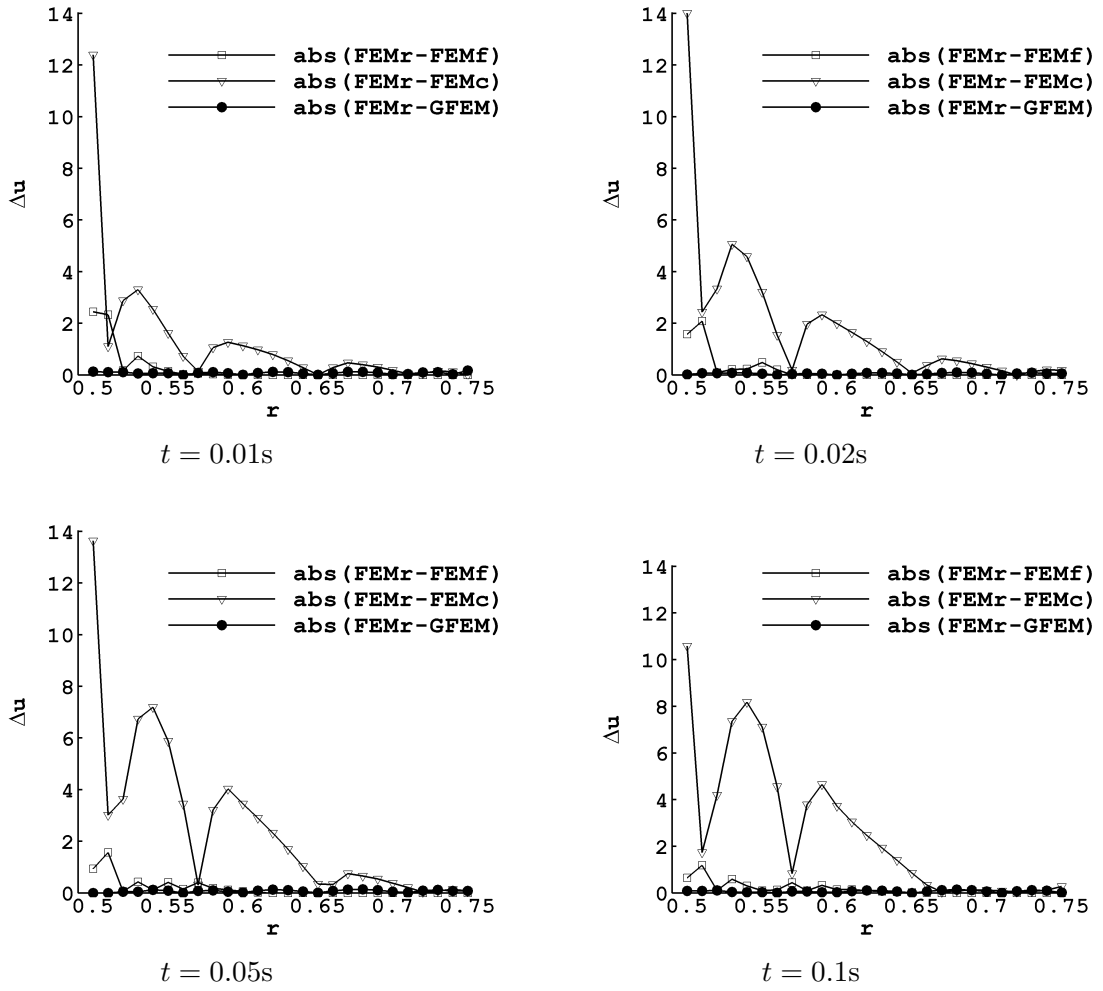

Fig. 4.28 Absolute differences in temperatures along the radial direction between FEMr and FEMc, FEMf and GFEM solutions.

approach over the standard FEM, three different example problems are considered. To quantify the errors in both approaches, a problem with a known analytical solution is considered as a first example. It is concluded that for a comparable accuracy, GFEM requires less DOFs than the conventional FEM. Numerical results show that with GFEM, the total DOFs are less than 5% of that used for the standard FEM. The coarse meshes used with GFEM made the computational time only a small fraction of that for the FEM solution. Also the time-independent nature of the enrichment functions resulted in remarkable reduction in the total computation time for large number of steps. To investigate the performance of GFEM further, two more example

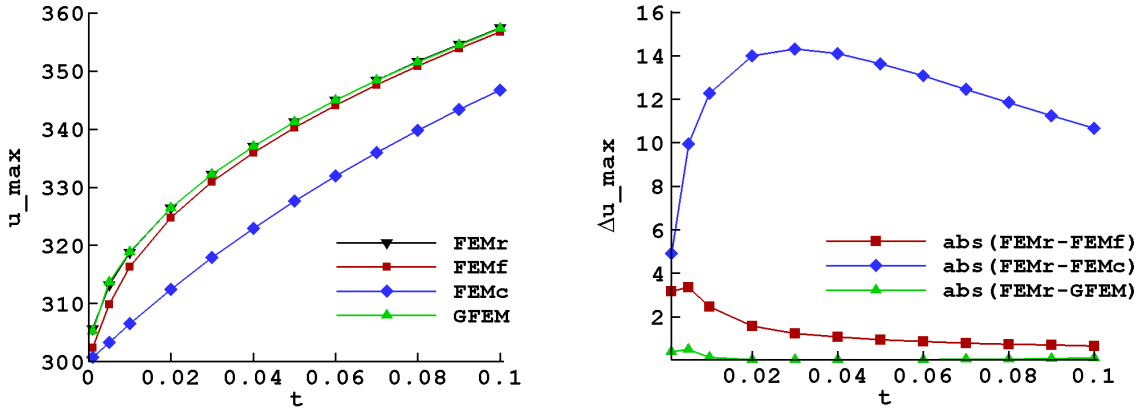

(a) (b)

Fig. 4.29 Time evolution of (a) maximum temperatures (b) difference in maximum temperatures.

problems are considered for which the analytical solutions are not known. Example problem 2 considered a cubic domain while Example problem 3 assessed the method on an annular computational domain. Exponential Gaussian functions are used for example problem 1 and 2 while hyperbolic tangent functions are used for the third example due to the different nature of the problem. Both enrichment approaches are shown to be successful in significantly reducing the computational effort and leading to better quality results compared to the standard FEM.

Regarding the last statement, it is important to mention that the enriched approach, GFEM, is a high order method while FEM with linear shape functions is a low order method and hence the comparison is not really fair. However, this comparison is for indication as low order polynomial based FEM are the most used in practice and multiplying the low order shape functions, linear in this case, by enrichment functions to obtain GFEM leads to an efficient tool to not only capture the sharp gradients but also to relax the mesh grids and reduce the overall computational cost.

Chapter 5

A-posteriori error estimate for GFEM for transient heat diffusion problems

5.1 Introduction

This chapter is dedicated to the development of an error estimate to assess the robustness of GFEM for a given coarse mesh grid and enrichment functions. A Detailed mathematical derivation of the proposed error estimate is presented for a two-dimensional case. It is then followed by numerical experiments to show its validity.

5.2 *a-posteriori* error estimation for transient heat diffusion problems

The current work explores rigorous computable *a-posteriori* error estimates for the approximate solutions provided by the time–dependent GFEM. In particular, we address enrichments in the whole spatial domain and for time-dependent problems. While suitable enrichment functions are easily proposed, such estimates provide rigorous insight

into the accuracy of the resulting numerical scheme and the relative benefits of different numbers and kinds of enrichment functions, as well as possible mesh refinements. Here we explore the relevance of a residual *a-posteriori* estimate for time–dependent simulations of heat transfer problems using multiple enrichment functions. While for standard h-method finite elements such residual error estimates have a long tradition and are known to give sharp upper bounds for the error as $h \to 0$ [191], for GFEM one is particularly interested in a fixed coarse mesh. Also, unlike for piecewise polynomial ansatz functions or the plane–wave enrichment for wave problems, little is known about the approximation provided by the heuristically chosen enrichment functions. Nevertheless, our simple error estimates are rigorously shown to provide reliable and practically useful upper bounds for the numerical error. Numerical experiments indicate that they efficiently capture the decrease of the error as the number of enrichment functions is increased or the time discretization is refined. Both the global error in the whole space–time domain and local error indicators in the individual time steps and elements of the mesh are studied, with a view towards the adaptive selection and refinements of the enrichment functions.

5.2.1 Boundary value problem and weak formulation

For an open bounded domain $\Omega \subset \mathbb{R}^2$ with polygonal boundary Γ and a given time interval $]0, T]$, we consider the time dependent heat diffusion problem defined by expressions (3.1)−(3.3). The weak formulation of the considered problem is given by (3.14), and rewritten here

$$\int_\Omega (\nabla P_r \cdot \nabla u^{n+1} + P_r k u^{n+1}) d\Omega + \int_\Gamma P_r h u^{n+1} d\Gamma = \int_\Omega P_r F^{n+1} d\Omega + \int_\Gamma P_r g^{n+1}\, d\Gamma \ . \quad (5.1)$$

Our aim is to find the GFEM solution of the form (3.16) for the above weak formulation. The global enrichment functions defined by (3.18) are used to find the approximate GFEM solution.

5.2.2 A residual *a-posteriori* error estimate

From the numerical solution u^{n+1} at time t_{n+1} we define, by piecewise constant, respectively piecewise linear interpolation, the numerical solutions for all positive t:

$$u(t,\mathbf{x}) = \frac{t-t_n}{t_{n+1}-t_n}\, u^{n+1}(\mathbf{x}) + \frac{t_{n+1}-t}{t_{n+1}-t_n}\, u^n(\mathbf{x}) \ ,$$
$$\hat{u}(t,\mathbf{x}) = u(t_{n+1},\mathbf{x}),\ \hat{f}(t,\mathbf{x}) = f(t_{n+1},\mathbf{x}), \hat{g}(t,\mathbf{x}) = g(t_{n+1},\mathbf{x}) \text{ for } t \in]t_n, t_{n+1}] \ .$$

Note from (3.13) that the GFEM discretization (5.1) is equivalent to finding u^{n+1} of the form (3.16) such that $u^0 = u_0$ and for all $r = 1, \ldots, MQ$

$$\int_\Omega (P_r \partial_t u + \lambda \nabla P_r \nabla \hat{u})\, d\Omega + \int_\Gamma \lambda P_r h \hat{u}\ d\Gamma = \int_\Omega P_r \hat{f}\ d\Omega + \int_\Gamma \lambda P_r \hat{g}\ d\Gamma \ . \tag{5.2}$$

In this notation, we obtain a classical *a-posteriori* estimate of residual type for the error of the GFEM solution, similar to extensively used estimates for adaptive h- and hp-finite element methods. It is given by computable error indicators $\eta_1, \ldots, \eta_6$, and the following theorem shows that it is *reliable*, in the sense that $\eta_1, \ldots, \eta_6$ rigorously bound the error.

As a main point, the estimate does not depend on the choice of the enrichment functions and little can be said about their approximation properties, in general. This will allow to choose the enrichment adaptively. Also, for GFEM we are concerned with a fixed, coarse mesh grids.

Theorem 1 *Let U be the solution of the exact weak formulation* (3.12) *and u the solution of the GFEM discretization* (3.24)*. Then there exists a constant $c > 0$ such that:*

$$\int_\Omega |U(T,\boldsymbol{x}) - u(T,\boldsymbol{x})|^2 d\Omega + \lambda \int_0^T \int_\Omega |\nabla(U-\hat{u})|^2 d\Omega\ dt \\ \leq c\{\eta_1^2 + \eta_2^2 + \eta_3^2 + \eta_4^2 + \eta_5^2 + \eta_6^2\}, \tag{5.3}$$

where

$$\eta_1^2 = \|U_0 - u_0\|^2_{L^2(\Omega)} \tag{5.4}$$

$$\eta_2^2 = \sum_K \int_0^T \left\| \hat{f} - \partial_t u + \lambda \Delta \hat{u} \right\|^2_{H^{-1}(K)} dt \tag{5.5}$$

$$\eta_3^2 = \int_0^T \left\| f - \hat{f} \right\|^2_{H^{-1}(\Omega)} dt + \lambda \int_0^T \|\hat{g} - g\|^2_{H^{-1/2}(\Gamma)} \; dt \tag{5.6}$$

$$\eta_4^2 = \lambda \int_0^T \|\nabla(u - \hat{u})\|^2_{L^2(\Omega)} \, dt \tag{5.7}$$

$$\eta_5^2 = \sum_{E \cap \Gamma = \emptyset} \int_0^T \left\| \left[\frac{\partial \hat{u}}{\partial n} \right] \right\|^2_{L^2(E)} dt \tag{5.8}$$

$$\eta_6^2 = \lambda \int_0^T \left\| \hat{g} - \frac{\partial \hat{u}}{\partial n} - h\hat{u} \right\|^2_{H^{-1/2}(\Gamma)} dt \tag{5.9}$$

The left hand side of expression (5.3) measures the (typically unknown) size of the actual error between the GFEM and exact solutions. The error indicators on the right hand side, η_1^2 to η_6^2, however can be computed. The theorem proves that the error is at most $c\{\eta_1^2 + \cdots + \eta_6^2\}$, in particular the η_j never underestimate the error.

For the h-method one can often show that a residual error estimate is *efficient*, in the sense that it does not overestimate the error by more than a fixed multiplicative constant [191]. Proving such a result would require a detailed analysis of the particular enrichment functions; it is less relevant for key applications such as adaptive refinements, where Theorem 1 is crucial. The numerical experiments in Section 5.2.4 will investigate the relation between the error indicators and the actual error numerically.

The error indicators η_1^2 to η_6^2 in Theorem 1 have clear physical meanings: η_1 and η_3 describe the error in the approximation of the initial condition ad the source term respectively. We will usually consider situations in which the exact initial condition and the source term are used in the computation, so that η_1 and η_3 vanish. The violation of the original PDE (3.1) is measured by η_2 and the violation of the boundary condition (3.3) is measured by η_6. Finally, η_5 measures that the numerical heat flux is not conserved across element edges, while η_4 involves the error in the time discretization.

Proof 1 (Proof of Theorem 1) *Let $\hat{e} = U - u$, π some stable projection onto the*

space of basis functions and $\hat{e}_I = \pi\hat{e}$. *We start by applying the Fundamental Theorem of Calculus to the first term in expression* (5.3)*:*

$$\begin{aligned}\int_\Omega |U(T,\boldsymbol{x}) - u(T,\boldsymbol{x})|^2 d\Omega &= \int_\Omega |U(0,\boldsymbol{x}) - u(0,\boldsymbol{x})|^2 d\Omega \\ &\quad + 2\int_0^T \int_\Omega (\partial_t U(t,\boldsymbol{x}) - \partial_t u(t,\boldsymbol{x}))(U(t,\boldsymbol{x}) - u(t,\boldsymbol{x}))\ d\Omega\ dt \\ &= \eta_1^2 + 2\int_0^T \int_\Omega (\partial_t U(t,\boldsymbol{x}) - \partial_t u(t,\boldsymbol{x}))\hat{e}(t,\boldsymbol{x})\ d\Omega\ dt\ .\end{aligned}$$

Now adding and subtracting the same quantities

$$\begin{aligned}&\int_0^T \int_\Omega (\partial_t U - \partial_t u)\hat{e}\ d\Omega\ dt + \lambda\int_0^T \int_\Omega |\nabla(U-\hat{u})|^2\ d\Omega\ dt \\ &= \int_0^T \int_\Omega (\partial_t U - \partial_t u)(\hat{e}-\hat{e}_I)\ d\Omega\ dt + \int_0^T \int_\Omega (\partial_t U - \partial_t u)\hat{e}_I\ d\Omega\ dt \\ &\quad + \lambda\int_0^T \int_\Omega \nabla(U-\hat{u})\nabla(\hat{e}-\hat{e}_I)\ d\Omega\ dt + \lambda\int_0^T \int_\Omega \nabla(U-\hat{u})\nabla\hat{e}_I\ d\Omega\ dt \\ &\quad + \lambda\int_0^T \int_\Omega \nabla(U-\hat{u})\nabla(u-\hat{u})\ d\Omega\ dt\ .\end{aligned}$$

Using the exact weak formulation (3.12)*, this equals*

$$\begin{aligned}&-\int_0^T \int_\Omega \partial_t u(\hat{e}-\hat{e}_I)\ d\Omega\ dt - \int_0^T \int_\Omega \partial_t u\ \hat{e}_I\ d\Omega\ dt \\ &\quad - \lambda\int_0^T \int_\Omega \nabla\hat{u}\nabla(\hat{e}-\hat{e}_I)\ d\Omega\ dt - \lambda\int_0^T \int_\Omega \nabla\hat{u}\nabla\hat{e}_I\ d\Omega\ dt \\ &\quad + \lambda\int_0^T \int_\Omega \nabla(U-\hat{u})\nabla(u-\hat{u})\ d\Omega\ dt \\ &\quad + \int_0^T \int_\Omega f(\hat{e}-\hat{e}_I)\ d\Omega\ dt + \int_0^T \int_\Gamma \lambda g(\hat{e}-\hat{e}_I)\ d\Gamma\ dt - \int_0^T \int_\Gamma \lambda h U(\hat{e}-\hat{e}_I)\ d\Gamma\ dt \\ &\quad + \int_0^T \int_\Omega f\hat{e}_I\ d\Omega\ dt + \int_0^T \int_\Gamma \lambda g\hat{e}_I\ d\Gamma\ dt - \int_0^T \int_\Gamma \lambda h U\hat{e}_I\ d\Gamma\ dt\ .\end{aligned}$$

Further, using the GFEM equation (5.2)*, the sum of the second and fourth terms becomes*

$$\int_0^T \int_\Gamma \lambda h\hat{u}\hat{e}_I\ d\Gamma\ dt - \int_0^T \int_\Omega \hat{f}\hat{e}_I\ d\Omega\ dt - \int_0^T \int_\Gamma \lambda\hat{g}\hat{e}_I\ d\Gamma\ dt\ .$$

On each of the elements K of the mesh we integrate by parts in the third term,

$$-\lambda \int_0^T \int_\Omega \nabla \hat{u} \nabla(\hat{e} - \hat{e}_I) \; d\Omega \; dt = \lambda \sum_K \int_0^T \int_K \Delta \hat{u} \; (\hat{e} - \hat{e}_I) \; d\Omega \; dt \\ - \lambda \sum_K \int_0^T \int_{\partial K} \frac{\partial \hat{u}}{\partial n} \; (\hat{e} - \hat{e}_I) \; d(\partial K) \; dt \; .$$

The second sum over K can be written as a sum over interior and boundary edges,

$$\begin{aligned} & - \lambda \sum_K \int_0^T \int_{\partial K} \frac{\partial \hat{u}}{\partial n} \; (\hat{e} - \hat{e}_I) \; d(\partial K) \; dt \\ & = -\lambda \sum_{E \cap \Gamma = \emptyset} \int_0^T \int_E \left[\frac{\partial \hat{u}}{\partial n} \right] (\hat{e} - \hat{e}_I) \; dE \; dt - \lambda \int_0^T \int_\Gamma \frac{\partial \hat{u}}{\partial n} \; (\hat{e} - \hat{e}_I) \; d\Gamma \; dt \; . \end{aligned}$$

We conclude

$$\begin{aligned} & \int_0^T \int_\Omega (\partial_t U - \partial_t u) \hat{e} \; d\Omega \; dt + \lambda \int_0^T \int_\Omega |\nabla(U - \hat{u})|^2 \; d\Omega \; dt \\ & = \sum_K \int_0^T \int_K (\hat{f} - \partial_t u + \lambda \Delta \hat{u}) \; (\hat{e} - \hat{e}_I) \; d\Omega \; dt \\ & \quad - \lambda \sum_{E \cap \Gamma = \emptyset} \int_0^T \int_E \left[\frac{\partial \hat{u}}{\partial n} \right] (\hat{e} - \hat{e}_I) \; dE \; dt + \lambda \int_0^T \int_\Omega \nabla(U - \hat{u}) \nabla(u - \hat{u}) \; d\Omega \; dt \\ & \quad + \int_0^T \int_\Gamma \lambda \left(\hat{g} - \frac{\partial \hat{u}}{\partial n} - h \hat{u} \right) (\hat{e} - \hat{e}_I) \; d\Gamma \; dt - \int_0^T \int_\Gamma \lambda h (U - \hat{u})(\hat{e} - \hat{e}_I) \; d\Gamma \; dt \\ & \quad + \int_0^T \int_\Omega (f - \hat{f}) \hat{e} \; d\Omega \; dt + \int_0^T \int_\Gamma \lambda (g - \hat{g}) \hat{e} \; d\Gamma \; dt - \int_0^T \int_\Gamma \lambda h (U - \hat{u}) \hat{e}_I \; d\Gamma \; dt \quad . \end{aligned} \tag{5.10}$$

Note that

$$\begin{aligned} & - \int_0^T \int_\Gamma \lambda h (U - \hat{u})(\hat{e} - \hat{e}_I) \; d\Gamma \; dt - \int_0^T \int_\Gamma \lambda h (U - \hat{u}) \hat{e}_I \; d\Gamma \; dt \\ & \quad = \int_0^T \int_\Gamma \lambda h (-\hat{e} + \hat{u} - u) \hat{e} \; d\Gamma \; dt \; . \end{aligned}$$

As we do not have further information about the approximation properties of the basis functions, we do not lose much by choosing $e_I = 0$. With the Cauchy–Schwarz inequality $ab \leq \frac{\varepsilon a^2}{2} + \frac{b^2}{2\varepsilon}$ for any $a, b \in \mathbb{R}$, $\varepsilon > 0$, the third term on the right hand side of

(5.10) *is smaller than* $\frac{\varepsilon\lambda}{2}\int_0^T\int_\Omega|\nabla(U-\hat{u})|^2d\Omega\,dt+\frac{1}{2\varepsilon}\eta_4^2$*, and for small* $\varepsilon>0$ *we may move the first of these summands to the left hand side.*

The continuity of the bilinear pairing between H^1 *and* H_0^1 *and the Sobolev inequality similarly result in* η_2^2 *and* η_3^2 *from the first term and the term involving* $f-\hat{f}$*, respectively. Finally, the trace theorem* $\|V\|_{H^{1/2}(\Gamma)}\leq c\|V\|_{H^1(\Omega)}$ *in the same manner leads to* η_5^2 *from the second term on the right hand side, to* η_6^2 *from the fourth term, and* η_3^2 *from the penultimate term involving* $g-\hat{g}$*.*

For the remaining terms, the trace theorem and the Sobolev inequality allow to estimate them by η_4^2*.*

5.2.3 Algorithmic considerations

This section discusses the detailed implementation of the error indicator of Theorem 1. We compute η_2^2 as $\eta_2^2=\sum_{n=0}^{N_t}\sum_K\eta_2^2(n,K)$, with

$$\begin{aligned}\eta_2^2(n,K)&=\int_{t_n}^{t_{n+1}}\left\|\hat{f}-\partial_t u+\lambda\Delta\hat{u}\right\|^2_{H^{-1}(K)}\\&\leq\int_{t_n}^{t_{n+1}}dt\int_K\left(\hat{f}-\partial_t u+\lambda\Delta\hat{u}\right)^2d\Omega\\&=\delta t\int_K\left(f^{n+1}-\frac{u^{n+1}-u^n}{\delta t}+\lambda\left(\frac{\partial^2u^{n+1}}{\partial x^2}+\frac{\partial^2u^{n+1}}{\partial y^2}\right)\right)^2d\Omega\,.\end{aligned}$$

Here, the final line is efficiently computable and is only a slight overestimate of η_2. The values of f and u^n are calculated at each integration point and then accumulated over the whole domain. They are updated at every time step. Values from the present and previous time steps are used in the calculation of $\eta_2^2(n,K)$.

The indicator $\eta_4^2=\sum_{n=0}^{N_t}\sum_K\eta_4^2(n,K)$ evaluates the change in the derivative of u in every time step. We calculate the derivative of the temperature as above at times

t_n and t_{n+1} at every integration point and then accumulate over the whole domain:

$$\begin{aligned}\eta_4^2(n,K) &= \lambda \int_{t_n}^{t_{n+1}} \|\nabla(u-\hat{u})\|^2_{L^2(K)} \\ &= \lambda \int_{t_n}^{t_{n+1}} \left(\frac{t_{n+1}-t}{t_{n+1}-t_n}\right)^2 dt \int_K \left[\left(\frac{\partial u^{n+1}}{\partial x} - \frac{\partial u^n}{\partial x}\right)^2 + \left(\frac{\partial u^{n+1}}{\partial y} - \frac{\partial u^n}{\partial y}\right)^2\right] d\Omega \\ &= \frac{\lambda \delta T}{3}\left(\int_K \left(\frac{\partial u^{n+1}}{\partial x} - \frac{\partial u^n}{\partial x}\right)^2 d\Omega + \int_K \left(\frac{\partial u^{n+1}}{\partial y} - \frac{\partial u^n}{\partial y}\right)^2 d\Omega\right) \ .\end{aligned}$$

Here we use, by definition,

$$u(t,\mathbf{x}) - \hat{u}(t,\mathbf{x}) = -\frac{t_{n+1}-t}{t_{n+1}-t_n}\left(u^{n+1}(\mathbf{x}) - \ u^n(\mathbf{x})\right) \ .$$

For $\eta_5^2 = \sum_{n=0}^{N_t}\sum_E \eta_5^2(n,E)$ error indicator, it calculates the jump of $\frac{\partial \hat{u}}{\partial n}$ across the interior edges E of the mesh. At each integration point these values are calculated for adjacent edges of the elements. The difference between these values at the adjacent elements is then calculated and integrated over the whole domain. This means

$$\begin{aligned}\eta_5^2(n,E) &= \int_{t_n}^{t_{n+1}} \left\| \left[\frac{\partial \hat{u}}{\partial n}\right] \right\|^2_{L^2(E)} \ dt \\ &= \int_{t_n}^{t_{n+1}} \left\| \left[\nabla u^{n+1} \cdot \mathbf{n}\right] \right\|^2_{L^2(E)} \ dt \\ &= \int_{t_n}^{t_{n+1}} \int_E \left(\nabla u_{E_1}^{n+1} n_1 + \nabla u_{E_2}^{n+1} n_2\right)^2 dE \ dt \\ &= \int_{t_n}^{t_{n+1}} \int_E \left(\nabla u_{E_1}^{n+1} n_1 - \nabla u_{E_2}^{n+1} n_1\right)^2 dE \ dt \\ &= \delta t \int_E \left(\left(\frac{\partial u^{n+1}}{\partial x} n_{1_x} + \frac{\partial u^{n+1}}{\partial y} n_{1_y}\right)_{E_1} - \left(\frac{\partial u^{n+1}}{\partial x} n_{1_x} + \frac{\partial u^{n+1}}{\partial y} n_{1_y}\right)_{E_2}\right)^2 dE \ ,\end{aligned}$$

where E_1 refers to the boundary value of the function on the edge taken from the first element and E_2 refers to the boundary value of the function on the same edge, but taken from the second element. We denote by $n_1 = (n_{1_x}, n_{1_y})$ and $n_2 = (n_{2_x}, n_{2_y})$ the unit normals for elements 1 and 2, respectively.

5.2.4 Numerical experiments

This section investigates the relevance and sharpness of the *a-posteriori* error estimate in Theorem 1 through numerical experiments. We compute the numerical solution of the heat transfer problem (3.1) - (3.3) by computing the solution of the GFEM discretization (3.16).

For the experiments, we choose a quadrilateral mesh with piecewise bilinear shape functions. The parameters in the GFEM basis functions G_q are taken to be $R_c = \sqrt{\frac{2800}{239}}$ and $C = \sqrt{\frac{200}{239}}$, and $R_0 = |\mathbf{x} - \mathbf{x}_c|$ is the distance from the point $\mathbf{x}_c = (1, 1)$. All integrals over Ω are evaluated numerically, using a high Gauss–Legendre quadrature. For example, 22 integration points are used in each direction, i.e., 484 points per element. In the numerical examples, we consider the error estimators η_1 and η_3, which arise from the approximation of the initial condition and the source terms, are either identically 0 or negligible. The same holds for the the violation of the boundary condition, η_6. Both the numerical and exact solutions themselves are either 0 or very close to 0 at the boundary.

To compare the results for different model problems, we focus on the relative error between the exact solution U and its GFEM approximation u, defined as

$$\left(\frac{\int_\Omega |U-u|^2 d\Omega + \lambda \int_0^T \int_\Omega |\nabla(U-\hat{u})|^2 d\Omega \; dt}{\int_\Omega |U|^2 d\Omega + \lambda \int_0^T \int_\Omega |\nabla U|^2 d\Omega \; dt} \right)^{1/2} \tag{5.11}$$

The corresponding relative error indicator is given as

$$\left(\frac{\eta_2^2 + \eta_4^2 + \eta_5^2}{\int_\Omega |U|^2 d\Omega + \lambda \int_0^T \int_\Omega |\nabla U|^2 d\Omega \; dt} \right)^{1/2} \tag{5.12}$$

If the exact solution U is not known, we consider a reference solution obtained by a polynomial based FEM on a fine mesh grid.

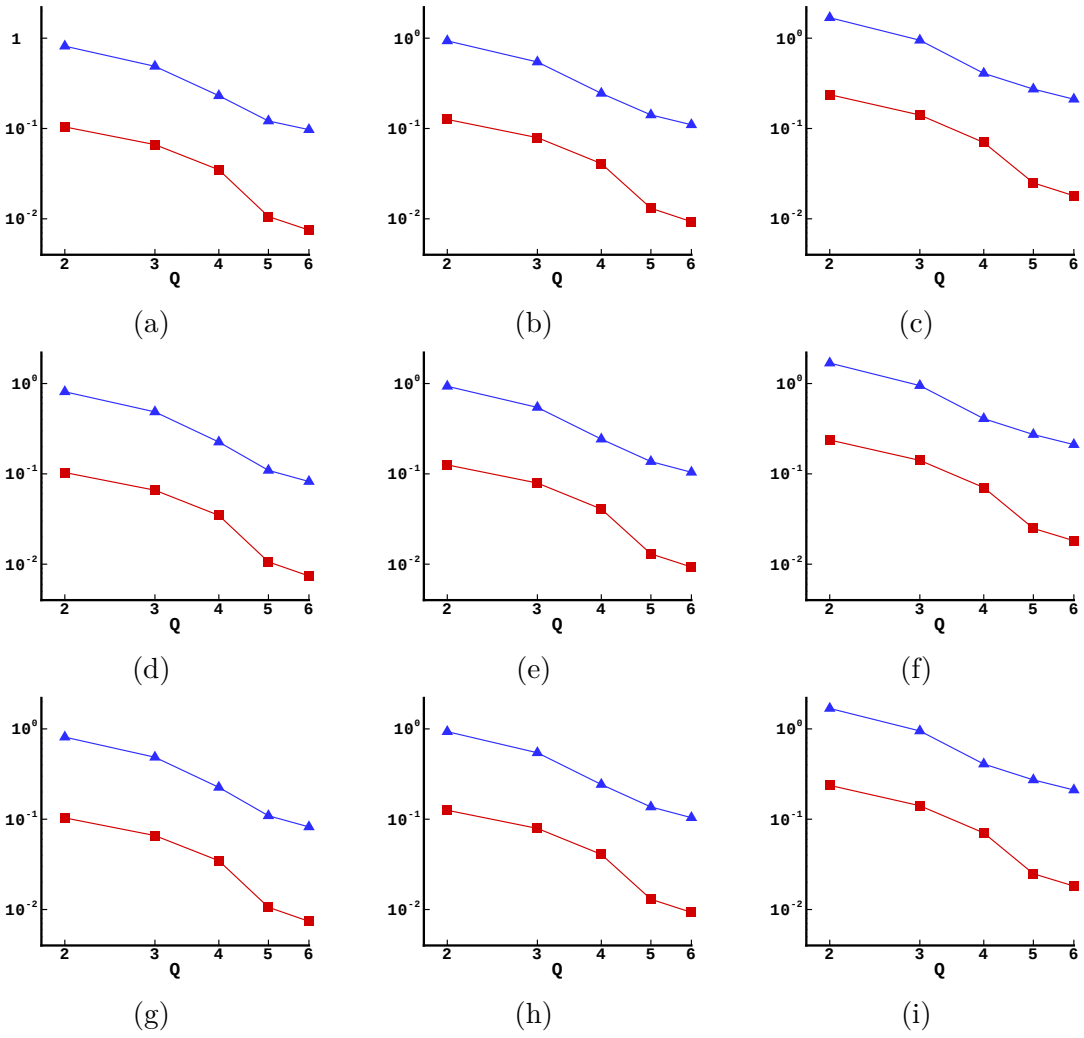

Fig. 5.1 Comparison of relative error (■) and relative error indicator (▲) for $\Delta t = 0.01$s (top row), $\Delta t = 0.001$s (middle row) and $\Delta t = 0.0001$s (bottom row) at times $t = 0.05,\ 0.1$ and 1.0s from left to right.

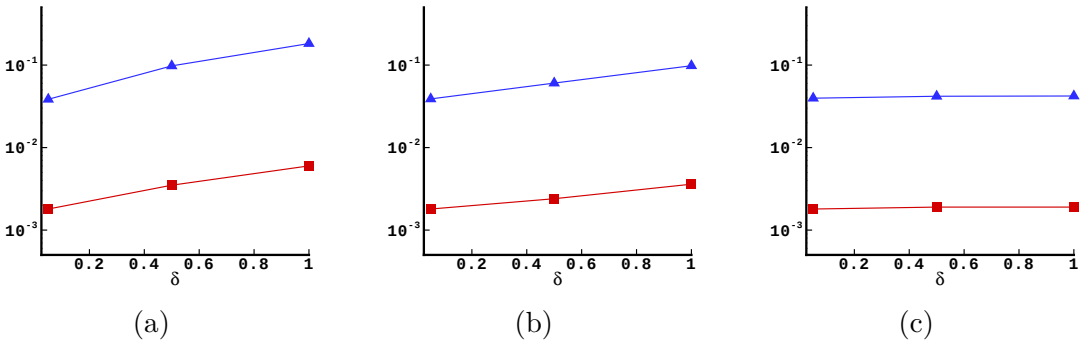

Fig. 5.2 Comparison of relative error (■) and relative error indicator (▲) for $\Delta t = 0.05,\ 0.5$ and 1.0s at $t = 5$s (a), $t = 10$s (b) and $t = 100$s (c).

5.2.4.1 Example problem 1

In this example we test the error indicator by comparing it to the computed error for a problem with a given exact solution that is proposed in [129]. We consider a square domain $\Omega = \{(x, y) \in \mathbb{R}^2 : 0 \leq x, y \leq 2\}$ with a heat diffusion coefficient $\lambda = 0.1\text{kgm}/^\circ\text{Cs}^2$ and convection heat transfer coefficient $h = 1\text{kg}/^\circ\text{Cs}^2$. The data f, g and U_0 are chosen such that

$$U(t, \mathbf{x}) = x^{20}y^{20}(2 - x)^{20}(2 - y)^{20}(1 - e^{-\lambda t}) \tag{5.13}$$

is the exact solution to the problem defined by expressions (3.1) - (3.3).

For a fixed coarse spatial mesh of 25 elements we vary the number of enrichment functions $Q = 2, \ldots, 6$. We compute both the actual error of the GFEM solution and the error indicators, and compare these values as in Theorem 1. In Figure 5.1, we show the relative error (5.11) of the GFEM solution and the relative error indicator (5.12), for different numbers Q of enrichment functions at times $t = 0.05, 0.1$ and 1s. In each of the cases we do so for different time steps $\Delta t = 0.01,\ 0.001$ and 0.0001s.

In all cases, the actual error of the GFEM solution and the error indicator show a similar decrease as we increase the number of enrichment functions. The ratio of the estimator and the error is close to 10, consistently in all cases. This corresponds to a constant $c \sim 10^{-1}$ in Theorem 1. In this sense, the error indicator efficiently captures the behaviour of the real error.

Figure 5.2 investigates the influence of the time step Δt when the spatial discretization error is small. We use a uniform of with 100 elements with $Q = 6$, and compare the relative error and the error indicator for $\Delta t = 0.05,\ 0.5$ and 1.0s. The results are plotted at $t = 5,\ 10$ and 100s. At $t = 5$s the error decreases significantly for smaller time steps. As time progresses the error becomes insensitive to the time step which can be seen at 100s. This is due to the large temperature differences between the central part and the rest of the domain. As time passes, heat propagates from the central part to the rest of the domain, hence the temperature gradient reduces. Figure 5.2 shows

remarkable consistency between the behaviour of the error indicator and the actual error. The behaviour described above is accurately captured by the error indicator. For a residual *a-posteriori* estimate, the multiplicative constant between the indicator and the actual error is essentially the constant c.

5.2.4.2 Example problem 2

The second example considers a square domain with a square heat source as shown in Figure 5.3. The source is switched on from $t = 0$ to $t = 0.02$s, and then it is switched off. The source diffuses heat at two rates. For $x, y \in [0.8, 1.2]$, the central part of the source f is constant and given by $f = 200°\text{C/s}$. Outside this part, f decreases linearly to $f = 0$ on the external boundaries of the source, where either x or y is equal to 0.4 or 1.6. In this example the thermal conductivity is taken as $\lambda = 0.1\text{kgm/}°\text{Cs}^2$ and the convective heat transfer coefficient as $h = 1\text{kg/}°\text{Cs}^2$. The initial temperature U_0 and the boundary sources g are both chosen to be 0. This example assesses the error estimates for a more realistic heat transfer problem and makes a first step towards an adaptive selection of enrichment functions.

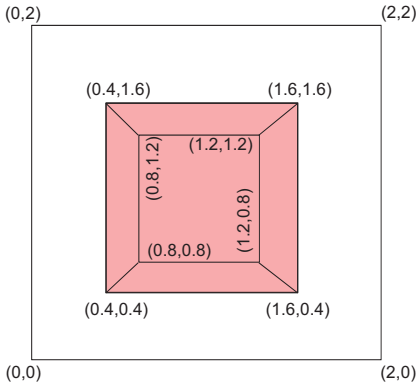

Fig. 5.3 Domain configuration for Example problem 2 with a heat source in the centre.

Here, we only compute the error indicator because the exact solution is not known. The magnitude of the error indicator is considered relative to a reference value defined by Equation (5.11), where the exact solution U is replaced with a reference FEM

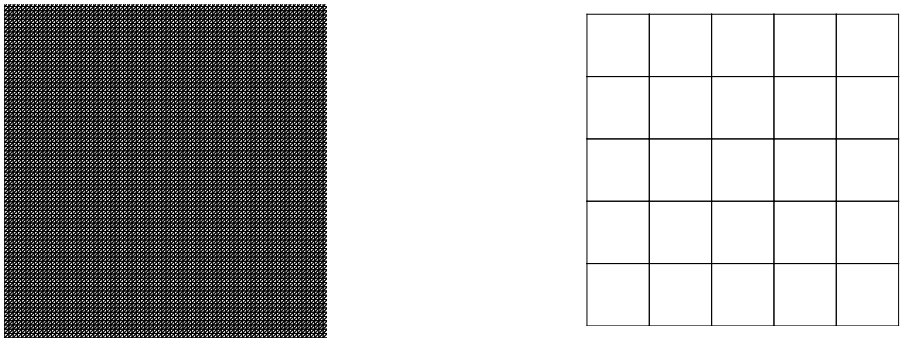

(a) FEM mesh

(b) GFEM mesh

Fig. 5.4 Meshes used in the computations.

Table 5.1 Conditioning number for different Q and Δt (s).

Q	Δt		
	0.001	0.0001	0.00001
2	1.461E+05	1.509E+05	1.514E+05
3	2.534E+07	2.727E+07	2.748E+07
4	4.302E+09	4.805E+09	4.862E+09
5	5.118E+11	6.270E+11	6.416E+11
6	1.637E+13	1.992E+13	2.037E+13

solution on a fine uniform mesh of 12800 triangular elements with piecewise linear basis functions. Both FEM and GFEM meshes are shown in Figure 5.4.

For the GFEM solution, we fix a coarse mesh of 25 elements and vary the number of enrichment functions $Q = 2, \ldots 6$. Figure 5.5 shows the temperature distribution of the FEM solution and the GFEM solution. Figure 5.6 shows the relative error indicators as a function of the number Q of enrichment functions at times $t = 0.01,\ 0.05,\ 0.1,\ 0.15$ and 0.2s. In each of the cases, the considered time steps are: $\Delta t = 0.001,\ 0.0001$ and 0.00001s. The results show a decrease in the error indicator as we increase the number of enrichment functions. For all the values of Δt and at early times the results show similar trends (as in Figure 5.6(a)). However, at later times and for the smallest considered time step $\Delta t = 0.00001$s the error indicator with higher Q starts to increase rapidly. This can be seen clearly for $Q = 5$ and 6 in Figure 5.6(d) and Figure 5.6(e).

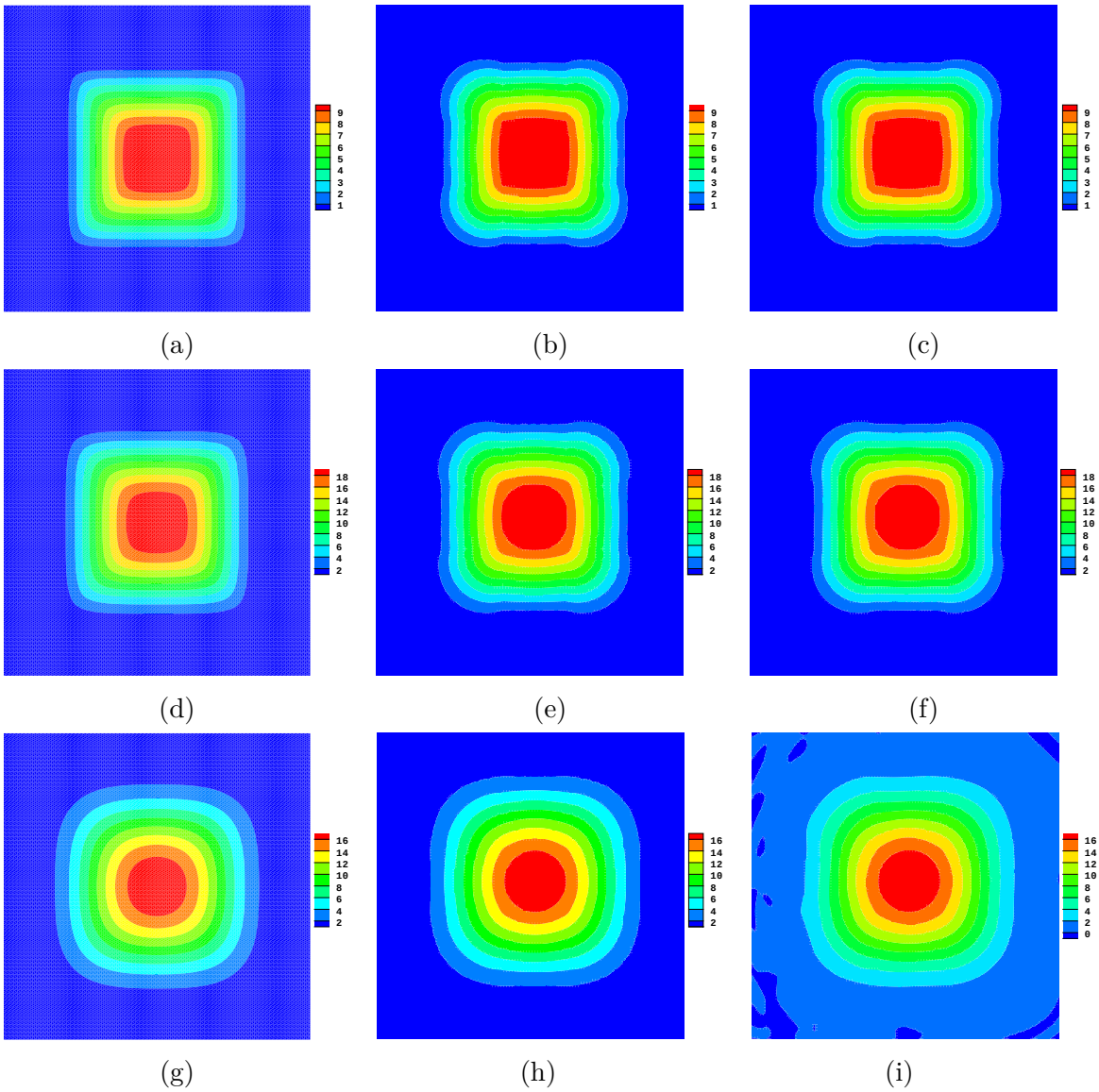

Fig. 5.5 Temperature distribution for the reference solution (FEM) (left column), GFEM solution with $Q = 4$ (middle column) and GFEM solution with $Q = 6$ (right column) at $t = 0.05$s (top row), $t = 0.1$s (middle row) and $t = 0.2$s (bottom row). The distribution is obtained with $\Delta t = 0.00001$s.

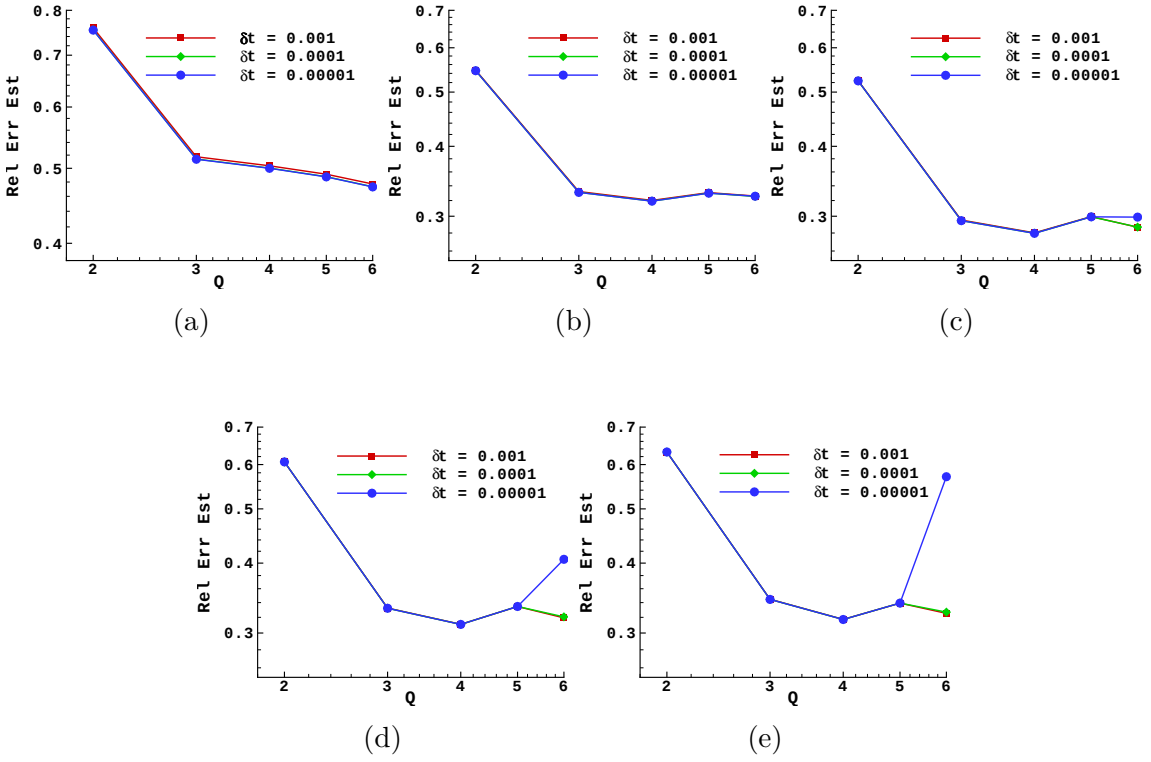

Fig. 5.6 Relative error indicator for $\Delta t = 0.01$s, $\Delta t = 0.001$s and $\Delta t = 0.0001$s at $t = 0.01$s (a), $t = 0.05$s (b), $t = 0.1$s (c), $t = 0.15$s (d) and $t = 0.2$s (e).

For example in the case with $Q = 6$ the error indicator increases from less than 0.3 in Figure 5.6(c) to more than 0.6 in Figure 5.6(e).

The rapid increase can be attributed to two facts. First, at higher number of enrichment functions, the system matrix from Equation (3.24) becomes ill conditioned as can be seen in Table 5.1. The size of the condition number is mostly determined by Q, with negligible dependence on Δt. For example the condition number increases from about 1.5E+5 with $Q = 2$ and $\Delta t = 0.001$s to about 2.0E+13 with $Q = 6$ and $\Delta t = 0.00001$s. The increase in the condition number affects the solution and leads to an increase in the error. This behaviour seems to be reflected accurately by the error indicator as can be seen in Figure 5.6. Second, smaller values of Δt require more time steps to cover the same time span. This accumulates the computational errors, in particular floating point errors which increase with higher condition numbers. To verify this, in Figure 5.5 we compare the temperature distribution obtained with the

Table 5.2 Details of the q-bands.

Case	Band	Case	Band
1	$q = 1, 2, 3$	11	$q = 2, 3, 6$
2	$q = 2, 3, 4$	12	$q = 2, 3, 5$
3	$q = 3, 4, 5$	13	$q = 3, 5, 6$
4	$q = 4, 5, 6$	14	$q = 3, 4, 6$
5	$q = 1, 2, 4$	15	$q = 1, 3, 4$
6	$q = 1, 2, 5$	16	$q = 1, 3, 5$
7	$q = 1, 2, 6$	17	$q = 1, 3, 6$
8	$q = 2, 5, 6$	18	$q = 1, 4, 5$
9	$q = 2, 4, 6$	19	$q = 1, 4, 6$
10	$q = 2, 4, 5$		

reference solution to the GFEM solution with 4 and 6 enrichment functions, with $\Delta t = 0.00001$s. The solution at the early time steps shown in the figure, namely $t = 0.05$s and 0.01s, seems very similar in all three cases. However, at later times ($t = 0.2$s), the distribution is still similar for FEM and GFEM with 4 enrichment functions, but it deteriorates with 6 enrichment functions.

Two final experiments investigate the possible use of *a-posteriori* error estimates as in Theorem 1 for adaptive selection of the enrichment functions or refinement procedures. Indeed little is known about the approximation properties of the enrichment functions.

Figure 5.7 calculates the relative time–integrated error indicator over the whole domain Ω for different choices of enrichment functions and different time intervals $t = 0.01$, 0.05, 0.1, 0.15 and 0.2s, with a fixed time step $\Delta t = 0.001$s. For the enrichments stated in Table 5.2, we observe that the three enrichment functions $q = 1, 2, 3$ (Case 1) consistently give rise to the lowest error indicator. Especially for long times, enrichment with steep functions such as $q = 4, 5, 6$ (Case 4) is seen to yield worse numerical approximations. More generally, in each instance the enrichment function with $q = 1$ leads to a substantial improvement of the error indicator.

In order to decide about locally adaptive enrichment, the spatial distribution of the error indicators proves useful. In Figure 5.8, we depict the time–integrated error indicators for each element of the mesh for the optimal choice of enrichment functions

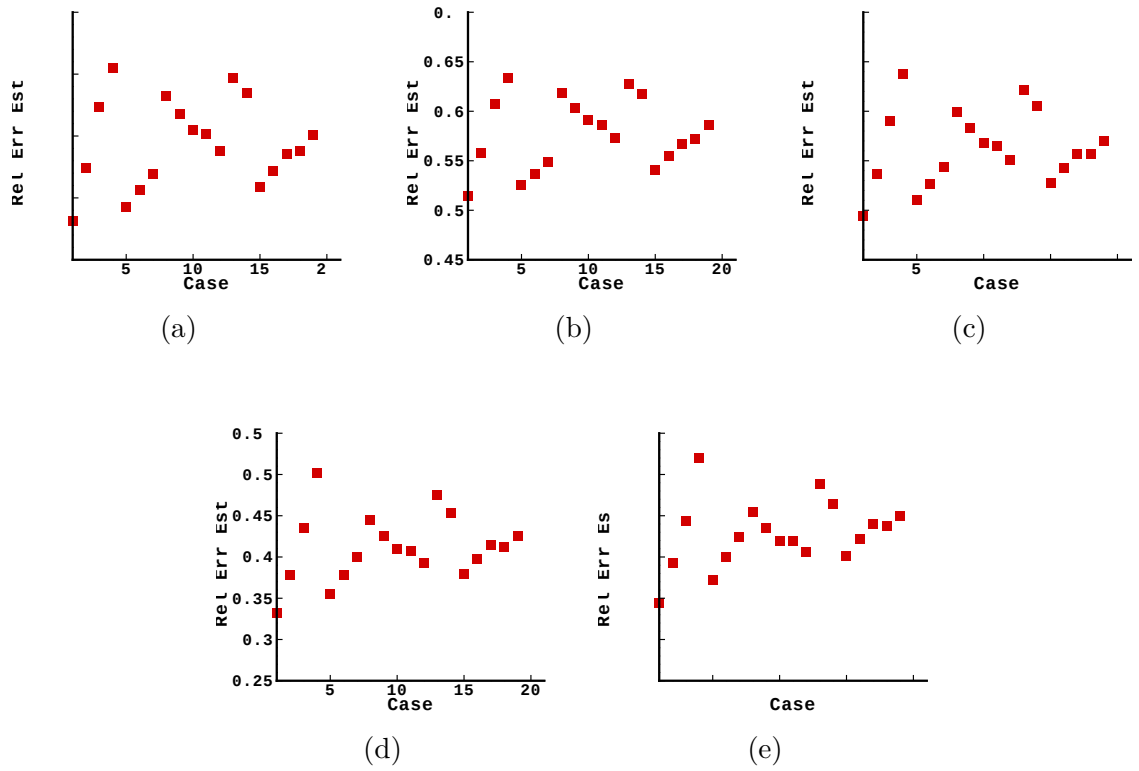

Fig. 5.7 Relative error indicator for different q-bands with $\Delta t = 0.001$s at $t = 0.01$s (a), $t = 0.05$s (b), $t = 0.1$s (c), $t = 0.15$s (d) and $t = 0.2$s (e).

$q = 1, 2, 3$ (Case 1) from Figure 5.7. Short ($t = 0.05$s), intermediate ($t = 0.1$s) and longer ($t = 0.2$s) time intervals are considered, with $\Delta t = 0.001$s. The contribution from the interior edges, η_5, is assigned in equal parts to the adjacent elements. It should be noted that the enrichment functions have a radial symmetry, which is not present in the exact solution for short times. Correspondingly, for short times the error indicator exhibits large contributions along both diagonals of the square domain. It also concentrates in the hot central element of the mesh, while the sharp gradient seems to be captured by the enrichment functions for short and intermediate times. For larger times, $t = 0.2$s, both the solution and the error indicators include contributions near the boundary, but we also observe increasing contributions from the large gradients.

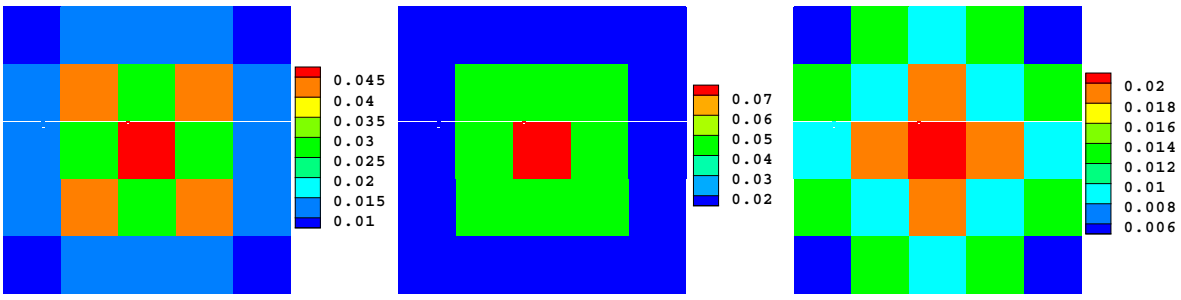

(a) (b) (c)

Fig. 5.8 Spatial distribution of the relative error indicator for Case 1 at $t = 0.05$s (a), $t = 0.1$s (b) and $t = 0.2$s (c).

5.2.5 Conclusions

An *a-posteriori* error estimate for time–dependent generalized finite element simulations of heat transfer problems is proposed. It does not depend on the choice of the enrichment functions and it is shown to efficiently and reliably reflect the behaviour of the numerical error of the GFEM approach. It reflects the contribution of various errors incurred in the poorly conditioned systems typically encountered in enriched finite element methods, in particular GFEM.

The error estimate is shown to capture the decrease in the error as the number of enrichment functions is increased or the time discretization is refined. The estimate is also used to predict the behaviour of the error for problems with for which the exact solution is not available. The investigation of local error indicators, on sub-domains or elements of the mesh grid, in individual time steps creates a basis towards the adaptive selection and refinement of the enrichment functions. this facilitates the adaptive local choices of the number and type of enrichment functions, in general.

Chapter 6

Local adaptive q–enrichment

6.1 Introduction

This chapter explores the use of *a-posteriori* error estimates for the adaptive selection of enrichment functions in the approximate solutions of time–dependent heat diffusion problems using GFEM. The components of the error estimate proposed in the previous chapter are shown to efficiently assess the quality of the solution with increasing number of enrichment functions. Up to this stage, the enrichment approach is uniformly applied to all sub-domains of the computational domain.

Here, we explore the relevance of the proposed error estimate to adaptively enrich the elements in the domain with relatively higher errors. Both the global error in the whole space–time domain and local error indicators in the individual elements of the mesh, are studied with a view towards the adaptive selection of the enrichment functions. An adaptive algorithm is proposed to identify the elements with higher errors and further enrichment functions are added only in those elements. The approach of the proposed algorithm is tested on different example problems.

The next section details the weak formulation of the considered problems followed by the proposed algorithm applied to the chosen test examples.

6.2 Problem description

We consider the transient heat diffusion problem defined by expressions (3.1)−(3.3). The weak formulation for the problem is given by (3.14). We aim to find an approximate solution u^{n+1} of the weak form (3.14) using the generalized finite element method. To do so, we look for u^{n+1} of the form

$$u^{n+1}(\mathbf{x}) = \sum_{j=1}^{M} \sum_{q=1}^{Q_j} A_{j,q}^{n+1} \; N_j(\mathbf{x}) \; G_j^q(\mathbf{x}) \; . \tag{6.1}$$

Here $A_{j,q}^{n+1} \in \mathbb{R}$ and N_j is a piecewise polynomial shape function for the j-th element $\square_j$. We choose the local enrichment functions G_q to be of the form

$$G_j^q(\mathbf{x}) = 1, \; e^{-\left(\frac{x-x_c}{C}\right)^q}, \; e^{-\left(\frac{y-y_c}{C}\right)^q} \text{ or } \; e^{-\left(\frac{x-x_c}{C}\right)^q - \left(\frac{y-y_c}{C}\right)^q} \; . \tag{6.2}$$

Here (x_c, y_c) is a given point, and we always use all four of these functions in a given mesh element. The functions N_j are piecewise polynomials of degree 3 separately in x and in y, such that $\sum_j N_j(x) = 1$ and $N_j(y) = 1$, whenever $x|y \in \square_j$ and the distance of $x|y$ to the boundary of $\square_j$ is at least 25% of the width of $\square_j$. The functions $N_j(x)$ and $N_j(y)$ are defined as

$$N_j(x) = \frac{(x_j - 0.25 \times WT - x)^2 \times (x_j + 2 \times 0.25 \times WT - x)}{4 \times (0.25 \times WT)^3} \tag{6.3}$$

$$N_j(y) = \frac{(y_j - 0.25 \times HT - y)^2 \times (y_j + 2 \times 0.25 \times HT - y)}{4 \times (0.25 \times HT)^3} \tag{6.4}$$

where WT, HT are the width and height of an element. For a 2D square domain $\Omega = [0, 2]^2$ with a 5×5 uniform mesh, the functions $N_j(x)$ and $N_j(y)$ for element-1 can be written as

$$N_1(x) = \frac{(x_1 - 0.25 \times WT - x)^2 \times (x_1 + 2 \times 0.25 \times WT - x)}{4 \times (0.25 \times WT)^3} \tag{6.5}$$

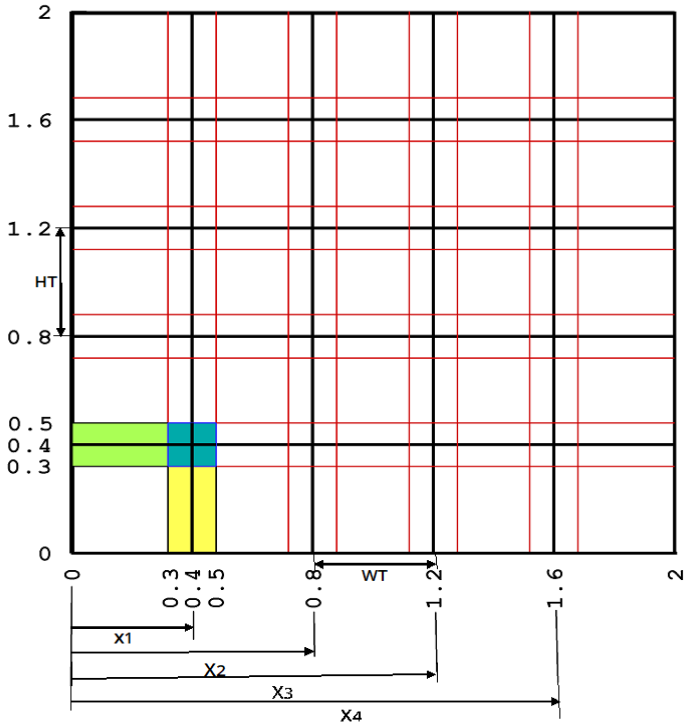

Fig. 6.1 Mesh grid with partitioned elements.

$$N_1(y) = \frac{(y_1 - 0.25 \times HT - y)^2 \times (y_1 + 2 \times 0.25 \times HT - y)}{4 \times (0.25 \times HT)^3} \tag{6.6}$$

Figure 6.1 shows the mesh grids with elements partitioned in the x and y directions.

21	22	23	24	25
16	17	18	19	20
11	12	13	14	15
6	7	8	9	10
1	2	3	4	5

Fig. 6.2 Detail of element numbering.

The original elements are shown by black outline. The red lines in the horizontal and vertical directions divide the elements near the interfaces at 25%WT in the $x-$direction and 25%HT in the $y-$direction. $N_1(x)$ in the patch between element-1 and element-2 shown by yellow colour is defined by equation (6.5), whereas $N_1(y)$ in the patch between element-1 and element-6 shown by green colour is defined by equation (6.6). The patch between elements 1, 2, 6 and 7 shown by blue colour is influenced by both $N_1(x)$ and $N_1(y)$, so both are used in this patch. Figure 6.2 shows the arrangement of element numbers in the mesh.

With $W = N_j\ G_j^q$, the resulting GFEM discretization of the weak formulation (3.14) then reads:

Find u^{n+1} of the form (6.1) such that $u^0 = u_0$ and for all q and j

$$\int_\Omega (\nabla(N_j\ G_j^q)\cdot\nabla u^{n+1} + kN_j\ G_j^q\ u^{n+1})d\Omega = \int_\Omega N_j\ G_j^q\ F^{n+1}d\Omega + \int_\Gamma N_j\ G_j^q\ g^{n+1}\ d\Gamma\ . \quad (6.7)$$

From the numerical solution u^{n+1} at time t_{n+1} we define, by piecewise constant, resp. piecewise linear interpolation, the numerical solutions for all positive t:

$$u(t,\mathbf{x}) = \frac{t-t_n}{t_{n+1}-t_n}\ u^{n+1}(\mathbf{x}) + \frac{t_{n+1}-t}{t_{n+1}-t_n}\ u^n(\mathbf{x})\ ,$$
$$\hat{u}(t,\mathbf{x}) = u(t_{n+1},\mathbf{x}),\ \hat{f}(t,\mathbf{x}) = f(t_{n+1},\mathbf{x}) \text{ for } t \in]t_n, t_{n+1}]\ .$$

In this notation, from Chapter 5 we obtain the following *a-posteriori* estimate for the error of the GFEM solution. Even though here we use a modified GFEM, the proof of the estimate follows verbatim.

Theorem 2 *Let U be the solution of the exact weak formulation* (3.12) *and u the solution of the GFEM discretization* (6.7)*. Then there exists a constant $c > 0$, such that*

$$\int_\Omega |U(T,\boldsymbol{x}) - u(T,\boldsymbol{x})|^2 d\Omega + \lambda \int_0^T \int_\Omega |\nabla(U-\hat{u})|^2 d\Omega\ dt \le c\{\ \eta_1^2 + \eta_2^2 + \eta_3^2 + \eta_4^2 + \eta_5^2 + \eta_6^2\ \}\ , \quad (6.8)$$

where $\eta_1^2, ... + \eta_6^2$ are defined by (5.4)–(5.9).

The left hand side of expression (6.8) measures the size of the actual error between the GFEM and exact solutions. In Chapter 5, it is shown that the error indicators on the right hand side, η_1^2 to η_6^2, provide a reliable estimate for the unknown error, and we use them here to steer an adaptive algorithm.

Error indicators such as from the *a-posteriori* error estimate Theorem 2 lead to an adaptive algorithm, based on the following four steps

$$\textbf{SOLVE} \longrightarrow \textbf{ESTIMATE} \longrightarrow \textbf{MARK} \longrightarrow \textbf{REFINE} \ .$$

SOLVE The problem is solved at the beginning of the algorithm and at the start of every new iteration.

ESTIMATE Based on the solution obtained in the first step, the error indicator η is estimated in each element and then accumulated for the whole domain.

MARK The elements with highest values of η are marked for refinement.

REFINE Elements marked in the previous step are refined with further enrichment functions.

We implement this strategy here in the context of q–refinements for adaptivity in space. Neglecting the error from the approximation of initial and boundary conditions and data, we use the error indicator $\eta^2(\square) = \eta_2^2(\square) + \eta_4^2(\square)$, where

$$\eta_2^2(\square) = \int_0^T \left\| \hat{f} - \partial_t u + \lambda \Delta \hat{u} \right\|_{L^2(\square)}^2 dt \ ,$$
$$\eta_4^2(\square) = \lambda \int_0^T \|\nabla(u - \hat{u})\|_{L^2(\square)}^2 dt \ .$$

Note that η_5^2, which measures the numerical heat flux across the element edges is very small and neglected in the computations.

Adaptive Algorithm for q–refinements:

Input: Spatial mesh $\mathscr{T}$ with M as the total number of elements ($\square$) and $L \leq M$ as the enriched elements, enrichments $\mathscr{Q} = \{q = 1 \text{ in every } \square \in \mathscr{T}\}$, refinement parameter

$\theta \in (0,1)$, tolerance $\epsilon > 0$, maximum condition number $\mathscr{K}$, data f.

1. Solve GFEM equation (3.14) on $\mathscr{T}$ with enrichment $\mathscr{Q}$.
2. Compute the error indicators $\eta(\square)$ for every $\square \in \mathscr{T}$.
3. Stop if $\sum_{i=1}^{M} \eta^2(\square_i) < \epsilon^2$ or condition number $\kappa \geq \mathscr{K}$.
4. Order $\square_j$ such that $\eta(\square_j) \leq \eta(\square_i)$ if $i \leq j$.
5. Mark $\square_1, \ldots, \square_L \in \mathscr{T}$ until $\sum_{j=1}^{L} \eta^2(\square_j) \geq \theta^2 \times \sum_{j=1}^{M} \eta^2(\square_j)$.
6. Add the enrichment functions G_j^q in $\square_1, \ldots, \square_L$ to obtain a new, local enrichment $\mathscr{Q}$.
7. Go to 1.

Output: Approximation of u.

The new shape functions N_j are a crucial ingredient in this method: One main advantage of generalized finite element methods is their use of very coarse meshes. Shape functions like N_j which are associated to a particular mesh element $\square$ allow localised modification of the enrichment in a small neighbourhood of $\square$. Standard hat functions would spread this enrichment over all $\square$ which contain the associated node.

As in Chapter 5, we implement the error indicators approximately: $\widetilde{\eta}_2^2(\square) = \sum_{n=0}^{N_t} \widetilde{\eta}_2^2(n, \square)$, where

$$\widetilde{\eta}_2^2(n, \square) \simeq \delta t \int_{\square} \left(f^{n+1} - \frac{u^{n+1} - u^n}{\delta t} + \lambda \left(\frac{\partial^2 u^{n+1}}{\partial x^2} + \frac{\partial^2 u^{n+1}}{\partial y^2} \right) \right)^2 d\Omega \ .$$

The integral is evaluated using a 2-dimensional composite high order Simpson's rule. Typically, 21×21 integration points are used.

Similarly $\eta_4^2(\square) = \sum_n \eta_4^2(n, \square)$, with

$$\eta_4^2(n, \square) = \frac{\lambda \delta T}{3} \left(\int_{\square} \left(\frac{\partial u_i^{n+1}}{\partial x} - \frac{\partial u_i^n}{\partial x} \right)^2 d\Omega + \int_{\square} \left(\frac{\partial u_i^{n+1}}{\partial y} - \frac{\partial u_i^n}{\partial y} \right)^2 d\Omega \right) \ .$$

6.3 Numerical experiments

This section investigates the relevance and sharpness of the *a-posteriori* error estimate in Theorem 2 through numerical experiments. We find numerical approximations to the heat transfer problem defined by expressions (3.1) - (3.3) by computing the solution to the GFEM discretization (6.1).

For the experiments, we choose a square mesh with piecewise linear shape functions. All integrals over Ω are evaluated numerically, using a high order Gauss–Legendre quadrature, and we typically used 22 integration points in each direction. We neglect the error estimators η_1 and η_3, which arise from the approximation of the initial condition and the source terms. Initial condition is taken as zero and the source term is applied exactly. In the examples below, also the contribution of η_6, the violation of the boundary condition, will be negligible. This is because both the numerical and exact solutions themselves are already very small at the boundary. Also η_5, the jump of solution across element boundaries is very small.

To compare the results of uniform enrichments and adaptive $q-$enrichments for different model problems, we calculate the error indicator η in each element as well as in the whole domain.

The error indicator for an individual element is calculated as

$$\eta(\square_i) = \sqrt{(\eta_2^2 + \eta_4^2)_{\square_i}} \ , \qquad i = 1, 2, ...K \tag{6.9}$$

and for the whole domain, it is calculated as

$$\eta(\mathscr{T}) = \sqrt{\sum(\eta_2^2 + \eta_4^2)_{\square_i}} \ , \qquad i = 1, 2, ...K \tag{6.10}$$

Here K represents the total elements in the spatial mesh. Note that in the previous chapter we calculated the relative values of the error indicators but here we calculate their absolute values. In expression (5.12) the value of η was divided by the exact

solution and its derivatives. For problems with no known exact solution, the same was divided by values of a very fine meshed FEM solution. For a problem with known exact solution, the term in the denominator of (5.12) can be easily calculated during the solution process. But for other general problems, calculating the denominator with fine mesh FEM solution will reduce the actual benefit of the adaptivity. To gain maximum benefit from the proposed adaptivity algorithm, the need for fine mesh FEM solution is eliminated in the current computations. It is worthwhile to mention that calculating the relative or absolute values of (6.9) and (6.10) lead to the same refinements. To show the working of the proposed adaptive algorithm, the considered model problems are first solved with uniform enrichments in the whole domain. The adaptive algorithm is then used to selectively add enrichment functions in elements with relatively higher values of η.

6.3.1 Example problem 1

The first experiment compares the error in the solution and the corresponding error indicator for a problem with a given exact solution. The Example problem 1 considered in the previous chapter is studied again here for adaptive refinement. The problem is considered on a square domain $\Omega = \{(x, y) \in \mathbb{R}^2 : 0 \leq x, y \leq 2\}$ with the exact solution given by (5.13). The parameters λ, h, and the data f, g are also taken to be the same.

6.3.1.1 Uniform q–enrichments

The considered problem is first solved with uniform number of enrichment functions in every element. For a fixed coarse spatial mesh of 25 elements, we start with zero enrichment in the whole domain and then increase the number of enrichment functions $Q = 1, \ldots 5$. With zero enrichment function we get the standard FEM solution. We then introduce enrichments in the finite element space and assess how the errors and the condition number κ change with the introduction of enrichment functions. With every added enrichment function, we calculate the error indicator in individual

Table 6.1 Variation of L_2 error and $\eta(\mathscr{T})$ along with condition number for uniform numbers of Q with $\Delta t = 0.01$s and at $t = 1.0$s for Example problem 1.

Q	DOFs	$\varepsilon\%$	$\eta(\mathscr{T})$	$\kappa(\mathscr{T})$
0	25	31.06	1.79E-01	1.63E+03
1	100	10.09	8.76E-02	1.38E+06
2	175	1.51	3.19E-02	1.82E+09
3	250	0.68	1.67E-02	3.39E+12
4	325	0.64	1.57E-02	4.24E+15
5	400	0.59	1.89E-02	6.57E+15

Table 6.2 Variation of L_2 error and $\eta(\mathscr{T})$ along with condition number for uniform numbers of Q with $\Delta t = 0.001$s and at $t = 1.0$s for Example problem 1.

Q	DoFs	$\varepsilon\%$	$\eta(\mathscr{T})$	$\kappa(\mathscr{T})$
0	25	30.85	1.79E-01	1.63E+03
1	100	10.00	8.75E-02	1.38E+06
2	175	1.47	3.18E-02	1.82E+09
3	250	0.62	1.65E-02	3.39E+12
4	325	0.57	1.57E-02	4.24E+15
5	400	11.33	4.42E-01	7.40E+15

Table 6.3 Variation of L_2 error and $\eta(\mathscr{T})$ along with condition number for uniform number of Q with $\Delta t = 0.0001$s and at $t = 1.0$s for Example problem 1.

Q	DoFs	$\varepsilon\%$	$\eta(\mathscr{T})$	$\kappa(\mathscr{T})$
0	25	30.83	1.79E-01	1.63E+03
1	100	9.99	8.75E-02	1.38E+06
2	175	1.48	3.18E-02	1.82E+09
3	250	0.62	1.65E-02	3.39E+12
4	325	0.59	1.58E-02	4.24E+15
5	400	-	-	-

elements and their cumulative value in the whole domain, denoted by $\eta(\square)$ and $\eta(\mathscr{T})$ respectively. Similarly $\kappa(\square)$ and $\kappa(\mathscr{T})$ are calculated. With the exact solution given by (5.13), we also calculate the L_2 errors and show how these vary with increasing

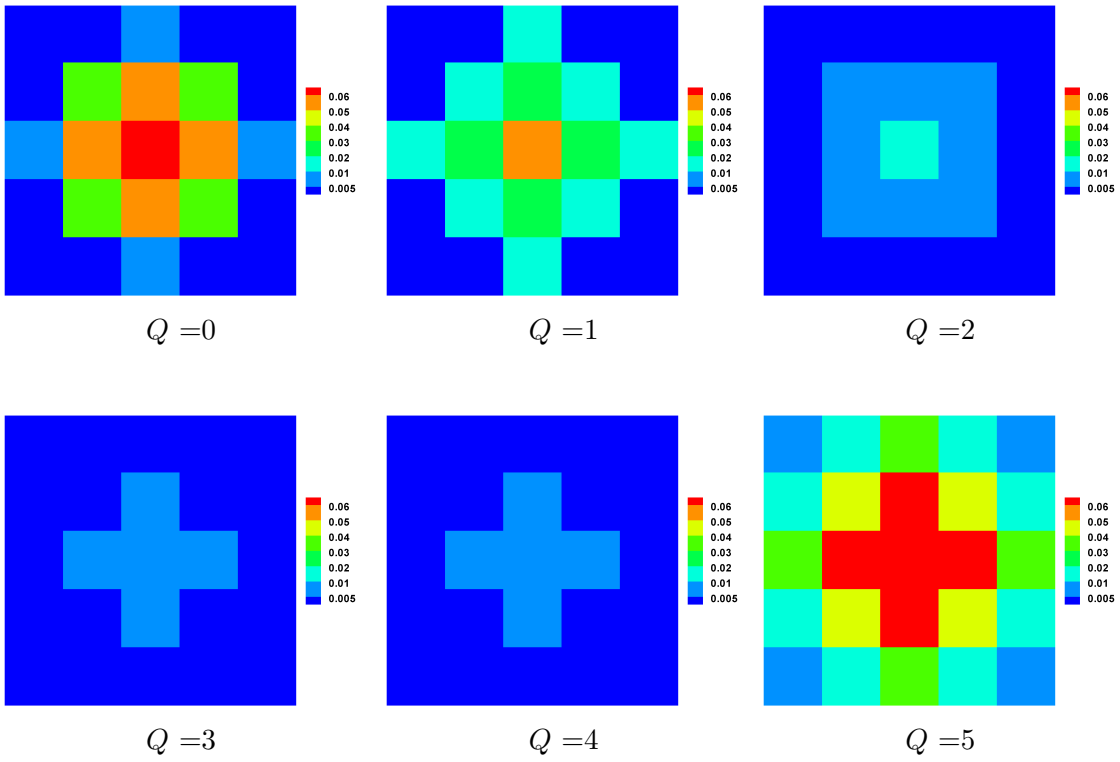

Fig. 6.3 Distribution of $\eta(\square)$ in each element for uniform enrichments with $\Delta t = 0.01$s and at $t = 1.0$s for Example problem 1.

numbers of enrichment functions. To test the quality of our error estimates in Theorem 2, we use three different values of time step sizes $\Delta t = 0.01,\ 0.001$ and 0.0001s. Table 6.1 shows the L_2 error and the error indicator $\eta(\mathscr{T})$ along with the condition number $\kappa(\mathscr{T})$ for increasing numbers of enrichment functions using $\Delta t = 0.01$s.

Table 6.1 shows that with the introduction of first enrichment function, the $\eta(\mathscr{T})$ reduces from $1.79E-01$ to $8.76E-02$ and the L_2 error decreases from 31.06% to 10.09%. The additional enrichment functions improves these results further. With 4 enrichment functions ($Q = 4$), the $\eta(\mathscr{T})$ and the L_2 error reduce to $1.57E-02$ and 0.64%, respectively. With $Q = 5$, the L_2 error further reduces to 0.59%, but the $\eta(\mathscr{T})$ starts increasing. This is due to the very high condition number $(6.57E+15)$. With $Q = 6$ (results not presented) the condition number becomes too high $(2.31E+17)$, and we do not obtain any reliable results. Table 6.2 and Table 6.3 present similar sets of results for $\Delta t = 0.001$s and $\Delta t = 0.0001$s, respectively. In Figure 6.3 is shown the

variation of the $\eta(\square)$ in each element with increasing number of Q. The maximum value of $\eta(\square)$ is observed in the central element.

6.3.1.2 Adaptive q–enrichments

The proposed adaptive algorithm is used to add enrichment functions adaptively rather than using uniform enrichments. As mentioned in the adaptive algorithm, we calculate $\eta(\square)$ and add more enrichment functions only in elements where $\eta(\square)$ is high. The adaptive procedure is explained below in detail for the first iteration. The subsequent iterations are carried out in the same manner.

1. As a first iteration, we start with the standard FEM solution, i.e., zero enrichment in each element.

2. We estimate the $\eta(\square)$ in each element and mark the elements that have relatively higher values. Figure 6.2 shows how the elements are numbered. Table 6.4 shows the values of $\eta(\square)$ in each element for the first iteration.

3. The third step is skipped for the first iteration. In the subsequent steps the solution will be checked for $\sum_{i=1}^{M} \eta^2(\square_i) < \epsilon^2$ or $\kappa \geq \mathscr{K}$.

4. In step 4, the elements ar ordered in the descending order of magnitude of $\eta(\square)$. Table 6.4 also serves this purpose. The first column shows the elements in their natural sorting order. The estimated $\eta(\square)$ for each element is mentioned in the second column. From maximum to minimum, the $\eta(\square)$ are organized in the third column. The corresponding elements are ordered in column 4. The last column shows the progressive sum of $\eta(\square)$ values.

5. After sorting, the elements with larger $\eta(\square)$ values are marked for further refinement. From the third column of Table 6.4, it is clear that element 13 has the highest $\eta(\square)$ value of $1.20E-01$, and elements 8, 12, 14 and 18 having the second highest values of $5.79E-02$ each. It is noted that these five elements constitute more than 60% of the total value of $\eta(\mathscr{T})$. Adding the next four

Table 6.4 Details of $\eta(\square)$ in each element along with their progressive sums for iteration-1

Elem No.	$\eta(\square)$	$\eta(\square)$ (Desc order)	Elem No. (Desc order)	Progressive sum of η
1	7.08E-04	1.20E-01	13	1.20E-01
2	2.88E-03	5.79E-02	8	1.78E-01
3	5.56E-03	5.79E-02	12	2.36E-01
4	2.88E-03	5.79E-02	14	2.94E-01
5	7.08E-04	5.79E-02	18	3.52E-01
6	2.88E-03	3.18E-02	7	3.84E-01
7	3.18E-02	3.18E-02	9	4.15E-01
8	5.79E-02	3.18E-02	17	4.47E-01
9	3.18E-02	3.18E-02	19	4.79E-01
10	2.88E-03	5.56E-03	3	4.85E-01
11	5.56E-03	5.56E-03	11	4.90E-01
12	5.79E-02	5.56E-03	15	4.96E-01
13	1.20E-01	5.56E-03	23	5.01E-01
14	5.79E-02	2.88E-03	2	5.04E-01
15	5.56E-03	2.88E-03	4	5.07E-01
16	2.88E-03	2.88E-03	6	5.10E-01
17	3.18E-02	2.88E-03	10	5.13E-01
18	5.79E-02	2.88E-03	16	5.16E-01
19	3.18E-02	2.88E-03	20	5.18E-01
20	2.88E-03	2.88E-03	22	5.21E-01
21	7.08E-04	2.88E-03	24	5.24E-01
22	2.88E-03	7.08E-04	1	5.25E-01
23	5.56E-03	7.08E-04	5	5.26E-01
24	2.88E-03	7.08E-04	21	5.26E-01
25	7.08E-04	7.08E-04	25	5.27E-01

elements, 7, 9, 17, 19, which have the third highest values, the cumulative $\eta(\square)$ value for these 9 elements sums up to more than 90% of the total value for the whole domain. This corresponds to $\theta^2 = 0.9$ in the adaptive algorithm, i.e.

$$\sum \eta(\square_i) > 0.9 \times \eta(\mathscr{T}) \ , \qquad i = 7, 8, 9, 12, 13, 14, 17, 18, 19$$

Now rather than adding enrichments everywhere we target these nine elements only. The selection of θ^2 value depends on the required level of accuracy. It

Table 6.5 Variation of L_2 error and $\eta(\mathscr{T})$ along with condition number for adaptive $q-$enrichments with $\Delta t = 0.01$s and at $t = 1.0$s for Example problem 1.

Iteration No	DOFs	$\varepsilon\%$	$\eta(\mathscr{T})$	$\kappa(\mathscr{T})$
1	25	31.06	1.79E-01	1.63E+03
2	52	9.96	8.82E-02	1.35E+06
3	79	2.13	3.55E-02	1.80E+09
4	106	0.70	1.72E-02	3.35E+12
5	133	0.92	3.39E-02	4.47E+15

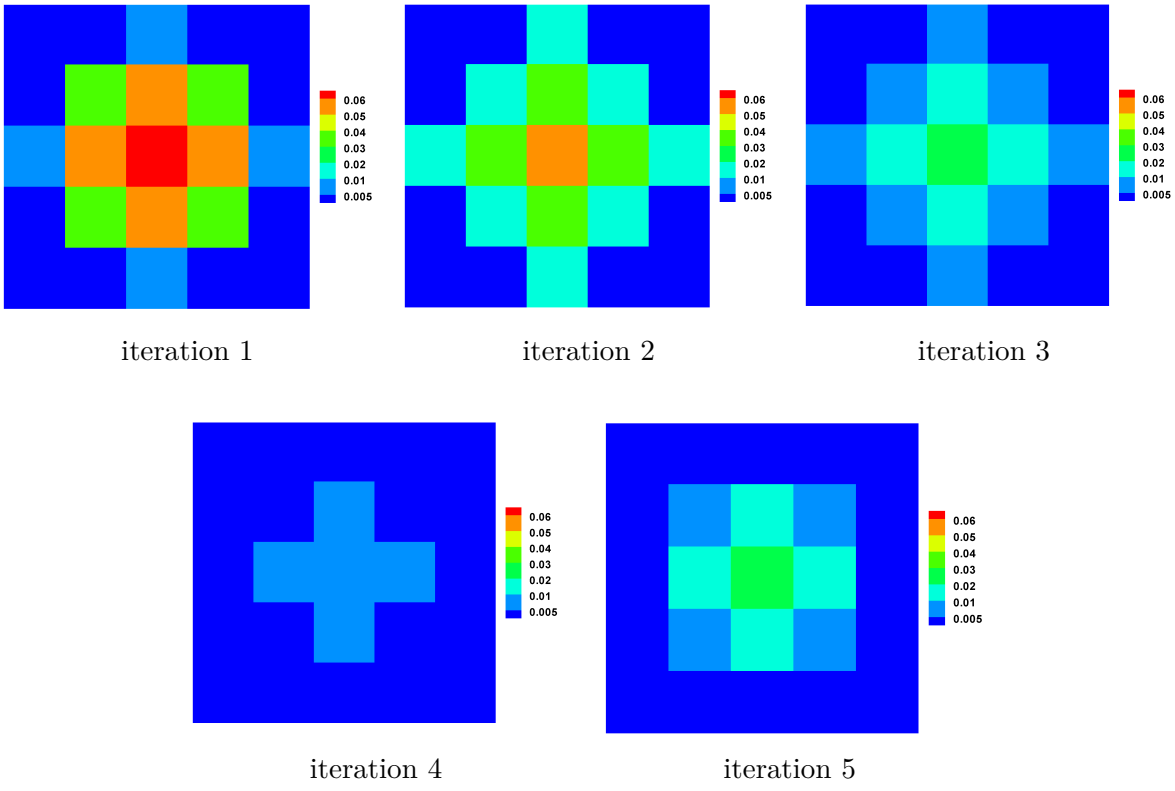

Fig. 6.4 Distribution of η in each element with adaptive q–enrichments for Example problem 1.

is worthwhile to mention that the cumulative value of η reduces with every iteration; depending on the requirements, the θ^2 value may also be reduced for the subsequent iterations. Again the selection of θ^2 will depend on the required accuracy.

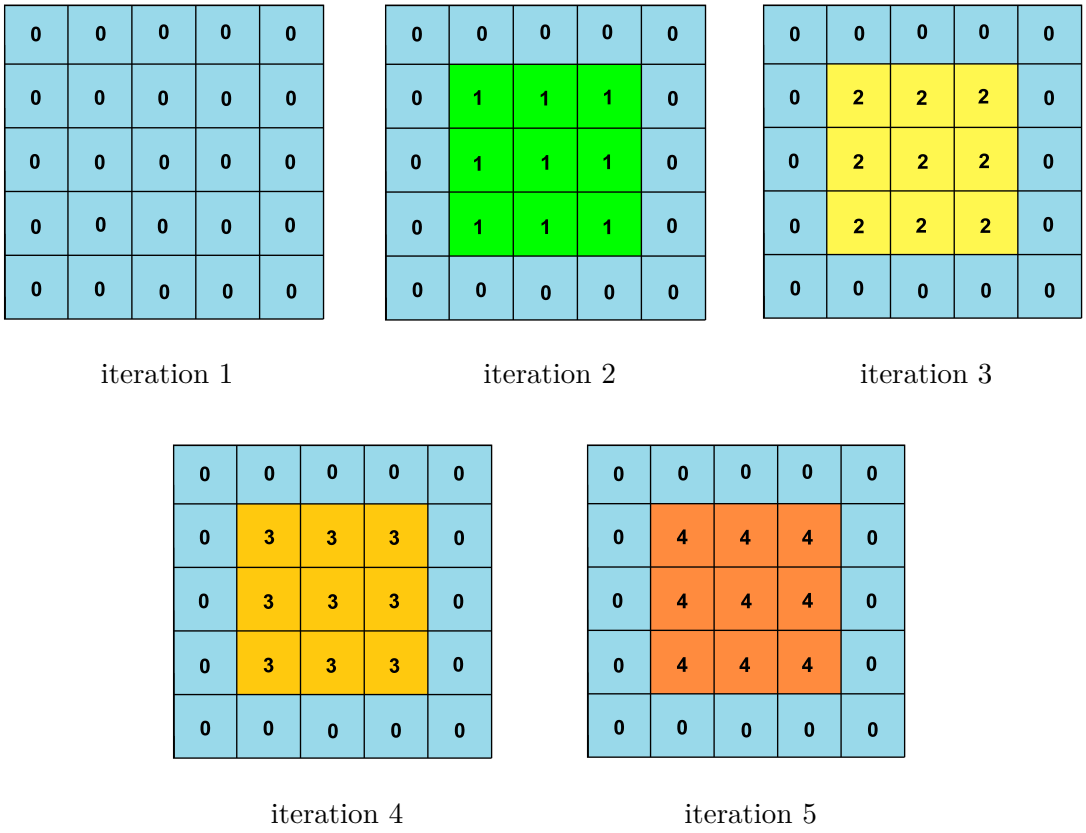

Fig. 6.5 Details of enrichment functions used in each element for adaptive q–enrichments for Example problem 1.

6. In step 6, one enrichment is added in the selected nine elements.

7. The process is repeated for next iteration.

For the second iteration, the values of $\eta(\square)$ and L_2 error are calculated again after the addition of one enrichment function in the selected nine elements. Also, the effect on condition number is assessed with every enrichment. Again the elements are organized in the descending order of magnitude of $\eta(\square)$ and elements with higher values are marked for further refinement as in the previous iteration. This process is repeated until we get the required accuracy. Table 6.5 shows the results of these iterations. Figure 6.4 shows the variation of $\eta(\square)$ for each iteration. The maximum $\eta(\square)$ is seen to be in the centre element followed by four neighbouring elements. The values being maximum in the first iteration and decrease subsequently when more

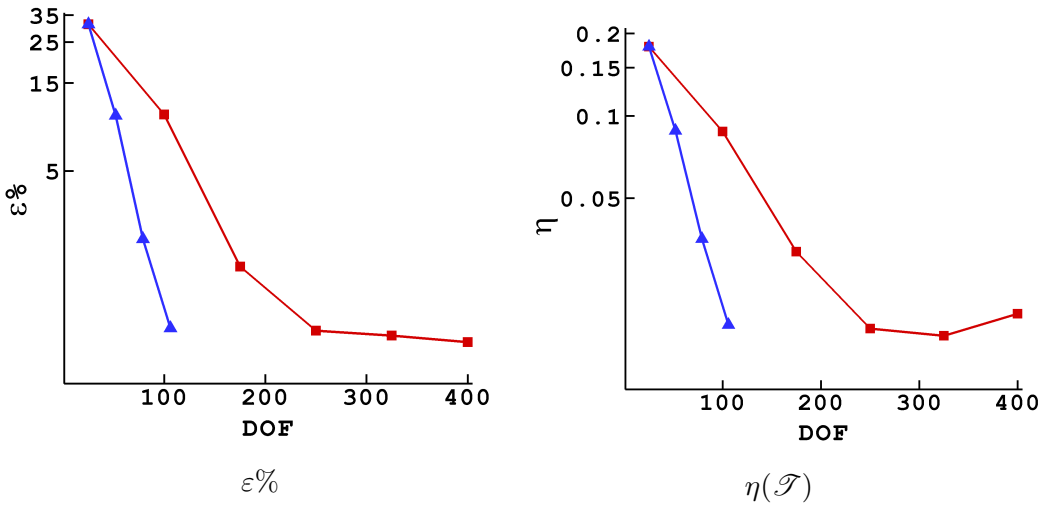

$\varepsilon\%$ $\eta(\mathscr{T})$

Fig. 6.6 Comparison of L_2 error and $\eta(\mathscr{T})$ for uniform enrichments (■) and adaptive q–enrichments (▲) for Example problem 1.

enrichments are added. The results decrease upto iteration 4, and with the addition of another enrichment function in iteration 5, the η starts increasing. This violates the criteria of $\epsilon > 0$, so we stop the iterations. The best results being obtained from iteration 4. Figure 6.5 gives details of the number of enrichment functions used in every element for each iteration.

To compare the results of adaptive q–enrichments with those obtained with uniform enrichments, in Figure 6.6 is shown the L_2 error and $\eta(\mathscr{T})$ for both the cases against total DOFs. It is clear from these figures that in case of adaptive refinement, we get comparable results with less DOFs. A reduction of 60% in DOFs is observed which proves the usefulness of the proposed adaptive algorithm.

6.3.1.3 Effect of the Condition Number (κ)

The condition number is one of the important parameters and should be monitored closely as it has adverse effect on the accuracy of the solution. The results discussed in the previous sections show that the addition of enrichment functions decreases the L_2 error and the error indicator η. But the results improve only up to a certain limit, after which they start to deteriorate because of the ill-conditioning of the system matrix.

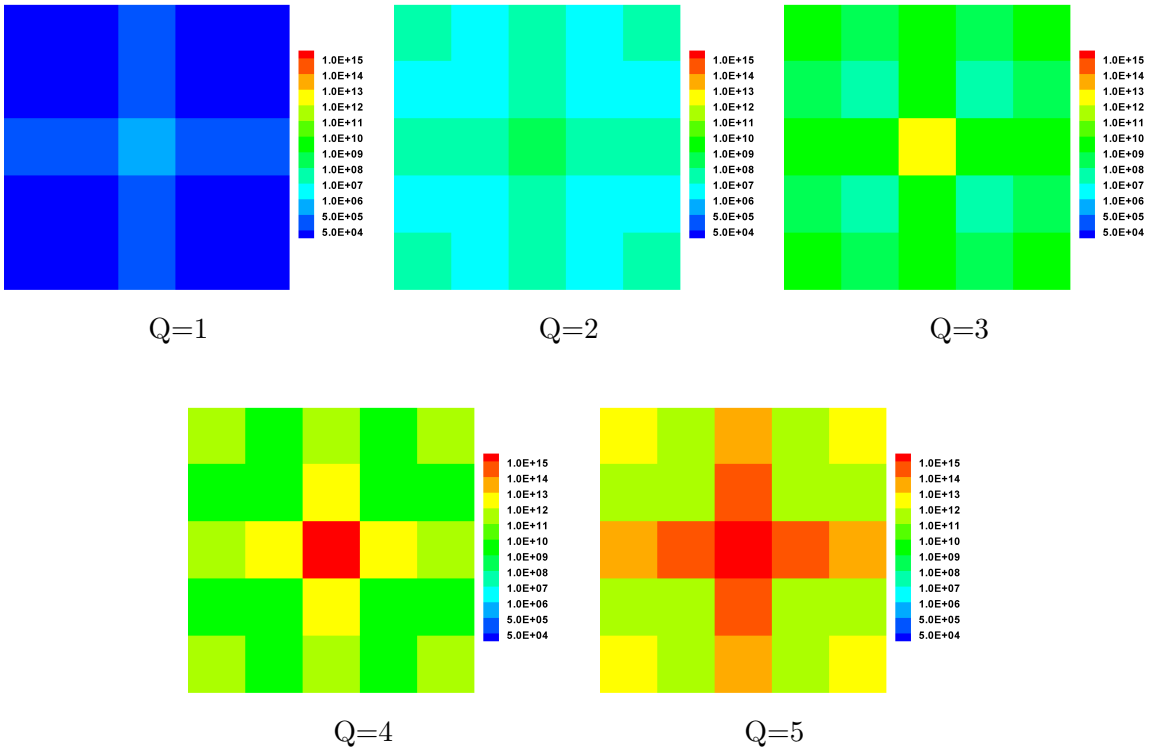

Fig. 6.7 Condition number in each element with uniform enrichments for Example problem 1.

For the uniform enrichment case, we see from Table 6.1 that the results improve up to $Q = 4$. With the addition of fifth enrichment function, the L_2 error still decreases by a small amount but the η starts increasing due to very high condition number. With $Q = 6$ (results not presented), the condition number becomes too high to get any reliable results. Figure 6.7 shows the variation of condition number in each element with increasing number of enrichment functions.

Figure 6.8 shows the variation of the condition number for the adaptive refinements. The maximum condition number is observed in the centre element followed by the adjoining four elements. Table 6.5 shows that from iteration 1 to 4 the results improve very quickly. For iteration 4 the total condition number becomes $3.35E + 12$. In iteration 5, the condition number increases to $4.47E + 15$ and the L_2 error and the error indicator η start to deteriorate.

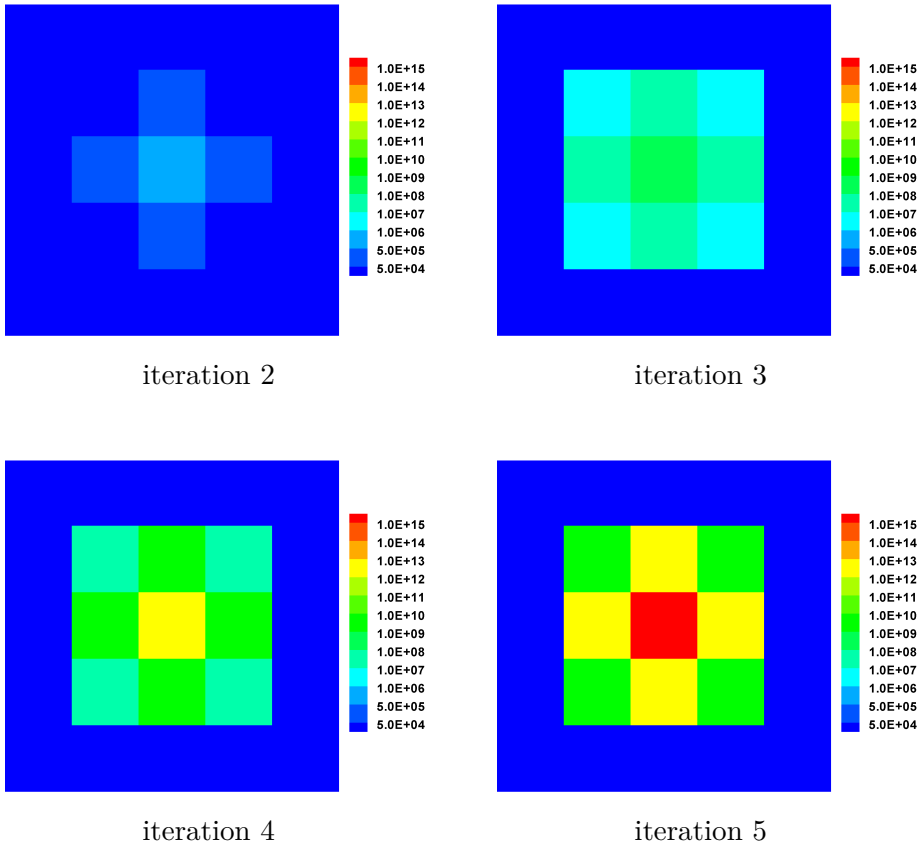

iteration 2 iteration 3

iteration 4 iteration 5

Fig. 6.8 Condition number in each element with adaptive q–enrichments for Example problem .1

6.3.2 Example problem 2(a)

The first example considered a problem with a known exact solution. In the second example, a general problem with no known solution is considered. For this model problem, we consider a square domain $\Omega = \{(x, y) \in \mathbb{R}^2 : 0 \leq x, y \leq 3.6\}$ with the same mesh density as in Example problem 1.

In this example problem, we consider a heat source in the centre of the domain with a constant heat source $f = 200°\text{C/s}$ in the central part i.e., $x, y \in [1.6, 2.0]$. The source decreases linearly to $f = 0$ when either x or y equal to 1.2 or 2.4. The convection heat transfer coefficient h is taken as zero on the boundaries while the heat diffusion coefficient in the domain is taken as $\lambda = 0.01\text{kgm}/°\text{Cs}^2$.

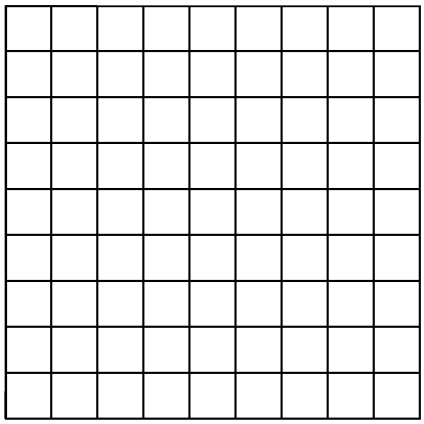

Fig. 6.9 Mesh used for Example problem 2(a).

We take the initial temperature u_0 to be zero, like the heat source at the boundary g. With $\Delta t = 0.001$s, the total solution time is $t = 0.1$s. The heat source f is kept on for the first half i.e., from $t = 0$ to $t = 0.05$s and then turned off for rest of the computation time. The error indicator in each element $\eta(\square)$ is calculated as defined by (6.9) and the cumulative value $\eta(\mathscr{T})$ for the whole domain as given by (6.10). The problem is solved on a fix coarse mesh of 81 elements, shown in Figure 6.9.

6.3.2.1 Uniform q–enrichments

To start with, the problem is solved with zero enrichment function. We then introduce enrichments in the FEM solution space and evaluate the results by varying the number of enrichment functions $Q = 1, 2, ..5$. The values of $\eta(\square)$ and the cumulative value for the domain $\eta(\mathscr{T})$ are calculated with every refinement. Figure 6.10 shows the variation of $\eta(\mathscr{T})$ with Q. The figure depicts that $\eta(\mathscr{T})$ decreases as Q is increased. The decrease is observed up to 3 enrichment functions, and with further enrichments, the $\eta(\mathscr{T})$ starts increasing. With $Q = 4$ it increases by a small amount and grows further with $Q = 5$. Also in Figure 6.11 is shown the spread of $\eta(\square)$ in the domain with every refinement. The maximum value is observed in the central element which decreases to minimum at the boundaries. The values blow up with $Q = 5$ as depicted in Figure 6.11(f). This behaviour is attributed to the rise of condition number as Q is

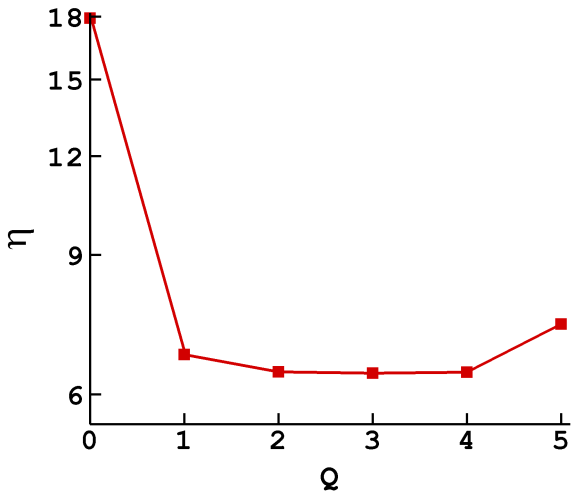

Fig. 6.10 Variation of $\eta(\mathscr{T})$ with uniform Q for Example problem 2(a).

increased.

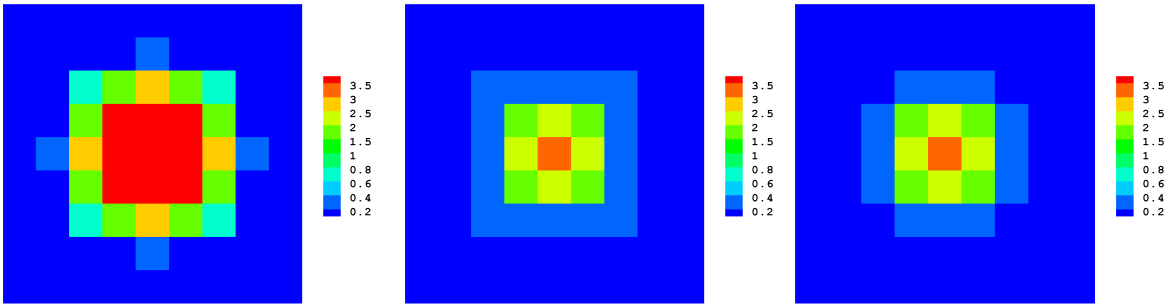

(a) Q =0 (b) Q =1 (c) Q =2

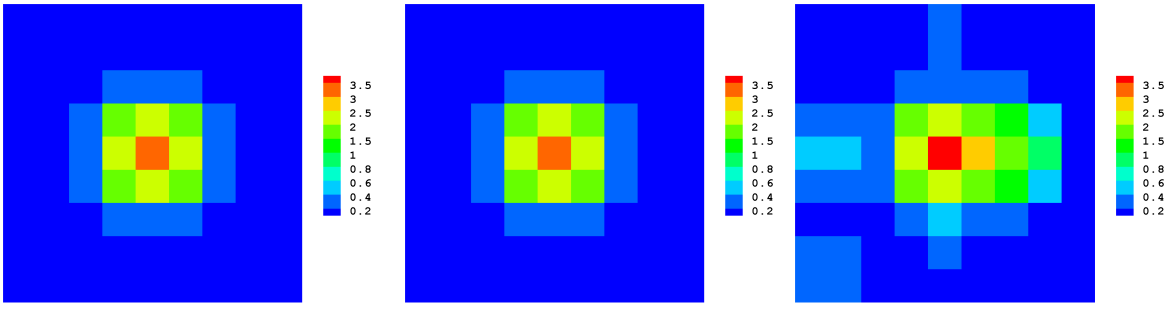

(d) Q =3 (e) Q =4 (f) Q =5

Fig. 6.11 Distribution of $\eta(\square)$ in each element with uniform enrichments for Example problem 2(a).

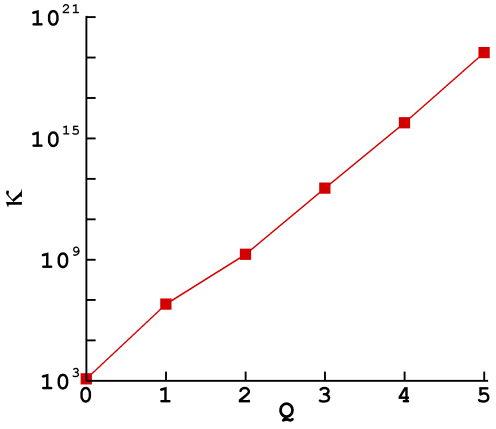

Fig. 6.12 Variation of $\kappa(\mathscr{T})$ with uniform Q for Example problem 2(a).

6.3.2.2 Adaptive q–enrichments

For adaptive q–enrichments, we start with the standard FEM solution. Following the adaptive algorithm, enrichment functions are added only in elements with higher values of the error indicator. For each iteration, the error indicator in each element,$\eta(\square)$, and the cumulative value for the domain $\eta(\mathscr{T})$ is calculated. Also, the condition number in each element $\kappa(\square)$ and the overall value for the domain $\kappa(\mathscr{T})$ is calculated. Figure 6.13 shows the variation of $\eta(\mathscr{T})$ and the condition number $\kappa(\mathscr{T})$ with each iteration. The error indicator $\eta(\mathscr{T})$ decreases with each refinement. A rapid decrease is observed with the second and third refinements. The fourth and fifth iterations also decrease the error indicator but only by a small amount. The distribution of error indicator in each element, $\eta(\square)$, is shown in Figure 6.14. A visible decrease in error indicator in each element is also depicted in Figure 6.14 for iteration 2 and 3. For iterations 4 and 5, there is only a slight improvement in the values of $\eta(\square)$. The condition number for the fifth iteration rises to the order of $E + 15$ as shown in Figure 6.13(b).

To compare the results of uniform enrichments and adaptive q–enrichments, in Figure 6.15 is shown the comparison of $\eta(\mathscr{T})$ against total DOFs for both cases. It is clear from the figure that with the proposed adaptive algorithm, we get almost similar results with less DOFs. For a comparable accuracy, a reduction of more than 70% in

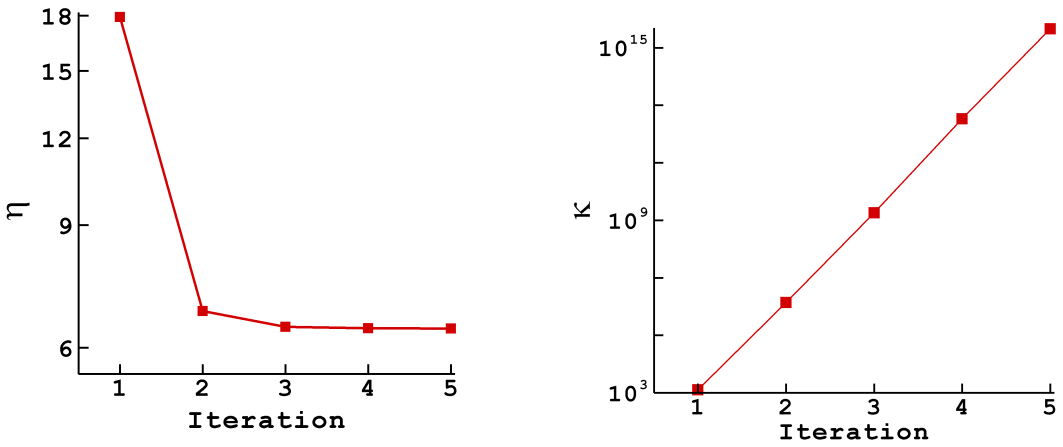

(a) $\eta(\mathscr{T})$ (b) $\kappa(\mathscr{T})$

Fig. 6.13 Variation of $\eta(\mathscr{T})$ and $\kappa(\mathscr{T})$ for each iteration with adaptive $q-$enrichments for Example problem 2(a).

DOFs is noted with the adaptive $q-$refinement as compared to the uniform refinement. The enrichment functions used in each iteration for the adaptive refinement is shown in Figure 6.16. For iteration 2, one enrichment is added in the 13 central elements. The cumulative value of $\eta(\square)$ for these 13 elements is more than 70% of the total value for the whole domain. This corresponds to $\theta^2 = 0.7$ in the adaptive algorithm.

6.3.3 Example problem 2(b)

The proposed adaptive procedure is more beneficial for the cases where we deal with large domains and concentrated heat sources. If we consider the same heat source, but with a larger domain, the reduction in the total DOFs will be even better. To show this, In the current example, we consider the same heat source as in Example problem 2 but with a larger domain $\Omega = \{(x, y) \in \mathbb{R}^2 : 0 \leq x, y \leq 4.4\}$ with 11 elements in each direction. Again the mesh density is kept same as in the previous example. Figure 6.17 shows the mesh used for computations.

The heat source is defined as $f = 200°\text{C/s}$ which is constant in the central part i.e., $x, y \in [2.0, 2.4]$ and decreases linearly to $f = 0$ on the external boundaries of the source, where either x or y is one of $\in \{1.6, 2.8\}$. The convection heat transfer

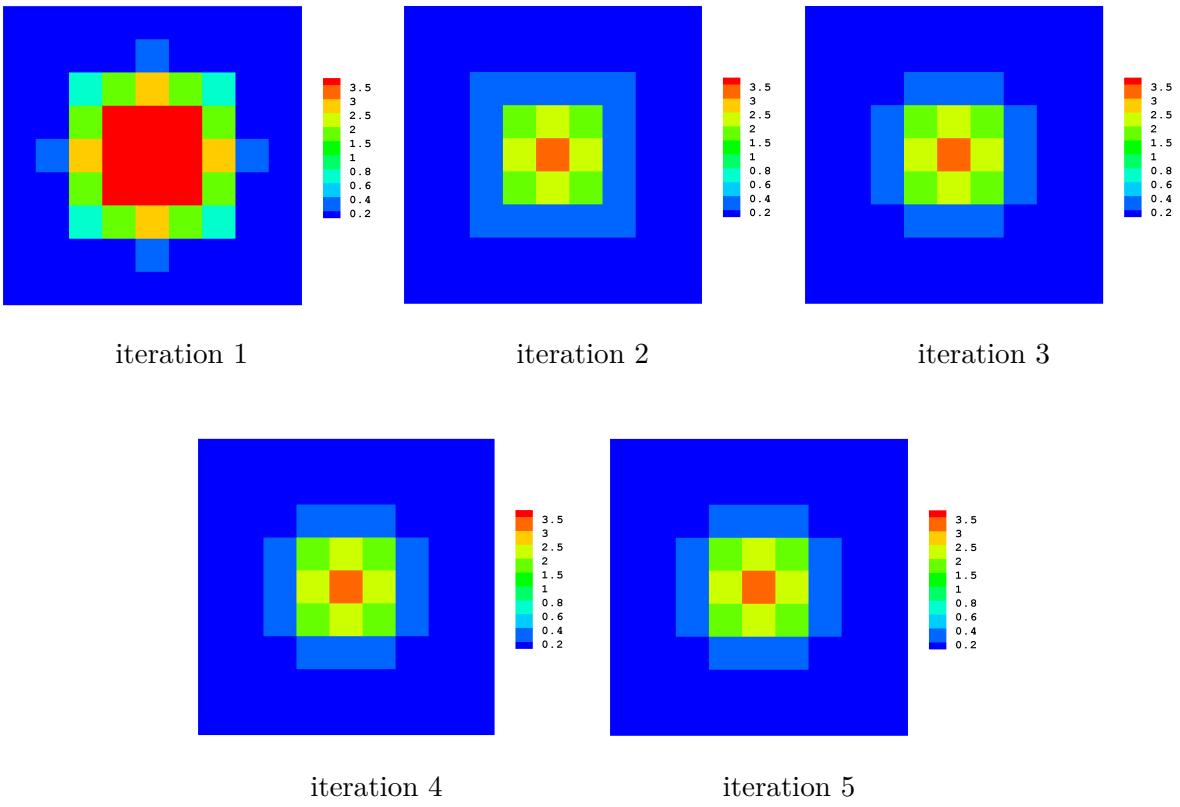

Fig. 6.14 Distribution of $\eta(\square)$ with adaptive q–enrichments for Example problem 2(a).

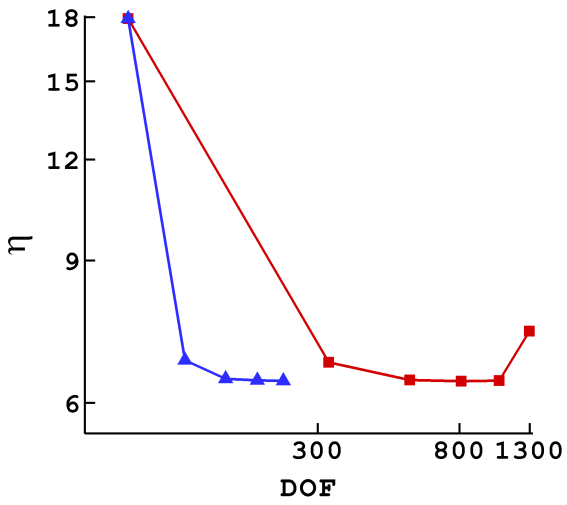

Fig. 6.15 Comparison of $\eta(\mathscr{T})$ for uniform enrichments (■) and adaptive q–enrichments (▲) for Example problem 2(a).

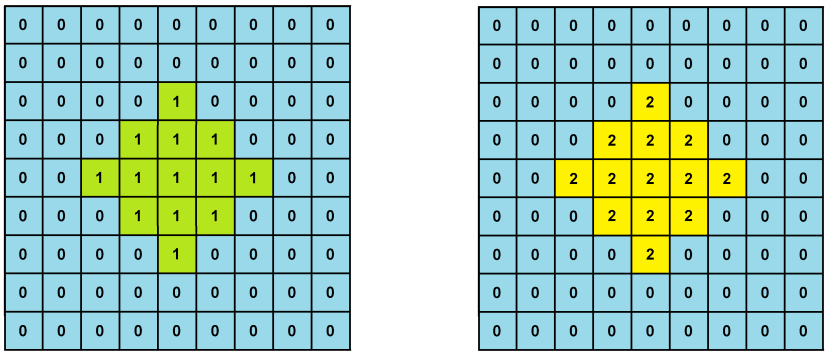

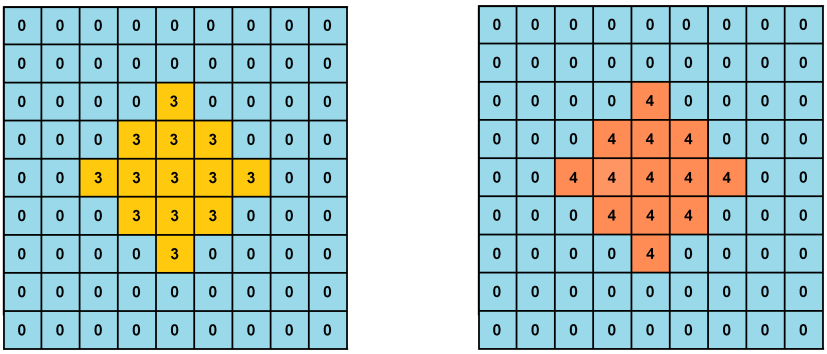

Fig. 6.16 Enrichment functions used in each element with adaptive q–enrichments for Example problem 2(a).

coefficient h, the thermal conductivity λ, the initial temperature u_0 and the heat source g at the boundary are the same as in the previous example. The total solution time is also kept the same i.e. $t = 0.1$s, with the heat source f kept on only for the first half of the computation time.

6.3.3.1 Uniform q–enrichments

Starting with the standard FEM solution, the error indicator η and the condition number κ are calculated with zero enrichment function. The solution space is then enriched with multiple enrichment functions, and with each refinement, the values of η and κ are calculated. Figure 6.18 shows the variation of $\eta(\mathscr{T})$ and $\kappa(\mathscr{T})$ with

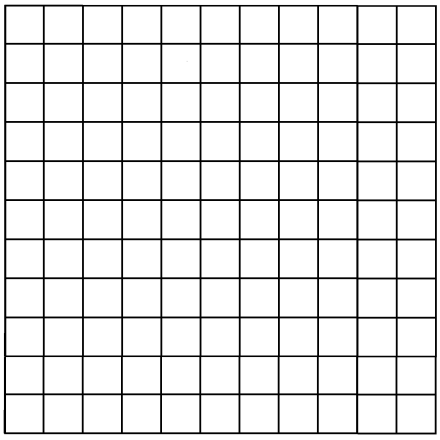

Fig. 6.17 Mesh used for Example problem 2(b).

increasing Q. Figure 6.18(a) shows that the $\eta(\mathscr{T})$ decreases up to $Q = 3$. With further addition of enrichment functions, the results deteriorate, and we do not get any reliable values. The condition number with three enrichment functions remains in the order of $E + 16$ which shoots up to the order of $E + 29$ with fourth enrichment functions as depicted in Figure 6.18(b). Figure 6.19 shows the distribution of $\eta(\square)$ in each element with uniform enrichments in the whole domain.

6.3.3.2 Adaptive q–enrichments

The standard FEM solution with zero enrichment functions as our iteration-1, we estimate the error indicator and the condition number in each element as well as their cumulative values for the whole domain. Following the adaptive algorithm, elements with higher values of error indicator are enriched adaptively. The error indicators in each element $\eta(\square)$ and their cumulative value $\eta(\mathscr{T})$, reduces with each refinement. The decrease of $\eta(\mathscr{T})$ with every refinement is shown in Figure 6.20(a). The corresponding condition number $\kappa(\mathscr{T})$ for each iteration is shown in Figure 6.20(b). As depicted in Figure 6.20(a), the $\eta(\mathscr{T})$ is maximum for the first iteration and minimum for iteration 6.

As observed in the previous examples, the results deteriorate with very high condition number. The results improve up to a certain limit, and with further addition

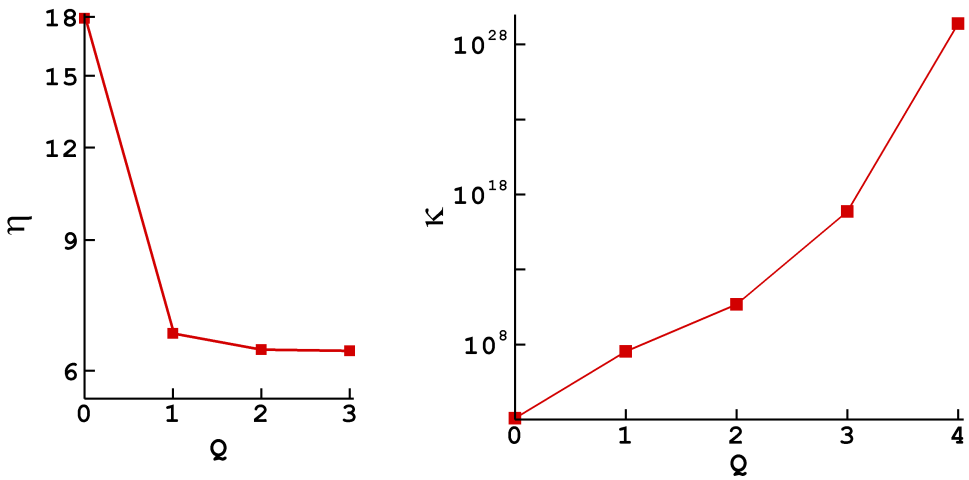

(a) $\eta(\mathscr{T})$ (b) $\kappa(\mathscr{T})$

Fig. 6.18 Variation of $\eta(\mathscr{T})$ and $\kappa(\mathscr{T})$ with uniform enrichments for Example problem 2(b).

of enrichment functions, the condition number becomes too high and the results start to deteriorate. The proposed adaptive algorithm gives us the liberty to put a limit on the $\kappa(\square)$ in any element as well as on the cumulative value $\kappa(\mathscr{T})$. It can be seen from Figure 6.20(b) that for iteration 5, the condition number is of the order $E+15$. The maximum condition number being in the central element as shown in Figure 6.21. The condition number in the central element in iteration 5, is $2.8E+15$. In iteration 5, 4 enrichment functions are used in each of the nine central elements as shown in Figure 6.22(d). To reduce the condition number in the central element, one enrichment function is decreased from the central element. Iteration 6 is performed with 3 enrichment functions in the central element, and 4 in each of the surrounding eight elements as shown in Figure 6.22(e). The condition number for the whole domain decreases from $4.5E+15$ to $6.1E+12$ as shown in Figure 6.22(b). Although the total DOFs are decreased in iteration 6, the results still improve by a small amount due to the drop in the condition number. Figure 6.23 shows the distribution of $\eta(\square)$ in each element. The decrease for the first two refinements is evident. For further refinements, the results still improve by a small amount.

Figure 6.24 compares the results of uniform enrichments and adaptive q–enrichments.

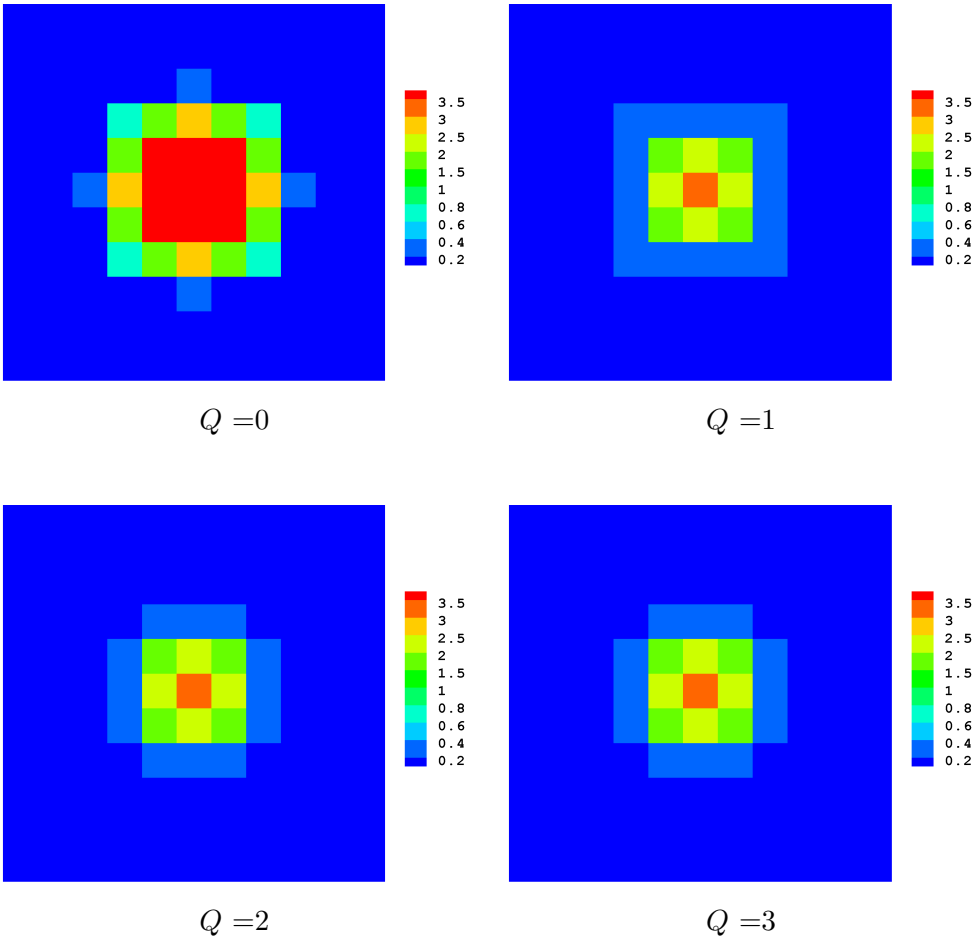

Fig. 6.19 Distribution of $\eta(\square)$ in each element with uniform enrichments for Example problem 2(b).

The $\eta(\mathscr{T})$ is plotted against total DOFs for both cases. The figure clearly shows that proposed adaptive algorithm gives similar results with less DOFs. For a comparable accuracy, a reduction of 70% in total DOFs was observed for the Example problem 2(a). In the current example, a reduction of more than 80% is noted with the adaptive algorithm. In case of uniform refinement, we get minimum value of $\eta(\mathscr{T}) = 6.38$ with total 1210 DOFs. In comparison, with the adaptive algorithm we get a comparable value of $\eta(\mathscr{T}) = 6.39$ with only 238 DOFs, giving a total reduction of 972 DOFs.

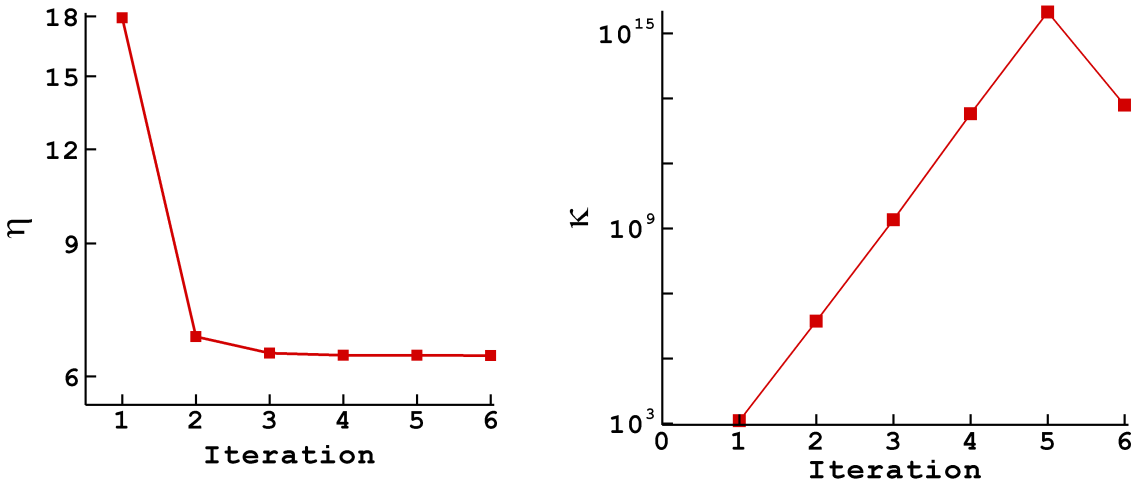

(a) $\eta(\mathscr{T})$ (b) $\kappa(\mathscr{T})$

Fig. 6.20 Variation of $\eta(\mathscr{T})$ and $\kappa(\mathscr{T})$ with adaptive $q-$refinements for Example problem 2(b).

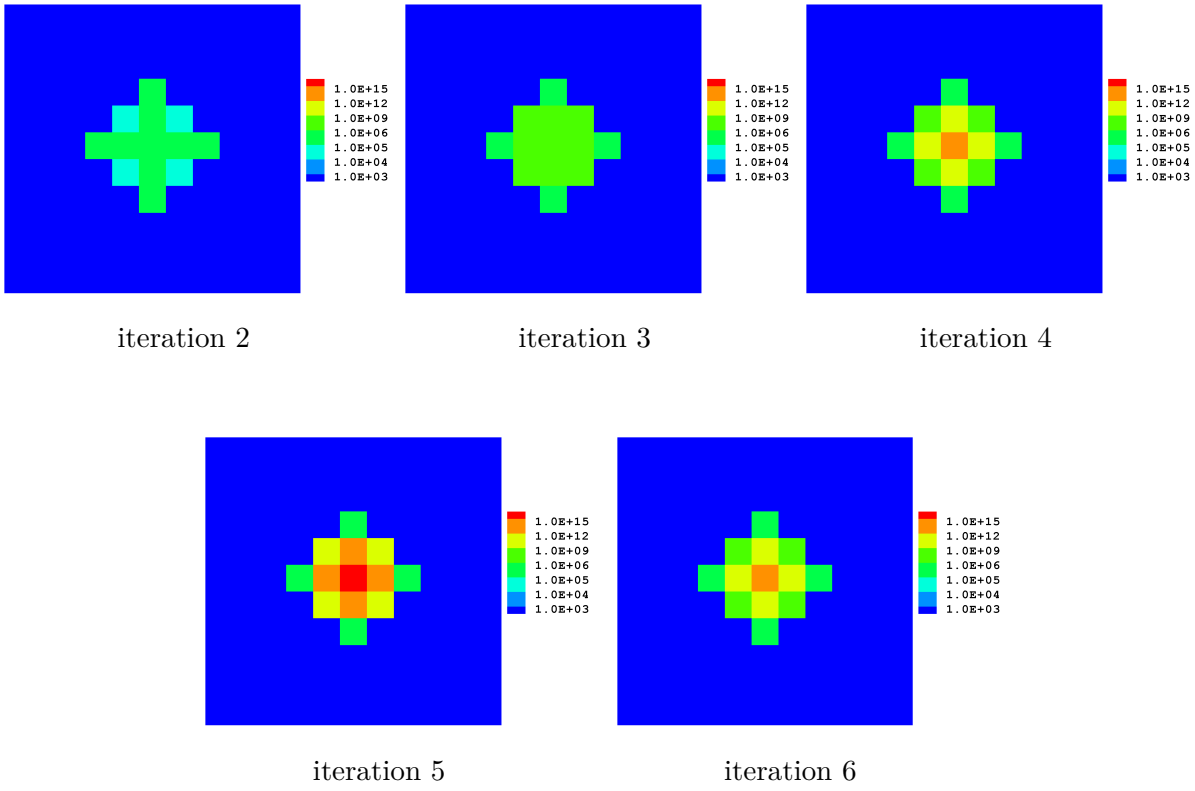

Fig. 6.21 Distribution of $\kappa(\square)$ in each element with adaptive $q-$refinement for Example problem 2(b).

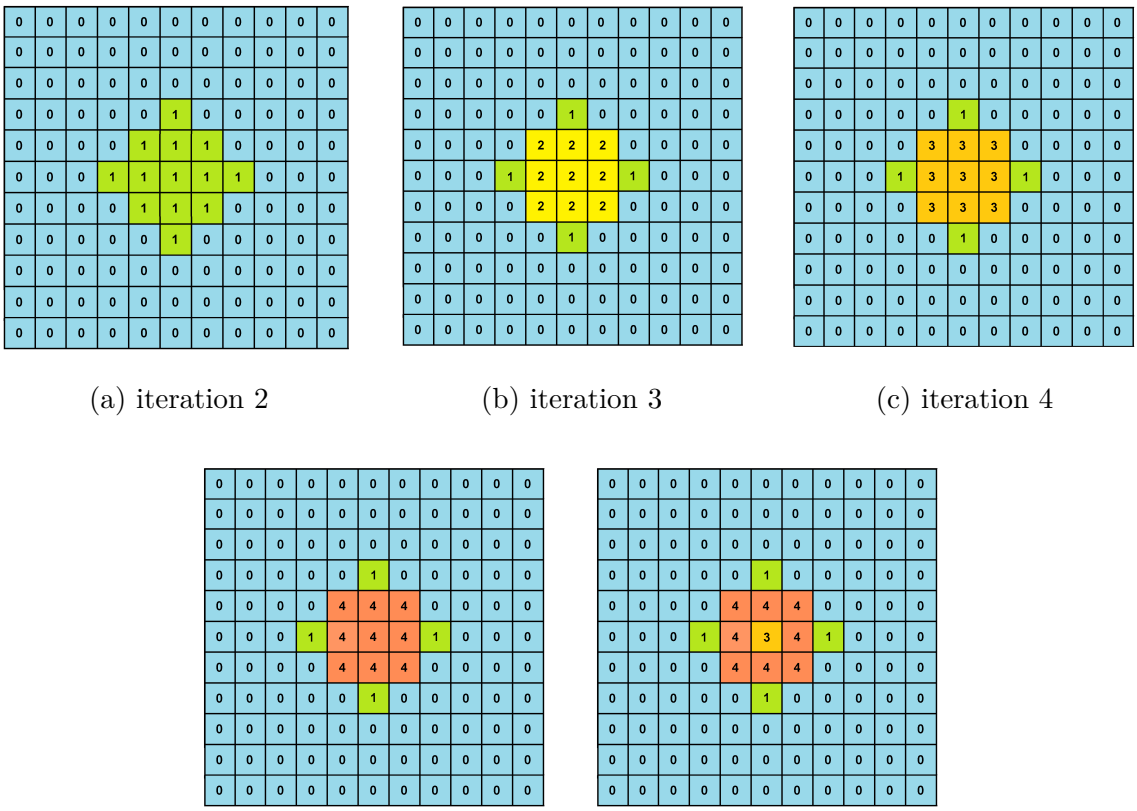

(a) iteration 2 (b) iteration 3 (c) iteration 4

(d) iteration 5 (e) iteration 6

Fig. 6.22 Enrichment functions used in each element with adaptive $q-$enrichments for Example problem 2(b).

6.4 Conclusions

An adaptive algorithm is proposed to selectively add enrichment functions in elements with relatively higher error indicators. The algorithm is tested on different example problems. Results are obtained for both cases of uniform enrichment and adaptive enrichment. It is concluded that for a comparable accuracy, the proposed adaptive algorithm offers a reduction of up to 80% in the total number of degrees of freedom. The effect of the condition number on the quality of the results is also investigated. It is concluded that the addition of enrichment functions improve the results only up to a certain limit. Adding further enrichment functions makes the system matrix ill-conditioned, which in turn affects the quality of the results. With the proposed

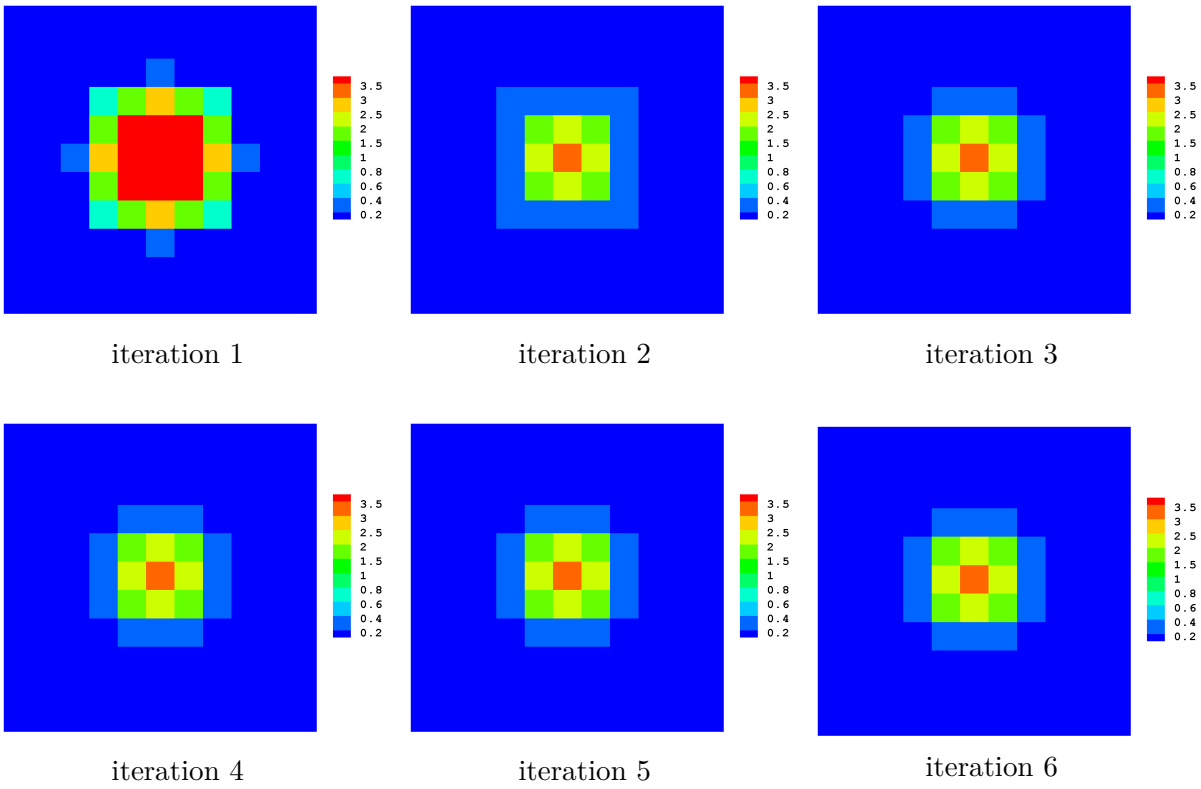

Fig. 6.23 Distribution of $\eta(\square)$ in each element with adaptive $q-$enrichments for Example problem 2(b).

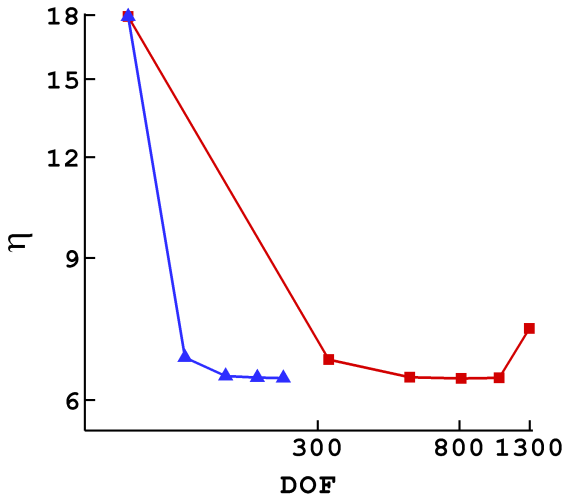

Fig. 6.24 Comparison of $\eta(\mathscr{T})$ for uniform enrichments (■) and adaptive q–enrichments (▲) for Example problem 2(b).

algorithm, the condition number may be capped by a given limit. Elements with higher condition numbers are marked and the number of enrichment functions is reduced in the selected elements. This is shown to decrease the overall condition number of the system matrix while improving the quality of the results and achieving computational cost savings.

Chapter 7

Error estimation for three-dimensional problems

7.1 Introduction

The current chapter extends the concept of the error estimates to the three-dimensional case of transient heat diffusion problems. In Chapter 4 the GFEM approach is tested for three-dimensional problems. Having shown the benefits of GFEM for 3D problems, it is proposed to reconsider the error estimates developed in Chapter 5 for three-dimensional problems as well. For the two-dimensional case, it is shown that the implemented residual estimates quantify reliably an upper bound of the numerical errors of GFEM on coarse mesh grids.

The next sections outline the transient heat diffusion problem along with the definition of error estimates for 3D problems. The expressions of the error estimate (relative η) components are pretty similar to the 2D case, however, the integration scheme is applied on three-dimensional domains. Numerical experiments on two test problems are presented to show the effectiveness of the error estimate in 3D.

7.2 GFEM discretization and error estimates

Considering the transient heat diffusion problem defined by (3.1) - (3.3), the weak formulation of the problem in a 3D domain $\Omega \subset \mathbb{R}^3$ is given by (4.1). The GFEM discretization (3.16) is used to find the approximate numerical solution of the considered problem. If U and u are the exact and GFEM solution of this problem, we rewrite Theorem 1 defined in Chapter 5 as;

$$\int_\Omega |U(T,\mathbf{x}) - u(T,\mathbf{x})|^2 d\Omega + \lambda \int_0^T \int_\Omega |\nabla(U-\hat{u})|^2 d\Omega \, dt \\ \leq c\{\eta_1^2 + \eta_2^2 + \eta_3^2 + \eta_4^2 + \eta_5^2 + \eta_6^2\}, \qquad (7.1)$$

with the definitions of η_1^2 - η_6^2 given by (5.4) - (5.9), but now in a three-dimensional domain. The left hand side (LHS) of expression (7.1) measures the actual errors between the approximate GFEM solution and the exact solution, while the right hand side (RHS) represents the computable error indicators, η_1^2 to η_6^2. For an acceptable solution, LHS should always be less than RHS. Theorem 1 proves that the error indicators η_1^2 to η_6^2 never underestimate the actual error. As before we will compute η_2^2, η_4^2 and η_5^2 only. For three-dimensional problems these are defined as

$$\begin{aligned}
\eta_2^2(n,K) &= \int_{t_n}^{t_{n+1}} \left\| \hat{f} - \partial_t u + \lambda \Delta \hat{u} \right\|^2_{H^{-1}(K)} \\
&\leq \int_{t_n}^{t_{n+1}} dt \int_K \left(\hat{f} - \partial_t u + \lambda \Delta \hat{u} \right)^2 d\Omega \\
&= \delta t \int_K \left(f^{n+1} - \frac{u^{n+1} - u^n}{\delta t} + \lambda \left(\frac{\partial^2 u^{n+1}}{\partial x^2} + \frac{\partial^2 u^{n+1}}{\partial y^2} + \frac{\partial^2 u^{n+1}}{\partial z^2} \right) \right)^2 d\Omega \, .
\end{aligned}$$

$$\begin{aligned}
\eta_4^2(n,K) &= \lambda \int_{t_n}^{t_{n+1}} \|\nabla(u-\hat{u})\|^2_{L^2(K)} \\
&= \lambda \int_{t_n}^{t_{n+1}} \left(\frac{t_{n+1} - t}{t_{n+1} - t_n} \right)^2 dt \int_K \left[\left(\frac{\partial u^{n+1}}{\partial x} - \frac{\partial u^n}{\partial x} \right)^2 + \left(\frac{\partial u^{n+1}}{\partial y} - \frac{\partial u^n}{\partial y} \right)^2 \right] d\Omega \\
&= \frac{\lambda \delta T}{3} \left(\int_K \left(\frac{\partial u^{n+1}}{\partial x} - \frac{\partial u^n}{\partial x} \right)^2 d\Omega + \int_K \left(\frac{\partial u^{n+1}}{\partial y} - \frac{\partial u^n}{\partial y} \right)^2 d\Omega + \int_K \left(\frac{\partial u^{n+1}}{\partial z} - \frac{\partial u^n}{\partial z} \right)^2 d\Omega \right) \, .
\end{aligned}$$

$$
\begin{aligned}
\eta_5^2(n,E) &= \int_{t_n}^{t_{n+1}} \left\| \left[\frac{\partial \hat{u}}{\partial n} \right] \right\|_{L^2(E)}^2 \, dt \\
&= \int_{t_n}^{t_{n+1}} \left\| \left[\nabla u^{n+1} \cdot \mathbf{n} \right] \right\|_{L^2(E)}^2 \, dt \\
&= \int_{t_n}^{t_{n+1}} \int_E \left(\nabla u_{E_1}^{n+1} n_1 + \nabla u_{E_2}^{n+1} n_2 \right)^2 dE \, dt \\
&= \int_{t_n}^{t_{n+1}} \int_E \left(\nabla u_{E_1}^{n+1} n_1 - \nabla u_{E_2}^{n+1} n_1 \right)^2 dE \, dt \\
&= \delta t \int_E \Bigg(\left(\frac{\partial u^{n+1}}{\partial x} n_{1_x} + \frac{\partial u^{n+1}}{\partial y} n_{1_y} + \frac{\partial u^{n+1}}{\partial z} n_{1_z} \right)_{E_1} \\
&\quad - \left(\frac{\partial u^{n+1}}{\partial x} n_{1_x} + \frac{\partial u^{n+1}}{\partial y} n_{1_y} + \frac{\partial u^{n+1}}{\partial z} n_{1_z} \right)_{E_2} \Bigg)^2 dE \, .
\end{aligned}
$$

7.3 Numerical experiments

This section investigates the *a-posteriori* error estimates proposed in Theorem 1 for three-dimensional transient heat diffusion problems. To show the effectiveness of Theorem 1 we consider two different numerical examples. The first example considers a problem where the exact solution is known. The exact solution can be used to find the relative L_2 error of the approximate GFEM solution. It is also used to compute the right hand side of the expression (7.1). The second example considers the problem of transient heat transfer with a single heat source in the centre of the domain. This example is considered to show the usefulness of the proposed error estimates for a general case where the exact solution is not known.

As in Chapter 4, the numerical solution for both the experiments is computed using hexahedral elements with 8 nodes and piecewise linear shape functions. The parameters R_c and C in the GFEM basis functions G_q are constants which control the shape of the enrichment functions, and $R_0 = |\mathbf{x} - \mathbf{x}_c|$ is the distance of any point $\mathbf{x}$ from the centre of the domain $\mathbf{x}_c = (1, 1, 1)$. A thorough study with different values of R_c and C is presented for the optimal selection of the enrichment functions. All integrals over Ω are evaluated numerically, using a Gauss–Legendre quadrature with 20 integration points in each spatial direction.

To compare the results for different model problems, we focus on the relative error between the exact solution U and its GFEM approximation u, defined as

$$\left(\frac{\int_\Omega |U-u|^2 d\Omega + \lambda \int_0^T \int_\Omega |\nabla(U-\hat{u})|^2 d\Omega \; dt}{\int_\Omega |U|^2 d\Omega + \lambda \int_0^T \int_\Omega |\nabla U|^2 d\Omega \; dt}\right)^{1/2} \tag{7.2}$$

The corresponding rel η is given as

$$\left(\frac{\eta_2^2 + \eta_4^2 + \eta_5^2}{\int_\Omega |U|^2 d\Omega + \lambda \int_0^T \int_\Omega |\nabla U|^2 d\Omega \; dt}\right)^{1/2} \tag{7.3}$$

For Example problem 1, both quantities (7.2) and (7.3) are computed, and their values are compared. For the second example where no exact solution is known, only (7.3) is calculated and the exact solution U is replaced by a reference FEM solution on a fine mesh.

7.3.1 Example problem 1

To show the relevance of Theorem 1, we calculate the actual errors in the GFEM solution as defined by LHS of expression (7.1) and then compare it to RHS by calculating the error indicators. A problem with known exact solution in a 3D domain Ω is considered for this purpose which is similar to Example Problem 1 of Chapter 4 and for which the exact solution is given by (4.2). The relative L_2 norm error given by (7.3) is also calculated. For consistency with the problems considered in Chapter 5 for error estimation of 2D problems, the parameters h,and λ are taken to be the same, i.e., h = 1kg/°Cs^2 and λ = 0.1kgm/°Cs^2. The time step value is taken to be Δt = 0.01s with a total solution time of t = 1.0s. Four different numerical studies are performed to show the working of the proposed error estimates under different conditions.

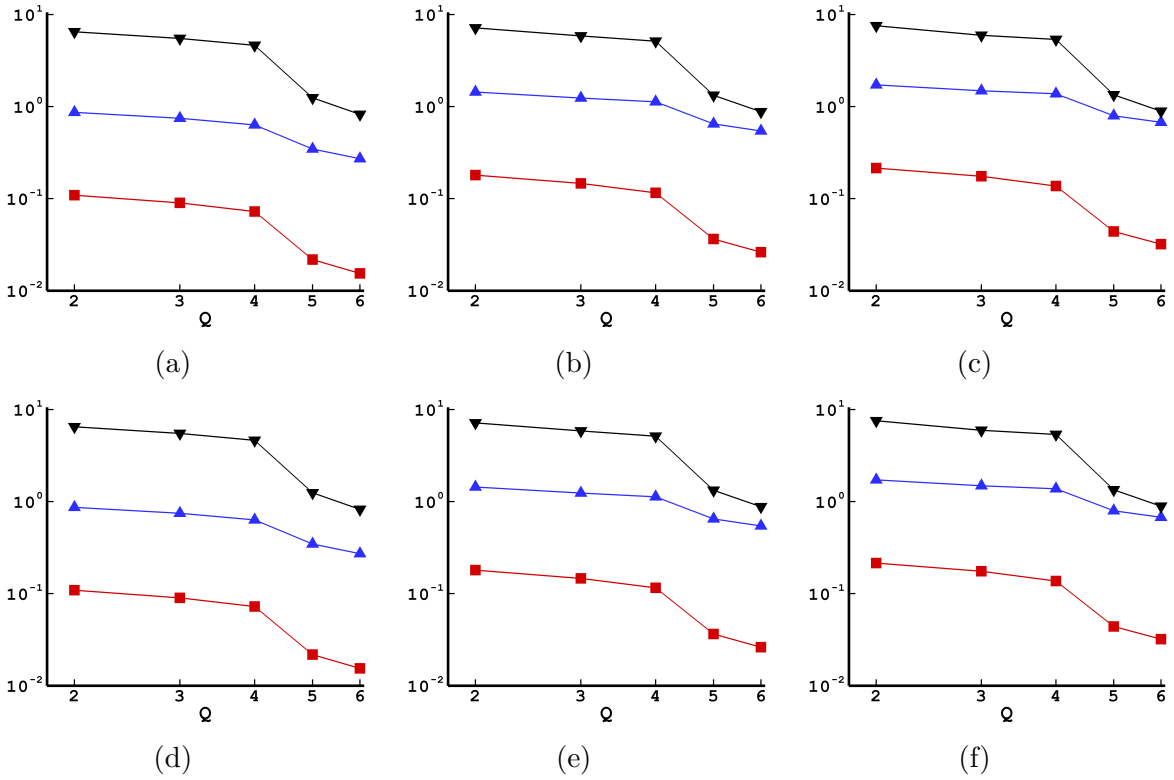

Fig. 7.1 Variation of relative error (■), rel η (▲) and $\varepsilon\%$ (▼) for $\Delta t = 0.01$s (top row) and $\Delta t = 0.001$s (bottom row) at times $t = 0.1, 0.5$ and 1.0s from left to right.

7.3.1.1 Study 1: Effect of $q-$refinement

The first study evaluates the effect of number of enrichment functions on the variation of error estimates and the actual errors in the numerical solution. For computations, a fixed coarse mesh of 125 elements is selected with different number of enrichment functions $Q = 2, \ldots, 6$. The the mesh density is taken to be the same as in 2D problems i.e., 5 elements in each spatial direction of the cube. For 2D problems, a mesh with 5 elements in each spatial direction of the square was considered. Both the actual errors and the error indicators are computed and their values are compared using varying number of enrichment functions. The L_2 norm error is also calculated to show that the proposed error estimates give similar trends as produced by the L_2 norm error.

Figure 7.1 compares the relative error of the GFEM solution defined by (7.2) and

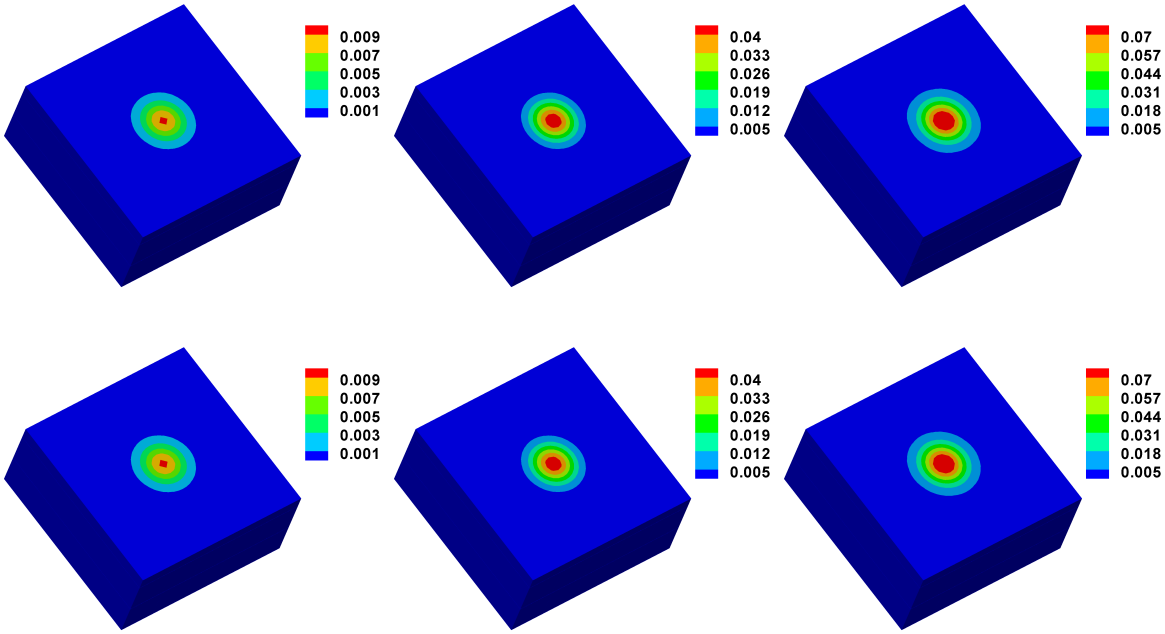

Fig. 7.2 Temperature distribution for the exact solution (top row) and GFEM solution with $Q = 6$ (bottom row) at times $t = 0.1, 0.5$ and 1.0s from left to right. The distributions are obtained with $\Delta t = 0.01$s.

the rel η defined by (7.3) for increasing number of enrichment functions Q. The results are presented for three different simulation times, $t = 0.1$, 0.5 and 1.0s with two different values of time steps, i.e., $\Delta t = 0.01$s and $\Delta t = 0.001$s . In the graph, the number of enrichment functions Q is presented on the abscissa while the relative error (■), rel η (▲) and relative L_2 norm error (▼) are shown on the ordinate.

The results show that in all the cases the relative error of GFEM solution is less than the rel η. The actual error decreases as the number of enrichment functions is increased. A similar decrease is observed in the error estimate which effectively bounds the actual error. The ratio of the error estimator and the actual error is close to 10 in all the cases. This is to be emphasized that the proposed estimates show similar trends as those captured by the relative L_2 norm error. For problems with no known exact solutions, where the the relative L_2 norm error cannot be calculated, the proposed error estimate can serve the purpose of evaluating the solution accuracy.

In the computations of the indicators η_2^2, η_4^2 and η_5^2, it is observed that the overall

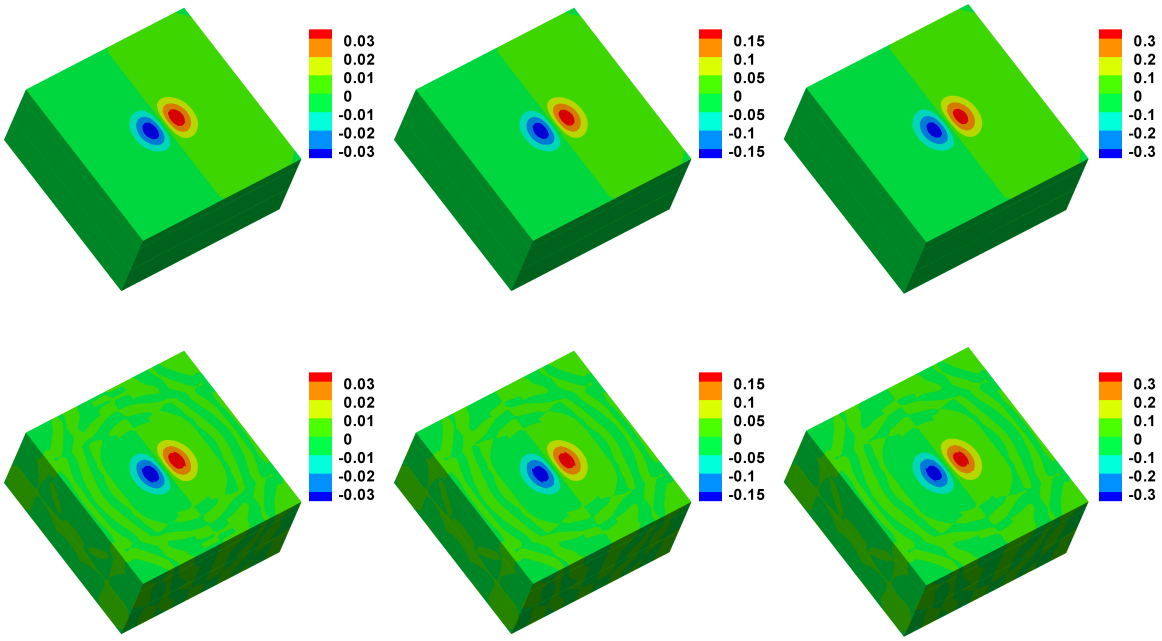

Fig. 7.3 First derivatives of the solution in x-direction for the exact solution (top row) and GFEM solution with $Q = 6$ (bottom row) at times $t = 0.1, 0.5$ and 1.0s from left to right. The distributions are obtained with $\Delta t = 0.01$s.

value of the error estimate is dominated by η_2^2. This is attributed to the presence of large second derivative of the solution. The values of the solution as well as its first derivatives are very low as compared to the second derivatives. Figure 7.2 shows the solution captured by GFEM and exact solutions at different simulation times. Both solutions present very similar temperature profiles. The same is observed in the first derivatives of the solution in the x-direction as shown in Figure 7.3. GFEM closely approximates the first derivatives of the exact solution. Due to the symmetry of the problem and the enrichment functions, similar profiles of the derivatives are observed in the y and z directions. From Figure 7.2 and Figure 7.3, it is evident that the maximum value of the solution at $t = 1.0$s is 0.07 while that of the first derivative at the same simulation time is 0.3 in the positive direction and -0.3 in the negative direction. At the same simulation time, comparatively high values of the second derivatives are observed as shown in Figure 7.4. Here the second derivatives of the solution in the x-direction captured by both GFEM and exact solutions are presented at differ-

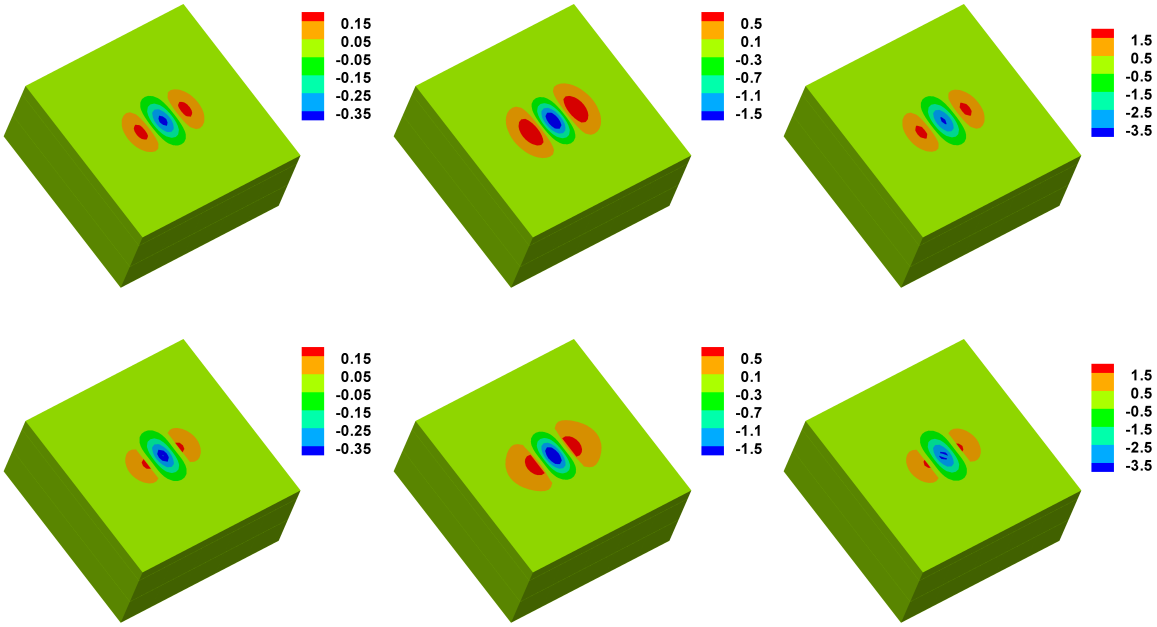

Fig. 7.4 Second derivatives of the solution in x-direction for the exact solution (top row) and GFEM solution with $Q = 6$ (bottom row) at times $t = 0.1, 0.5$ and 1.0s from left to right. The distributions are obtained with $\Delta t = 0.01$s.

ent simulation times. It can be seen from Figure 7.4 that the values of the second derivatives at $t = 1.0$s are +1.5 and -3.5 which explains the high value of η_2^2. Although very similar profiles of the solution and its first derivatives are obtained by the exact and GFEM solutions; there are still some dissimilarities in the profiles of their second derivatives. One can tune the enrichment functions to give a very smooth approximation to the second derivative as well, but this would be very specific to the problem under consideration, unlike the general nature of the method. In the current study, they are kept in the general form, as used in [88, 126, 129].

7.3.1.2 Study 2: Effect of $h-$refinement

The second study is performed to determine the effect of $h-$refinement on the proposed error estimates. Three different mesh grids as shown in Figure 7.5 are considered for the computations. We start with a very coarse mesh of 64 elements in the 3D cube and enrich the solution space with different numbers of enrichment functions $Q =$

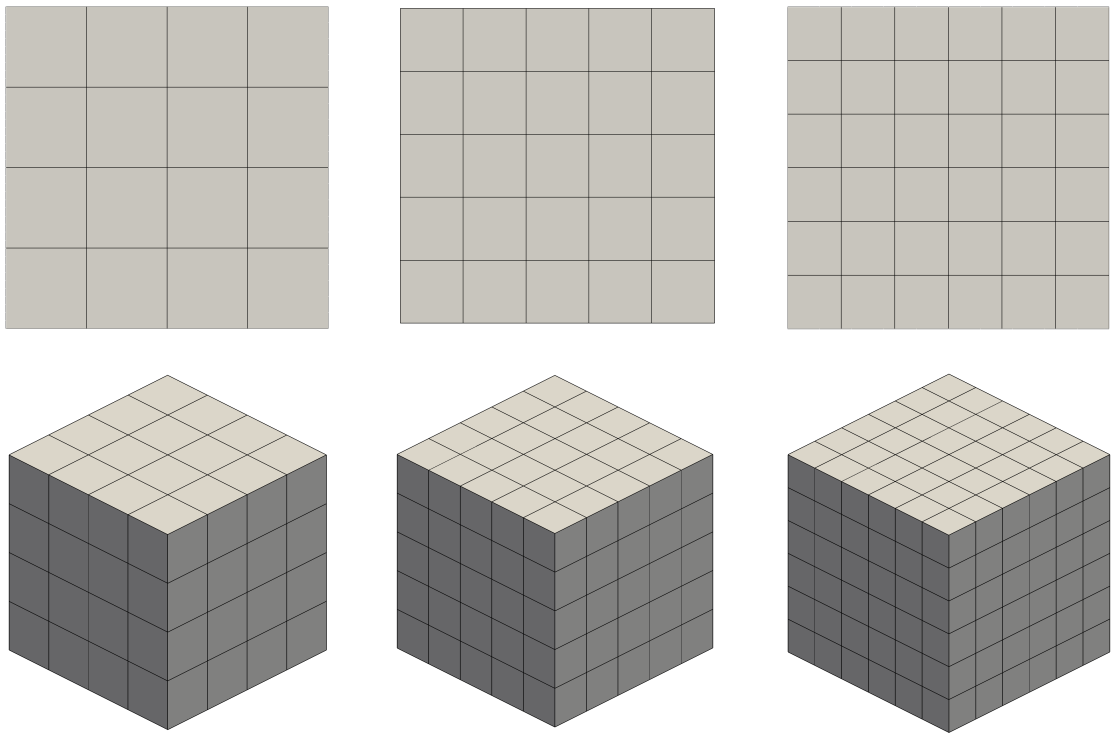

Fig. 7.5 Different meshes used for the computations.

2,3...6. We then refine the mesh to a total of 125 elements in the whole domain, with 5 elements in each direction. Again we consider the same enrichment functions Q = 2,3...6. A third refinement of 216 elements with Q = 2,3...6 is also considered to improve the results further. In the coming discussion, the computations with 64 elements will be referred as GFEM1, and with 125 and 216 elements as GFEM2 and GFEM3, respectively. The relative error, rel η and relative L_2 norm error are calculated for all the three mesh grids.

Figure 7.6 compares the results of GFEM1, GFEM2 and GFEM3 computations at three different simulation times. The relative error (■), rel η (▲) and relative L_2 norm error (▼) are presented against the number of degrees of freedom. For all the computations, the error estimate consistently bounds the actual errors in the solution. As in the previous study, the relative error and rel η decrease as the number of enrichment functions are increased, with similar trends as shown by the relative L_2

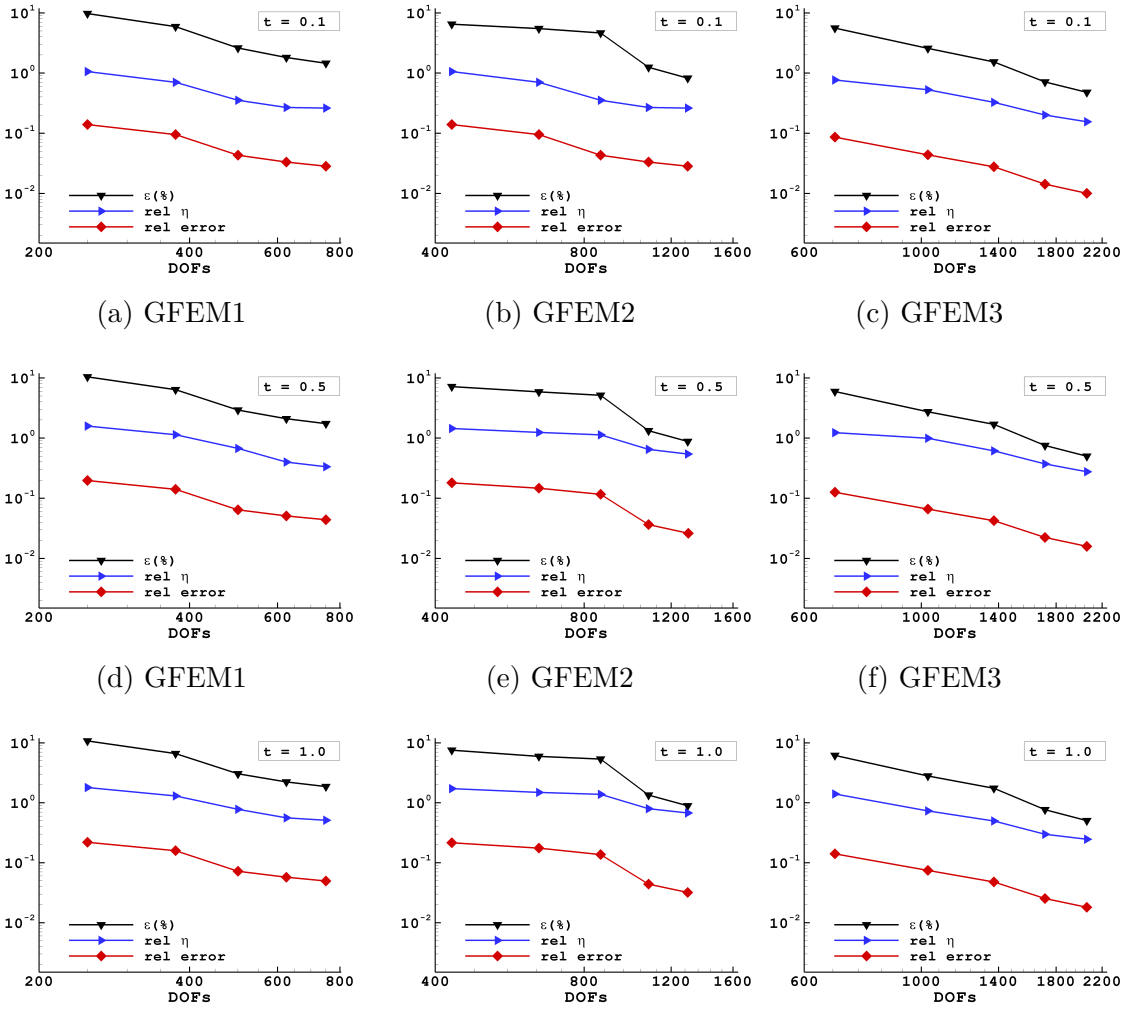

(a) GFEM1 (b) GFEM2 (c) GFEM3

(d) GFEM1 (e) GFEM2 (f) GFEM3

(g) GFEM1 (h) GFEM2 (i) GFEM3

Fig. 7.6 Variation of relative error (■), rel η (▲) and $\varepsilon\%$ (▼) for GFEM1, GFEM2 and GFEM3 at times $t = 0.1, 0.5$ and 1.0s.

norm error. As expected, GFEM3 having the finest mesh grid of all the three meshes, produces lower errors, which are efficiently captured by the presented error estimate.

7.3.1.3 Study 3: $q-$band analysis

This study investigates the possible use of *a-posteriori* error estimates for the optimal selection of the combination of enrichment functions. The computations are performed with a coarse mesh of 64 elements and three enrichment functions. With $Q = 3$ and q varied between $1, ...6$, out of the different possible combinations of q, four combination

Table 7.1 q-bands used for Study 3.

Case	$q-$bands
1	$q = 1, 2, 3$
2	$q = 2, 3, 4$
3	$q = 3, 4, 5$
4	$q = 4, 5, 6$

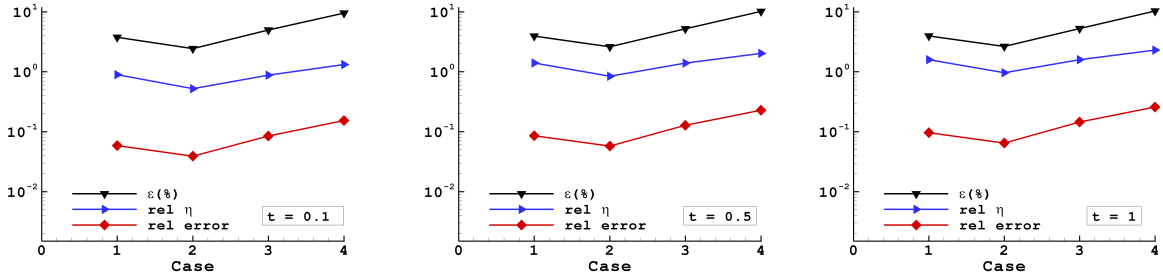

(a) $t = 0.1$ (b) $t = 0.5$ (c) $t = 1.0$

Fig. 7.7 Variation of relative error (■), rel η (▲) and $\varepsilon\%$ (▼) for different $q-$bands.

as shown in Table 7.1 are used in this present study.

Figure 7.7 calculates the relative time–integrated error, and rel η over the whole domain Ω for different choices of enrichment functions and different time intervals $t = 0.1$, 0.5 and 1.0s. The variation of relative L_2 norm error is also calculated with the selected combinations. It is observed from Figure 7.7 that the second combination of $q = 2, 3, 4$ (Case 2) produces the lowest errors at all the simulation times. The enrichment functions with flatter gradients such as $q = 4, 5, 6$ (Case 4) yield the worst numerical approximation. As in the previous studies, very similar patterns of results are obtained with the rel η and L_2 norm error. The presented study can be useful for the adaptive selection of the enrichment functions for $q-$refinement when little or no information are known about the approximation properties of the enrichment functions. Although only four combinations as stated in Table 7.1 are selected to show the working of the presented error estimate, a thorough study with different $q-$bands can be performed to select the optimal combination.

Table 7.2 Different combinations of C and R_c used for Study 4.

Case	C	R_c
1	$\sqrt{3}$	$\sqrt{10}$
2	$\sqrt{2}$	$\sqrt{10}$
3	$\sqrt{1}$	$\sqrt{10}$
4	$\sqrt{1}$	$\sqrt{5}$
5	$\sqrt{1}$	$\sqrt{2}$
6	$\sqrt{1}$	$\sqrt{1}$

7.3.1.4 Study 4: Enrichment function optimization

The effectiveness of GFEM depends on the proper selection of enrichment functions [11]. A suitably chosen enrichment function provide better approximation than the standard polynomial shape functions used in the classical finite element method. This current study is designed to exploit the error estimate for the proper selection of enrichment functions. While the presented formulation can be used to test and compare different enrichment functions for optimal solution, in the current study the selected enrichment function (3.18) is optimized for minimum error. As stated in section (7.3), the constants C and R_c in (3.18) control the shape of the enrichment functions. To get the optimum shape of the enrichment function that best approximates the solution of the considered problem, different values of C and R_c as shown in Table 7.2, are considered in this study. Figure 7.8 depicts the results of the relative error and rel η along with the relative L_2 norm error for the selected cases at three stated simulation times. For Case-1 with $C = \sqrt{3}$ and $R_c = \sqrt{10}$, the errors are noted to be the maximum of all the presented six cases. For all the simulation times, Case-3 with values of $C = \sqrt{1}$ and $R_c = \sqrt{10}$ produces the minimum errors. Although further combinations of C and R_c can be tested for best possible solution, the purpose here is only to detail the possible use of the proposed error estimate for the optimal selection of the enrichment functions. From Figure 7.8 it is clear that the proposed error estimate captures the same solution trends as obtained by the relative L_2 error. While for problems where the exact solution is known, the L_2 norm error can be used to select the optimal enrichment function, but for problems with no known exact solution, the

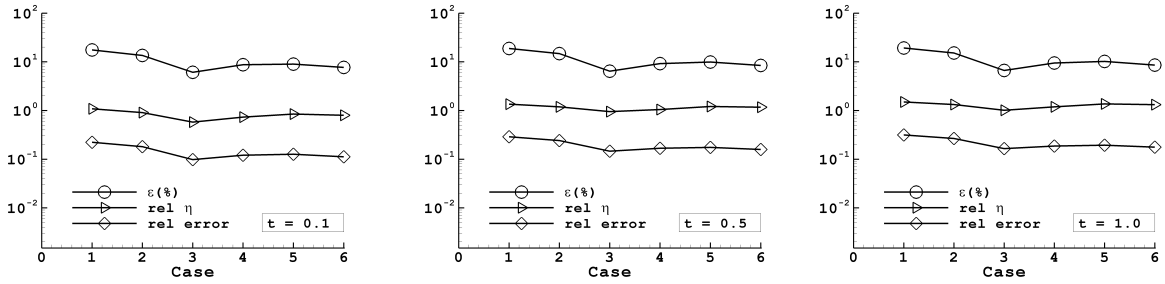

(a) $t = 0.1$ (b) $t = 0.5$ (c) $t = 1.0$

Fig. 7.8 Variation of relative error (■), rel η (▲) and $\varepsilon\%$ (▼) for different values of parameters C and R_c.

proposed error estimate can serve this purpose.

7.3.1.5 Study 5: Effect of the Condition Number (κ)

A major drawback of the GFEM is the ill-conditioning of the stiffness matrix [112]. Although the method has shown remarkable accuracy with lesser DOFs as compared to the standard FEM, but the problem of ill-conditioning is an inherent property of the GFEM when finer meshes or higher number of enrichment functions are used. Babuška and Banerjee [10] investigated the conditioning issue of the GFEM while proposing a modified GFEM, called SGFEM. They showed that in case of GFEM, the conditioning number of the system matrix grows very quickly as compared to the standard FEM.

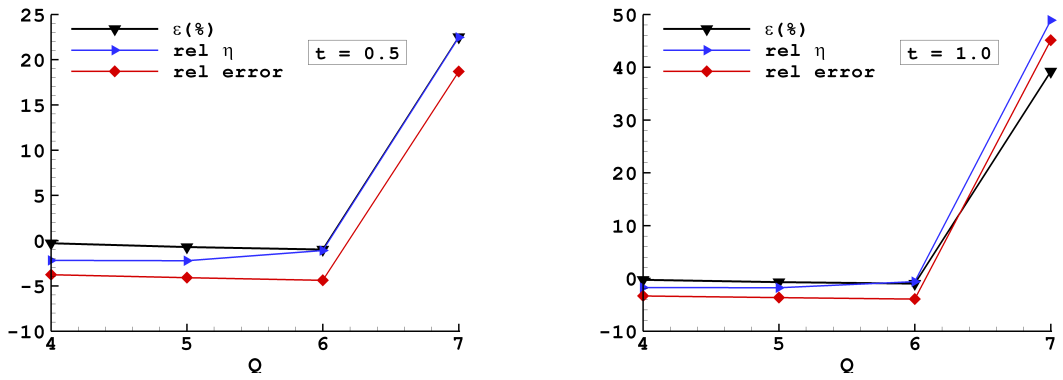

(a) $t = 0.5$ (b) $t = 1.0$

Fig. 7.9 Variation of relative error (■), rel η (▲) and $\varepsilon\%$ (▼) for GFEM4 with increasing Q.

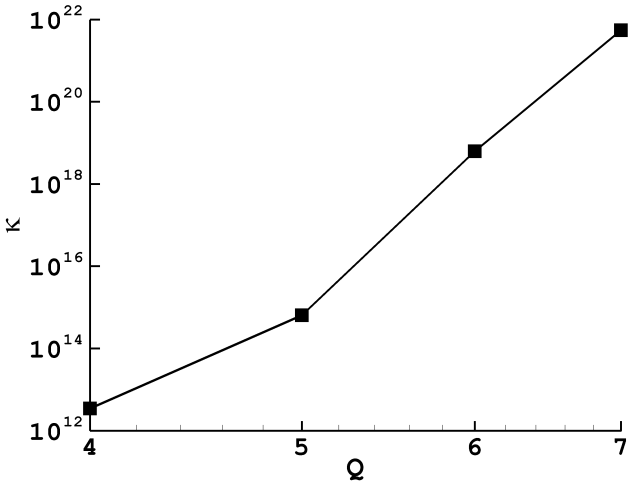

Fig. 7.10 Variation of Condition Number (κ) with increasing Q for GFEM4.

This present study is designed to show that the proposed error estimate can be used as a tool to detect the deterioration of the numerical results when condition number grows very high. An $8 \times 8 \times 8$ mesh with uniform elements is selected with $Q = 4, ...7$ to perform the numerical computations, referred as GFEM4. Figure 7.9 shows the log values of relative error (■), rel η (▲) and $\varepsilon\%$ (▼) against the number of enrichment functions Q. An important observation made from Figure 7.9 is that upto $Q = 5$ both the relative L_2 norm error and the rel η show a decreasing trend. A small decrease is observed in the relative L_2 norm error For $Q = 6$, but the rel η starts increasing. As described in Chapter-6, the proposed error estimate is more sensitive to the condition number than the relative L_2 norm error. This is attributed to the presence of derivative terms in the error estimate. In comparison to the relative L_2 norm error, the proposed error estimate gives an early indication about the ill-conditioning of the system matrix and consequently the deterioration of the numerical results. Figure 7.10 shows the variation of the conditioning number κ for increasing Q. For $Q = 7$, the condition number increases to a value as high as $5.5E + 21$, which deteriorates the numerical results.

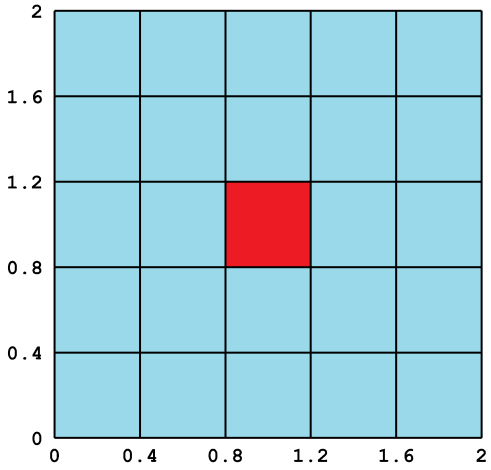

Fig. 7.11 x-section of the 3D domain for Example problem 2 with a heat source in the centre.

7.3.2 Example problem 2

The second example considers a transient heat diffusion problem in a 3D domain $\Omega = [0, 2]^3$ with a heat source in the central part that dissipates heat symmetrically throughout the domain. A cross section through the middle of the domain is shown in Figure 7.11. For the central part $\mathbf{x} \in [0.4, 0.8]^3$, the source dissipates heat at a constant rate f =200°C/s and is zero in the rest of the domain. The total simulation time is taken to be $t = 0.2$s with a time step value of $\Delta t = 0.001$s. The source dissipates heat for half of the simulation time, i.e., from $t = 0$ to $t = 0.1$s, and then it is switched off and the medium is allowed to cool down for the remaining half of the simulation. For consistency, the same values of parameters h, λ are used as in Chapter 5 for 2D problem, i.e. h= 1kg/°Cs^2 and $\lambda = 0.1$kgm/°Cs^2. The time step value is fixed at $\Delta t = 0.01$s.

Example Problem 2 assesses the effectiveness of the proposed error estimates for a more general problem where one can expect high thermal gradients. As the exact solution is not known in this case, only the rel η defined by (7.3) is computed. The quantities U and ∇U in the denominator of expression (7.3) are computed from a reference FEM solution on a very fine mesh of 125000 elements. For the GFEM solution, a coarse mesh of 125 elements is considered. The meshes used for the reference

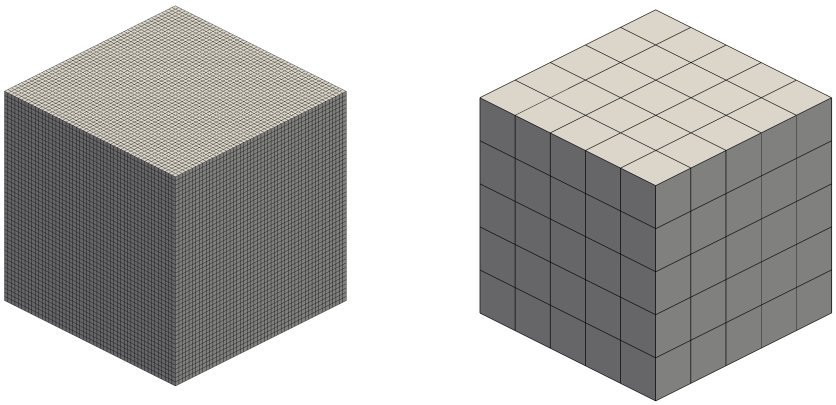

(a) FEM mesh (b) GFEM mesh

Fig. 7.12 Meshes used for the reference FEM and GFEM solutions.

FEM and GFEM solutions are shown in Figure 7.12. To investigate the possible use of the presented error estimate for a problem with no known analytical solution, two different studies are performed. The first study is performed to show the effect of $q-$refinement on the solution obtained with GFEM, and the other investigates the the $q-$band analysis as performed in the previous Example problem.

7.3.2.1 Effect of $q-$refinement

To evaluate the effect of $q-$refinement for Example problem 2, GFEM solution is calculated with a $5 \times 5 \times 5$ mesh using different numbers of enrichment functions, Q = 2,3,...6. Figure 7.13 shows the variation of the rel η as a function of the number of enrichment functions Q at times $t = 0.05, 0.1, 0.15$ and 0.2s. In each of these cases, two different values of the time step are considered: $\Delta t = 0.001$ and 0.0001s. As in the previous example, the rel η decreases as the number of enrichment functions is increased. This shows that the error estimate captures the behaviour of the solution efficiently and improves with every additional enrichment function. Similar trends are achieved for both values of Δt with slightly better results with $\Delta t = 0.0001$s. Figure 7.14 shows the temperature distributions for both FEM and GFEM solutions. Both the coarse mesh GFEM and fine mesh FEM solutions show similar temperature profiles. In

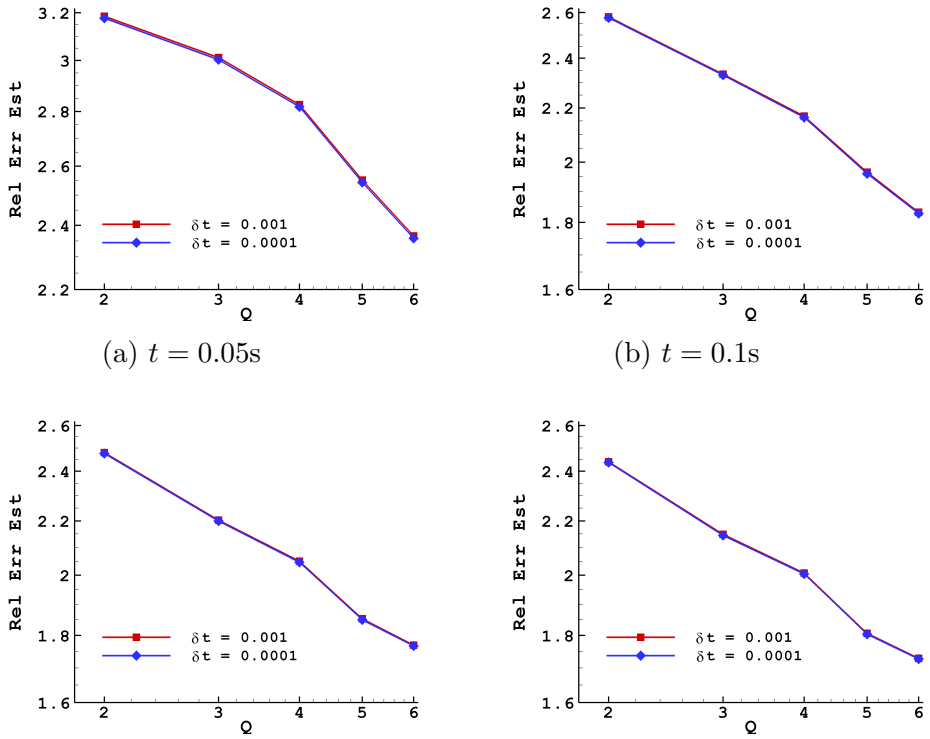

(a) $t = 0.05$s (b) $t = 0.1$s

(c) $t = 0.15$s (d) $t = 0.2$s

Fig. 7.13 Variation of rel η with enrichment functions for Example problem 2.

Figure 7.15 and Figure 7.16 are shown the first and second derivatives with respect to x respectively, of the GFEM solution. Again, the overall error estimate is dominated by the η_2^2 and very high values of the second derivatives are observed as compared to the value of the solution and its first derivatives.

7.3.2.2 Effect of $q-$bands

To ascertain the effect of different combinations of $q-$bands, computations are performed with three enrichment functions. With $Q = 3$, the same $q-$bands as shown in Table 7.1 are considered again for Example problem 2. Figure 7.17 depicts the rel η over the whole domain Ω for different combinations of enrichment functions at four different simulation times, $t = 0.05$, 0.1, 0.15 and 0.2s. For the selected four combinations, the Case-2 with combination $q = 2, 3, 4$ produces the lowest errors at all the simulation times, followed by Case-1 with combination $q = 1, 2, 3$. The last

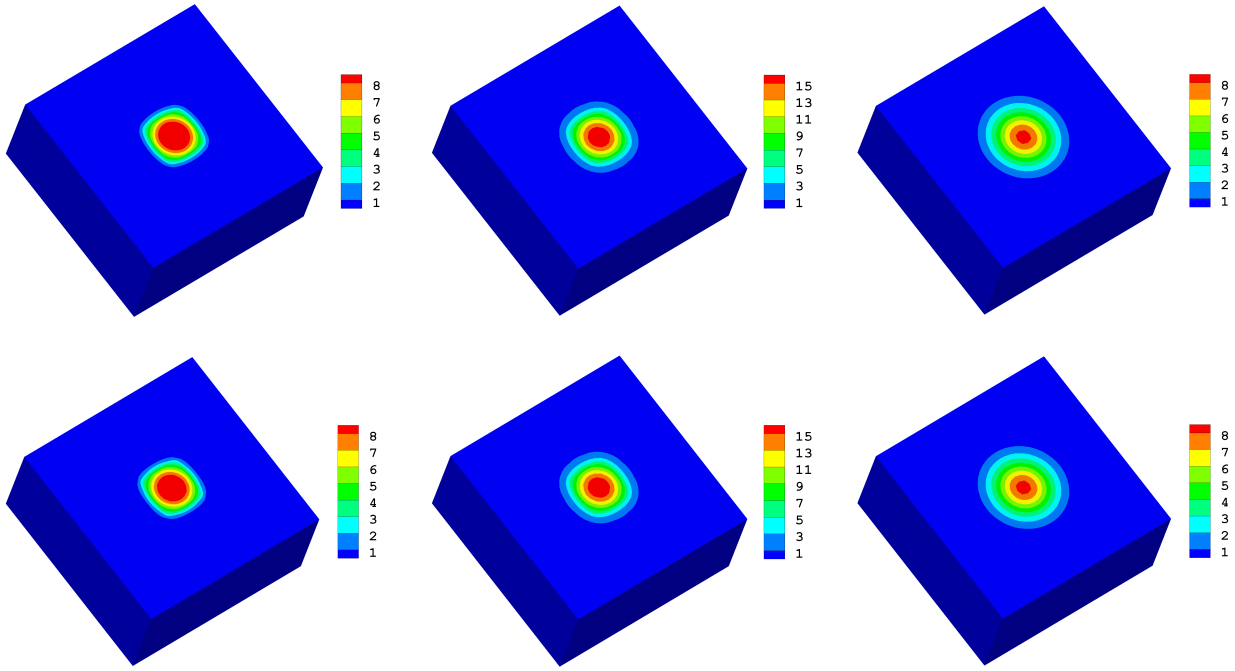

Fig. 7.14 Temperature distribution for the reference FEM solution (top row) and GFEM solution with $Q = 6$ (bottom row) at times $t = 0.05, 0.1$ and 0.2s from left to right. The distributions are obtained with $\Delta t = 0.001$s.

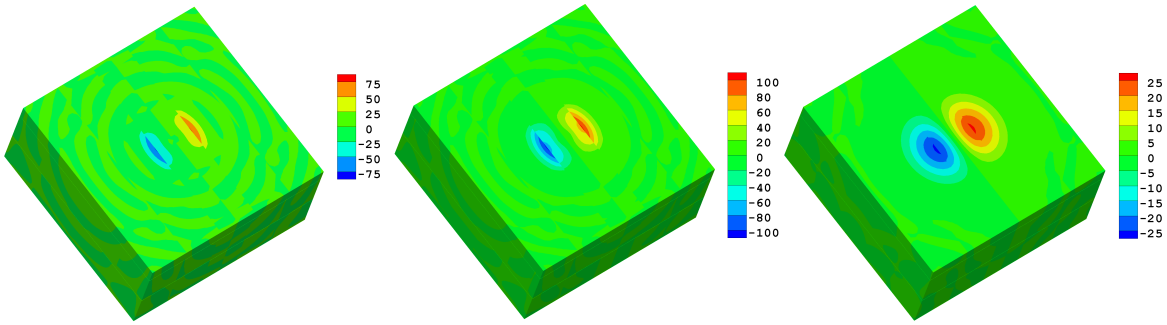

Fig. 7.15 First derivatives of the solution in the x-direction for the GFEM solution at times $t = 0.1, 0.5$ and 1.0s from left to right. The distributions are obtained with $\Delta t = 0.001$s.

combination $q = 4, 5, 6$ (Case-4) having enrichment functions with comparatively flatter gradients results in higher errors. Further enrichment functions with more possible combinations can also be used for the optimal selection of $q-$bands for any considered problem. A suitably selected combination can improve the accuracy considerably. For problems with unknown analytical solutions, the presented error estimate can be used

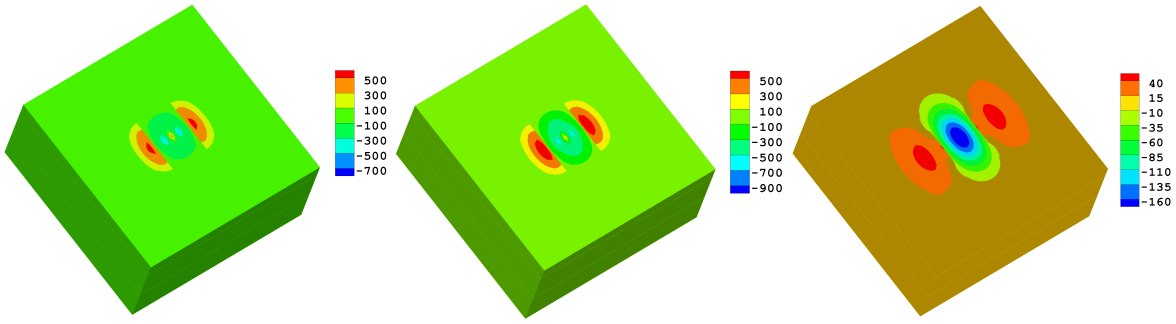

Fig. 7.16 Second derivatives of the solution in the x-direction for the GFEM solution at times $t = 0.1, 0.5$ and 1.0s from left to right. The distributions are obtained with $\Delta t = 0.001$s.

to select the optimal $q-$combination.

7.4 Conclusions

In this chapter, the effectiveness of the proposed *a-posteriori* error estimate for GFEM solutions of time–dependent heat transfer problems in 3D domains is investigated. The proposed error estimate is tested for two example problems. In the first example, with a known analytical solution, the error estimates are compared to the computed relative errors obtained from the GFEM results and the analytical solution. It is concluded that the proposed error estimate efficiently bound the actual errors of the GFEM solution and the ratio of the error estimator to the actual error in about 10, in all cases. The presented error estimate is also compared with the L_2 norm error and it is shown that both follows similar trends at all the simulation times. To show the possible use of the proposed error estimate for the optimal selection of enrichment function and subsequently better accuracy of the approximate solution, different numerical studies are performed. For all the studies, it is shown that the error estimate effectively capture the solution trends and can be used an alternative for the L_2 norm error for problems with no known analytical solution. The second example considers a problem where the exact solution is not known. Again, a similar behaviour seen in the previous test example is observed where the error estimates are shown to decrease as the number

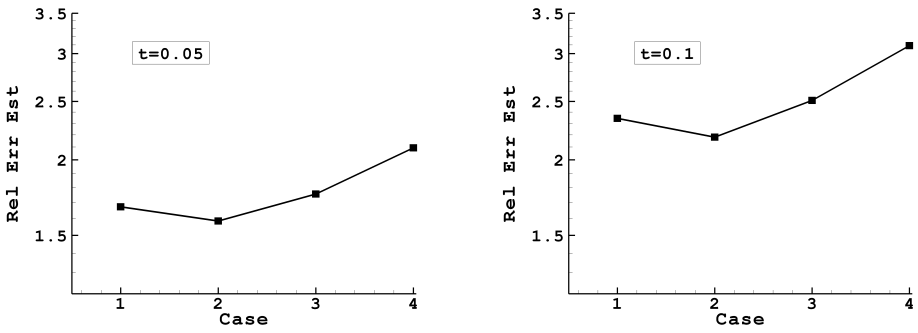

(a) $t = 0.05$s

(b) $t = 0.1$s

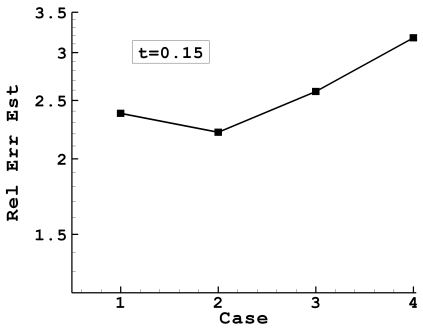

(c) $t = 0.15$s

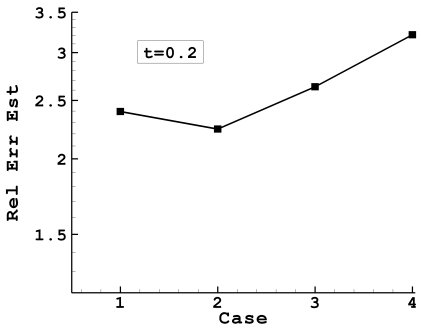

(d) $t = 0.2$s

Fig. 7.17 Variation of rel η with different $q-$bands for Example problem 2.

of enrichment functions is increased. Also a comparatively better $q-$combination is evaluated for Example problem 2 with the help of the proposed error estimate. Although the proposed approach is studied for one type of enrichment functions, the same approach can be followed with any other type of enrichment functions.

Chapter 8

Conclusions and Future Development

8.1 Conclusions

The work presented in this thesis addresses a limitation of the classical FEM for efficient solution of time dependent heat transfer problems with sharp gradients. The proposed alternative is based on field enrichment with time-independent functions. The new shape functions are therefore the product of Gaussian functions with various decay rates, to capture the sharp variations of the temperature field, and linear Lagrange functions, to automatically ensure inter-element continuity. This approach has proven efficient in solving time dependent heat transfer problems with sharp gradients on coarse mesh grids. Moreover, given that the enriching functions are time-independent, the problem matrix is evaluated only at the first time step and reused at the subsequent time steps. This aspect and the enrichment technique used on the coarse mesh grid has led to significant reduction of the computational effort, in comparison to the widely used low-order classical FEM.

Indeed GFEM with time-independent enrichment is shown to produce better quality results and requires less DOFs in comparison to the classical FEM. However, com-

paring GFEM to a low-order FEM is not fair since GFEM is considered as a high-order method. This comparison is of practical interest in the sense FEM codes based on low order elements, in particular Lagrange linear elements, can easily be adapted by incorporating enrichment functions and introducing minor changes to produce efficient approaches to solve challenging issues, such as steep gradient in time-dependent heat diffusion problems.

The extension of GFEM to the three-dimensional case has confirmed the main advantages of the enrichment approach achieved in the two-dimensional case, in comparison to FEM. For 3D case and for a comparable accuracy, a reduction of more than 95% of the required degrees of freedom is achieved with GFEM. Both h and q refinements are considered and it is concluded that such methods perform better on coarse mesh grids and more enrichment functions, rather than refined mesh grids and low enrichment. However, the number of field enrichment functions can only be increased up to a certain level after which the system matrix ill-conditioning aspect starts affecting the quality of the results.

The other contribution of this work consists in the development of an *a-posteriori* error estimate for the GFEM approach to evaluate upper bounds of the numerical errors in the solutions of time–dependent heat transfer problems. A detailed mathematical formulation is presented for the 2D case first and the concept is then extended to 3D. The residual estimate does not depend on the choice of enrichment functions and is shown to efficiently and reliably reflect the behaviour of the numerical error of GFEM on coarse mesh grids. It also reflects the errors incurred in the poorly conditioned systems typically encountered in field enriched methods.

The results indicate the potential of the *a-posteriori* error estimate to be used for an adaptive local choice of the number of the enrichment functions. An adaptive algorithm is proposed to selectively add enrichment functions in elements with relatively

higher error indicators. The results obtained for the uniform enrichment case and the adaptive enrichment case show that, for a comparable accuracy, the proposed adaptive algorithm offers a further reduction in the computational cost, in terms of the required DOFs, as compared to the uniform enrichment case and hence also reducing the required computational time.

The effect of condition number on the quality of results is also investigated. It is concluded that further adding enrichment functions improves the results only up to a certain limit. Any further enrichment makes the system matrix ill-conditioned and thus affecting the quality of the results. With the developed adaptive enrichment algorithm, it is proposed to cap the condition number to a certain limit and reduce the number of enrichment functions at elements exceeding this limit. This decreases the overall condition number of the system matrix and improves the results while further reducing the computational cost.

8.2 Ideas for Further Work

Based on the achievements of this work, there are many potential ideas for future work in order to further enhance the capabilities of GFEM for effective solutions of time dependent heat transfer problems with sharp gradients. Here are some examples:

- In this work, mainly Gaussian functions were used as enrichment functions in the GFEM approach. It is worth exploring the use of other potential functions which may effectively model the solution behaviour while keeping the conditioning within acceptable limits. Such functions do not have to be solutions of the scalar transient diffusion equation. They may be intuitively devised functions based on practical experience of the problem.

- To address the issue of ill-conditioning of the standard GFEM, the concept of Stable Generalized Finite Element Method (SGFEM) may be investigated. It is claimed that the SGFEM conditioning to be of the same order as in standard FEM. This may allow the use of higher numbers of enriching functions and thus further reducing the computational cost.

- The developed *a-posteriori* error estimate is proposed and tested on 2D problems and the concept was then extended to 3D problems. For 2D problems, an adaptive refinement procedure is also devised to further reduce the necessary DOFs for a prescribed accuracy. This can be applied to 3D problems too, for which the reduction in the required DOFs should be more significant.

- In the current work, the employed enrichment functions are tailored to effectively capture sharp gradients on coarse mesh grids. The same concept can be used to devise enrichment functions to deal with time-dependent heat diffusion problems with singularities. In fact developing GFEM for problems exhibiting both strong boundary layers and singularities would be of great interest.

- Finally, the developed error estimate in this thesis is based on residual errors. However, goal-oriented errors are another avenue whereby for a given temperature at a boundary, for example, the field variable is adaptively computed so that the error in the defined goal quantity is as small as possible. This approach may be well suited for GFEM and the choice of enrichment functions.

References

[1] Abaqus, V. (2014). 6.14 documentation. *Dassault Systemes Simulia Corporation*.

[2] Abdelaziz, Y. and Hamouine, A. (2008). A survey of the extended finite element. *Computers & Structures*, 86(11-12):1141–1151.

[3] Ainsworth, M. and Oden, J. T. (1993). A unified approach to a posteriori estimation using element residual methods. *Numerische Mathematik*, 65(1):23–50.

[4] Ainsworth, M. and Oden, J. T. (1997). A posteriori error estimation in finite element analysis. *Computer Methods in Applied Mechanics and Engineering*, 142(1-2):1–88.

[5] Ainsworth, M. and Oden, J. T. (2011). *A posteriori error estimation in finite element analysis*, volume 37. John Wiley & Sons.

[6] Amara, M., Calandra, H., Dejllouli, R., and Grigoroscuta-Strugaru, M. (2012). A stable discontinuous Galerkin-type method for solving efficiently Helmholtz problems. *Computers & Structures*, 106:258–272.

[7] Ancey, C., Coussot, P., and Evesque, P. (1996). Examination of the possibility of a fluid-mechanics treatment of dense granular flows. *Mechanics of Cohesive-frictional Materials*, 1(4):385–403.

[8] Aquino, W., Brigham, J., Earls, C., and Sukumar, N. (2009). Generalized finite element method using proper orthogonal decomposition. *International Journal for Numerical Methods in Engineering*, 79(7):887–906.

[9] Axeelsson, O. (2004). *Finite Difference Methods, Encyclopedia of Computational Mechanics*. John Wiley & Sons Inc.

[10] Babuška, I. and Banerjee, U. (2012). Stable generalized finite element method (SGFEM). *Computer Methods in Applied Mechanics and Engineering*, 201:91–111.

[11] Babuška, I., Banerjee, U., and Osborn, J. E. (2002). On principles for the selection of shape functions for the generalized finite element method. *Computer Methods in Applied Mechanics and Engineering*, 191(49):5595–5629.

[12] Babuška, I., Banerjee, U., and Osborn, J. E. (2003). Survey of meshless and generalized finite element methods: a unified approach. *Acta Numerica*, 12:1–125.

[13] Babuška, I., Banerjee, U., and Osborn, J. E. (2004). Generalized finite element methods—main ideas, results and perspective. *International Journal of Computational Methods*, 1(01):67–103.

[14] Babuška, I., Caloz, G., and Osborn, J. E. (1992). Special finite element methods for a class of second order elliptic problems with rough coefficients. Technical report, DTIC Document.

[15] Babuška, I., Caloz, G., and Osborn, J. E. (1994). Special finite element methods for a class of second order elliptic problems with rough coefficients. *SIAM Journal on Numerical Analysis*, 31(4):945–981.

[16] Babuška, I., Ihlenburg, F., Strouboulis, T., and Gangaraj, S. (1997). A posteriori error estimation for finite element solutions of Helmholtz' equation. Part I: The quality of local indicators and estimators. *International Journal for Numerical Methods in Engineering*, 40(18):3443–3462.

[17] Babuška, I. and Melenk, J. M. (1997). The partition of unity method. *International Journal for Numerical Methods in Engineering*, 40(4):727–758.

[18] Babuška, I. and Miller, A. (1987). A feedback finite element method with a posteriori error estimation: Part I. the finite element method and some basic properties

of the a posteriori error estimator. *Computer Methods in Applied Mechanics and Engineering*, 61(1):1–40.

[19] Babuška, I. and Rheinboldt, W. C. (1978a). A-posteriori error estimates for the finite element method. *International Journal for Numerical Methods in Engineering*, 12(10):1597–1615.

[20] Babuška, I. and Rheinboldt, W. C. (1978b). Error estimates for adaptive finite element computations. *SIAM Journal on Numerical Analysis*, 15(4):736–754.

[21] Babuska, I. and Rheinboldt, W. C. (1981). A posteriori error analysis of finite element solutions for one-dimensional problems. *SIAM Journal on Numerical Analysis*, 18(3):565–589.

[22] Babuška, I. and Strouboulis, T. (2001). *The finite element method and its reliability*. Oxford university press.

[23] Babuška, I., Whiteman, J., and Strouboulis, T. (2010). *Finite elements: an introduction to the method and error estimation*. Oxford University Press.

[24] BabuškaRID, I., GuoRID, B., et al. (2000). Optimal estimates for lower and upper bounds of approximation errors in the p-version of the finite element method in two dimensions. *Numerische Mathematik*, 85(2):219–255.

[25] Banerjee, S. and Sukumar, N. (2017). Exact integration scheme for planewave-enriched partition of unity finite element method to solve the Helmholtz problem. *Computer Methods in Applied Mechanics and Engineering*, 317:619–648.

[26] Bank, R. E. and Weiser, A. (1985). Some a posteriori error estimators for elliptic partial differential equations. *Mathematics of Computation*, 44(170):283–301.

[27] Barros, F., Proença, S., and de Barcellos, C. (2004). On error estimator and p-adaptivity in the generalized finite element method. *International Journal for Numerical Methods in Engineering*, 60(14):2373–2398.

[28] Barros, F. B., de Barcellos, C. S., Duarte, C. A., and Torres, D. A. (2013). Subdomain-based error techniques for generalized finite element approximations of problems with singular stress fields. *Computational Mechanics*, 52(6):1395–1415.

[29] Bathe, K.-J. (2006). *Finite element procedures*. Klaus-Jurgen Bathe.

[30] Bayliss, A., Goldstein, C. I., and Turkel, E. (1985). On accuracy conditions for the numerical computation of waves. *Journal of Computational Physics*, 59(3):396–404.

[31] Belytschko, T. and Black, T. (1999). Elastic crack growth in finite elements with minimal remeshing. *International Journal for Numerical Methods in Engineering*, 45(5):601–620.

[32] Belytschko, T., Gracie, R., and Ventura, G. (2009). A review of extended/generalized finite element methods for material modeling. *Modelling and Simulation in Materials Science and Engineering*, 17(4):043001.

[33] Bespalov, A., Praetorius, D., Rocchi, L., and Ruggeri, M. (2018). Goal-oriented error estimation and adaptivity for elliptic pdes with parametric or uncertain inputs. *arXiv preprint arXiv:1806.03928*.

[34] Bettess, P. (2004). Short–wave scattering: problems and techniques. *Philosophical Transactions of the Royal Society of London A: Mathematical, Physical and Engineering Sciences*, 362(1816):421–443.

[35] Bettess, P. and Bettess, J. A. (1986). A profile matrix solver with built-in constraint facility. *Engineering Computations*, 3(3):209–216.

[36] Bordas, S. and Duflot, M. (2007). Derivative recovery and a posteriori error estimate for extended finite elements. *Computer Methods in Applied Mechanics and Engineering*, 196(35):3381–3399.

[37] Bordas, S., Duflot, M., and Le, P. (2008). A simple error estimator for extended finite elements. *Communications in Numerical Methods in Engineering*, 24(11):961–971.

[38] Borker, R., Farhat, C., and Tezaur, R. (2017). A discontinuous galerkin method with lagrange multipliers for spatially-dependent advection–diffusion problems. *Computer Methods in Applied Mechanics and Engineering*, 327:93–117.

[39] Bouillard, P. and Ihlenburg, F. (1999). Error estimation and adaptivity for the finite element method in acoustics: 2D and 3D applications. *Computer Methods in Applied Mechanics and Engineering*, 176(1):147–163.

[40] Cessenat, O. and Despres, B. (1998). Application of an ultra weak variational formulation of elliptic PDEs to the two-dimensional Helmholtz problem. *SIAM Journal on Numerical Analysis*, 35(1):255–299.

[41] Chadwick, E., Bettess, P., and Laghrouche, O. (1999). Diffraction of short waves modelled using new mapped wave envelope finite and infinite elements. *International Journal for Numerical Methods in Engineering*, 45(3):335–354.

[42] Coppola-Owen, A. and Codina, R. (2005). Improving eulerian two-phase flow finite element approximation with discontinuous gradient pressure shape functions. *International Journal for Numerical Methods in Fluids*, 49(12):1287–1304.

[43] Cosimo, A., Fachinotti, V., and Cardona, A. (2013). An enrichment scheme for solidification problems. *Computational Mechanics*, 52(1):17–35.

[44] de Borst, R. (2004). *Solids and Structures: Introduction and Survey, Encyclopedia of Computational Mechanics.* John Wiley & Sons Inc.

[45] de La Bourdonnaye, A. (1994). Une methode de discretisation microlocale et son application a un problemede diffraction. *Comptes rendus de l'Académie des sciences. Série 1, Mathématique*, 318(4):385–388.

[46] Demkowicz, L., Oden, J., and Strouboulis, T. (1984). Adaptive finite elements for flow problems with moving boundaries. part I: Variational principles and a posteriori estimates. *Computer Methods in Applied Mechanics and Engineering*, 46(2):217–251.

[47] Desmet, W. and Vandepitte, D. (2002). Mid-frequency vibro-acoustic modelling: challenges and potential solutions. In *Proceedings of ISMA*, volume 2, page 12.

[48] Diwan, G., Mohamed, M., Seaid, M., Trevelyan, J., and Laghrouche, O. (2015). Mixed enrichment for the finite element method in heterogeneous media. *International Journal for Numerical Methods in Engineering*, 101(1):54–78.

[49] Dolbow, J. and Belytschko, T. (1999). A finite element method for crack growth without remeshing. *International Journal for Numerical Methods in Engineering*, 46(1):131–150.

[50] Dolbow, J., Moës, N., and Belytschko, T. (2000). Discontinuous enrichment in finite elements with a partition of unity method. *Finite elements in analysis and design*, 36(3-4):235–260.

[51] Dolbow, J. E. (1999). *An extended finite element method with discontinuous enrichment for applied mechanics.* PhD thesis, Northwestern University, USA.

[52] Drolia, M., Mohamed, M., Laghrouche, O., Seaid, M., and Trevelyan, J. (2017). Enriched finite elements for initial-value problem of transverse electromagnetic waves in time domain. *Computers & Structures*, 182:354–367.

[53] Duarte, A. and Simone, A. (2012). An introduction to partition of unity and generalized finite element methods. *Departament of Civil Enginnering, UNICAMP, Campinas, Brazil*.

[54] Duarte, C. A. (1996). *The hp cloud method*. PhD thesis, The University of Texas at Austin, Austin, TX, USA.

[55] Duarte, C. A., Babuška, I., and Oden, J. T. (2000). Generalized finite element methods for three-dimensional structural mechanics problems. *Computers & Structures*, 77(2):215–232.

[56] Duarte, C. A. and Kim, D.-J. (2008). Analysis and applications of a generalized finite element method with global–local enrichment functions. *Computer Methods in Applied Mechanics and Engineering*, 197(6):487–504.

[57] Duarte, C. A., Kim, D.-J., and Babuška, I. (2007). A global-local approach for the construction of enrichment functions for the generalized FEM and its application to three-dimensional cracks. In *Advances in Meshfree Techniques*, pages 1–26. Springer.

[58] Duarte, C. A. and Oden, J. T. (1996a). An *h-p* adaptive method using clouds. *Computer Methods in Applied Mechanics and Engineering*, 139(1):237–262.

[59] Duarte, C. A. and Oden, J. T. (1996b). *H-p* clouds–An *h-p* Meshless Method. *Numerical Methods for Partial Differential Equations*, 12(6):673–706.

[60] Duflot, M. and Bordas, S. (2008). A posteriori error estimation for extended finite elements by an extended global recovery. *International Journal for Numerical Methods in Engineering*, 76:1123–1138.

[61] El Kacimi, A. and Laghrouche, O. (2009). Numerical modelling of elastic wave scattering in frequency domain by the partition of unity finite element method. *International Journal for Numerical Methods in Engineering*, 77(12):1646–1669.

[62] El Kacimi, A. and Laghrouche, O. (2010a). Improvement of PUFEM for the numerical solution of high-frequency elastic wave scattering on unstructured triangular mesh grids. *International Journal for Numerical Methods in Engineering*, 84(3):330–350.

[63] El Kacimi, A. and Laghrouche, O. (2010b). Numerical analysis of two plane wave finite element schemes based on the partition of unity method for elastic wave scattering. *Computers & Structures*, 88(23):1492–1497.

[64] Evangelista, F., Roesler, J. R., and Duarte, C. A. (2013). Two-scale approach to predict multi-site cracking potential in 3-D structures using the generalized finite element method. *International Journal of Solids and Structures*, 50(13):1991–2002.

[65] Farhat, C., Harari, I., and Franca, L. P. (2001). The discontinuous enrichment method. *Computer Methods in Applied Mechanics and Engineering*, 190(48):6455–6479.

[66] Frank, M., Klar, A., Larsen, E. W., and Yasuda, S. (2007). Time-dependent simplified P_N approximation to the equations of radiative transfer. *Journal of Computational Physics*, 226(2):2289–2305.

[67] Fries, T.-P. (2008). A corrected XFEM approximation without problems in blending elements. *International Journal for Numerical Methods in Engineering*, 75(5):503–532.

[68] Fries, T.-P. and Belytschko, T. (2010). The extended/generalized finite element method: an overview of the method and its applications. *International Journal for Numerical Methods in Engineering*, 84(3):253–304.

[69] Gabard, G. (2007). Discontinuous galerkin methods with plane waves for time-harmonic problems. *Journal of Computational Physics*, 225(2):1961–1984.

[70] Gago, D. S., Kelly, D., Zienkiewicz, O., Babuska, I., et al. (1983). A posteriori error analysis and adaptive processes in the finite element method: Part II—adaptive mesh refinement. *International Journal for Numerical Methods in Engineering*, 19(11):1621–1656.

[71] Gallimard, L. and Panetier, J. (2006). Error estimation of stress intensity factors for mixed-mode cracks. *International Journal for Numerical Methods in Engineering*, 68(3):299–316.

[72] Gamallo, P. and Astley, R. (2006). The partition of unity finite element method for short wave acoustic propagation on non-uniform potential flows. *International Journal for Numerical Methods in Engineering*, 65(3):425–444.

[73] González-Estrada, O. A., Ródenas, J. J., Bordas, S., Duflot, M., Kerfriden, P., and Giner, E. (2012). On the role of enrichment and statical admissibility of re-

covered fields in a posteriori error estimation for enriched finite element methods. *Engineering Computations*, 29(8):814–841.

[74] González-Estrada, O. A., Ródenas, J. J., Bordas, S., Nadal, E., Kerfriden, P., and Fuenmayor, F. J. (2015). Locally equilibrated stress recovery for goal oriented error estimation in the extended finite element method. *Computers & Structures*, 152:1–10.

[75] Grätsch, T. and Bathe, K.-J. (2005). A posteriori error estimation techniques in practical finite element analysis. *Computers & Structures*, 83(4):235–265.

[76] Guo, M. and Zhong, H. (2017). Strict upper and lower bounds for quantities of interest in static response sensitivity analysis. *Applied Mathematical Modelling*, 49:17–34.

[77] Gupta, V., Kim, D.-J., and Duarte, A. (2013). Extensions of the two-scale generalized finite element method to nonlinear fracture problems. *International Journal for Multiscale Computational Engineering*, 11(6).

[78] Gupta, V., Kim, D.-J., and Duarte, C. A. (2012). Analysis and improvements of global–local enrichments for the generalized finite element method. *Computer Methods in Applied Mechanics and Engineering*, 245:47–62.

[79] Ham, S. and Bathe, K.-J. (2012). A finite element method enriched for wave propagation problems. *Computers & Structures*, 94:1–12.

[80] Hansbo, A. and Hansbo, P. (2004). A finite element method for the simulation of strong and weak discontinuities in solid mechanics. *Computer Methods in Applied Mechanics and Engineering*, 193(33):3523–3540.

[81] Higdon, R. L. (1986). Absorbing boundary conditions for difference approximations to the multidimensional wave equation. *Mathematics of Computation*, 47(176):437–459.

[82] Hinton, E. and Campbell, J. (1974). Local and global smoothing of discontinuous finite element functions using a least squares method. *International Journal for Numerical Methods in Engineering*, 8(3):461–480.

[83] Huttunen, T., Gamallo, P., and Astley, R. J. (2009). Comparison of two wave element methods for the Helmholtz problem. *Communications in Numerical Methods in Engineering*, 25(1):35–52.

[84] Huttunen, T., Monk, P., Collino, F., and Kaipio, J. P. (2004). The ultra-weak variational formulation for elastic wave problems. *SIAM Journal on Scientific Computing*, 25(5):1717–1742.

[85] Huttunen, T., Monk, P., and Kaipio, J. P. (2002). Computational aspects of the ultra-weak variational formulation. *Journal of Computational Physics*, 182(1):27–46.

[86] Ihlenburg, F. and Babuška, I. (1995). Finite element solution of the Helmholtz equation with high wave number Part I: The *h*-version of the FEM. *Computers & Mathematics with Applications*, 30(9):9–37.

[87] Ihlenburg, F. and Babuska, I. (1997). Finite element solution of the Helmholtz equation with high wave number Part II: the *hp*-version of the FEM. *SIAM Journal on Numerical Analysis*, 34(1):315–358.

[88] Iqbal, M., Gimperlein, H., Mohamed, M. S., and Laghrouche, O. (2017). An a posteriori error estimate for the generalized finite element method for transient heat diffusion problems. *International Journal for Numerical Methods in Engineering*, 110(12):1103–1118.

[89] Jin, Y., González-Estrada, O., Pierard, O., and Bordas, S. (2017). Error-controlled adaptive extended finite element method for 3D linear elastic crack propagation. *Computer Methods in Applied Mechanics and Engineering*.

[90] Kalashnikova, I., Farhat, C., and Tezaur, R. (2009). A discontinuous enrichment method for the finite element solution of high péclet advection–diffusion problems. *Finite elements in Analysis and Design*, 45(4):238–250.

[91] Kelly, D., Gago, D. S., Zienkiewicz, O., Babuska, I., et al. (1983). A posteriori error analysis and adaptive processes in the finite element method: Part I—error analysis. *International Journal for Numerical Methods in Engineering*, 19(11):1593–1619.

[92] Kergrene, K., B. I. and Banerjee, U. (2016). Stable generalized finite element method and associated iterative schemes; application to interface problems. *Computer Methods in Applied Mechanics and Engineering*, 305:1–36.

[93] Kergrene, K., Prudhomme, S., Chamoin, L., and Laforest, M. (2017). A new goal-oriented formulation of the finite element method. *Computer Methods in Applied Mechanics and Engineering*, 327:256–276.

[94] Kim, D.-J., Duarte, C. A., and Pereira, J. P. (2008). Analysis of interacting cracks using the generalized finite element method with global-local enrichment functions. *Journal of Applied Mechanics*, 75(5):051107.

[95] Kim, D.-J., Duarte, C. A., and Proença, S. P. (2012). A generalized finite element method with global-local enrichment functions for confined plasticity problems. *Computational Mechanics*, 50(5):563–578.

[96] Kim, D.-J., Pereira, J., and Duarte, C. (2010). Analysis of three-dimensional fracture mechanics problems: A two-scale approach using coarse-generalized FEM meshes. *International Journal for Numerical Methods in Engineering*, 81(3):335–365.

[97] Kim, J. and Duarte, C. (2015). A new generalized finite element method for two-scale simulations of propagating cohesive fractures in 3-D. *International Journal for Numerical Methods in Engineering*, 104(13):1139–1172.

[98] Klar, A., Lang, J., and Seaïd, M. (2005). Adaptive solutions of SPN-approximations to radiative heat transfer in glass. *International Journal of Thermal Sciences*, 44(11):1013–1023.

[99] Klose, A. D. and Larsen, E. W. (2006). Light transport in biological tissue based on the simplified spherical harmonics equations. *Journal of Computational Physics*, 220(1):441–470.

[100] Komijani, M. and Gracie, R. (2017). An enriched finite element model for wave propagation in fractured media. *Finite Elements in Analysis and Design*, 125:14–23.

[101] Ladevèze, P. (1996). A new computational approach for structure vibrations in the medium frequency range. *Comptes Rendus de L Academie des Sciences Serie II Fascicule B-Mecanique Physique Chimie Astronomie*, 322(12):849–856.

[102] Ladeveze, P., Rouch, P., Riou, H., and Bohineust, X. (2003). Analysis of medium-frequency vibrations in a frequency range. *Journal of Computational Acoustics*, 11(02):255–283.

[103] Laghrouche, O. and Bettess, P. (2000). Short wave modelling using special finite elements. *Journal of Computational Acoustics*, 8(01):189–210.

[104] Laghrouche, O., Bettess, P., and Astley, R. J. (2002). Modelling of short wave diffraction problems using approximating systems of plane waves. *International Journal for Numerical Methods in Engineering*, 54(10):1501–1533.

[105] Laghrouche, O., Bettess, P., Perrey-Debain, E., and Trevelyan, J. (2003). Plane wave basis finite-elements for wave scattering in three dimensions. *Communications in Numerical Methods in Engineering*, 19(9):715–723.

[106] Laghrouche, O., Bettess, P., Perrey-Debain, E., and Trevelyan, J. (2005). Wave interpolation finite elements for Helmholtz problems with jumps in the wave speed. *Computer Methods in Applied Mechanics and Engineering*, 194(2):367–381.

[107] Laghrouche, O. and Mohamed, M. (2010). Locally enriched finite elements for the Helmholtz equation in two dimensions. *Computers & Structures*, 88(23):1469–1473.

[108] Langdon, S. and Chandler-Wilde, S. N. (2006). A wavenumber independent boundary element method for an acoustic scattering problem. *SIAM Journal on Numerical Analysis*, 43(6):2450–2477.

[109] Lewis, P. E. and Ward, J. P. (1991). *The Finite Element Method: Principles and Applications*. Addison-Wesley.

[110] Li, B. (1994). A generalized conjugate gradient model for the mild slope equation. *Coastal Engineering*, 23(3-4):215–225.

[111] Lin, Z., Zhuang, Z., You, X., Wang, H., and Xu, D. (2012). Enriched goal-oriented error estimation applied to fracture mechanics problems solved by XFEM. *Acta Mechanica Solida Sinica*, 25(4):393–403.

[112] Lins, R., Ferreira, M., Proença, S., and Duarte, C. (2015). An a-posteriori error estimator for linear elastic fracture mechanics using the stable generalized/extended finite element method. *Computational Mechanics*, 56(6):947–965.

[113] Liszka, T., Duarte, C., and Tworzydlo, W. (1996). hp-meshless cloud method. *Computer Methods in Applied Mechanics and Engineering*, 139(1-4):263–288.

[114] Liu, G. and Gu, Y. (2010). *An Introduction to Meshfree Methods and Their Programming*. Springer Publishing Company, Incorporated.

[115] Liu, G.-R. (2009). *Meshfree methods: moving beyond the finite element method*. Taylor & Francis.

[116] Loehnert, S., Mueller-Hoeppe, D., and Wriggers, P. (2011). 3D corrected XFEM approach and extension to finite deformation theory. *International Journal for Numerical Methods in Engineering*, 86(4-5):431–452.

[117] Loehnert, S., Prange, C., and Wriggers, P. (2012). Error controlled adaptive multiscale XFEM simulation of cracks. *International Journal of Fracture*, 178(1-2):147–156.

[118] LS-DYNA, I. (2013). LS-DYNA user's manual. *LS-DYNA, Livermore Software Technology Corporation, Livermore, CA, USA*, 4.

[119] Mahmood, M., Laghrouche, O., Trevelyan, J., and El Kacimi, A. (2017). Implementation and computational aspects of a 3D elastic wave modelling by PUFEM. *Applied Mathematical Modelling*, 49:568–586.

[120] Malekan, M., Barros, F. B., Pitangueira, R. L., and Alves, P. D. (2016). An object-oriented class organization for global-local generalized finite element method. *Latin American Journal of Solids and Structures*, 13(13):2529–2551.

[121] Mayer, P. and Mandel, J. (1997). *The finite ray element method for the Helmholtz equation of scattering: first numerical experiments*. University of Colorado at Denver, Center for Computational Mathematics Denver.

[122] Melenk, J. M. (1995). *On generalized finite element methods*. PhD thesis, The University of Maryland,USA.

[123] Melenk, J. M. and Babuška, I. (1996). The partition of unity finite element method: basic theory and applications. *Computer Methods in Applied Mechanics and Engineering*, 139(1):289–314.

[124] Melenk, J. M. and Babuška, I. (1997). The partition of unity method. *International Journal for Numerical Methods in Engineering*, 40:727–758.

[125] Melenk, J. M. and Wohlmuth, B. I. (2001). On residual-based a posteriori error estimation in hp-fem. *Advances in Computational Mathematics*, 15(1-4):311–331.

[126] Mohamed, M., Seaid, M., Trevelyan, J., and Laghrouche, O. (2013a). A partition of unity FEM for time-dependent diffusion problems using multiple enrichment

functions. *International Journal for Numerical Methods in Engineering*, 93(3):245–265.

[127] Mohamed, M. S. (2010). *Numerical aspects of the PUFEM for efficient solution of Helmholtz problems*. PhD thesis, Heriot-Watt University.

[128] Mohamed, M. S., Laghrouche, O., and El-Kacimi, A. (2010). Some numerical aspects of the PUFEM for efficient solution of 2D Helmholtz problems. *Computers & Structures*, 88(23):1484–1491.

[129] Mohamed, M. S., Seaïd, M., Trevelyan, J., and Laghrouche, O. (2013b). Time-independent hybrid enrichment for finite element solution of transient conduction–radiation in diffusive grey media. *Journal of Computational Physics*, 251:81–101.

[130] Mohamed, M. S., Seaïd, M., Trevelyan, J., and Laghrouche, O. (2014). An enriched finite element model with q-refinement for radiative boundary layers in glass cooling. *Journal of Computational Physics*, 258:718–737.

[131] Monk, P. and Wang, D.-Q. (1999). A least-squares method for the Helmholtz equation. *Computer Methods in Applied Mechanics and Engineering*, 175(1-2):121–136.

[132] Munts, E. A., Hulshoff, S. J., and De Borst, R. (2003). The partition-of-unity method for linear diffusion and convection problems: Accuracy, stabilization and multiscale interpretation. *International Journal for Numerical Methods in Fluids*, 43(2):199–213.

[133] Nguyen, V. P., Rabczuk, T., Bordas, S., and Duflot, M. (2008). Meshless methods: A review and computer implementation aspects. *Mathematics and Computers in Simulation*, 79(3):763–813.

[134] Oden, J. and Brauchli, H. (1971). On the calculation of consistent stress distributions in finite element approximations. *International Journal for Numerical Methods in Engineering*, 3(3):317–325.

[135] Oden, J. T., Demkowicz, L., Rachowicz, W., and Westermann, T. (1989). Toward a universal hp adaptive finite element strategy, part 2. a posteriori error estimation. *Computer Methods in Applied Mechanics and Engineering*, 77(1-2):113–180.

[136] Oden, J. T., Duarte, C., and Zienkiewicz, O. C. (1998). A new cloud-based hp finite element method. *Computer Methods in Applied Mechanics and Engineering*, 153(1):117–126.

[137] Oden, J. T. and Prudhomme, S. (2001). Goal-oriented error estimation and adaptivity for the finite element method. *Computers & Mathematics with Applications*, 41(5-6):735–756.

[138] Oden, J. T., Prudhomme, S., and Demkowicz, L. (2005). A posteriori error estimation for acoustic wave propagation problems. *Archives of Computational Methods in Engineering*, 12(4):343–389.

[139] O'Hara, P. (2007). *Finite element analysis of three-dimensional heat transfer for problems involving sharp thermal gradients*. Master's thesis, University of Illinois at Urbana-Champaign, USA.

[140] O'Hara, P., Duarte, C., and Eason, T. (2010). Investigation of allowable time-step sizes for generalized finite element analysis of the transient heat equation. *Interaction and Multiscale Mechanics*, 3(3):235–255.

[141] O'Hara, P., Duarte, C., and Eason, T. (2011). Transient analysis of sharp thermal gradients using coarse finite element meshes. *Computer Methods in Applied Mechanics and Engineering*, 200(5):812–829.

[142] O'Hara, P., Duarte, C., and Eason, T. (2016). A two-scale generalized finite element method for interaction and coalescence of multiple crack surfaces. *Engineering Fracture Mechanics*, 163:274–302.

[143] O'Hara, P., Duarte, C. A., and Eason, T. (2009). Generalized finite element anal-

ysis of three-dimensional heat transfer problems exhibiting sharp thermal gradients. *Computer Methods in Applied Mechanics and Engineering*, 198(21):1857–1871.

[144] O'Hara, P., Duarte, C. A., Eason, T., and Garzon, J. (2013). Efficient analysis of transient heat transfer problems exhibiting sharp thermal gradients. *Computational Mechanics*, 51:743–764.

[145] Ortiz, P. (2004). Finite elements using a plane-wave basis for scattering of surface water waves. *Philosophical Transactions of the Royal Society of London A: Mathematical, Physical and Engineering Sciences*, 362(1816):525–540.

[146] Ortiz, P. and Sanchez, E. (2001). An improved partition of unity finite element model for diffraction problems. *International Journal for Numerical Methods in Engineering*, 50(12):2727–2740.

[147] Panetier, J., Ladeveze, P., and Chamoin, L. (2010). Strict and effective bounds in goal-oriented error estimation applied to fracture mechanics problems solved with XFEM. *International Journal for Numerical Methods in Engineering*, 81(6):671–700.

[148] Pannachet, T., Díez, P., Askes, H., and Sluys, L. J. (2010). Error assessment and mesh adaptivity for regularized continuous failure models. *Computer Methods in Applied Mechanics and Engineering*, 199(17):961–978.

[149] Pannachet, T., Sluys, L. J., and Askes, H. (2009). Error estimation and adaptivity for discontinuous failure. *International Journal for Numerical Methods in Engineering*, 78(5):528–563.

[150] Pereira, J. P., Kim, D.-J., and Duarte, C. (2012). A two-scale approach for the analysis of propagating three-dimensional fractures. *Computational Mechanics*, 49(1):99–121.

[151] Perrey-Debain, E., Laghrouche, O., Bettess, P., and Trevelyan, J. (2004a). Plane-wave basis finite elements and boundary elements for three-dimensional wave

scattering. *Philosophical Transactions of the Royal Society of London A: Mathematical, Physical and Engineering Sciences*, 362(1816):561–577.

[152] Perrey-Debain, E., Trevelyan, J., and Bettess, P. (2004b). Wave boundary elements: A theoretical overview presenting applications in scattering of short waves. *Engineering Analysis with Boundary Elements*, 28(2):131–141.

[153] Plews, J. and Duarte, C. (2015). Bridging multiple structural scales with a generalized finite element method. *International Journal for Numerical Methods in Engineering*, 102(3-4):180–201.

[154] Plews, J. and Duarte, C. (2016). A two-scale generalized finite element approach for modeling localized thermoplasticity. *International Journal for Numerical Methods in Engineering*.

[155] Prange, C., Loehnert, S., and Wriggers, P. (2012). Error estimation for crack simulations using the XFEM. *International Journal for Numerical Methods in Engineering*, 91(13):1459–1474.

[156] Prudhomme, S. (2015). A posteriori error estimates of quantities of interest. *Encyclopedia of Applied and Computational Mathematics*, pages 1–5.

[157] Prudhomme, S. and Oden, J. T. (1999). On goal-oriented error estimation for elliptic problems: application to the control of pointwise errors. *Computer Methods in Applied Mechanics and Engineering*, 176(1-4):313–331.

[158] Rannou, A., Gravouil, A., and Baietto-Dubourg, M. (2009). A local multigrid XFEM strategy for 3-D crack propagation. *International Journal for Numerical Methods in Engineering*, 77(5):581–600.

[159] Rao, S. S. (2005). *The finite element method in engineering*. Butterworth-heinemann.

[160] Rivière, B., Wheeler, M. F., and Girault, V. (2001). A priori error estimates for finite element methods based on discontinuous approximation spaces for elliptic problems. *SIAM Journal on Numerical Analysis*, 39(3):902–931.

[161] Ródenas, J. J., González-Estrada, O. A., Díez, P., and Fuenmayor, F. J. (2010). Accurate recovery-based upper error bounds for the extended finite element framework. *Computer Methods in Applied Mechanics and Engineering*, 199(37):2607–2621.

[162] Rodenas, J. J., González-Estrada, O. A., Fuenmayor, F. J., and Chinesta, F. (2013). Enhanced error estimator based on a nearly equilibrated moving least squares recovery technique for FEM and XFEM. *Computational Mechanics*, 52(2):321–344.

[163] Ródenas, J. J., González-Estrada, O. A., Tarancón, J. E., and Fuenmayor, F. J. (2008). A recovery-type error estimator for the extended finite element method based on singular+ smooth stress field splitting. *International Journal for Numerical Methods in Engineering*, 76(4):545–571.

[164] Seaïd, M. (2007). Multigrid Newton–Krylov method for radiation in diffusive semitransparent media. *Journal of Computational and Applied Mathematics*, 203(2):498–515.

[165] Seaïd, M. (2009). An Eulerian–Lagrangian method for coupled parabolic-hyperbolic equations. *Applied Numerical Mathematics*, 59(3):754–768.

[166] Seaıd, M., Frank, M., Klar, A., Pinnau, R., and Thömmes, G. (2004). Efficient numerical methods for radiation in gas turbines. *Journal of Computational and Applied Mathematics*, 170(1):217–239.

[167] Shao, Q., Fernández-González, R., Mikdam, A., Bouhala, L., Younes, A., Núñez, P., Belouettar, S., and Makradi, A. (2014). Influence of heat transfer and fluid flow on crack growth in multilayered porous/dense materials using XFEM: Application

to solid oxide fuel cell like material design. *International Journal of Solids and Structures*, 51(21):3557–3569.

[168] Simpson, R. and Trevelyan, J. (2011a). Evaluation of J_1 and J_2 integrals for curved cracks using an enriched boundary element method. *Engineering Fracture Mechanics*, 78(4):623–637.

[169] Simpson, R. and Trevelyan, J. (2011b). A partition of unity enriched dual boundary element method for accurate computations in fracture mechanics. *Computer Methods in Applied Mechanics and Engineering*, 200(1):1–10.

[170] Soghrati, S. (2014). Hierarchical interface-enriched finite element method: an automated technique for mesh-independent simulations. *Journal of Computational Physics*, 275:41–52.

[171] Soghrati, S., Aragón, A. M., Armando Duarte, C., and Geubelle, P. H. (2012). An interface-enriched generalized FEM for problems with discontinuous gradient fields. *International Journal for Numerical Methods in Engineering*, 89(8):991–1008.

[172] Soghrati, S. and Geubelle, P. H. (2012). A 3D interface-enriched generalized finite element method for weakly discontinuous problems with complex internal geometries. *Computer Methods in Applied Mechanics and Engineering*, 217:46–57.

[173] Song, J.-H., Areias, P., and Belytschko, T. (2006). A method for dynamic crack and shear band propagation with phantom nodes. *International Journal for Numerical Methods in Engineering*, 67(6):868–893.

[174] Strouboulis, T., Babuška, I., and Copps, K. (2000a). The design and analysis of the generalized finite element method. *Computer Methods in Applied Mechanics and Engineering*, 181(1):43–69.

[175] Strouboulis, T., Babuška, I., and Hidajat, R. (2006a). The generalized finite element method for Helmholtz equation: theory, computation, and open problems. *Computer Methods in Applied Mechanics and Engineering*, 195(37):4711–4731.

[176] Strouboulis, T., Copps, K., and Babuska, I. (2000b). The generalized finite element method: an example of its implementation and illustration of its performance. *International Journal for Numerical Methods in Engineering*, 47(8):1401–1417.

[177] Strouboulis, T., Copps, K., and Babuška, I. (2001). The generalized finite element method. *Computer Methods in Applied Mechanics and Engineering*, 190(32):4081–4193.

[178] Strouboulis, T. and Hidajat, R. (2006). Partition of unity method for Helmholtz equation: q-convergence for plane-wave and wave-band local bases. *Applications of Mathematics*, 51(2):181–204.

[179] Strouboulis, T., Hidajat, R., and Babuška, I. (2008). The generalized finite element method for Helmholtz equation. Part II: Effect of choice of handbook functions, error due to absorbing boundary conditions and its assessment. *Computer Methods in Applied Mechanics and Engineering*, 197(5):364–380.

[180] Strouboulis, T., Zhang, L., Wang, D., and Babuška, I. (2006b). A posteriori error estimation for generalized finite element methods. *Computer Methods in Applied Mechanics and Engineering*, 195(9):852–879.

[181] Sukumar, N., Chopp, D. L., Moës, N., and Belytschko, T. (2001). Modeling holes and inclusions by level sets in the extended finite-element method. *Computer Methods in Applied Mechanics and Engineering*, 190(46):6183–6200.

[182] Sussman, T. and Bathe, K.-J. (1986). Studies of finite element procedures—stress band plots and the evaluation of finite element meshes. *Engineering Computations*, 3(3):178–191.

[183] Szabo, B. A. and Babuška, I. (1991). *Finite element analysis*. John Wiley & Sons.

[184] Tabbara, M., Blacker, T., and Belytschko, T. (1994). Finite element deriva-

tive recovery by moving least square interpolants. *Computer Methods in Applied Mechanics and Engineering*, 117(1-2):211–223.

[185] Taylor, R. L., Zienkiewicz, O. C., and Oñate, E. (1998). A hierarchical finite element method based on the partition of unity. *Computer Methods in Applied Mechanics and Engineering*, 152(1):73–84.

[186] Tezaur, R. and Farhat, C. (2006). Three-dimensional discontinuous Galerkin elements with plane waves and Lagrange multipliers for the solution of mid-frequency Helmholtz problems. *International Journal for Numerical Methods in Engineering*, 66(5):796–815.

[187] Tezaur, R., Zhang, L., and Farhat, C. (2008). A discontinuous enrichment method for capturing evanescent waves in multiscale fluid and fluid/solid problems. *Computer Methods in Applied Mechanics and Engineering*, 197(19):1680–1698.

[188] Thömmes, G., Pinnau, R., Seaïd, M., Götz, T., and Klar, A. (2002). Numerical methods and optimal control for glass cooling processes. *Transport Theory and Statistical Physics*, 31:513–529.

[189] Torii, A. J., Machado, R. D., and Arndt, M. (2015). GFEM for modal analysis of 2D wave equation. *Engineering Computations*, 32(6):1779–1801.

[190] Van der Meer, F., Al-Khoury, R., and Sluys, L. (2009). Time-dependent shape functions for modeling highly transient geothermal systems. *International Journal for Numerical Methods in Engineering*, 77(2):240.

[191] Verfürth, R. (1996). *A review of a posteriori error estimation and adaptive mesh-refinement techniques*. John Wiley & Sons Inc.

[192] Viskanta, R. and Anderson, E. E. (1975). Heat transfer in semitransparent solids. *Advances in Heat Transfer*, 11:317–441.

[193] Wells, G. and Sluys, L. (2001). A new method for modelling cohesive cracks using finite elements. *International Journal for Numerical Methods in Engineering*, 50(12):2667–2682.

[194] Xiao, Q. and Karihaloo, B. L. (2006). Improving the accuracy of XFEM crack tip fields using higher order quadrature and statically admissible stress recovery. *International Journal for Numerical Methods in Engineering*, 66(9):1378–1410.

[195] Yu, T. and Gong, Z. (2013). Numerical simulation of temperature field in heterogeneous material with the XFEM. *Archives of Civil and Mechanical Engineering*, 13(2):199–208.

[196] Zhang, L., Tezaur, R., and Farhat, C. (2006). The discontinuous enrichment method for elastic wave propagation in the medium-frequency regime. *International Journal for Numerical Methods in Engineering*, 66(13):2086–2114.

[197] Zienkiewicz, O. C. and Zhu, J. Z. (1987). A simple error estimator and adaptive procedure for practical engineerng analysis. *International Journal for Numerical Methods in Engineering*, 24(2):337–357.

[198] Zienkiewicz, O. C. and Zhu, J. Z. (1992a). The superconvergent patch recovery and a posteriori error estimates. Part 1: The recovery technique. *International Journal for Numerical Methods in Engineering*, 33(7):1331–1364.

[199] Zienkiewicz, O. C. and Zhu, J. Z. (1992b). The superconvergent patch recovery and a posteriori error estimates. Part 2: Error estimates and adaptivity. *International Journal for Numerical Methods in Engineering*, 33(7):1365–1382.